This electronic thesis or dissertation has been downloaded from Explore Bristol Research, http://research-information.bristol.ac.uk

Author:
Garcia-Granada, Andres-Amador

Title:
The effect of creep and mechanical load on cold expanded fastener holes.

General rights
The copyright of this thesis rests with the author, unless otherwise identified in the body of the thesis, and no quotation from it or information derived from it may be published without proper acknowledgement. It is permitted to use and duplicate this work only for personal and non-commercial research, study or criticism/review. You must obtain prior written consent from the author for any other use. It is not permitted to supply the whole or part of this thesis to any other person or to post the same on any website or other online location without the prior written consent of the author.

Take down policy
Some pages of this thesis may have been removed for copyright restrictions prior to it having been deposited in Explore Bristol Research. However, if you have discovered material within the thesis that you believe is unlawful e.g. breaches copyright, (either yours or that of a third party) or any other law, including but not limited to those relating to patent, trademark, confidentiality, data protection, obscenity, defamation, libel, then please contact: open-access@bristol.ac.uk and include the following information in your message:

- Your contact details
- Bibliographic details for the item, including a URL
- An outline of the nature of the complaint

On receipt of your message the Open Access team will immediately investigate your claim, make an initial judgement of the validity of the claim, and withdraw the item in question from public view.

“THE EFFECT OF CREEP AND MECHANICAL LOAD ON COLD EXPANDED FASTENER HOLES”

BY

Andrés–Amador García–Granada

October 2000

A thesis submitted to the University of Bristol
in accordance with the requirements of
the degree of Doctor of Philosophy
in the Department of Mechanical Engineering
in the Faculty of Engineering

Engineering Materials and Structural Integrity Group,
University of Bristol, Department of Mechanical Engineering,
Bristol BS8 1TR, UK.

Number of words: 52563

ABSTRACT

This thesis describes numerical studies undertaken principally to determine the effect of external mechanical loads and creep on RS (residual stresses) generated from a cold expansion process. These studies ended with predictions of fatigue crack growth within RS to analyse the benefit of cold expansion of fastener holes.

The first aim is to determine the RS field introduced by cold expansion on a new aluminium alloy at room temperature. The second aim is to study the effect of mechanical loading at room and high temperature on the RS. The final aim is to study the effect of mechanical loading on plates containing cracks emanating from the hole edge in order to compare fatigue lives for cold expanded and non–cold expanded holes.

First, a finite element (FE) simulation was used to simulate the expansion produced by an oversized mandrel pulled through the hole. The mechanical properties were obtained from experiments. The RS show a complex three–dimensional distribution resulting from combinations of radial and axial plastic deformation. The simulated RS distribution is in agreement with experimental measurements obtained by Sachs boring and X–Ray diffraction.

Application of tensile loads to cold expanded holes at room temperature showed a superposition of RS and mechanical loading, while compressive loads lead to redistribution of RS. Mechanical loading of cold expanded holes at high temperature (150°C) showed relaxation of the RS. This creep relaxation of RS is faster close to the hole edge, but smaller when compared to application of compressive loads.

Fatigue crack growth is predicted from stress intensity factors obtained from FE simulations. Several external loads, crack geometry and RS distributions are studied using both two–dimensional and three–dimensional FE simulations. The prediction of fatigue life show longer lives for cold expanded holes in comparison to non–cold expanded holes.

The prediction of RS using FE has been validated using experimental X–ray diffraction and Sachs boring measurements. A new experimental method known as the Garcia–Sachs method was developed to measure non–axisymmetric RS in cylindrical components. This method has been used to measure RS around cold expanded and non–cold expanded holes in plates subjected to external loads and/or creep.

DEDICATION AND ACKNOWLEDGEMENTS

First of all I would like to thank my supervisors Professor David J. Smith and Doctor Martyn Pavier for providing their experience on the subject and assistance in discussions about analytical and numerical simulations.

I would like to thank, for their kind help and patience, the members of the Research Group on Engineering Materials and Structural Integrity at the University of Bristol, including technicians and University staff. I would particularly like to thank my colleague Vesna Lacarac who provided her huge experience on experimental material testing.

In addition, I am grateful to DERA/DTi (Defence Evaluation Research Agency / Department of Trade and Industry), not only for their financial sponsorship but also for their continuous help and advice. In particular, I would like to thank Robin Cook and Phil Holdway for their supervision of the project and for the material data they provided.

Finally, I thank those I left at home, hoping that my studies were to be successful and for all the love and understanding they gave to me.

To my parents, Andrés y Elena.

AUTHORS DECLARATION

This thesis, submitted for the degree of doctor of Philosophy at the University of Bristol, is entirely the work of the author. This work has not been submitted for any other degree or diploma at this University or any other institution. No work is the result of collaboration, nor is any work of another researcher used, except where clearly referenced.

The views and opinions expressed in this thesis are solely those of the author and not the University of Bristol.

I declare that the above statements are true.

Signed: **Andrés–Amador García–Granada**

Date: October 2000

CONTENTS

PART A FINITE ELEMENT PREDICTION OF THE INTERACTION OF RESIDUAL STRESSES FROM COLD EXPANSION WITH EXTERNAL LOAD AND TEMPERATURE.

PART B NEW EXPERIMENTAL METHOD BASED ON SACHS BORING TO MEASURE RESIDUAL STRESSES AROUND HOLES.

APPENDIX

LIST OF TABLES

Tables in Chapter 3

Tables in Chapter 4

Tables in Chapter 6

LIST OF FIGURES

Figures in Chapter 1

Figures in Chapter 2

Figures in Chapter 3

Figures in Chapter 4

Figures in Chapter 5

Figures in Chapter 6

Figures in Chapter 7

Figures in Chapter 8

Figures in Chapter 9

LIST OF NOTATIONS

Roman notation:

A, B, C, D, m, n	Material constants.
x, y, z	Cartesian co–ordinates x being the loading direction.
r, θ, z	Cylindrical co–ordinates central in the hole.
a	Hole radius. Sachs boring initial cutting position.
b	Outer radius of plate/disc. Sachs boring strain reading position.
c	Crack length.
C^*	Creep crack contour integral.
d	Sachs boring current cutting position.
E	Young's modulus.
f	Fatigue frequency.
h	Plate thickness.
ΔH	Activation energy.
J	Elastic–plastic crack contour integral.
N	Number of fatigue cycles.
p	Internal pressure applied on cold expansion.
r_c	Radial distance from the crack tip.
R	Ratio of fatigue. Boltzmann's constant.
t	Time.
T	Temperature.
U	Displacement.

Subscript notation:

c	Creep.
e	Elastic.
eq	Equivalent.
f	Fatigue.
max,min	Maximum and Minimum values.
p	Plastic.
r,θ,z	Cylindrical co–ordinate system central in the hole.
res	Residual Stress.
t	Thermal.
x,y,z	Cartesian co–ordinate system x being the loading direction.

Greek notation:

α	Thermal expansion coefficient.
δ	Mobile dislocation density.
ν	Poisson's ratio.
$\bar{\nu}$	Dislocation velocity.
ε	Strain.
ϕ	Stress function.
θ	Angle in cylindrical co–ordinates
ρ' , ρ''	Forward and reversed radius of elastic–plastic boundary.
σ	Stress.
σ_y' , σ_y''	Forward and reversed yielding stress.
ψ	Crack angle between *r* and *z*.

Abbreviations:

BAe	British Aerospace Ltd.
BEF	Bauschinger effect factor.
BEM, BE	Boundary Element method
cw	Cold expanded hole, cracked and loaded in tension.
cwcp	Cold expanded hole, loaded in compression, unloaded, cracked and loaded in tension.
cwcr	Cold expanded hole, loaded in tension, crept at 150 °C, unloaded, cracked and loaded in tension.
cwht	Cold expanded hole, crept at 150 °C, cracked and loaded in tension.
DERA	Defence Evaluation Research Agency
DTi	Department of Trade and Industry
EDM	Electro discharge machining
FEA, FE	Finite Element Analysis
FTI	Fatigue Technology Inc., Seattle, Washington U.S.A.
LVDT	Linear variable differential transformer.
ncw	Non–cold expanded hole, cracked and loaded in tension.
RS	Residual stress.
SST	Supersonic Transport.

Chapter 1
INTRODUCTION

This introduction first describes the motivation for carrying out this research. Next, a description of the cold expansion process is presented, describing in more detail the split–sleeve method currently used in commercial applications. The material investigated is a new aluminium alloy designated Al 2650, designed for creep resistance. A short description is provided of tests carried out to find the material behaviour. Finally, an introduction to the FE simulations and experimental techniques used during the research is given. The thesis is therefore divided in two sections describing the simulations and experiments, mainly focused on a new method developed from the Sachs boring technique.

1.1. Motivation

Mechanical joints incorporating pins, bolts or rivets through holes are commonly used in aircraft structures. These joints enable easy assembly and dismantling, they are also able to transfer as well as to distribute the loads applied to the structure. The major drawback of such joints is that the fatigue life of the component is reduced by the presence of the hole. This is a direct consequence of the stress concentration that occurs when the plate containing the hole is subjected to a far field load during the flight as shown in figure 1.1a. This stress distribution around the hole is described by Sternberg and Sadowsky (1949) and Greenwood (1989). The higher stress around the hole is found in the direction normal to the applied load (θ=90) for tangential stress. This tangential stress near the hole may be reduced by increasing the panel section, or by reinforcing the hole by introducing compressive residual stresses around its edge as shown in figure 1.1b. The combination of compressive residual stresses and far field loads result in a lower tensile tangential stress at the hole edge in the position normal to the loading direction (θ=90°) as shown in figure 1.1c.

The option of introducing compressive residual stresses has been used in recent years by employing several techniques to introduce a residual stress field around the hole as shown in figure 1.1b. Some of the techniques used are:

(i) Interference fit fastener. An oversized bolt is forced into the hole. (Hsu and Forman, 1975, Rich and Impellizzeri, 1977, and Segerfröjd and Blom, 1999)

(ii) Oversized and interference fit fastener. An oversized titanium bolt is pushed into the hole to expand it. The final decrease in section of the bolt once pushed through allows relief of the expansion applied but still ensures some degree of interference. (Duprat et al., 1996).

(iii) Cold expansion by means of a tapered mandrel and pin roller bearings. (Hermann and Reid, 1991, Hermann and Moffat, 1991 and Hermann, 1994).

(iv) Split–sleeve cold expansion. A pre–lubricated split sleeve is positioned to reduce friction and contact defects before a tapered mandrel is pulled through the hole. (Mann et al., 1989 and Özdemir and Edwards, 1996).

(v) Combinations of cold expansion and ring indentation near the fastener hole. Ring punches are indented around the hole to generate additional compressive residual stresses. (Lim et al., 1998)

(vi) Solid sleeve cold expansion. A tapered mandrel is pulled through the hole protected by a closed sleeve. The sleeve is therefore cold expanded and can be left in the hole. (Moore, 1978)

(vii) Bushing cold expansion. A bush is installed between hole and mandrel with a high interference fit. Its higher yield limit allows higher compressive tangential residual stress to be achieved. (Reid, 1997 and Reid et al., 1997).

(viii)Split–mandrel cold expansion. A sleeveless tapered hollow mandrel with four longitudinal slots is used for the expansion. The slots make the mandrel collapsible for installation purposes. (Leon, 1998).

The use of the cold expansion process has been widely accepted by the civil aircraft industry as a safety factor for crack retardation but its effect has not been included during design. The benefit achieved in modifying the local stress distributions is schematically shown in figure 1.1c when compared to 1.1a. The retardation, or even arrest, of cracks emanating from fastener holes has become a detailed research field in engineering as described by Petrak and Stewart (1974).

One of the diagrams used to show the benefit of cold expansion is shown in figure 1.2 for Al 2024 (data obtained from Priest, 1997 and Metals Handbook, 1987), where the number of cycles to fatigue failure are shown for different applied stresses. As a reference, the fatigue failure curve for a plate without a hole is included and compared to open and filled holes. A difference is made between filled holes with and without interference also known as neat fit fasteners. Fatigue failure occurred for a shorter number of cycles in plates containing reamed open non–cold expanded holes than in neat fit fasteners in cold expanded holes. Cold expanded holes in some cases improved the behaviour in comparison with a plate without a hole. During this research, open holes are studied, as they are conservative in comparison to filled holes, and because of simplicity in theory, simulation and experimentation, the reasons given by Lacarac (2000).

In a typical wide–bodied civil aircraft more than 3 million fastener holes are cold expanded. This implies a significant time and money effort in installation during aircraft assembly (Jupp and Price, 1998). Supersonic transport (SST) aircraft, such as Concorde, are subjected to the effect of higher temperatures (Polmear et al., 1996) and there is concern that the beneficial residual stresses from cold expansion may relax due to creep. Creep relaxation of residual stresses has been examined widely for shot–peening residual stresses as shown in figure 1.3 for steel cylinders (Lillamand and Barrallier, 1996). Stress relaxation was produced in the area were the residual stresses were more compressive. Therefore a complete study of creep relaxation is needed to assess the benefit of cold expanding for SST.

1.2. Background

During the three–year period (1993–1995) at the University of Bristol, a similar project was carried out using analytical and numerical studies by Poussard (1995) and experimental studies by Priest (1997). These studies examined aluminium alloy 2024, using the split–sleeve cold expansion process marketed by Fatigue Technology Inc. (FTI, 1991). They also examined the fatigue crack growth of both cold expanded and non–cold expanded holes at room temperature. Finite element analyses (FEA) were combined with experimental tests.

A large number of suggestions for further work were produced, which the current project has examined.

1.3. Introduction to the Cold Expansion Process

Cold working is defined as a procedure applied to a sample at or near room temperature in order to introduce plastic deformation in some areas of the sample. In order to produce this plastic deformation the yield stress (σ_Y') must be achieved within the specimen during the forward loading process. The unloading or reversed loading process is usually elastic until an equilibrium state is achieved between residual stresses and plastic deformations. It is possible that the reversed yield stress (σ_Y'') is achieved during unloading producing a new plasticity effect known as reyielding. Cold expansion is a cold working process where a hole is plastically deformed by expansion of its radius.

A representation of the cold expansion of circular discs is shown in figure 1.4 where the behaviour of two parallel bars of the same cross–section but different lengths are subjected to elastic–plastic deformation. Both bars are subjected to the same applied displacement. The short bar 'a' and long bar 'b' are similar to two circular strips of material near the hole and outer edges respectively, also shown in figure 1.4. Strain is a function of displacement and length, hence the two bars sustain different stresses during a first state of elastic loading, the short bar 'a' being subjected to higher stresses. Therefore, a second state can be achieved where bar 'a' yields in tension. The third state of elastic unloading follows until an equilibrium is achieved between the two bars (long bar 'b' in tension, short bar 'a' in compression). However, during unloading a fourth state can be achieved where short bar 'a' reyields in compression. This example helps to understand how to produce compressive residual stresses when applying a tensile expansion and the four steps involved in cold expansion. The examination of inner and outer rings of a disc to be cold expanded, could be interpreted as a two bar model with the hole edge (*r=a*) being a short bar of length 'a' and the outer edge (*r=b*) of the disc a long bar of length 'b'.

In figure 1.5 the same steps are shown for the stresses across the section of a cold expanded disc, from the hole edge (*r=a*) to the outer edge (*r=b*). Cold expansion, a cold working process, is the term used to describe the introduction of radial plastic deformation around a hole as follows. The stresses are plotted as a function of radius when an internal pressure (*p*) is applied at the hole edge. This produces compressive radial stresses within the disc. The elastic distribution of radial and tangential stresses follows the equations given for a thick walled cylinder as described by Timoshenko and Goodier (1987). The plastic region expands from the hole edge (*r=a*) to a distance ($r=\rho'$) as a function of the pressure applied, the material thickness and the mechanical properties of the material. Once the maximum expansion is achieved, the internal pressure is removed so that the material recovers elastically until an equilibrium state is achieved. During the removal of pressure, reyielding may occur.

The evolution of the tangential and radial stresses near the hole edge are plotted in figure 1.6 during the expansion process. For simplicity, a perfectly plastic material yield surface and plane stress are assumed. In cold expansion yielding is achieved with multiaxial stresses while stresses in the simple two–bar model were uniaxial.

As described earlier different processes can be used to cold expand holes. The process used depends on the geometry of the hole, from narrow tubes to holes in thin plates. For example the split–sleeve method has been used in the civil aircraft industry for over twenty years. FTI created a standard process for specific hole diameters and expansion values providing the sleeves, mandrel and other accessories to complete the operation. This standard process was the result of a collaboration between FTI and the American aircraft company Boeing and is the method examined in this study.

In the split–sleeve method, an oversized tapered mandrel is pulled through the hole so that the movement in the axial direction causes an increase in radial dimension of the hole. A partial section through the FTI split–sleeve cold expansion is shown in figure 1.7. A lubricated split–sleeve is placed in the hole to reduce friction and to avoid direct contact between the mandrel and the hole surface. The split in the sleeve opens slightly during the expansion. This opening is proportional to the radial displacement, or expansion, of the hole. The mandrel is made of hardened stainless steel of high stiffness and therefore can be considered to remain undeformed. The nominal degree of cold expansion can be defined as:

$$\%\, cw = 100 \times (mmd + 2 \times st - hd)/\, hd \qquad (1.1)$$

where

$\%\, cw$ is degree of cold expansion, mmd is maximum mandrel diameter, st is sleeve thickness and hd is hole diameter.

During this research aluminium plates of thickness h=6 mm and hole radius a=3 mm were 4% cold expanded using the split–sleeve method.

1.4. Structure of thesis

This thesis is divided into two parts: part A, corresponding to FE simulation studies and part B, corresponding to experimental measurement of residual stresses using a new method.

1.4.1. Part A. Finite element prediction of the interaction of residual stresses from cold expansion with external load and temperature

In part A, a literature review on theoretical studies related to cold expansion is given first. The analytical methods are used to achieve an understanding of the subject while FE work is described in more detail.

Later, in Chapter 3, the material studied in this work is described. The current project examines a new aluminium alloy referred to as Al 2650, which was developed from Concorde's old alloy RR58 (similar to Al 2618A). The new alloy was developed to be creep resistant. An examination of its composition and properties was carried out. The properties relevant to the cold expansion process and operation at high temperature were examined.

New computations have been added to previous work (Poussard, 1995) to determine the effect of temperature change and of creep relaxation in Chapter 5. Significant differences were predicted in the relaxation of samples with and without the application of external loading.

The effect of cracks has been examined in Chapter 6 using effective stress intensity factors as in Poussard (1995). The relaxation of crack tip stresses due to creep was also described. Three–dimensional corner cracks were compared to through–thickness cracks for different crack lengths. The cracks were introduced in different residual stress fields from Chapters 4 and 5. With the stress intensity factors, fatigue crack growth rates were predicted.

1.4.2. Part B. New experimental method based on Sachs boring to measure residual stresses around holes.

Part B in this thesis describes a new experimental method and several applications related to this research. The motivation for this was the realisation that conventional methods for measurement of axisymmetric residual stresses provided significant errors in measurement of non–axisymmetric stresses.

A literature review on experimental measurement techniques of residual stresses is given in Chapter 7. Special attention was given to the two methods used during parallel research by Lacarac (2000) namely X–ray diffraction and Sachs boring.

In Chapter 8 the new method is described with FE benchmarks to demonstrate its validity. In Chapter 9 experimental measurements are compared to FE predictions.

Finally, a summary of conclusions of all the results is given in Chapter 10 together with suggestions for further work.

PART A

FINITE ELEMENT PREDICTION OF THE INTERACTION OF RESIDUAL STRESSES FROM COLD EXPANSION WITH EXTERNAL LOAD AND TEMPERATURE.

Chapter 2
LITERATURE REVIEW FOR THEORETICAL STUDIES

A substantial number of analytical developments, numerical analyses and experimental methods have been conducted to determine the residual stress field surrounding cold expanded fastener holes. The theory involved in cold expansion is analysed in this chapter. The influence of higher temperature, and in particular the creep relaxation of residual stresses have also been studied for different aluminium alloys. Finally, studies of fatigue crack growth within residual stress fields are reviewed.

2.1. Analytical study of cold expanded holes

Several analytical solutions have been reported that predict residual stress fields in cold expanded fastener holes and autofrettaged thick walled cylinders. All of these analytical methods take into account the material properties, geometry and the degree of expansion applied. The generation of a closed form solution avoids the use of more time consuming numerical analysis. However the solutions are one–dimensional, in other words, the residual stresses are a function of radius only and therefore do not predict any angular or through–thickness variation.

The basic equations of all analyses found in the literature are based on the definition of a uniform radial displacement of a thick walled cylinder. For example, Sachs and Hoffman (1953) took account of plasticity during radial expansion. Before the onset of plasticity the stresses are distributed as in an elastic thick walled cylinder, as described by Timoshenko and Goodier (1987).

A number of analyses have been used which attempt to cover the mechanisms present during cold expansion. In these analyses it is assumed that the geometry is defined as a flat circular disc of outer radius $r=b$, with a concentric hole of radius $r=a$. The mandrel movement is simulated by a constant pressure p or an equivalent radial displacement U_{rr} applied on the hole edge. In most cases an expansion of 4% is considered. This is a typical expansion used in civil aircraft structures.

All the different solutions include four common steps to describe the cold expansion. First the stresses and strains are found due to an elastic expansion of the inner radius. Second, plasticity is introduced as the loading is increased, the radius of plasticity ($r=\rho'$) being defined as the boundary between the elastic and plastic region. The third step is to define the stresses inside the plastic region produced during the loading as a function of the yield criteria. In this step it is possible to calculate the radius of plasticity. The removal of the expansion (or unloading) can be added to these stresses as an elastic distribution from step one. Finally the possibility of achieving yielding during the unloading is introduced. This includes the influence of different parameters such as the BEF and strain hardening.

Some of the basic material models used for the various analyses are represented in figure 2.1 including perfect plasticity, isotropic and kinematic hardening and bilinear hardening taking into account the Bauschinger effect factor (BEF) as suggested by Chen (1986). In figure 2.2 the BEF of isotropic and kinematic models are compared to experimental results for Al 2024, from Poussard (1995).

Analyses that included elastic loading with plasticity in loading are summarised and described in detail by McNeill and Heston (1987) and a complete literature review is found in Poussard (1995). Experimental measurements of residual stresses produced by Priest et al. (1994), Özdemir et al. (1994), Özdemir and Edwards (1996), Ball and Lowry (1998) were compared to analytical solutions provided by Hsu and Forman (1975) and Rich and Impellizzeri (1977). Special attention is paid in this review to the plasticity criterion (step 2) and reyielding on unloading (step 4) as several improvements have been developed for hardening materials taking into account the BEF.

These four analytical steps are next described in detail.

2.1.1. Stress distribution during elastic hole expansion.

Analytical models consider only a one–dimensional axisymmetric state, where plane stress, plane strain or generalised plane strain can be applied. Therefore analytical methods do not provide information about the through–thickness and angular residual stress variations. A polar or cylindrical co–ordinate system is used to simplify the calculations.

The three–dimensional equilibrium equations and boundary conditions can be found in Chapter 8. The simplified equilibrium equation for the one–dimensional axisymmetric case is:

$$\frac{\sigma_{rr}-\sigma_{\theta\theta}}{r}+\frac{\partial\sigma_{rr}}{\partial r}=0 \qquad (2.1)$$

By applying a uniform internal pressure p at the inner radius surface it is possible to determine the elastic stress distribution. The boundary conditions are that the radial and shear stresses are zero at the outer radius ($r=b$) and at the inner radius the radial stress must be equivalent to the applied pressure. The final stress distribution is given in many references such as Timoshenko and Goodier (1987) and is as follows:

$$\left\{ \begin{array}{l} \sigma_{rr} = \dfrac{pa^2}{b^2 - a^2}\left(1 - \dfrac{b^2}{r^2}\right) \\ \sigma_{\theta\theta} = \dfrac{pa^2}{b^2 - a^2}\left(1 + \dfrac{b^2}{r^2}\right) \\ \tau_{r\theta} = 0 \\ \end{array} \right\} \tag{2.2}$$

For plane strain conditions axial stress can be calculated because axial strain is assumed to be zero ($\varepsilon_{zz} = 0$), and therefore the axial stress can be solved from Hooke's law. The axial stress for plane strain is given by:

$$\sigma_{zz} = \nu(\sigma_{rr} + \sigma_{\theta\theta}) = \frac{2\nu pa^2}{b^2 - a^2} \tag{2.3}$$

Note that the axial stress is constant for this case and not a function of radius as it is for radial and tangential stresses.

2.1.2. Plasticity criterion. Stress distribution within the elastic region.

The cold expansion process attempts to produce residual stresses by introducing plastic deformation around the hole. The plastic deformation is introduced once the onset of plasticity is achieved, where the onset is defined by a yield criterion. The two commonly used yield criteria are the von–Mises and Tresca yield criteria. For both cases a yield stress is defined which depends on the plasticity model used, for example perfect plasticity, isotropic and kinematic hardening, bilinear hardening, and Ramberg–Osgood. A short description of von–Mises and Tresca yield criteria follows.

Von–Mises criterion

Yielding is assumed to start when the stress state reaches a critical value defined by the yield stress (σ_y'). However the stress state may be a function of three–dimensional stresses. The von–Mises condition of yielding can be expressed in terms of the six components of stress in cylindrical co–ordinates by:

$$\sigma_y' = \sqrt{\frac{(\sigma_{rr} - \sigma_{\theta\theta})^2 + (\sigma_{rr} - \sigma_{zz})^2 + (\sigma_{zz} - \sigma_{\theta\theta})^2 + 6(\tau_{rz}^{\ 2} + \tau_{\theta z}^{\ 2} + \tau_{r\theta}^{\ 2})}{2}} \tag{2.4}$$

The criterion can be simplified for axisymmetric distributions under both plane stress and plane strain conditions:

(i) Plane stress (used for thin plates):

$$\sigma_y' = \sqrt{\sigma_{rr}^{\ 2} + \sigma_{\theta\theta}^{\ 2} - \sigma_{rr}\sigma_{\theta\theta}} \tag{2.5}$$

(ii) Plane strain (used for thick plates), can be simplified by assuming Poisson's ratio ν=0.5 as follows:

$$\sigma_y' = \frac{\sqrt{3}}{2}[\sigma_{rr} - \sigma_{\theta\theta}] \tag{2.6}$$

In plasticity calculations, Hooke's law is only valid to describe elastic strains, and therefore the Poisson's ratio is not used. The relation between stress and strain is therefore found assuming material incompressibility (constant volume). Several researchers such as Rich and Impellizzeri (1977) assumed an “equivalent Poisson's ratio" of 0.5 to ensure incompressibility, and also assumed perfect plasticity.

Once the yield criteria has been defined it is possible to calculate the internal pressure that initiates yielding at the hole edge. Once more, this has been reported in the literature (Rich and Impellizzeri, 1977) and depends on the plane stress or plane strain assumptions.

(i) For plane stress conditions and an elastic stress distribution, plasticity will start at the hole radius ($r=a$), for an internal pressure (p) given by:

$$\sigma_y' = \frac{p}{b^2 - a^2}\sqrt{a^4 + 3b^4} \tag{2.7}$$

For higher values of internal pressure this yield stress is satisfied at the elastic–plastic boundary ($r=\rho'$). Therefore with a knowledge of this boundary condition the elastic stress distribution is given for radius $\rho' < r < b$ and is:

$$\left\{\begin{array}{l} \sigma_{rr} = \dfrac{\sigma_y'}{\sqrt{3 + \dfrac{\rho'^4}{b^4}}} \dfrac{\rho'^2}{b^2}\left(1 - \dfrac{b^2}{r^2}\right) \\ \sigma_{\theta\theta} = \dfrac{\sigma_y'}{\sqrt{3 + \dfrac{\rho'^4}{b^4}}} \dfrac{\rho'^2}{b^2}\left(1 + \dfrac{b^2}{r^2}\right) \\ \sigma_{zz} = 0 \end{array}\right\} \tag{2.8}$$

The calculation for the radius of the elastic–plastic boundary and distribution of stresses within the plastic region will be described later, in the third step. This step is also a function of hardening.

(ii) For plane strain conditions and using eq. (2.6) to define the yield criterion, the pressure that causes yielding at the hole edge ($r=a$) is:

$$\sigma_y' = \frac{\sqrt{3}\left|pb^2\right|}{b^2 - a^2} \tag{2.9}$$

As for plane stress conditions at the elastic–plastic boundary ($r=\rho'$) the yield stress is satisfied and for higher pressures the elastic stress distribution for $\rho'<r<b$ is:

$$\left\{\begin{aligned} \sigma_{rr} &= \frac{\sigma_y'}{\sqrt{3}}\frac{\rho'^2}{b^2}\left(1-\frac{b^2}{r^2}\right) \\ \sigma_{\theta\theta} &= \frac{\sigma_y'}{\sqrt{3}}\frac{\rho'^2}{b^2}\left(1+\frac{b^2}{r^2}\right) \\ \sigma_{zz} &= \frac{\sigma_y'}{\sqrt{3}}\frac{\rho'^2}{b^2} \end{aligned}\right\} \tag{2.10}$$

In order to solve the elastic–plastic boundary, ρ', the analysis must be completed in the plastic region in step three (section 2.1.3).

Tresca criterion

Yielding is assumed now to start when the maximum shear stress reaches a critical value. The shear stress criterion can be expressed for a one–dimensional axisymmetric situation by:

$$\sigma_y' = \left|\sigma_{rr} - \sigma_{\theta\theta}\right| \tag{2.11}$$

For an initial elastic stress distribution, plasticity starts at the hole radius ($r=a$), reacting to an internal pressure (p) for both plane stress and plane strain conditions, when this pressure satisfies:

$$\sigma_y{}'=\frac{2\left|pb^2\right|}{b^2-a^2} \tag{2.12}$$

At the elastic–plastic boundary (r=ρ') this yield stress is satisfied even for higher pressures and therefore the elastic stress distribution for ρ'<r<b is:

$$\left\{\begin{aligned}\sigma_{rr}&=\frac{\sigma_y{}'}{2}\frac{\rho'^2}{b^2}\left(1-\frac{b^2}{r^2}\right)\\ \sigma_{\theta\theta}&=\frac{\sigma_y{}'}{2}\frac{\rho'^2}{b^2}\left(1+\frac{b^2}{r^2}\right)\end{aligned}\right\} \tag{2.13}$$

This equation is valid for both plane stress and plane strain conditions. The axial stress in the elastic region can be found for a plane strain state as:

$$\sigma_{zz}=\nu\sigma_y{}'\frac{\rho'^2}{b^2} \tag{2.14}$$

Once more, in order to solve the elastic–plastic boundary, ρ', the analysis must be completed in the plastic region. This is described next.

2.1.3. Stress distribution in the plastic region during hole expansion. Work hardening and elastic unloading.

Earlier, the elastic stress distribution was found once yielding had occurred for different plasticity criteria. To complete the stress distribution it is necessary to investigate the plastic region where the equilibrium equation (2.1) must also be valid.

The boundary conditions are the applied internal pressure p at $r=a$ and the yield stress σ_y' at $r=\rho'$, as calculated previously. The solution will depend on the yield criterion adopted and whether plane stress or plane strain conditions are assumed. The solution will also depend on the work hardening of the material beyond the yield stress. Here the solution for the Tresca criterion is presented for perfect plasticity for both plane stress and plane strain assumptions.

By combining the Tresca criterion (2.11) and the equilibrium equation (2.1) for axisymmetric conditions and after integrating the stresses from the edge of the hole ($r=a$) to the radius of plasticity ($r=\rho'$), the stress distribution in the plastic region is:

$$\left\{\begin{aligned} \sigma_{rr} &= \sigma_y'\left[ln\left(\frac{r}{\rho'}\right)-\left(\frac{b^2-\rho'^2}{2b^2}\right)\right] \\ \sigma_{\theta\theta} &= \sigma_y'\left[ln\left(\frac{r}{\rho'}\right)+\left(\frac{b^2+\rho'^2}{2b^2}\right)\right] \end{aligned}\right\} \tag{2.15}$$

If the plane strain condition is assumed and the incompressibility of the material considered, the axial stress is:

$$\sigma_{zz} = \sigma_y'\left[ln\left(\frac{r}{\rho'}\right)+\frac{\rho'^2}{2b^2}\right] \tag{2.16}$$

Now it is possible to find the elastic–plastic boundary ρ' for a perfect plasticity material model where the yield stress is constant. (The material models are shown in figure 2.1). A more realistic material model behaviour would include a dependency of the yield stress on plastic strain. The following researchers used a Ramberg–Osgood hardening model in their work: Wanlin (1993), Ball (1994), Arora and Simha (1996), Jahed and Dubey (1996 and 1997) and Lazzarin and Livieri (1997). In these cases an iterative method was required to obtain a solution.

The same procedure can be used considering the von–Mises yield criterion but more complicated results are obtained. Clark (1982) determined a closed analytical form using this criterion for thick–walled tubes.

Work hardening

In a number of metallic alloys the post–yield stress–strain behaviour can be approximated by a power–law relation, such as the Ramberg–Osgood model. In this model the equivalent stress σ_{eq} depends on plastic strain ε_p and material constants A_p and n_p:

$$\sigma_{eq} = \sigma_y' + A_p \varepsilon_p^{\,n_p} \tag{2.17}$$

The movement of the yield surface can be achieved through two different mechanisms. A shift of the centre of the yield surface, which corresponds to kinematic hardening, or an expansion of the yield surface, which corresponds to isotropic hardening.

Megahed (1990), and Megahed and Abbas (1991) examined pressurised thick–walled tubes assuming that the material exhibited power–law work hardening. They also examined the influence of the Bauschinger effect on the plastic strain. The material then reyields at a lower stress in compression. Studies that incorporated this effect are presented next.

Stress distribution during unloading.

Once the stress distribution has been calculated when the internal pressure is applied, subsequent pressure relief must be analysed. The unloading process can be initially considered elastic, as in step two using equation (2.2) to describe the stress change. The final residual stresses are found by the combination of stresses with the load applied plus the stresses that would elastically generate a negative pressure (pressure relief) at the hole edge.

However reyielding is usually produced during the unloading. This is considered in the following section.

2.1.4. Reyielding on unloading. Bauschinger effect.

The process of cold expansion of holes in plates used in the aircraft industry usually involves reyielding of the material during unloading. This generates an area close to the hole edge known as the reversed yield area. To predict the stresses in this area accurately, account must be taken of work hardening, which in most cases is different from the first yielding. This is known as the Bauschinger effect in the unloading process after prior elastic–plastic loading.

Bauschinger effect

The stress–strain behaviour can be different in some metallic alloys after the first yield is produced. For rolled sheets, first yielding and subsequent work hardening is usually close to perfect plasticity while the reyielding (yielding in reverse loading only) gives a smooth change of stresses, with the introduction of new plastic strains starting at a lower stress level (Bauschinger, 1886).

A cold expanded hole during unloading attempts to recover all the strain stored during the expansion. The high plastic deformation at the hole edge can lead to reyielding and therefore the Bauschinger effect must be considered.

Milligan (1970) compared an analytical method with experimental results. The analytical method assumed perfect plasticity for yielding and reyielding using the Tresca criterion. The experimental compressive tangential stresses at the hole edge were found to be 50% less than the estimated value.

Rich and Impellizzeri (1977) used an elastic–perfectly plastic solution with the simplified von–Mises criterion expressed by equation (2.7) and including reyielding. Results were found to be in agreement with a FE solution. Their equations are as follows:

(i) Maximum expansion:

For the elastic area ($\rho' < r < b$) the tangential stress distribution can be found as in equation (2.10) by:

$$\sigma_{\theta\theta} = \frac{\sigma_y'}{\sqrt{3}} \frac{\rho'^2}{b^2} \left(1 + \frac{b^2}{r^2} \right) \tag{2.18}$$

For the plastic area ($a < r < \rho'$) the stress distribution can be found as in (2.15), but here using a von–Mises instead of a Tresca criterion:

$$\sigma_{\theta\theta} = \frac{\sigma_y'}{\sqrt{3}} \left[2 ln \left(\frac{r}{\rho'} \right) + \frac{b^2 + \rho'^2}{b^2} \right] \tag{2.19}$$

In order to calculate the elastic–plastic boundary, $r = \rho'$ the radial stress is computed at the hole radius and solved using the internal pressure. This analysis finds ρ' from the radial displacement imposed at the hole edge.

(ii) Unloaded residual stresses:

An elastic stress from the unloading must be added to those obtained when the internal pressure is applied as expressed in (2.18) and (2.19). This elastic stress is applicable within the area that is not reyielding ($\rho'' < r < b$), where ρ'' is the reyielding boundary.

$$\Delta\sigma_{\theta\theta} = \frac{\sigma_y'}{\sqrt{3}}\left[2\,ln\left(\frac{r}{\rho'}\right) + \frac{b^2 + \rho'^2}{b^2}\right]\left\{\frac{a^2}{r^2}\left(\frac{r^2 + b^2}{b^2 - a^2}\right)\right\} \qquad (2.20)$$

The reyielding is produced at a radius ρ'' given by:

$$\rho'' = \sqrt{\frac{(ba)^2}{2\left(b^2 - a^2\right)}\left[2\,ln\left(\frac{\rho'}{a}\right) + \frac{b^2 - \rho'^2}{b^2}\right]} \qquad (2.21)$$

and the tangential residual stress at the hole edge is:

$$\sigma_{\theta\theta}\Big]_{r=a}^{res} = \frac{4\sigma'}{\sqrt{3}}\left[-\gamma + \frac{a^2}{b^2}e^{\gamma}\right] \qquad (2.22)$$

where:

$$\gamma = \left[\frac{1}{2} - \frac{a^2}{b^2} + \frac{1}{2}\frac{\rho'^2}{b^2}\right] \qquad (2.23)$$

Analytical solutions presented by Rich and Impellizzeri (1977) are shown in figure 2.3 for a 4% expansion of Al 2024 aluminium alloy plates. Results are compared to FE simulations carried out by Poussard (1995).

The generation of an analytical solution becomes progressively more complicated when attempting to introduce all these effects. Furthermore, all the reported analytical solutions present axisymmetric distributions of residual stresses without any through–thickness variation.

A comparison of three analytical models can be found in figure 2.4. This shows the results obtained from Chen (1986) who considered a plane strain assumption using a Tresca criterion for plasticity. The reverse yielding in compression after initial loading in tension considered the Bauschinger effect and work hardening for a linear stress–strain relation as shown in figure 2.1. Chen's results show that the maximum compressive stress occurs at the hole edge, despite reversed yielding.

Jahed and Dubey (1997) realised the importance of the consideration of a variable Bauschinger effect factor in prediction of reverse yield initiation. Lazzarin and Livieri (1997) used a numerical analysis with Runge–Kutta iterations to take into account the work hardening during unloading as well as the variability of the Bauschinger effect.

2.2. Numerical analysis of cold expanded holes

Two main numerical analysis techniques have been used to model the cold expansion process: boundary element method (BEM) and finite element analysis (FEA). Applications of these methods to predict residual stresses arising from cold expansion are presented next.

2.2.1. Boundary element.

The boundary element method has been mainly used to describe the fatigue crack growth of fastener holes and autofrettaged tubes (Bourke et al., 1991, Parker et al., 1991, and Becker et al., 1993). However limited descriptions of the generation of residual stresses were provided.

Özdemir et al. (1993) used two–dimensional boundary element analyses with plane stress and isotropic hardening to model residual stresses around a 4% cold expanded hole. The material examined was Al 7050–T76 in plates 5 mm thick containing a hole 6.35 mm in diameter. The BE results overpredicted (more compressive) the experimental measurements of the tangential residual stresses. They concluded the BEM was not suitable as it did not take into account the through–thickness variation of residual stresses, nor the Bauschinger effect.

Liu and Hong (1994) used an axisymmetric BEM with three material hardening models to take into account the Bauschinger effect. They modelled the autofrettage process in steels. Residual stresses were measured at the outer surface and compared to BE and FE predictions, obtaining the best agreement for models considering a linear hardening model for the initial yield and a Ramberg–Osgood elastoplastic unloading model.

2.2.2. Finite element.

The FEM has been used extensively to analyse the cold expansion process in two dimensions. For these two–dimensional simulations, several have been made using plane stress and plane strain conditions as well as using several hardening models. In figure 2.5 FE results obtained for cold expanded holes in an Al 2024 alloy from Poussard (1995) are shown for thin plates. It was concluded that the plane stress model with kinematic hardening was the best representation of material behaviour and therefore gave the best prediction of residual stress fields in comparison to the experimental measurements. This model predicted the least compressive tangential residual stress near the hole edge in comparison to plane strain and isotropic hardening models.

More recently, two–dimensional axisymmetric and three–dimensional FEA have been performed where the cold expansion process is modelled in detail, rather than as a one–dimensional hole expansion process. The results of these 3D analyses will now be summarised and results compared with the two–dimensional case.

Through–thickness variations of residual stresses were first studied using an axisymmetric model. Rufin (1993) modelled a 3.68 mm thick titanium plate and assumed von–Mises yield criterion and isotropic hardening. The mandrel movement was simulated by applying radial and axial loads to the hole edge sequentially through–thickness, from entrance face to exit face. These loads were obtained from experimental measurements of mandrel pull through. The tangential stress distribution was close to zero for the inlet surface increasing in magnitude to a compressive value for the outlet face.

Forgues et al. (1993) used an axisymmetric model with a rigid element to simulate the mandrel. They did not include the sleeve placed between the mandrel and plate. A friction coefficient was included in their simulation using contact elements with movement of the rigid mandrel. In comparison to Rufin (1993) they obtained a similar through–thickness variation of residual stresses.

More recently, Priest et al. (1994), Poussard (1995), Poussard et al. (1995) and Pavier et al. (1995) carried out several through–thickness simulations on a 6 mm thick Al 2024 plate. Axisymmetric models were carried out initially with uniform radial displacement of the hole and finally using a rigid mandrel pulled through the hole. Both isotropic and kinematic hardening material models were used. The results indicate that using isotropic hardening provides more compressive residual stresses within the region of reversed yielding. Once more, entrance face tangential residual stresses were shown to be small. These results are shown in figure 2.6, and are compared to 2D simulations in figure 2.7. In general these results are in agreement with those presented by Forgues et al. (1993). In addition to this work, a three–dimensional simulation of the cold expansion was carried out to analyse the effect of through–thickness cracks (Pavier et al., 1998 and 1999). However these simulations predicted residual stresses as a function of only radius and axial position (*r* and *z*), and ignored the effect of the split in the sleeve.

A similar FE and experimental study was carried out by Bernard et al. (1995) on Al 7475–T7351 alloy. Cold expansion of holes up to 5.58% in two steps was analysed. The two step process was used in order to increase the compressive tangential residual stresses at the inlet face. They pulled a second mandrel through the plate, either in the same direction or in the opposite direction to the first mandrel. Low compressive tangential residual stresses were still found at the entry face after a second cold expansion as in a one step cold expansion. These results are presented from the original paper in figure 2.8a for one mandrel and in figure 2.8b for a second mandrel pulled through the hole in the reverse direction.

Only one reference was found where residual stresses were determined in a three–dimensional state, as a function of radius, angle and axial position. Papanikos and Meguid (1998) carried out simulations for adjacent holes in aluminium alloy 7075–T651. The cold expansion process was simulated with a rigid mandrel pulled through with a coefficient of friction μ=0.15. Tangential residual stresses close to the hole were found to be tensile for adjacent holes, with a decrease in compressive residual stress at the entry face for decreasing distance between expanded holes.

However, previous work has not examined three–dimensional residual stress distributions arising from the split in the sleeve.

2.3. Creep and temperature influence on mechanical properties

The effect of high temperature on the mechanical properties of aluminium alloys has been studied to understand the mechanisms of creep. In this section some of the background to the mechanisms of creep in aluminium will be described. First the dependence of the elastic–plastic properties on temperature is examined.

Material properties can be found for different temperatures in the Metals Handbook (1987) for several aluminium alloys. For these alloys the Young's modulus and yield stress are observed to decrease with increasing temperature. The closest alloy in composition to Al 2650 (described in chapter 3) catalogued in the Metals Handbook is Al 2048–T851.

2.3.1. Mechanisms of creep in aluminium alloys.

In order to understand the creep mechanisms responsible for residual stress redistribution that occurs in cold expanded aluminium alloys, the temperature and stress regime must be known. The deformation mechanism maps for pure aluminium presented by Ashby and Frost (1982) can be used to identify the significant creep mechanism. The deformation maps for pure aluminium are presented in figure 2.9 for two different grain sizes (10 μm and 1 mm). It is shown that Harper–Dorn creep replaces diffusional flow at large grain sizes for the conditions of interest.

Harper–Dorn creep is produced at low stress and is a typical process for aluminium. Similar behaviour has been observed for lead and tin. Linear viscous creep is observed, but at rates much higher than those obtained by diffusional flow.

The most plausible explanation is that of climb–controlled creep under conditions such that the dislocation density does not change with the stress.

In order to understand the creep processes a brief description follows. There are two dominant mechanisms called dislocation and diffusional creep. In the former, defects known as dislocations in the crystalline lattice structure of the metal can overcome the natural stiffness of the crystal, and other obstacles introduced in an alloy to prohibit creep, so as to move through the lattice. At low stresses, this dislocation motion stops or slows down but creep can continue through the bulk movement of atoms from one atomic site to another in tension. Dislocation creep has a highly non–linear dependence on stress while the diffusional creep exhibits a more or less linear viscous dependence on stress.

Diffusional flow is related to the diffusional transport through and round the grains. The strain–rate may be limited by the rate of diffusion or by that of an interface reaction. It is noted the influence of alloying on diffusional flow. A solid solution can impose a drag on boundary dislocations slowing the rate of creep.

Power–law breakdown for aluminium occurs when the stresses are too high for simple power–law to be accurate: the measured strain–rates are greater than those predicted by power–law creep. The process is evidently a transition from climb–controlled to glide–controlled flow of dislocations.

Other models have been examined. Aktaa and Schinke (1997) used a Chaboche model to describe damage of a steel at 850°C. Eigenmann et al. (1994) analysed the relaxation of shot peening residual stresses on a steel at 250–450°C using Avrami's equations (Vöhringer, 1983). For aluminium at 150°C, Kowaleski et al. (1994) used a “sinh” hyperbolic function to define rupture, while Blankenship and Kaisand (1996) based their calculations in creep crack growth tests giving little detail about creep modelling. The current study is focused on power–law creep for multiaxial stress (Lu and Weng, 1996).

2.3.2. Creep models of strain accumulation at constant load.

There are many theories about creep as described by Boyle and Spence (1983). A power–law is often used and can be expressed as a combination of Norton and Bailey theories:

$$\varepsilon_c = C_c e^{-\frac{\Delta H}{RT}} \sigma^{n_c} t^{m_c} \tag{2.24}$$

where ε_c is the accumulation of creep strain, ΔH is the activation energy, R is the Boltzmann's constant, T is the absolute temperature, t is time and σ is the equivalent stress. C_c, n_c and m_c are material constants to be determined.

This behaviour can be caused by dislocation glide alone or by climb–plus–glide. The latter occurs at high temperatures as described as power–law breakdown. Power–law creep by glide alone for isothermal conditions from equation (2.24) gives:

$$\varepsilon_c = B_c \sigma^{n_c} t^{m_c} \tag{2.25}$$

A classical creep curve for a metallic alloy usually consists of three regimes which are defined as: primary, secondary or steady–state and tertiary creep. When $m_c<1$ then equation 2.25 describes primary creep, when $m_c=1$ equation 2.25 represents secondary creep. These three regimes are shown in figure 2.10. In tertiary creep ($m_c>1$) the increase in strain rate is largely the result of the change in dimensions of the cross–section of the specimen as deformation proceeds. Also deterioration, in the form of internal cavitation, may have altered the effective load–bearing cross–section.

Few results have been found in the literature for the new aluminium alloy examined in this work. An earlier project evaluated a number of aluminium alloys for SST design (Polmear et al., 1996). They compared this new alloy with Al 2618A used previously in Concorde. However, only one test was presented for Al 2650 showing the minimum secondary strain rate and one of the longest rupture lives (for a stress of 250 MPa while other alloys were tested at 300 MPa). All the results were obtained from tensile creep tests.

Evans and Wilshire (1985) and Miller (1946) defined the requirements for evaluating the creep behaviour in compression and provided a grip design to convert a tensile test rig to provide compressive stresses in a specimen. For a tensile load the stress on the specimen increases as the cross–section reduces. For a compressive load the stress on the specimen decreases as the cross–section increases. A strain correction was presented as a function of the power–law creep parameter, n_c. After the correction a similar behaviour for tensile and compressive tests could be observed.

Biscaya (1971) and Huston (1972) studied the effect of prestrain at 20°C on the tensile creep behaviour of RR58 aluminium alloy (Al 2618A) at 150°C. In order to avoid buckling in compression for uniaxial specimens they tested torsion specimens instead. Torsion was first applied in one direction to produce plastic strains and creep was followed in the same and opposite directions. Afterwards they translated the shear strains into equivalent direct strains. They found that the primary shear creep rate is always higher when prestrain is introduced. Also, a prestrain in the same direction as creep loading accelerates secondary creep (similar to tension prestrain and tension creep). This may be caused by an increase on the dislocation density. On the other hand, a prestrain introduced in the opposite direction as creep loading slows down the secondary creep (similar to compression prestrain and tension creep), probably caused by a change in hardness or recrystallisation.

In order to avoid buckling they used biaxial stress torsion tests. Their results for creep accumulation tests are shown in figure 2.11 for a torsion stress of 128 MPa.

Evans and Wilshire (1985) described the influence of prior plasticity on pure aluminium and aluminium–2.93wt% magnesium alloy. Pure aluminium showed a decrease in the creep rate with plastic strain while the alloy showed an increase for a load of 20.7 MPa at 250°C. For pure aluminium, creep is recovery or climb controlled. Prestraining should reduce the initial creep rate because it increases the dislocation density, so that it behaves as in the secondary creep state. For the aluminium –2.93wt% magnesium alloy creep is controlled by solute–drag processes, and the creep rate is determined by the number of moving dislocations:

$$\frac{\partial \varepsilon_c}{\partial t} \propto \delta \bar{v} \tag{2.26}$$

where $\bar{v}$ is the dislocation velocity which is determined by the rate at which the solute atoms can move along with the dislocations and would vary linearly with stress, and δ is the mobile dislocation density. Al–Mg alloys showed this kind of behaviour called Class I. An initial prestrain increases the density of dislocations and therefore the initial creep rate.

2.3.3. Stress relaxation at constant strain models for creep.

There are two main theories that consider stress relaxation due to creep under constant strain conditions. They are known as time hardening and strain hardening creep theories, developed from primary power–law creep behaviour. A more detailed study including secondary creep can be found in García–Granada (1998a) and Martínez (1998).

Time hardening

Time hardening relaxation is faster and leads to a lower final stress when compared to strain hardening. The creep strain rate is assumed to depend upon the current stress and time. The rate of change of the creep and elastic strains are:

$$\frac{\partial \varepsilon_e}{\partial t}+\frac{\partial \varepsilon_c}{\partial t}=\frac{1}{E}\frac{\partial \sigma}{\partial t}+B_c\sigma^{n_c}m_c t^{m_c-1}=0 \qquad (2.27)$$

The solution to this differential equation for the stress σ as a function of time is obtained assuming that the initial stress (σ_o) for time t=0 is known, where:

$$\sigma=\left[\sigma_o+B_c E(1-n_c)t^{m_c}\right]^{\frac{1}{1-n_c}} \qquad (2.28)$$

Strain hardening

Strain hardening assumes that the creep strain rate depends on the current stress and the accumulated creep strain. An equation can be derived for the creep strain rate by substituting strain for time using the Norton–Bailey power–law equation 2.25 and substituting it into equation 2.28 to give:

$$\frac{\partial \varepsilon_e}{\partial t}+\frac{\partial \varepsilon_c}{\partial t}=\frac{1}{E}\frac{\partial \sigma}{\partial t}+m_c B_c^{\,1/m_c}\sigma^{n_c/m_c}\varepsilon_c^{(m_c-1)/m_c}=0 \qquad (2.29)$$

The solution to this equation requires numerical integration, together with an assumed initial stress. The initial strain is based on elastic behaviour alone.

Both hardening models can be used, but the strain hardening assumption is considered more accurate than the time hardening assumption (Boyle and Spence, 1983).

Multiaxial formulations of the creep laws are usually based on the von–Mises equivalent stress criterion and the Prandtl–Reuss flow rule. Lu and Weng (1996) provided a more detailed study on multiaxial creep for aircraft engine nickel based alloys.

2.4. Crack growth behaviour

The real improvement or benefit of cold expansion is experimentally verified by fatigue and fracture testing. Several investigations proved that there is a significant benefit from cold expansion in terms of fatigue life improvement of fastener systems. For the work described in this thesis, crack growth is examined not only as a consequence of cyclic fatigue loading but also due to creep at high temperature. The literature review was focused on the calculation of effective stress intensity factors using FE simulations, which are necessary for crack growth predictions. A good summary of experimental results can be found in McNeill and Heston (1987).

2.4.1. Fatigue / creep crack growth background.

There are two factors involved in crack growth: crack initiation and crack extension. The first topic is dependent on the technique used to identify crack lengths, as microcracks may exist in the component prior to fatigue loading. Therefore, crack initiation is often defined as the number of cycles to reach a determined detectable crack length. Fatigue crack growth is usually fitted to Paris law equations (Suresh, 1991). Crack length is then predicted as a function of the number of cycles for a determined load magnitude, load amplitude and geometry. A typical fatigue crack growth curve is shown in figure 2.12. The stresses ahead of the crack tip, typically at maximum stress in a fatigue cycle, are shown in figure 2.13 as a function of distance to the crack tip in the direction normal to the applied load. Solutions for those stresses include elastic and plastic behaviour (Anderson, 1995) with characteristic slopes using a power plasticity law such as Ramberg–Osgood.

For tests carried out at high temperature, cracks can grow due to creep under static loading. Crack growth is then given as a function of time for a determined applied load and geometry (Nikbin et al., 1986). For an elastic creeping material the stresses ahead of the crack tip follow the same shape shown in figure 2.13 with the plastic strains replaced by creep strains.

In general, it has been shown that inducing fatigue during creep increases the crack growth rate. The most damaging situation is said to occur during tensile dwell periods at constant load (Fookes, 1996). A combination of both fatigue and creep crack growth, is given by addition of both phenomena:

$$\frac{\partial c}{\partial N} = C_f (\Delta K)^{m_f} + \frac{D_c}{f} C^{*0.85} \tag{2.30}$$

where f is the frequency of the cycle, C_f, D_c and m_f are experimental material parameters. C^* is the line or surface integral that encloses the crack front from one crack surface to the other. It is used to characterise the local creep strain rate and stress fields at any instant around the crack tip at constant load (for example, maximum load). The stress intensity factor range ΔK is a function of the maximum and minimum loads applied for a particular geometry.

2.4.2. Retardation mechanism and closure effect and the influence of residual stresses.

Compressive residual stresses behind the crack tip are beneficial as they provide crack closure, and therefore decrease the generation of tensile stresses near the crack tip. Parker (1981) defined the interaction between residual stresses and external loading and analysed the use of analytical, FE and BE methods to model cracks. This study concluded that BE provided higher accuracy as there is no internal subdivision and therefore, no approximation is imposed on the solution at internal points.

Several investigations considered the benefit of residual stresses arising from overloads during the fatigue testing for aluminium alloys (Hammouda et al., 1998 and Lang and Marci, 1999). They found a decrease on the fatigue crack growth due to the plasticity originated ahead of the crack tip. This decrease was recovered once the crack went beyond the region dominated by plastic strain. For interference–fit fasteners in Al 2219–T851 plates a similar approach was carried out by Rudd et al. (1978) comparing experimental and predicted crack growth for different levels of interference and initial crack lengths.

There are many experimental studies showing fatigue testing of cold expanded holes. Priest (1997) carried out several tests for Al 2024 at room temperature and compared the results between cold and non–cold expanded holes. Results are shown in figure 2.14 when the maximum remote stress in the fatigue cycle was 1/2 and 1/3 of the yield stress σ_y'. Crack arrest was observed for the maximum stress of $\sigma_y'/3$ applied to cold expanded holes where the combination of applied stress and residual stress was not sufficient to propagate a crack.

Jones et al. (1999) used both the weight function (Grandt and Kullgren, 1983) and distribute dislocation (Hills et al., 1996) methods to predict crack growth from Al

7050 cold expanded holes. They found better agreement with experimental data for the dislocation approach. Both methods calculate effective stress intensity factors. Typical effective stress intensity factors from Grandt (1975) are shown in figure 2.15. However, these methods do not take into account the redistribution of residual stresses during crack growth which affects the crack growth behaviour for negative *R*, where *R* is the ratio of the minimum to the maximum applied remote stress. Ball and Lowry (1998) carried out several crack growth tests on Al 2124–T851 cold expanded samples until arrest or critical crack size (onset of fracture) was achieved. The results of fatigue crack growth for constant amplitude loading were compared to analytical models obtaining a good agreement for through–thickness starter cracks.

Finally, Bernard et al. (1995) examined the effect of pre–cold expansion on fatigue life enhancement of Al 7475 fastener holes. They used FEA to predict residual stresses and fatigue crack growth testing to demonstrate the benefit of a second cold expansion on a previously cold expanded hole in a plate. The life improvement of cold expansion was increased by a second expansion in some cases up to a factor of 3 when compared to non–cold expanded holes.

2.4.3. Determination of stress intensity factors in FE.

Simulations of crack growth are not a simple issue (Dusi et al., 1993), especially if the crack is intended to grow within compressive residual stress fields providing closure. It is however, less complicated to determine stress intensity factors (*K*) and creep integrals (C^*) for a determined crack length and residual stress state. These values are usually found through integral paths around the crack tip. Kaguchi and Nikbin (1993) concluded that three–dimensional analysis needed further improvements for the evaluation of *J* and C^* integrals. For this reason Pavier et al. (1998 and 1999) used a fitting technique to the HRR solutions of the stress distribution ahead of the crack tip to obtain the stress intensity factors.

This technique is complicated, especially for corner cracks. Alternatively, a crack opening technique has been used to calculate stress intensity factors and compared to analytical solutions (Chen et al., 1991). Several studies have been carried out for elliptical cracks in pipes. Carpinteri et al. (1999a and 1999b) obtained stress intensity factors from a quarter point displacement method and assuming plane strain conditions for different initial crack sizes. Fatigue crack growth was calculated using these stress intensity factors and a Paris fatigue crack growth law. Lin and Smith (1997) used a similar analysis for autofrettaged tubes. Stress intensity factors at different positions along the crack front were obtained. Results from their work are shown in figure 2.16 with and without crack contact (crack closure). Lin and Smith (1998) also studied corner cracks at fastener holes. They simulated the crack growth by automatically modifying the FE mesh to move with the crack front. With this technique the change of crack shape was also predicted to change from elliptical to circular shapes.

2.5. Conclusions.

(i) The Bauschinger effect is important in modelling residual stresses in cold expanded fastener holes particularly close to the hole edge where reyielding occurs.

(ii) Analytical models are only suitable for predicting residual stresses as a function of radius. Numerical analyses are needed to take into account the Bauschinger effect.

(iii) Plane stress and kinematic hardening has been used in two–dimensional FE models of cold expansion of thin aluminium plates. Axisymmetric models have been used to take into account the effect of the mandrel pull through. Less compressive tangential residual stresses were found close to the entrance face.

(iv) Creep for the aluminium alloy examined in this research at 150°C may be modelled using a power–law relationship. A large influence of prior strain on creep properties was found for a similar aluminium alloy.

(v) Fatigue crack growth in the presence of residual stresses has been predicted using effective stress intensity factors. These can be obtained from opening displacements at the crack tip in FE simulations.

Chapter 3
Al 2650 ALUMINIUM ALLOY PROPERTIES

The material used in this research is a new aluminium alloy, known as Al 2650, for which the composition and heat treatment are given. In order to examine the material response to external mechanical loading at different temperatures, several experimental tests were carried out. The elastic–plastic behaviour was examined first at room temperature, including tensile, tension–compression and cyclic hardening tests. These tests are necessary to obtain material constants for the simulations of the cold expansion process using both analytical and FEM. The study of the material behaviour at 150°C involved more tensile tests plus a study of the creep properties at high temperature. The effect of prior plasticity introduced at room temperature before creep starts was also studied. Finally, fatigue crack growth was examined to obtain Paris law parameters for FE predictions of fatigue loading.

3.1. Material composition.

The Al 2650 aluminium alloy was developed for the supersonic aerospace industry to replace components that were fabricated using the older aluminium alloy RR58. The older alloy is similar in composition to aluminium alloy Al 2618A. In subsonic aircraft, aluminium alloys such as the Al 2024–T351 are widely used. The good ratio between yield stress and mass density for this alloy provides good resistance to fatigue loading, fracture and fatigue crack growth. Typical properties for general aluminium alloys obtained from the Metals Handbook (1987) are shown in table 3.1. Since the new alloy has been designed for SST and specifically for creep resistance, chemical elements such as magnesium and manganese were added (Evans and Wilshire, 1985).

In this case the material was supplied by Alcan International Limited as 4 hot–rolled plates 15 mm thick, 1000 mm long in the rolling direction and 450 mm wide. The plates were hot–rolled from a 170 mm thick die cast ingot with the nominal and actual compositions shown in table 3.2.

The plates had been solution heat treated for one hour at 530°C, cold water quenched, uniaxially stretched 2% and finally aged for 19 hours at 190°C. As a result of this process a slightly elongated grain size was obtained varying from 42 to 300 μm in the rolling direction and from 40 to 150 μm in the transverse direction (Lacarac, 2000). The average grain size was 132 μm in the rolling direction and 92 μm in the transverse direction. Since the plate was hot–rolled, it is anticipated that large plastic strains were produced during the rolling. The implications for modelling the cyclic stress–strain behaviour are discussed in chapter 4

3.2. Elastic–plastic properties in monotonic loading.

The material was tested at both room temperature (about 20°C) and 150°C. Some results were provided by British Aerospace Ltd. (BAe, private communication) from tensile tests in the longitudinal, transverse and 45 degrees to the rolling direction for both temperatures.

Further tensile tests were conducted on material extracted from the received plates in the directions parallel (longitudinal), transversal and 45 degrees to the rolling direction. Tensile tests were carried out following the procedure given by Poussard (1995), and the complete stress–strain behaviour up to fracture obtained. The specimens shown in figure 3.1 were designed following the ASTM (1992) standards for circular cross–section samples. The diameter and the initial gauge length were measured using a "Mondo" shadow graph to within 0.01 mm. The button end specimens were fitted with locking nuts and split collets to a 100 kN DARTEC servo–electric test machine. Extensometry was attached to the specimen using a pair of divots. Two linear variable differential transducer (LVDT) were used to obtain averaged strains along the gauge length using the techniques described by Priest (1980).

The strain rate during the tensile tests at room temperature was set to minimise viscoelastic effects to 6.7×10^{-5} s^{-1} (ASTM, 1992). To determine the effect of creep relaxation in tests at higher temperature a constant load rate was used. This provided a constant strain rate during elastic behaviour but a higher strain rate once the yield stress was achieved. The yield stress was determined at +0.1% plastic strain.

The mechanical behaviour of the Al 2650 alloy at room temperature, is shown in figure 3.2. This alloy was observed to give a higher yield stress when compared with Al 2024 alloy, and has a similar elastic modulus. Al 2650 showed smaller hardening compared to Al 2024, and therefore the stress at high values of strain is quite similar for both materials. The monotonic loading stress–strain relation is shown in figure 3.2(a).

A small influence of specimen orientation on the tensile behaviour at 20°C and 150°C was found for Al 2650 alloy as shown in figure 3.2(b). For the tensile behaviour at 45 degrees, the yield stress was lower than for both the longitudinal and transverse directions. Average stress–strain behaviour from all the orientations were used for FE analysis (described in chapter 4) in order to simulate an isotropic material behaviour. These averaged material properties are given in table 3.3.

For tests carried out at 150°C two K type thermocouples were attached to the specimen using string. This was done because the spot welding did not work on the rounded aluminium faces of the specimen. Before the loading was applied the temperature was held at 150 ±2°C for 1 hour to ensure a homogenous temperature along the specimen. The stress–strain behaviour was similar to that for room temperature but with a lower yield stress and Young's modulus as shown in figure 3.2(a). The grain orientation showed even less influence than at room temperature as shown in figure 3.2(b).

The complete 3D stress–strain relation was not examined as it was not possible to test the material in the plate thickness direction. The Poisson's ratio was not experimentally measured but a value of $\nu=0.33$ was taken from the Metals Handbook (1987).

3.3. Cyclic behaviour.

The hardening behaviour in cyclic loading, and in particular the Bauschinger effect, were examined using the tensile test specimens shown in figure 3.1. A typical test involved loading the specimen in tension at a constant strain rate of $6.7 \text{x} 10^{-5}$ s^{-1} (ASTM, 1992) to a specified strain beyond the plastic strain. This introduced plastic deformation in the loading direction and a first yield stress, σ_y', was calculated for an initial plastic strain of 0.1%. Then the strain was set to return to the original zero. This involved the application of a compressive load, and a reyielding state where new plastic strains were introduced in the new (reverse) loading direction. A new yield stress, σ_y'', was obtained at a reversed plastic strain of 0.1%. The BEF was determined from the ratio of both yielding stresses $|\sigma_y''/\sigma_y'|$ as described by Poussard (1995), where a test involved the following sequence of loading plus unloading steps:

(i) Load to 2% total tensile strain.

(ii) Unload to 0% total strain with compressive stress.

(iii) Load to 4% total tensile strain.

(iv) Unload to 0% total strain with compressive stress.

(v) Load to 6% total tensile strain.

(vi) Unload to 0% total strain with compressive stress.

The results of the test are shown in figure 3.3(a). Beyond the first yielding σ_y' the material behaviour was close to perfect plasticity. Reversing the loading direction led to reyielding, showing the BEF. Once reyielding σ_y'' was reached, the material behaviour showed significant power–law type hardening in compression (similar to Ramberg–Osgood). Reyielding started at a relatively low stress compared with first yielding, and with BEF = $|\sigma_y''/\sigma_y'| < 0.2$ when using the 0.1% plastic strain definition. Using a proof stress at a plastic strain close to zero, reyielding started at a stress of about –25 MPa, resulting in an approximate BEF of 0.05.

It was considered interesting to investigate whether the same effect was observed where the initial loading was in compression and reyielding in tension. Unfortunately buckling instability was predicted around a 4% compressive strain. The specific test was carried out as follows:

(i) Load to 1% total compressive strain.

(ii) Unload to 0% total strain with tensile stress.

(iii) Load to 2.5% total compressive strain.

(iv) Unload to 0% total strain with tensile stress.

(v) Load to 4% total compressive strain.

(vi) Unload to 0% total strain with tensile stress.

Experimental results are shown in figure 3.3(b). A similar initial yielding stress σ_y'

was found for this compression–tension test compared to the tension–compression test. Buckling was observed after 3% total compressive strain, as shown in figure 3.3(b). Examination of the elastic relation between stresses and strains showed an elastic modulus, E, slightly higher for compressive loading as reported for most of the aluminium alloys (Metals Handbook, 1987). For a given offset plastic strain, i.e. 0.1%, the same Bauschinger effect was found in both cases varying from 1 to 0.2 as a function of plasticity.

The cyclic tests mentioned above were done on specimens manufactured in the rolling and transverse directions, obtaining similar results as for the tensile tests. The plate thickness, h = 15 mm, did not allow specimens to be extracted from the through–thickness direction to complete a 3D evaluation of the Bauschinger effect.

The cyclic hardening was also examined using different cyclic tests. In figure 3.4(a) the results of a cyclic strain controlled test are presented. The strain fluctuated between plus and minus one per cent. The specimen, test rig and strain rate of $6.7\text{x}10^{-5}$ s^{-1} were identical to those used for the previous tests (Martínez, 1998). The stress at +1% strain is plotted against the number of cycles in figure 3.4(b) showing a small softening or maximum stress relaxation of about 10%. This relaxation was stable after approximately 30 cycles.

3.4. Creep properties.

An important influence on the residual stresses at high temperature is stress relaxation due to creep. In order to find the creep properties, the results of several creep tests carried out by the DERA, (private communication) and BAe, (private communication) were used. In addition some tests were carried out at the University of Bristol.

First, the deformation maps from Ashby and Frost (1982) were examined in order to identify the creep behaviour expected from the material. It was found that for pure aluminium and its alloys at 100 ±80°C and in the range of stresses of interest (from 10 MPa up to yield stress σ_y'), the creep behaviour was within the power–law creep regime. The Norton and Bailey power–law described by Boyle and Spence (1983) in equation 2.25 is therefore used to fit the data obtained from the creep tests.

Several creep strain accumulation tests under constant load were carried out at different temperatures. The pin–hole type creep tensile specimen is shown in figure 3.5. The testing was carried out using lever–type creep test rigs. K–type thermocouples were attached to the specimens as described earlier for tensile tests at high temperature. The total strain was recorded automatically using a PC Alpha card and software developed for this purpose (García–Granada, 1998). A variety of test results are shown in figure 3.6.

The parameters presented by Polmear et al. (1996) for different aluminium alloys, including Al 2650, were used as initial estimates of material constants in equation 2.24 to fit experimental results for Al 2650. In figure 3.6(a) the effect of load is shown for experimental tests at 150°C. In figure 3.6(b) the effect of temperature is shown for different loads. The power–law constants C_c, ΔH, n_c and m_c, obtained from least–squares curve fitting to all the experiments, are shown in table 3.4.

Of particular interest to this research is the relaxation at high temperature of residual stresses, with the original residual stresses arising from cold expansion. Relaxation tests were also carried out in a DARTEC servo–electric test machine in order to be able to control the strain constant in the specimen during the relaxation. The specimens were identical to those used for the cyclic testing shown in figure 3.1. These results were used to complete the curve fitting technique for the creep power–law given in table 3.4, as the results from strain accumulation could be fitted with a large combination of parameters which would predict a completely different stress relaxation.

Cold expansion implies that the residual stress release occurs within regions plastically deformed at room temperature. Therefore, the effects of prior plasticity and the strain rate used to produce this prior plasticity were investigated (Martínez, 1998). Prior plasticity was introduced by both prior tensile and compression preloading. Two different strain rates were used: fast loading equivalent to $3.0\text{x}10^{-3}$ s^{-1} and slow loading at $6.7\text{x}10^{-5}$ s^{-1}. Prior plasticity was introduced at room temperature and then the specimens heated up to 150°C at zero load conditions. After 1 hour at this temperature a strain of 0.5% in tension was applied and held constant for a period of 48 hours during which the stress relaxed. A data logger was used to record voltages corresponding to strains, stresses and temperatures during the test. Results are shown in figure 3.7.

In figure 3.7(a) the stress relaxation is shown for four different specimens. The first one corresponds to the as–received material, the second to an application of 4% prior strain at the fast strain rate. The third specimen corresponds to a 4% prior plasticity at the slow strain rate and finally the fourth specimen to a compressive –2% prior plasticity at the slow strain rate. Due to the Bauschinger effect after application of prior plasticity, the stress corresponding to a 0.5% deformation was different for every sample, and therefore the initial stresses for relaxation were different. In figure 3.7(b) the relaxation is plotted as a percentage of the initial stress. It is shown that the least relaxation occurred for the as–received specimen with a relaxation around 15% of the initial stress. The maximum relaxation occurred for the specimen with a compressive –2% prior plastic strain, with a total relaxation after 10 hours of about 30%. From the specimens with a 4% prior plasticity, the prestrained sample initially loaded at a fast rate showed more relaxation. For all cases the relaxation seemed to achieved a maximum stable value after about 10 hours.

This effect on creep strain accumulation after prior plasticity was also found by Evans and Wilshire (1985), for a similar aluminium alloy, and by Biscaya (1971) and Huston (1972), for the RR58 alloy at 150°C. Higher creep strain accumulations after prior plasticity were obtained by these authors but stress relaxation was not investigated. However, it could be inferred from creep strain accumulation that there would be higher stress relaxation after prior plasticity.

Some agreement in stress relaxation is found with Gincburg (1957) where an extensive study was carried out on steel wires. This investigation also concluded that prior plasticity introduced at fast strain rates leads to lower stress relaxation compared to tests on wires not subjected to prior plasticity and wires where prior plasticity was induced at slower strain rates.

3.5. Fatigue crack growth properties.

The effect of fatigue on Al 2650 has been examined using a variety of tests by Lacarac (2000). The tests were conducted using flat plate specimens as suggested in ASTM (1992) standard E647. These specimens contained a centre hole of radius a=3 mm and had an overall length of 245 mm, width 100 mm and thickness 6 mm. Two corner notches were machined into the plate surface of each specimen, arising from the hole edge at ±90 degrees from the loading direction. The material was tested in a servo–hydraulic test machine with the loading parallel to the rolling direction. A comprehensive set of initial crack lengths, maximum loads and R values were examined by Lacarac, (2000). Typical results from this research are shown in figure 3.8.

Using equations to relate crack length, crack and specimen geometry with stress intensity factor, a Paris law (Suresh, 1991) was fitted to the experimental results. However the determination of stress intensity factors. The coefficients for the Paris law are presented in table 3.5. Test results shown in figure 3.8(a) were obtained from a specimen loaded with a maximum remote stress $\sigma_{app} = 162$ MPa, a ratio $R = 0.1$ and a frequency $f = 10$ Hz. Both crack lengths on the surface were monitored during the test. The crack growth rate and stress intensity factors were calculated and are shown in figure 3.8(b) and compared to the Paris law equation. Further tests are presented by Lacarac (2000) and include the effect of cold expansion in fatigue crack growth behaviour.

3.6. Conclusions.

(i) Improved creep resistance in comparison to RR58 is obtained in Al 2650 by additions of the alloying elements magnesium and manganese.

(ii) It is anticipated that large plastic strains were produced during the rolling process which reduced the 170 mm thick ingot to the 15 mm thick plate.

(iii) Tensile tests showed that there was a small influence of grain orientation (in rolling, transverse and 45 degrees direction) for the stress–strain behaviour.

(iv) Cyclic tests showed the importance of the Bauschinger effect. The BEF is similar for tension–compression and compression–tension tests.

(v) Relatively small cyclic softening was observed using symmetric strain controlled tests.

(vi) A power–law creep function was used to describe creep strain accumulation for different temperatures and different applied stresses.

(vii) Creep relaxation tests showed that prior plasticity resulted in slightly higher relaxation when compared to the as received material.

(viii) A Paris law equation was used to predict fatigue crack growth from stress intensity factors.

Chapter 4
Finite Element studies of Cold Expansion at Room Temperature

The studies described in this chapter use FEA to determine the residual stress field surrounding cold expanded fastener holes. Simulation of the cold expansion process was carried out using both two–dimensional and axisymmetric models. In the latter, the effect of the mandrel pull–through was included and a combined hardening material model was used to take into account the behaviour of Al 2650 in reverse loading. The effect of external tensile or compressive loads at room temperature was also studied. Residual stresses were found to redistribute after releasing the external load. Finally, a detailed 3D analysis examined the benefit of cold expansion during application of external tensile stresses.

4.1. Cold expansion analysis at room temperature.

Cold expansion residual stresses are obtained from the plastic deformation introduced around the hole. It was considered important to gain an understanding of the elastic–plastic material response. In previous analytical (Chen, 1986) and FE studies (Poussard, 1995) the influence of reverse yielding and the BEF were analysed. Therefore, it was considered interesting to include this effect in the material behaviour used in the FE studies. In figure 4.1a response to reverse loading for Al 2650 is compared to isotropic, kinematic and combined hardening models available in the commercial FE code ABAQUS (1999). The combined hardening model considers the influence of plastic strain and back–stress in the axial (z) direction due to machining and forming processes such as rolling. The combined hardening model was fitted to experimental data for cyclic softening tests (Martínez, 1998). Cyclic softening is shown in figure 4.1b for a strain controlled test and compared to FE predictions using the same combined hardening model on a single element analysis. However, this model is only suitable for three–dimensional or axisymmetric models as the BEF is obtained by means of an initial back–stress in the z direction. The mathematics involved in a combined hardening model are described by Martínez (1998) and are based on the combination of kinematic and isotropic hardening rules. The combined hardening was not suitable for future simulations of creep at high temperature. Therefore, a combination of different material models was used throughout the study. The simulation of cold expansion and results from the analysis are presented next.

4.1.1. Two–dimensional uniform radial expansion.

Initial FE studies of cold expansion were carried out using two–dimensional simulations. One quarter of a plate containing a centre hole was examined. The mesh is shown in figure 4.2, together with the boundary constraints to provide symmetry conditions. The FE mesh was refined near to the hole edge to account for high stress and strain gradients within the error tolerance of the calculations. The tolerance on residual force was set to 0.5% of the maximum force in the model. A total number of 32 elements around the hole and 40 elements in the radial direction were used to complete a square containing a hole of radius a=3 mm and width b=50 mm. Extra elements were added in the x direction to complete a length of $2b$=100 mm. In all cases, eight noded second order isoparametric elements with reduced integration were used. Both cartesian (x,y,z) and cylindrical (r,θ,z) co–ordinates were chosen to represent stresses and strains.

The cold expansion process was simulated as an application of a uniform radial displacement of the hole edge followed by displacement removal. Identical results were found by applying instead a uniform pressure to the hole edge followed by a pressure release. The simulations were carried out using both plane stress and plane strain conditions. An influence of hardening model was studied for kinematic and isotropic hardening as in previous research (Poussard, 1995). The results obtained are shown in figure 4.3. The plane stress condition showed less compressive tangential residual stresses close to the hole edge and a smaller plasticity region when compared to plane strain. Kinematic hardening models showed slightly less compressive tangential residual stresses close to the hole edge but also a slightly larger plasticity region when compared to isotropic hardening. Plane strain conditions led to more compressive residual stresses due to the influence of the axial (through–thickness) stress in the von–Mises plasticity criterion.

4.1.2. 2D axisymmetric simulation with a mandrel pulled through.

A 2D axisymmetric model of a rigid mandrel pulled through the hole is shown in figure 4.4 for a plate thickness h=6 mm, hole radius a=3 mm and outer disc radius b=16 mm. Cylindrical co–ordinates were used, defining the axial positions z=0 for mid–thickness, z=3 mm for the entrance face and z=–3 mm for the exit face.

As one of the consequences of axisymmetry, the split in the sleeve was not modelled. It was decided to incorporate the dimensions of the sleeve by increasing the size of the mandrel as in Poussard (1995) where it was concluded that an independent sleeve would increase the calculation time but would estimate similar residual stresses.

The mandrel was modelled as a rigid surface with a maximum diameter oversized by 4% with respect to the hole diameter. The diameter change was obtained by means of tapering at 0.05 mm/mm. The corners of the tapered mandrel were rounded to avoid problems during numerical calculations.

The aluminium plate was modelled using four noded axisymmetric elements with reduced integration. Contact elements were placed between the rigid mandrel and the hole edge to transfer pressure and avoid penetration of the mandrel inside the mesh of the plate. Eight noded elements (used in 2D analyses) were not used as they gave contact problems.

The elastic–plastic response was modelled using the combined hardening model, shown in figure 4.1a, to take into account the Bauschinger effect. This model was based on a Ramberg–Osgood power–law equation with the introduction of a compressive back–stress in the axial (through–thickness) direction and cyclic behaviour. The equations and parameters required by ABAQUS (1999) are shown in table 4.1 for Al 2650 as described by Martínez (1998).

Axial support of the plate was provided by non–linear spring elements placed near the hole edge up to r/a=1.16. This simulates the reaction force provided by the mandrel puller. The spring elements were defined to produce a high compressive force for negative displacements (stiffness $F_z/U_z=10^{11}$ N/m) but a small tensile force for positive axial displacements (stiffness $F_z/U_z=10^{-1}$ N/m). A schematic diagram of such behaviour is presented in figure 4.4.

The mandrel was pulled through the hole in incremental steps by imposing negative axial displacements to the mandrel. A large displacement scheme was used during the calculation, correcting the nodal position by adding the displacement after each increment. The expansion was completed in 120 increments of axial displacement. Several simulations were carried out and to improve the results the mesh was refined around the hole and near entrance and exit faces.

Once the mandrel was completely pulled through, residual stresses and permanent radial displacements of the hole and axial displacements of the entrance and exit faces were examined.

Results for radial and tangential residual stresses are shown in figure 4.5, and axial and von–Mises equivalent stresses in figure 4.6 for different positions through–thickness plus the average results through–thickness.

Radial residual stresses were found to be generally compressive as shown in figure 4.5a except at the entrance face and close to the hole edge. The highest compressive stresses of about –230 MPa were found at the exit face at a radial distance of r=5 mm (r/a=1.67). The average stresses along z were similar to those obtained for the mid–thickness position (z=0).

Tangential residual stresses also showed a variation with radius and axial (through–thickness) position as shown in figure 4.5b. The least compressive residual stresses close to the hole edge were found at the entrance face. They ranged from –60 to –100 MPa for radii between 3 mm (hole edge, r/a=1) and 4.5 mm (r/a=1.5). Poussard (1995), in his study on Al 2024, found less compressive and tensile residual stresses at this position close to the entrance face and the hole edge. The most compressive tangential residual stresses were found at the exit face at –420 MPa for a radius of about 4.0 mm (r/a=1.33). Once more, the average stresses along z were similar to those obtained for the mid–thickness position (z=0). The radius of plasticity, ρ', or area which has suffered some plastic deformation (Sanford and Link, 1989), can be obtained from the tangential stress profile (Armen et al., 1994). In this case the radius of plasticity was found to be approximately 7 mm (r/a=2.33).

The axial residual stresses were small in comparison to the radial and tangential stresses. This agrees with the plane stress assumptions commonly used for thin plates. Only significant values were found near the hole edge for z=2.50mm, in other words

0.5 mm below the entrance face of the aluminium plate. At this position large stress gradients were found with a maximum stress of about 200 MPa at the hole edge. Averaged through–thickness the axial residual stresses were small.

Finally, von–Mises stresses are shown in figure 4.6b. As a consequence of the Bauschinger effect the equivalent stress is not constant near the hole edge. In this case hardening in reverse yielding leads to higher stresses at the hole edge where the effects of reverse plasticity are more important. However, this maximum equivalent stress is below the initial yielding stress of 430 MPa. It is also possible to examine the radius of plasticity, ρ', from the averaged stresses along the thickness (z). In this case it is easier to define three different regions: the elastic region for a radius bigger than $\rho' = 7$ mm ($r/a > 2.33 = \rho'$), the plastic region for a radius between 5 and 7 mm ($1.67 < r/a < 2.33$), and the reverse plasticity region for a radius between 3 and 5 mm ($1.00 < r/a < 1.67 = \rho''$). The results show that the material at the entrance face does not reyield during hole expansion release.

The permanent deformations after cold expansion, in the axial direction for the entrance and exit faces, are shown in figure 4.7a as a function of radius. A maximum deformation of about 150 μm is detected at the hole edge for the exit face. The entrance face showed a smaller deformation of about 50 μm. In both cases the deformation was insignificant for a radius larger than 7 mm ($r/a > 2.33$).

The permanent deformations of the hole in the radial direction (U_{rr}) are shown in figure 4.7b as a function of the axial position (z). A maximum deformation of about 105 μm is shown near the entrance face with an average deformation of about 98 μm through–thickness of the plate. This deformation is equivalent to a permanent enlargement of 3.2% compared to the 4% nominal applied deformation during the cold expansion. Similar deformations were found for Al 2024 using FE models (Poussard, 1995) and experimental measurements (Priest, 1997).

Contour plots of the residual stresses predicted using the FE simulation are shown in figures 4.8a radial σ_{rr}, 4.8b shear τ_{rz}, 4.8c axial σ_{zz} and 4.8d tangential $\sigma_{\theta\theta}$. As a large displacement analysis was chosen, the plate appears in its final deformed state.

The influence of the hardening model was examined using a FE simulation with classical isotropic and kinematic hardening models (García–Granada et al., 1999a). Several researchers showed that a good approximation to the Bauschinger effect would generate less compressive tangential stresses near the hole edge in comparison to isotropic and kinematic models (Chen, 1986, Wanlin, 1993, Ball, 1994, Jahed and Dubey, 1996, and Lazzarin and Livieri, 1997). The results for tangential residual stresses obtained for Al 2650 using these models are shown in figure 4.9 for different positions through–thickness: (a) entrance face, (b) average through–thickness and (c) exit face.

The combined hardening model predicted less compressive tangential residual stresses close to the hole edge and a larger area of reverse yielding. This was due to the initiation of reverse yielding for lower equivalent stresses during the release of the hole expansion. This difference was not so important near the entrance face as the material did not reyield during unloading (figure 4.9a). Elsewhere, differences were significant between the hardening models. The tangential stress averaged through–thickness at the hole edge was about: –400 MPa for the isotropic hardening, –360 MPa for the combined hardening and –315 MPa for the new combined hardening model.

The results obtained from a two–dimensional simulation with plane stress and kinematic hardening are also shown in figure 4.9b compared to axisymmetric simulations averaged through–thickness. The 2D model predicted more compressive residual stresses near the hole edge, though the difference was small when compared to axisymmetric simulations with isotropic and kinematic hardening.

4.2. Cold expansion and mechanical loading analysis at room temperature.

Cold expansion is used to introduce beneficial compressive residual stresses around holes and to minimise the negative effect of the stress concentration. However, a complete study of such a benefit would only be justified by examining the interaction between residual stresses and applied external load. To study open holes in plates subjected to external loads, axisymmetric models are difficult to use. Therefore two–dimensional models considering plane stress and kinematic hardening were used. The first case studied the application of a uniaxial tensile stress to cold expanded holes with the intention of assessing superposition assumptions. The next model examined the effect of compressive stresses where residual stress redistribution was expected. Finally, three–dimensional simulations were carried out to examine the benefit of residual stresses through–thickness of the plate.

4.2.1. 2D plane stress simulation with uniaxial tensile external load.

A simple 2D FE simulation was carried out using a mesh similar to that shown in figure 4.2. The cold expansion for 2D models was described earlier. A plane stress state was chosen to represent the thin plate containing the hole. This assumption was considered to be more realistic after the observation that the residual axial stresses were small from axisymmetric simulations. Kinematic hardening was used as the best available option for two–dimensional simulations as isotropic hardening would over–

predict the residual stresses, and combined hardening can not be correctly used for 2D models.

First, the residual stresses were introduced in the plate by means of a uniform radial displacement at the hole edge. The external stress was then applied at the plate edge in the x direction ($\theta=0°$). Several magnitudes of external stress, ranging between $\sigma_y'/30$ and $2\sigma_y'/3$, were studied. Finally, the external stress was removed giving rise to a new residual stress distribution.

In figure 4.10a the tangential stresses are shown with the application of an external stress of 215 MPa = $\sigma_y'/2$. The original residual stresses arising from cold expansion are shown as a continuous solid line. The tangential stresses at an angle perpendicular to the applied load ($\theta=90°$) can also be obtained from the residual stress plus the elastic distribution of the stress around a hole (Timoshenko and Goodier, 1987 and Savin, 1966). In particular, the tangential stress at the hole edge: $\sigma_{\theta\theta}(r=a,\theta=90°)$, is equal to the tangential residual stress at the hole edge plus three times the applied stress. However the superposition effect is not valid for the direction of the applied load ($\theta=0°$). In this position, residual stresses close to the hole edge were highly compressive, and already on the yield surface. Therefore, external loading causes additional plasticity at this position.

The final residual stress distribution after unloading as a function of normalised radius is shown in figure 4.10b. A slight redistribution of residual stresses is found at $\theta=90°$ from the original residual stresses arising from cold expansion. The major redistribution is produced near the hole edge for $\theta=0°$. This residual stress distribution corresponds to cold expansion residual stresses and elastic unloading of the compressive stress at $\theta = 0$ originated by external loading. Timoshenko and Goodier (1987) described the tangential stress to be equal to the applied stress but compressive near the hole edge at this position. The relaxation is therefore similar to the applied external stress of 215 MPa.

For all cases studied, a substantial benefit from the cold expansion on tangential stress distributions in loaded conditions was found in the direction normal to the loading and near the hole edge. Yielding started at this position in non–cold expanded holes for applied stresses beyond one third of the yield stress ($\sigma_Y'/3$), while in cold expanded holes yielding was reached for applied stresses over 60% of the yield stress ($0.6\ \sigma_Y'$). Yielding occurred in compression for any tensile load in cold–expanded holes at $\theta=0$ or the loading direction near the hole edge. For applied stresses ranging between 0 and $\sigma_Y'/3$, the difference in tangential stress at the hole edge for $\theta=90^\circ$ between cold and non–cold expanded holes was about 400 MPa. This benefit decreased for higher loads as plasticity was introduced around cold expanded holes. For applied stresses over $0.6\ \sigma_Y'$, a similar tangential stress was found at the hole edge for both non–cold expanded and cold expanded plates.

4.2.2. 2D plane stress simulation with uniaxial compressive external load.

A similar simulation was carried out for compressive applied stresses. The same FE mesh, plane stress conditions and kinematic hardening rules were applied. The compressive stresses applied ranged between $-\sigma_Y'/3$ and $-\sigma_Y'/30$. After removal of the external stress a new residual stress distribution was generated.

The tangential stresses when an external stress of –143.33 MPa = $-\sigma_Y'/3$ was applied are shown in figure 4.11a as a function of radius for two different angular positions: parallel ($\theta=0^\circ$) and normal ($\theta=90^\circ$) to the applied load. The solid line represents the original residual stress distribution arising from cold expansion. For $\theta=0^\circ$, elastic superposition is applicable. At the hole edge the tangential stress can be found from the residual stress as: $\sigma_{\theta\theta}(r=a,\theta=0^\circ)$ is equal to the tangential residual stress at the hole edge plus the absolute applied stress. A very different effect occurred at θ=90° where large plasticity was introduced by means of reverse yielding. The tangential stresses increased slightly in magnitude (slightly more compressive) near the hole edge where further yielding continued from cold expansion. It was found that there was an increase in the reverse yielding radius ρ''.

Once the mesh was unloaded a new residual stress distribution was found as shown in figure 4.11b, obtaining small compressive tangential residual stresses for θ=90° and a distribution similar to the cold expansion residual stresses for θ=0°. This is in agreement with FE results published by Armen et al. (1984).

It was found that any compressive load would introduce plasticity and redistribute the cold expansion residual stresses at positions normal to the direction of the applied load. Compressive stresses over one third of the yield stress would generate tensile residual stresses at the hole edge for θ=90°.

4.2.3. 3D plane stress simulation with uniaxial tensile external load.

Two–dimensional FEA showed the benefit obtained by cold expansion of holes when uniaxial external tensile stresses were applied to the plate containing the hole. However the residual stress distribution obtained after simulating the cold expansion in two–dimensional models were more compressive than those obtained from axisymmetric models which also take into account the Bauschinger effect. Furthermore two–dimensional models did not take into account either the variation of stress concentration with thickness and axial position (Sternberg and Sadowsky, 1949), or the variation of residual stresses with axial position from the cold expansion process.

In order to complete the examination of the benefit of cold expansion it was decided to conduct three–dimensional simulations. However, it was found very time consuming to simulate the complete process. Poussard (1995) undertook a complete

3D analysis of the mandrel pulled through the hole without a sleeve, but the simulation time was very large. He also indicated an alternative method of solving the problem. He suggested importing residual stresses from an axisymmetric simulation into a 3D mesh and then to apply the external loading.

In this research it was decided to run a Fortran (Atkinson et al., 1989) subroutine called SIGINI (ABAQUS User Subroutines, 1997) to read residual stresses from axisymmetric models and input residual stresses into three–dimensional models. The correction for different meshing was done through interpolation. This interpolation dealt with the effect of introducing additional material as in the case of rectangular plates. Poussard showed little influence in residual stresses from cold expansion between circular discs or rectangular plates.

Once the residual stresses were introduced into the 3D mesh, equilibrium was ensured by computing a first step with no external loading. A kinematic hardening rule was used to model the material. Therefore any information about the combined hardening, in particular the evolution of plastic strains (and permanent deformations) and back–stresses, was lost during the transfer as indicated by Poussard (1995).

Two identical models were executed to simulate cold expanded and non–cold expanded holes. Only the first case used the subroutine to read residual stresses. Then external loading was applied as a uniformly distributed pressure at the plate edge to both models, and finally the stress distribution around the hole was analysed.

In figure 4.12 the tangential stress distribution is shown for both non–cold expanded hole and cold expanded hole. The external stress applied was (a) 143.33 MPa = $\sigma_y'/3$ and (b) 215 MPa = $\sigma_y'/2$. For the non–cold expanded hole the effect of the stress concentration lead to yielding near the hole edge. Higher tensile tangential stresses were found at the mid–thickness positions. This is because of the influence of axial stresses that are zero at top and bottom free surfaces but slightly compressive at mid–thickness.

For cold expanded holes, the distribution of stresses through–thickness is more important and is a consequence of the effect of pulling a mandrel through the hole. As expected, the minimum benefit was obtained near the hole at the entrance face. At this position tangential stresses reached values up to 300 MPa for (a) $\sigma_{app} = \sigma_y'/3$ and up to 470 MPa for (b) $\sigma_{app} = \sigma_y'/2$. However the tangential stresses were still compressive in some regions close to the hole edge.

4.3. Conclusions.

(i) Two–dimensional models were used with a kinematic hardening material model and plane stress state. These models were found to be the most realistic approach available for simulating cold expansion in thin plates of Al 2650.

(ii) Axisymmetric models of a mandrel pulled through the hole predicted small tangential compressive stresses at the inlet or mandrel entrance face. The outlet or mandrel exit face predicted slightly less compressive tangential stress at the hole edge when compared to the through–thickness average.

(iii) The variation through–thickness was only important for the first millimetre close to the entrance and exit surfaces. The mid–thickness distribution is similar to the average through–thickness.

(iv) The radial residual stress showed tensile values close to the hole edge for the inlet face.

(v) The hole suffered a permanent radial deformation of 3.4% near the entrance face.

(vi) The combined hardening model available for axisymmetric simulations fitted the stress strain behaviour of Al 2650 including the Bauschinger effect. This generated less compressive residual stresses when compared to kinematic and isotropic hardening models.

(vii) Using 2D models, the benefit of cold expansion was found for the application of tensile stresses. A considerable relaxation of residual stresses was shown after the application and release of compressive stresses.

(viii) A more detailed examination of the benefit of cold expansion was carried out using 3D models by introducing residual stresses from axisymmetric simulations. The least benefit was obtained near the hole edge at the entrance face.

Chapter 5
Finite Element studies of creep stress relaxation

In this chapter, FE simulations of creep relaxation are presented. Creep was simulated using power–law models and compared to creep strain accumulation tests under constant load. The simulations were also compared to stress relaxation tests under constant strain, including studies of the effect of prior plasticity. The results obtained are presented first as a relaxation of cold expansion residual stresses for both two–dimensional and axisymmetric models without the interaction of external loads. The interaction of creep and external loads was then examined using two–dimensional and three–dimensional models. For both cases, the evolution of stress and strain was obtained as a function of time and the final residual stress distribution presented once the external load was removed.

5.1. Creep stress relaxation at high temperature.

Creep is a time dependant deformation caused by thermally activated movement of vacancies, dislocations, etc. at high temperatures. This implies that creep strain is a function of stress, time and temperature. Several models are available and have been described in the literature review. For the aluminium alloy Al 2650 in use in this research, it was decided that a power–law model was to be used after examination of research by Polmear et al. (1996). The power–law was determined from experimental results in chapter 3 and described by table 3.4. The experimental results were a combination of strain accumulation under constant load and stress relaxation under constant strain conditions.

To validate the FE model of the creep, a single element simulation was carried out where the stress was held constant to measure creep strain accumulation and compare it to experimental results. In figure 5.1a the total (creep plus elastic) strain accumulation from experimental tests at 150°C for different loads are compared to the FE simulations. A good agreement is obtained at low stresses. For stresses over 300 MPa the agreement is less good due to the reduction of cross–section and the proximity to yield stress which would lead to plasticity (Ashby and Frost, 1982).

The research in this thesis is concerned on the relaxation of residual stresses. Therefore a single element was subjected to a uniform displacement and allowed to relax. Simulation results were compared to experimental tests as shown in figure 5.1b, where the effect of prior plasticity in the experiments is also shown. Plane stress and time hardening rules were chosen and are described later.

An explicit Euler method, also known as forward–difference method, was used during the time dependant calculations. Small time steps are required to ensure stability. The use of implicit calculations was dismissed, as frequent re–solving of the stiffness matrix is required. The FE simulations used the multi–axial form of the Norton–Bailey power–law given by equation 2.25. A description of the FE algorithms and procedures used in creep analysis can be found in Hinton (1980). The use of a time hardening rule to solve creep strains as a function of time has no influence in strain accumulation tests but predicts a larger stress relaxation under constant strain if compared to strain hardening calculations.

Time hardening was chosen to carry out the simulations with the constants given in table 3.4 as they produced the best fit to experimental results. However the least–squares technique was difficult to use with these experiments to obtain a good correlation because in a power–law there are many parameters to be fitted. The results of the curve fit were considered to be optimised for the conditions shown in figures 5.1a and 5.1b with time hardening, as they produced the best fit even considering the influence of prior plastic strain.

Simulations and models assumed a constant temperature distribution along the specimens and both creep strain accumulation and stress relaxation started at a temperature of 150°C. This assumption was considered to be suitable for thin plates of aluminium where the high thermal conductivity would assure a rapid uniform thermal distribution. This was checked experimentally by Lacarac (2000).

Two different approaches were used to simulate the change of temperature. The first considered a change of material properties followed by creep. In the second approach the creep analysis was undertaken without considering a change of yield stress or Young's modulus with temperature. However, this did not have a significant influence on the results.

5.1.1. 2D plane stress redistribution of residual stresses.

An initial creep stress relaxation analysis was performed using a two–dimensional FE simulation. Cold expansion was simulated as described in the previous chapter, using uniform radial expansion of the hole edge, a kinematic hardening material model and a plane stress state.

The effect of creep was modelled using the Norton–Bailey power–law model (table 3.4) with time hardening rules. During the simulation at 150°C, the plate was free of external loads leading to residual stress redistribution.

In figure 5.2a the redistribution, or relaxation, of radial residual stresses is shown for different times up to 1000 hours. Such relaxation is a consequence of the accumulation of creep strains in areas where the equivalent von–Mises stress is a maximum. In order to understand this relaxation, the redistribution of tangential residual stresses is shown in figure 5.2b for different times, as a function of distance from the hole centre. The highest stress relaxation occurred near the hole edge, where the equivalent stress was a maximum. This relaxation is in agreement with the experimental studies from Eigenmann et al. (1994) for shot peened 42CrMo4 after annealing at 400°C. They observed the highest relaxation close to the peened surface where residual stresses were most compressive. Similar experimental results were obtained by Lillamand and Barrallier (1996) for different temperatures and exposure times also in shot–peened steel specimens. A study of cold expansion was carried out by Throop et al. (1981) on autofrettaged steel cylinders, but in this case a thermal difference was obtained between the inside of the tube and the outside as in Beeston and Burr (1979) for a stainless steel. Therefore thermal stresses were added to residual stresses and played an important role in the relaxation.

The change in tangential strains with time for different radial positions is shown in figure 5.3a and for tangential stresses in figure 5.3b. The strain did not remain completely constant during relaxation. Strain changes up to 0.16% occurred near the hole edge. This is an important strain change, as the material accumulated small amounts of creep strain. This case is similar to problems of creep under constant displacement for specimens with a variable cross–section (Boyle and Spence, 1983).

5.1.2. 2D axisymmetric redistribution of residual stresses.

As described in the previous chapter the distribution of residual stresses arising from cold expansion was a function of the thickness or axial position (*z*). This effect was observed using simulations of a mandrel pulled through in axisymmetric models for three different hardening models: isotropic, kinematic and the combined hardening model which provided the best fit to Al 2650 elastic–plastic behaviour. Therefore, the creep relaxation of residual stresses in the axisymmetric model was studied.

The creep power law, with a time hardening rule, was used to simulate the time dependent process. However, in the version of ABAQUS (1999) available at the time of the study the combined hardening model of plasticity could not be used with creep models. Therefore, the creep distribution of residual stresses arising from combined hardening models was done on kinematic hardening models. The residual stresses from a combined hardening analysis were introduced in the creep simulation using the subroutine SIGINI (ABAQUS User Subroutines, 1997). During the simulation, the von–Mises equivalent stress was checked to guarantee that no additional plastic strains were introduced, as this would have an effect in the change from combined to kinematic hardening. The relaxation was purely elastic with generation of creep strains. For completeness, results were compared to axisymmetric models with residual stresses arising from isotropic and kinematic hardening material models.

Relaxation behaviour of the residual stresses obtained for the three hardening models are very similar, with faster relaxation obtained for the isotropic model where the initial residual stresses were maximum (most compressive) near the hole edge. The radial variation of the tangential residual stresses from the combined hardening model are shown in figure 5.4 after 1000 hours at 150°C. Residual stresses at the entrance and exit faces are shown, together with the average through–thickness residual stress before and after creep. The average through–thickness was similar to the residual stress distribution at the mid–thickness position in both cases.

The relaxation near the entrance face was insignificant, with the low compressive tangential stresses unaffected. The relaxation was significant near the hole edge elsewhere far from the entrance face. The tangential stresses near the exit face decreased in magnitude from values close to –380 MPa at $r/a = 1.4$ to –270 MPa after

1000 hours of creep. A similar effect occurred for the averaged stresses through–thickness. A small relaxation of the tensile stresses far from the hole edge was observed.

5.2. Creep stress relaxation with mechanical loading at high temperature.

Research into the behaviour of cold expanded holes in supersonic aircraft involves the study of creep at temperatures expected in wing components at supersonic speeds. However, such temperatures are achieved under flight conditions and therefore the effect of external loading must be taken into account.

As previously described, axisymmetric models can not be easily used for the application of uniaxial external loads, and therefore 2D models were used as a first approach to reproduce several loading and creep conditions. Finally 3D models were used to check the residual stress distribution as functions of radial, angular and axial positions (r, θ and z respectively). In these models, the technique of mapping residual stresses from axisymmetric models was used, as described in the previous chapter.

In all cases three steps were used after the introduction of residual stresses as an initial condition: first loading, then time–dependant creep and finally unloading.

5.2.1. 2D plane stress with uniaxial tensile external load.

Two–dimensional models were used as an efficient method of evaluating the creep behaviour for different combinations of external loads and exposure times. Kinematic hardening under plane stress conditions was used to be consistent with the earlier simulations at room temperature. The same procedure as described earlier for room temperature loading was used, then using creep redistribution, before unloading.

Results shown in figure 5.5 correspond to a simulation where the cold expanded plate was loaded in tension with a uniaxial stress of 143.33 MPa ($\sigma_y'/3$). The material properties were not changed as a function of temperature before and after running the creep analysis. As mentioned throughout the chapter this had a small influence in the final residual stress distributions.

The tangential stresses as a function of the normalised radius (*r/a*) with the load applied at 150°C before and after creep, are shown for an angular position $\theta=0°$ in figure 5.5a and for $\theta=90°$ in figure 5.5b. Finally, once the creep analysis was simulated for 1000 hours the samples were unloaded. A new residual stress distribution was found and is also shown in figure 5.5 for $\theta=0°$ and $\theta=90°$. Large stress relaxation was observed in the loading direction ($\theta=0°$ in figure 5.5a). The relaxation in the normal direction ($\theta=90°$ in figure 5.5b) was much smaller.

The variation of these residual stresses after 1000 hours of creep are shown in figure 5.6 as a function of angle for different radial positions. New shear residual stresses were generated as a result of relaxation. These shear stresses did not arise in the initial simulation of a cold expansion. As most of the stress relaxation occurred near the hole edge the variation with angle of residual stresses was observed only for $r/a<2.00$, with a maximum angular variation at the hole edge. In figure 5.6c the final tangential residual stresses are shown. At the hole edge the compressive stress varied from –115 MPa in the loading direction to –315 MPa at 90 degrees to the loading direction.

The relaxation at the position normal to the loading ($\theta = 90$) was less than the results obtained for creep relaxation without external load. The results of the latter case are shown in figure 5.2 where residual stress at the hole edge decreased to a less compressive tangential stress of –285 MPa, compared to –315 MPa for the case of relaxation with external loading. However, this difference is small and can not be generalised, as there are many factors such as the magnitude of the external loading and the relaxation time. The situation that gave the most extensive relaxation was a compressive load at high temperature with results similar to those given in figure 4.11 for room temperature conditions. The relaxation for compressive loading at high temperature was more important because in addition to plastic strains introduced during compressive loading at θ=90°, high values of creep relaxation were obtained. However, these conditions are not likely to occur during flying conditions for long times.

5.2.2. 3D simulations with uniaxial tensile external load.

Three–dimensional simulations were carried out by importing residual stresses from axisymmetric models and taking into account the through–thickness distribution of residual stresses and Bauschinger effects. The introduction of residual stresses was carried out using interpolation in the radial *r* and axial *z* direction to take into account different mesh densities, and change from axisymmetric circular free boundaries to plate rectangular edges. Equilibrium was checked after the introduction of residual stresses using a kinematic hardening material model. External loads were applied as a uniformly distributed pressure at the plate edge and the stresses were redistributed due to creep. Finally the external load was removed and new residual stresses were generated.

The tangential residual stresses before and after creep are shown in figure 5.7 for an external applied tensile stress of 143.3 MPa ($\sigma_Y'/3$) at 150°C for 1000 hours. The initial residual stresses were imported from axisymmetric distributions and therefore were the same for any angular position. After unloading the residual stresses are a function of angle. Two angular positions are shown: θ=0° in the loading direction and

θ=90° normal to the loading direction. Three positions through–thickness are shown in figure 5.7: (a) is the entrance face, (b) the average through–thickness and (c) the exit face.

The largest relaxation occurred in the loading direction where the loading imposed highly compressive tangential stresses. However, this effect is not shown near the entrance face where the tangential residual stresses arising from cold expansion were less compressive. Normal to the loading direction a small relaxation occurred for the averaged through–thickness stresses. Near the entrance face the tangential stresses even became slightly more compressive.

Comparing the relaxation of stresses averaged through–thickness from the 3D model with those obtained from the 2D models shows that similar results were obtained. The effect of the through–thickness distribution of residual stresses with unloaded samples in both the 2D and 3D cases were similar. The largest relaxation was produced near the hole and far from the entrance face.

5.3.Conclusions.

(i) Creep was studied as a time dependent phenomenon using power–law and time hardening rules for a constant temperature of 150°C.

(ii) The relaxation of residual stresses did not occur under constant strain conditions and therefore the combination of strain accumulation and stress relaxation tests was necessary to fit the creep parameters. The relaxation tests included some studies from Martínez (1998) about the influence of plastic strains in creep relaxation.

(iii) Two–dimensional models are a valid method to predict averaged through–thickness residual stress relaxation of cold expanded holes as they are comparable to the averaged through–thickness results from three–dimensional simulations.

(iv) Larger relaxation of residual stresses was found for the positions normal to the applied load in cold expanded holes without external load compared to loaded samples in tension.

(v) The worst case of residual stress distribution would occur for compressive loading and creep, but this is unlikely to happen in service.

(vi) Complicated three–dimensional residual stress distributions were generated after creep and external loading as functions of radius, angle and axial positions (r, θ and z respectively).

Chapter 6
Finite Element studies of cracks

Elastic–plastic FEA were carried out to simulate the presence of cracks in fastener holes. Different crack lengths and external loads were examined in models with several distributions of residual stress. These distributions included those for non–cold expanded holes, and cold expanded holes after different combinations of external load and creep. Two–dimensional models were combined with three–dimensional models of through–thickness and corner cracks. Stress intensity factors were calculated and from them fatigue crack growth behaviour was predicted. The benefit of cold expansion was demonstrated as a fatigue improvement method for Al 2650.

6.1. Effect of cracks on cold expanded holes with external load at room temperature.

FEA has been used to model the interaction between residual stresses and stress intensity factors. A review of FE techniques in fracture mechanics can be obtained from Gallagher (1978). Ball (1994) used an analytical solution to predict the fatigue life improvement of cold expanded holes as a function of the level of interference in Al 2219–T851 plates. These solutions were extended by Ball and Lowry (1997) using FEA to predict the fatigue crack growth in Al 2124–T851 as a function of the level of interference applied during the cold expansion process. Armen et al. (1984) also used FEA to predict fatigue crack growth in cold expanded holes after the application of compressive loading.

The combination of FE predictions and other methods, such as the BEM (Becker et al., 1993 and Bourke et al., 1991) and the widely used weight function analysis (Grandt, 1975 and Grandt and Kullgren, 1983) is recommended (Poussard, 1995). Such methods allow the interpretation of experimental results obtained from fatigue crack growth tests (Cook et al., 1994).

Pavier et al. (1998, 1999) using FE and weight function analysis for cold expanded holes with through–thickness cracks, obtained similar results for both techniques. In this current research, FE predictions are included for more cases of crack geometry and residual stresses than in previous work. All the cracks are studied at a position normal to the load applied (θ = 90 degrees), emanating from the hole edge ($r = a$) and considering several crack lengths (c). To avoid confusion the same cylindrical co–ordinate system as in previous chapters is used, with radius r measured from the hole centre and angle θ.

The FE mesh and contour paths were similar to those presented by Poussard (1995), with nodes concentrated near the hole edge and a refined mesh around the crack tip. For symmetry conditions only one quarter of a plate and hole was simulated with loads applied as uniform pressures at the plate edge. This means that the study is assuming the existence of double cracks on both sides of identical length.

6.1.1. 2D plane stress non–cold expanded holes with uniaxial load.

First, studies were made using two–dimensional models of cracks emanating in the radial direction from fastener holes of radius a=3 mm. Crack lengths ranged from c=0. 25 mm to c=4 mm. Load was applied as a constant pressure acting on the edge of the plate in the direction perpendicular to the crack. Only one quarter of the plate containing the hole was modelled by applying symmetry conditions. This meant that the model represented double cracks of equal length located at both sides of the hole. In order to account for the effect of crack closure, non–linear spring elements were located along the crack length. These springs provided high compressive reaction forces for small negative displacements (stiffness $F_z/U_z=10^{11}$ N/m), but insignificant tensile reaction forces for positive displacements (stiffness $F_z/U_z=10^{-1}$ N/m). This means that the crack faces can not cross each other. The results using non–linear spring elements were compared to results using contact elements to provide crack closure as used by Poussard (1995). The results for residual stresses were very similar, but the use of contact elements introduced difficulties for evaluation of the *J*–integral and therefore spring elements were chosen to complete the analyses.

Stress intensity factors were calculated directly from the values obtained for the *J*–integral based on the work by Rice (1968). *J* was calculated along different paths around the crack tip as explained by Poussard (1995). This analysis is completely implemented by ABAQUS (1999). These paths surrounded the crack tip with the first paths formed by the closest nodes to the crack tip position. The distance r_c is given to evaluate the distance from the crack tip to the path in the radial r direction.

The stress distribution ahead of the crack in the direction normal to the loading (θ = 90) of non–cold expanded holes for a crack length c=2 mm is shown in figure 6.1a. These stresses are normalised with respect to the yield stress, Young's modulus and the *J*–integral in figure 6.1b to show results independent of the applied external load. As the crack was placed normal to the applied load, the stress distribution at θ=90° in the direction of the loading is equivalent to tangential stress $\sigma_{\theta\theta}$. The slopes of the elastic and plastic regions are in agreement with HRR solutions (Hutchinson, 1968 and Rice and Rosengren, 1968) for a hardening material using a Ramberg–Osgood model to simulate the hardening behaviour. Two slopes are shown in this log–log plot for the elastic and plastic region. The elastic slope is $-1/2$ while the plastic slope is $-1/(n_p+1)$ where n_p is the hardening coefficient of the Ramberg–Osgood law (equation 2.17). However, the simulation did not use a Ramberg–Osgood power–law but a linear kinematic hardening model.

Poussard (1995) also used a linear kinematic hardening model for his FE analyses and obtained slopes which were not constant in the plastic region. He used different Ramberg–Osgood models, with decreasing hardening coefficients n_p for increasing plastic strains, to compare with the linear kinematic hardening, to provide a justification for the slopes.

The crack face opening shown in figure 6.2a and *J*–integral shown in figure 6.2b are evaluated for increasing loads applied to non–cold expanded holes with a crack length $c = 2$ mm. Several researchers such as Carpinteri et al. (1999a and 1999b), Lin and Smith (1997 and 1998) found a relation between the crack tip opening displacement and the *J*–integral. This is explained in detail later in this chapter. The crack was always open for a far field tensile stress with the largest opening near the hole edge. As expected the *J*–integral was path independent, i.e. the value of *J* did not depend on the contour chosen around the crack tip. In figure 6.2b *J* is plotted as a function of the radial distance, from the crack tip in the direction normal to the loading, which defines the midpoint of the path of the contour.

6.1.2. 2D plane stress cold expanded holes with uniaxial tensile load.

The study was repeated for cold expanded holes using the same mesh and integral paths as for non–cold expanded holes. First, cold expansion was simulated by means of a 4% uniform radial expansion and subsequent release to generate residual stresses. The crack was introduced in the model in the plane normal to the load to be applied ($\theta = 90$ degrees). Nodes were released along the crack length and crack closure was obtained from the spring elements. Finally, the external loads were applied as a uniformly distributed pressure at the plate edge. Values of local crack tip tangential stresses, crack opening and *J*–integral were examined.

In figure 6.3 the tangential stresses at $\theta = 90°$ for a crack length c=2 mm are plotted for different external loads, in 6.3a as a function of distance from crack tip and in 6.3b as function of radius from the centre of the hole. The presence of residual stresses makes it difficult to relate the slopes shown in figure 6.3a with HRR solutions. Nevertheless, Pavier et al. (1998, 1999), showed that curve fitting to HRR solutions was possible from the results obtained by Poussard (1995) for Al 2024 (E = 71 GPa and σ_Y' = 380 MPa). A stress singularity is found in figure 6.3b for loads over 50 MPa, the load that induced tensile tangential stresses near the crack tip. The original residual stress distribution is shown in figure 6.3a when the external load is 0 MPa.

Crack opening displacements are shown in figure 6.4a as a function of distance from the crack tip. The crack opened from the crack tip for a remote stress over 50 MPa. This is in accordance with the appearance of a stress singularity around the crack tip. For external loads over $\sigma_Y'/3$ the crack eventually opened at the hole edge. In all external load cases smaller opening displacements were obtained when compared to non–cold expanded holes.

The J–integral was evaluated for different contours around the crack tip. The results are shown in figure 6.4b for each of the loads applied to the same crack length of c=2 mm. The values obtained were found to be path dependent for all loading cases in the presence of residual stresses from cold expansion, consequently J must be evaluated by taking the limiting value near the crack tip (Anderson, 1995). FE can not determine the value of J at the crack tip position where a singularity is defined and therefore personal judgement is required to determine the J–integral following this method as FE values at the crack tip are not reliable. Only for the application of high loads, was it clear that there is a transition between a path independent J (near to the crack tip) and a path dependent J. A limiting value was determined from the path independent region (Poussard, 1995). It was also possible to determine a zero *J*–integral for loads below 50 MPa which did not generate stress singularity. Alternative methods of determining *J* are also evaluated later.

Finally in this section, the stress to force crack opening is predicted and shown for any crack length emanating from a cold expanded hole. The prediction of the applied stress is based on the elastic superposition of residual stresses and the effect of external loads around holes (Timoshenko and Goodier, 1987). The prediction calculates the position where the tangential stress becomes tensile which is an approximation to the position where crack opening takes place. To do so the tangential residual stress must be equal to the tangential stress from remote loading at the position of opening. The applied stress to achieve this effect for any radius is given by the following the relation:

$$\sigma_{app}(r) = \frac{-2\sigma_{\theta\theta}^{RS}(r)}{\left[2 + \left(\frac{a}{r}\right)^2 + 3\left(\frac{a}{r}\right)^4\right]} \tag{6.1}$$

The residual stress $\sigma_{\theta\theta}^{RS}(r)$ is obtained from the earlier plane stress kinematic hardening models of cold expansion shown in figure 6.5a. The applied stress necessary to cause crack opening calculated from equation 6.1 is also shown in figure 6.5a. The prediction establishes the region of tensile stress where it is assumed that the crack is open for any crack length. In figure 6.5a two examples, case 1 and case 2, are shown for a crack length of *c*=2 mm. For a remote stress of 100 MPa (case 1) the crack is predicted to open at the crack tip and to be closed near the hole edge. For a larger remote stress (case 2) the crack is predicted to open at both the hole edge and the crack tip but remain closed in between. For remote stresses over 220 MPa the crack is predicted to be fully open. These results are in agreement with opening displacements obtained from FE analysis and shown in figure 6.4a. However there is increasing error for the elastic analyses for increasing remote stress. This was due to plasticity introduced around the crack tip which is not taken into account using equation 6.1. Figure 6.5a shows curves of the crack opening ratio generated for different crack lengths, as a ratio of the crack length which is open c_0 to the total crack length c. An example for c=2 mm is shown in figure 6.5b showing the crack opening ratio from the crack tip, the hole edge and the total.

For cracks longer than c=2.5 mm, a tensile residual stress was predicted by FEA near the crack tip. This method calculates that a compressive far field stress is necessary to provide crack closure.

6.2.Effect of cracks on 4% cold expansion residual stress distribution due to creep.

The study of the effect of creep relaxation of residual stresses on components containing cracks was divided into two main sections: creep without an externally applied load, and creep with an externally applied load. Both cases were studied using two–dimensional models as the introduction of cracks into axisymmetric models is unrealistic. The 2D models used plane stress conditions together with a kinematic hardening plasticity model, power–law creep and time hardening at 150°C. In the cold expanded cases the residual stresses were introduced into uncracked specimens and then the crack was introduced into the model by node release.

The same material parameters used in the creep relaxation studies presented in chapter 5 were used in this work. The material parameters are given in table 3.4.

6.2.1. 2D plane stress cold expanded holes without external load.

Two–dimensional simulations of creep relaxation were carried out for crack lengths ranging from 0.25 to 4 mm using plane stress conditions. In all cases the mesh was refined around the crack tip and the cylindrical co–ordinate system from the centre of the hole was used. For short crack lengths, which placed the crack tip within the compressive tangential residual stresses (c<2 mm), the same relaxation as in uncracked samples was observed. This was because the crack remained closed during the simulation and no local stress singularity was obtained near the crack tip. Therefore, special attention was paid to simulations with long cracks, with the crack tip within the tensile residual stresses (c > 2 mm). For these cases, stress singularities were attained and the residual stress relaxations were different than in the case of uncracked samples. The tangential stresses from a simulation of a cold expanded hole containing a long crack of length c = 3 mm are shown in figure 6.6a for different positions ahead of the crack tip and in figure 6.6b as a function of radius, in both cases for θ=90° to the direction of the crack. The characteristic elastic slope (–1/2) was related to the kind of strain after creep in two areas: in the elastic region far from the crack tip it was still –1/2, but it became more related to creep ($-1/(n_c+1)$) near the crack tip. This was through a very localised effect with a very small influence on the stress relaxation occurring near the hole edge which was similar to uncracked samples.

Initially, when the nodes along the crack face were released, the crack slightly opened near the crack tip. The maximum crack opening displacement was of about 0.43 μm. Due to creep, the crack opening and J–integral decreased with time as shown in figure 6.7a and b respectively. Once more, two different regions are shown for the evaluation of J path independent near the crack tip and path dependent away from the crack tip.

6.3. Redistribution of stress singularity due to creep and external load.

The relaxation of stress singularities was studied for both cold and non–cold expanded models with the application of external uniaxial loads. Residual stresses, once the models were unloaded, were also predicted. Two–dimensional models were used as in previous sections and results for plane stress and kinematic hardening followed by power–law creep are described next.

6.3.1. 2D plane stress non–cold expanded holes with external load and creep.

Previous studies in section 6.1 showed that non–cold expanded holes containing cracks normal to the remote stress (θ = 90°) revealed high stress singularities when compared to cold expanded holes. Therefore high stress relaxation was expected near the crack tip when the material was allowed to creep.

For the case of a non–cold expanded hole with crack length c=2 mm, the tangential stresses directly ahead of the crack tip are shown in figure 6.8a and in figure 6.8b as a function of radius from the centre of the hole, for θ=90°, direction normal to the loading. The stress applied was one third of the yield stress at room temperature (σ_{app}=143.3 MPa) for 1000 hours of creep at 150°C. The slope of the stress versus distance from the crack tip in the initial plastic area increased during the stress relaxation to become a characteristic creep related slope. The stress singularity decreased as a consequence of stress relaxation and the accumulation of plastic strains near the crack tip. After the load was released, compressive tangential residual stresses were generated ahead of the crack tip.

In figure 6.9a results for crack opening displacement are shown. There was an increase in opening during creep strain accumulation. Indeed, the crack did not close once the external load was removed due to accumulated creep strains around the crack tip. The variation of the *J*–integral with increasing path length and time is shown in figure 6.9b. Initially *J* is path independent but with increasing time became path dependent. The interpretation of *J* becomes more difficult as shown in figure 6.9b where an initial path independent integral became path dependent due to the accumulation of creep strains around the crack tip.

6.3.2. 2D plane stress cold expanded holes with external load and creep.

FE simulations were carried out for combinations of crack lengths, loads and creep exposure times for cold expanded holes using identical meshes to non–cold expanded holes. The FE mesh was kept as for non–cold expanded holes to avoid problems in interpreting results from *J* integration, even though in some cases this was time consuming.

The tangential stresses shown in figure 6.10 correspond to a model with a crack length c=2 mm, with the application of an external load equivalent to one third of the yield stress at room temperature (σ_{app}=143.3 MPa). The remote stress was applied for 1000 hours of creep at 150°C. The load was removed and the tangential residual stresses in the direction of the crack (normal to the load) are also shown. In figure 6.10a the change of slope from elastic–plastic behaviour to elastic–creep behaviour observed in the results shown in figure 6.6 is not observed here. This is due to a smaller creep strain accumulation during the process in comparison to non–cold expanded samples. Stress relaxation is shown in figure 6.10b as a function of distance from the hole centre. Once the remote stress is removed compressive residual stresses ahead of the crack tip are obtained. Stress relaxation elsewhere was similar to uncracked samples, showing once more that a combination of creep and external load produced lower relaxation close to the hole edge than creep without external load.

Crack opening displacement was found to increase with time as for non–cold expanded holes but not in the case of long cracked cold expanded holes without external load. The crack opening displacement of a crack of 2 mm (c = 2 mm) is shown in figure 6.11a for small scale crack displacements. The crack remained slightly open close to the crack tip once the external load was removed as a consequence of the accumulation of plastic and creep strains. Once more, it was difficult to interpret a path independent *J*–integral. The plateau close to the crack tip gave an increase of J with time of creep exposure. Once the load was removed J decreased but it was difficult to determine the value near the crack tip.

6.4. 3D stress intensity factors.

In this section, models of through–thickness and corner cracks are described and compared with the 2D results presented earlier. Simulations were carried out using three–dimensional models for different crack lengths to evaluate the influence of five different residual stress distributions. The residual stresses arising from cold expansion were simulated using axisymmetric models and then mapped into the 3D mesh. Cracks were introduced in the model after the input of residual stresses and then six different uniaxial external loads (stresses) were applied. The aim was to evaluate stress intensity factors for cold expanded holes in different states when compared to non–cold expanded holes. The five simulations of residual stress distributions are:

(a) Non–cold expanded, cracked and finally loaded in tension, (ncw).

(b) Cold expanded hole, subjected to compression using a far field stress of one third of the yield stress, released from the external compression, cracked, and finally loaded in tension, (cwcp).

(c) Cold expanded hole, crept for 1000 h. at 150°C, cracked, and finally loaded in tension, (cwht).

(d) Cold expanded hole, loaded in tension using a far field stress of one third of the yield stress (σ_{app}=143.3 MPa), crept for 1000 h. at 150°C, released from the external tension, cracked, and finally loaded in tension, (cwcr).

(e) Cold expanded hole, cracked, and finally loaded in tension, (cw).

For completeness, the results are presented for uncracked specimens and five different crack lengths: c = 0.25, 1, 2, 3 and 4 mm respectively.

As described in chapter 4 the residual stresses from a 4% cold expansion were generated using a unique axisymmetric model with a rigid mandrel pulled through. The elastic–plastic material behaviour was modelled using the combined hardening model (shown in table 4.1) to take into account the Bauschinger effect. This model behaviour does not allow creep and therefore creep calculations were done once residual stresses are mapped into the 3D models.

The 3D models represented a quarter plate using 8000 eight–noded quadratic elements with eight integration points per element as suggested by Pickard (1986). The mesh was refined near the crack tip line for both through–thickness and corner cracks. The cracks were always placed normal to the loading direction (θ = 90). For corner cracks, the crack length was defined in the radial direction from the hole edge (c_r) and in the axial direction from the entrance face (c_z) and the simulations shown here are for circular cracks with equal lengths.

Residual stresses were introduced in the model using the subroutine SIGINI available in ABAQUS. An interpolation for the stresses allowed refinement of the FE meshes around the crack tip. With this subroutine, only stresses are transferred while other variables such as plastic strains and back–stresses are reset to zero. Therefore the Al 2650 aluminium alloy behaviour, once the residual stresses were mapped into the 3D model, was modelled as an elastic perfect plastic material model with a yield stress of 430 MPa, with viscoelastic creep power–law assuming time hardening for time dependent stress relaxation.

Crack closure was provided by spring elements of high stiffness (F_z/U_z=10^{11} N/m) in compression and close to zero stiffness (F_z/U_z=10^{-1} N/m) in tension. A total number of 165 spring elements were added along and across the crack face for both corner and through–thickness cracks.

The same procedure was repeated for 2D models using the same radial and angular FE mesh density as in 3D models with the mesh refined around the crack tip. 2D models were examined for both plane stress and plane strain conditions. The residual stresses were mapped into these 2D models from through–thickness averages of those obtained with a mandrel pulled through the hole, and the mechanism of crack closure provided by the same spring elements as in the 3D models. This was done to compare results of evaluation of J, crack opening and stress distribution ahead of the crack tip.

Table 6.0 shows the CPU times in seconds required for the simulations carried out. A total of 23 models were modelled (six 2D plane stress, six 2D plane strain, one 3D without crack, six 3D with through–thickness cracks and six 3D with corner cracks) shown in rows in table 6.0. For each model, five different residual stress distributions were considered as explained earlier. The name of each file is coded to be able to identify the model. So "2dzclsc–ncw" stands for 2D model with zero crack length (c = 0 mm) plane stress and non–cold expanded while "3dlccsc–cwcr" stands for 3D model with long corner crack length (c_r = c_z = 3 mm). A large reduction of computing time was obtained when compared to the analysis of Pavier et al. (1998, 1999).

The *J*–integral was first calculated for different volumes around the element at the crack tip, for three different positions through–thickness: entrance, mid–thickness and exit face. Results were found not to be in agreement with the 2D models due to the proximity of stress free surfaces. The *J*–integral was also calculated on planes containing the normal to the crack front. These results were also difficult to interpret. Therefore a number of alternative methods were explored.

Poussard (1995) used a curve fitting method to the HRR stress field assuming a hardening exponent. This approach was also attempted but the result was very poor as the curve fitting was not easy to define for the correct hardening slope.

Alternatively, a crack opening evaluation was developed as proposed by Lin and Smith (1997 and 1998). The crack opening of the node close to the crack tip was compared to a corresponding path independent *J*–integral. The stress intensity factor K was found from:

$$K = \frac{E}{2(1+\nu)}\sqrt{\frac{2\pi}{r_c}\frac{U_{\theta\theta}}{2(1+\nu)}} \tag{6.2}$$

where r_c is the distance behind the crack tip where the crack opening displacement $U_{\theta\theta}$ is measured. It should be noted that the above equation is only valid for positions close to the crack tip ($r_c \rightarrow 0$). The equation is for plane strain conditions but can be corrected for plane stress cases.

Results for 2D simulations of through–thickness cracks of different lengths of J obtained from ABAQUS are shown in figure 6.12a for a cold expanded hole and are compared to the crack opening displacement criteria used from Lin and Smith (1997 and 1998). The agreement between both methods is shown in figure 6.12a. HRR stresses were also fitted to stresses close to the crack tip as an alternative technique to obtain stress intensity factors. In figure 6.12b it is shown how difficult is to fit an elastic $-1/2$ slope to the HRR and therefore it was not used to produce results. The complete set of results comparing the *J*–integral and the crack tip opening displacement $U_{\theta\theta}$ for all the cracks are shown in tables 6.1 to 6.5 for the five cases of residual stresses analysed. Good agreement was found between the 2D ABAQUS *J*–integral and the 2D crack tip opening.

In figure 6.13 the residual stress distributions are shown for the five different simulations before the introduction of a crack in the model and subsequent loading. It is shown that samples (b) and (d) contain non–axisymmetric residual stresses as loading was involved in the final residual stress distribution. Sample (c) corresponding to a 4% cold expansion showed the maximum compressive stresses in the *y*, or $\theta=90°$, direction. Small compressive stresses were found near the hole edge all the way through–thickness for sample (b) which was cold expanded and compressed in that direction.

In figure 6.14 the tangential stresses are shown for uncracked specimens while subjected to an external load of 143.33 MPa = $\sigma_y'/3$. In the initial state before loading lower compressive stresses at the entrance face for cold expanded holes were obtained as shown in Chapter 5. The beneficial effect of cold expansion is shown for all cases except for case (b). Here a cold expanded hole was subjected to a compressive load and then reloaded in tension with 143.33 MPa as mentioned above to find high tensile stresses near the hole edge all the way through–thickness. This was a consequence of the low compressive residual stresses obtained after the removal of the initial compressive load. Cases (c), (d) and (e) showed that there were tensile stresses near the hole but only close to the entrance face. Therefore, corner cracks were introduced at this location.

Figure 6.15 shows tangential stresses in specimens containing a 2 mm long, through–thickness double crack, with the crack normal to the applied loading. The applied load was one third of the yield stress at room temperature. For a non–cold expanded hole containing a crack and loaded, the stresses are very high at the crack front. For the other four cases a significant benefit was obtained as lower stresses were found near the crack tip. These stresses are very similar for all the cases except for the non–cold expanded hole as the residual stresses were also quite similar in the region of the crack tip before loading. A difference can be observed though along the crack face where sample (e), which is a cold expanded hole, showed high compressive stresses and therefore crack closure.

The crack opening displacement for the same crack length and applied load is shown in figure 6.16 where crack closure is still found in some areas between the hole edge and crack tip far from the entrance face for cold expanded samples. This can be related to the tangential compressive stresses shown in figure 6.14. Smaller values of crack opening were found in all cases when compared to loaded non–cold expanded holes shown in figure 6.16a.

Corner cracks were also studied arising from the hole edge near the entrance face. The geometry of the crack was quarter circular, with the same crack length in the radial and axial directions. An example is shown in figure 6.17 for a crack length of $c_r = c_z = 2$ mm and external load of 143.33 MPa = $\sigma_y'/3$. In this case two stress concentration effects were acting together: the stress concentration around a hole and the stress singularity near the crack tip. This is shown for the loaded non–cold expanded sample where higher tensile tangential stresses were shown near the hole edge. The least benefit from cold expansion was obtained for case (b) which showed small compressive residual stresses near the hole edge. When the load was applied to this sample high tensile stresses where obtained near the hole edge and close to the crack tip.

The crack opening displacement for this corner crack is shown in figure 6.18. The maximum opening was found for a loaded non–cold expanded hole. In all cases (a) to (e) no crack closure was observed as the crack was placed at the entrance face where small compressive residual stresses were found for all cases.

The crack opening displacement method described earlier was used to evaluate stress intensity factors for three–dimensional simulations. The analysis was conducted for a range of crack lengths, applied loads and initial residual stress distributions. Figures 6.19 and 6.20 show stress intensity factors as a function of applied load for crack lengths c=0.25 and 4 mm respectively. The results are shown for 3D through–thickness and corner cracks and 2D cracks for both plane stress and plane strain. Several positions were shown for 3D cracks to examine the through–thickness effect.

For very short cracks, as shown in figure 6.19, the least benefit was obtained for cold expanded and compressed holes (cwcp, case b). The maximum benefit was obtained for cold expanded holes (cw, case e). Similar benefit from cold expansion was observed for all of the corner cracks.

For long cracks of crack length c = 4 mm, as shown in figure 6.20, the benefit was smaller as the crack tip was within the initial tensile tangential residual stress zone. For corner cracks the difference was significant near the hole edge. This would imply a faster crack growth from this position as a consequence of the stress concentration around the hole edge.

Figure 6.21 shows stress intensity factors as a function of crack length for an applied load of $\sigma_y'/3$. This is the most useful graph for fatigue crack growth predictions. The benefit associated with case b (cwcp) improved for increasing crack length as the compressive residual stresses were only small close to the hole edge. With increasing crack length the benefit from cold expansion of all cases when compared to the non–cold expanded hole became similar. Once more, corner cracks showed a different behaviour close to the hole edge.

6.5 Prediction of fatigue crack growth

Fatigue crack growth was predicted following the studies by Becker et al. (1993) using the Paris law described in chapter 3 for Al 2650 aluminium alloy. The number of cycles N for a crack to grow from c_i to c is given by:

$$N = \int_{c_i}^{c} \frac{\partial c'}{C_f \Delta K^{m_f}} \tag{6.3}$$

where C_f and m_f are fatigue constants of the material and ΔK is the stress intensity range. As in Becker et al. (1993), ΔK was considered to be the maximum stress intensity factor in the cycle. This implies that the crack face must close during the minimum stress in the cycle. Therefore the predictions presented here consider low fatigue ratios which would allow crack closure and in the extreme $R = 0$.

Integration of equation 6.3 was done using a trapezoidal rule for unequal increments of crack length (Δc). The calculation used the stress intensity factors shown in figure 6.21 obtained from FE crack tip opening displacements. The calculation did not take into account the redistribution of residual stresses during crack growth nor the change in shape of the crack. The calculation was made for a fictitious fatigue ratio R as a complete set of $K_{\max}$ and $K_{\min}$ would be required to take into account the stress redistribution when the crack tip is loaded and unloaded. This stress redistribution would imply a change in the maximum and minimum stress intensity factor. In the limit the calculations are for $R = 0$ where the minimum applied stress is set to zero and therefore the stress intensity range calculated as the maximum stress intensity factor.

Lacarac (2000) examined the influence of fatigue ratio R on the benefit of cold expansion. It was found that tests performed at high ratios did not improve the fatigue behaviour of fastener holes. This was due to the fact that the crack did not show any crack closure effect, and therefore the stress intensity factor range was similar for cold expanded and non–cold expanded samples.

In figure 6.22, predicted crack lengths are shown as a function of the number of cycles for the five cases of residual stresses when a maximum external load of one third of the yield stress was applied and K_{min} was assumed to be zero. The initial crack length was c_i=0.25 mm. In the 2D models, crack arrest was found for cold expanded holes with a crack length of about 0.5 mm in plane stress. Through–thickness cracks showed crack arrest for all samples except the non–cold expanded hole at the mid–thickness position. This implies that the crack shape would change during crack growth leading to a faster crack growth near the entrance and exit faces as seen in fractographic samples (Pell et al., 1989). No crack arrest was observed for corner cracks for this load, but once again different rates of growth for different positions suggested a change of the shape of the crack as shown by Stack and Stephens (1989).

In figure 6.23 the number of cycles to reach a critical crack size is plotted against the applied stress for the same initial crack length of c_i=0.25 mm. From 2D simulations it is possible to check the benefit in lifetime of cold expanded holes and also the minimum load needed to create crack propagation. In plane stress, the predictions calculated a minimum stress of about 170 MPa for cold expanded holes (sample e) and between 143.33 MPa and 107.5 MPa for cases b, c and d. On the other hand, non–cold expanded holes did not show crack arrest for any applied tensile stress.

Examination of through–thickness cracks showed shorter lives after examination of stress intensity factors near the entrance face when compared to mid–thickness and exit face predictions. This does not mean that a crack has different lives in different positions. The detailed examination of these curves predicts a faster crack growth near the entrance face for all cases which have been cold expanded. This is in agreement with experimental crack shapes shown by Ball and Lowry (1998). Once the crack shape change is produced, the life estimation could be done examining the mid–thickness stress intensity factors. From them a longer life is predicted for cold expanded holes (e) with crack arrest for applied stress below 165 MPa and once more a shorter life for non–cold expanded holes. The least improvement from cold expansion is obtained for case c which was cold expanded and crept without external loading. However this is close to cases b and d where crack arrest is predicted for applied stresses below 130 MPa.

Corner cracks were also investigated and fatigue lives once more predicted. As for through–thickness cracks, shorter lives were predicted near the entrance face which would mean a change in shape of the crack. For this crack shape, all cases of residual stresses predicted a similar fatigue crack growth as they started from a point with a very low compressive tangential stress near the hole edge and close to the entrance face. A difference is shown in the prediction of case b which showed crack arrest only for applied stresses below 55 MPa.

All these techniques should be criticised as the simulation makes too many assumptions. Existing techniques for the evaluation of crack growth (Dusi et al., 1993) should be used for each case of residual stress, initial crack geometry, and maximum and minimum applied stress.

6.6. Conclusions.

(i) Stress intensity factors using crack opening displacements were evaluated from FE simulations of cracked samples with different combinations of applied stresses ,crack shapes and crack lengths.

(ii) Crack tip stresses where studied during creep at 150°C for both cold expanded and non–cold expanded samples. The stress singularity ahead of the crack tip changed from plastic dominated to creep dominated.

(iii) Cold expanded holes with small cracks showed an identical relaxation to uncracked samples when the crack faces where within compressive tangential stress fields. This was because the crack was completely closed.

(iv) A technique to map stresses from an axisymmetric model into a 3D mesh was used to carry out three–dimensional simulations of through–thickness and corner cracks.

(v) Fatigue crack growth predictions were developed under conditions of constant crack shape and no redistribution of residual stresses during fatigue crack growth. A benefit in fatigue life of cold expanded holes was observed.

PART B

NEW EXPERIMENTAL METHOD BASED ON SACHS BORING TO MEASURE RESIDUAL STRESSES AROUND HOLES.

Chapter 7
REVIEW OF EXPERIMENTAL METHODS TO MEASURE RESIDUAL STRESSES

A substantial number of experimental techniques are available to measure residual stress distribution around cold expanded holes and autofrettaged tubes. A review of the commonly used techniques is given with a description of typical applications. The techniques are categorised into two groups as destructive techniques based on material removal and strain measurement such as Sachs boring, and non–destructive techniques such as X–ray diffraction. Particular attention is given here to the Sachs boring and X–ray diffraction methods, and a brief description of other methods is also given. More details about measurement techniques for cold expanded holes can be found in McNeill and Heston (1987) and more recently in Priest (1997) and Lacarac, (2000).

7.1. Sachs boring technique.

The Sachs boring method is a cutting and strain gauge based technique widely used for measuring the residual stress field around a cold expanded hole. This method was described by Sachs (1927) to measure axisymmetric residual stresses in autofrettaged tubes and it has been continuously revised since. For example, Lambert (1954) derived Sachs equations to take into account antisymmetric stresses in autofrettaged tubes arising from plastic bending. Weiss (1957) developed graphical computation methods to solve the equations and Voyiadjs et al. (1985) derived equations for materials exhibiting cylindrical elastic anisotropy. More recently, Nishimura (1978) presented new axisymmetric equations to calculate triaxial residual stresses in bars and tubes. In all methods there is an uncertainty about the real residual stress, and therefore it was difficult to determine the accuracy of the method and equations developed. Simulations of the boring process, using FE for example, would provide a good comparison between residual stresses and calculations from the strains as both residual stresses and boring strains are well known. A benchmark for autofrettaged tubes was presented by Sharman et al. (1997) to measure accurately the residual stress distribution using a curve fitting procedure for the strains.

Sachs boring is a destructive method based on the elastic relaxation of residual stresses in hollow cylindrical components such as discs or tubes. This relaxation is produced when cylindrical layers of material at any radius $r=d$ are removed. This removal is produced from $r=a$, where a is either inner radius or outer radius. A comparison between measurements in both directions is presented by Coppola et al. (1996) for cold drawn tubes. Measurement of the strain change at the circular face opposite the boring, $r=b$, allows calculation of the radial stress relieved. Tangential stresses are obtained from equilibrium equations. The boring out process is shown schematically in figure 7.1, where boring starts from the hole edge and strain gauges are attached at the disc edge.

For the cold expanded samples presented earlier in the thesis, the plate containing the cold expanded hole needs to be machined into a circular specimen central on the hole, also known as a washer or disc, of hole radius $r=a$, and outer radius $r=b$, before boring. Once started, the material removal should not introduce new plastic strains since these would introduce errors into the Sachs calculations.

Once the disc is machined and the strain gauges are attached, the boring process can start. Different techniques have been developed to remove the cylindrical layers of material, for example spark erosion with a stepped–tapered electrode as described by Hermann and Moffat (1991), and a mechanical cutting technique as described by Stacey et al. (1985). The boring process usually stops when there is no change in the strain readings, which means that the residual stresses have been completely released.

The Sachs boring technique has been used to measure various parameters involved in a cold expanded hole. Some of the parameters studied using the Sachs method in the cold expanded holes include: influence of the degree of cold expansion applied, relaxation of residual stresses by reaming the cold expanded hole, stress distribution at the pip position from an open sleeve and the through–thickness stress distribution. These parameters are described next in more detail.

Degree of cold expansion

Residual stresses in cold expanded specimens are a function of the degree of cold expansion. This is defined as the radial displacement applied to the hole edge in comparison to the initial radius of the hole. In the aircraft industry using the split–sleeve cold expansion method, the usual expansion has been set to 4% for fatigue improvement reasons.

An example of axisymmetric cold expansion was found in the studies carried out by Hermann and Moffatt (1991), Hermann and Reid (1991) and Hermann (1994), where pin roller bearings were used in conjunction with a tapered mandrel. First, the residual stress introduced in a 1.6 mm thick and 9 mm hole diameter 2091–T82 aluminium lithium alloy was examined by Hermann and Moffatt (1991), for cold expansion degrees ranging from 2.5 to 5%. The same analysis was repeated for a 10 mm hole diameter in a 8090–T651 Al–Li alloy by Hermann and Reid (1991) and finally both alloys were compared to a 6082–T651 Al–Li alloy in Hermann (1994). For all alloys, a smaller compressive residual tangential stress was found at the hole edge for a smaller applied cold expansion. The plastically deformed region and the compressive tangential stress area were found to be a function of the displacement applied at the hole edge. The maximum compressive tangential residual stress was located some distance away of the hole edge for the Al–Li 2091–T82 alloy. This suggested that reversed yielding was produced when the plastic limit is achieved during unloading. These results were in agreement with FE axisymmetric and two–dimensional predictions presented by Armen et al. (1984).

Studies of split–sleeve cold expanded holes were developed by Özdemir et al. (1993) and Özdemir and Edwards (1996). The effect of degree of cold expansion was studied in plates 300 mm long, 40 mm wide and 5 mm thick of Al 7050–T76 aluminium alloy with a central hole diameter of 9 mm, for 2%, 4% and 6% expansion of the hole. Washers of outer diameter 40 mm were machined ($r=b=20$ mm) after applying the FTI expansion procedure. The hole was not reamed to a specified final diameter and Sachs boring was carried out from the inside of the hole. The residual stresses were calculated from two strain changes measured by two strain gauges located at 90 degrees from the split sleeve position to measure tangential and axial strain change. The study found the presence of reversed yielding for all levels of cold expansion, and only small changes in the maximum compressive tangential residual stresses for higher degrees of cold expansion. Tangential residual stresses measured by Özdemir and Edwards (1996) are shown in figure 7.2 for 0, 2, 4 and 6% expansion. Compressive residual stresses were found close to the hole edge of non–cold expanded holes (0%). Those stresses arose from the drilling process to manufacture the hole in the plate. Their measurements did not take into account the non–axisymmetric residual stress distribution effect generated by the split–sleeve expansion. This effect is believed to increase in importance with the degree of expansion as it is directly proportional to the opening of the sleeve during the expansion.

Reaming process

The reaming process is used after the cold expansion of the hole in order to remove machining debris and to provide a defined hole diameter. The effect of the reaming process can be measured by application of the Sachs boring method.

Özdemir et al. (1993) and Özdemir and Edwards (1997) examined the influence of reaming 4% split–sleeve cold expanded holes. The hole diameter prior to expansion was 9 mm and it was reamed to a 9.52 mm (3/8") diameter. The material investigated was the aluminium alloy Al 7050–T76. The reaming operation was carried out using both a conventional cutting technique and an EDM method removing an approximately 0.3 mm thick layer of material. The standard reaming process was found to remove the reverse yielding area close to the hole edge by shifting the compressive tangential stresses to become more tensile, but obtaining a more compressive tangential stress at the hole edge. These results are shown in figure 7.3a before reaming and 7.3b after reaming for three different positions through–thickness. The EDM technique modified slightly the residual stress distribution with an increase in the peak stresses attributed to the introduction of new plastic deformations. It was concluded that the standard reaming process introduced plasticity near the hole edge, as in the drilling process, to generate the hole, modifying the residual stress field and decreasing fatigue endurance.

Through–thickness residual stresses

Residual stress predictions using FE showed a variation with axial (thickness) position (e.g. Papanikos and Meguid, 1998). Conventional Sachs boring, with different strain gauge locations through–thickness, has been used in the past to measure such variations.

Özdemir et al. (1993) presented results for the measurement of split–sleeve cold expansion residual stresses for three different positions through–thickness of Al 7050–T76 aluminium alloy plates. The results were also published in Özdemir and Edwards (1996 and 1997). They used 3 different pairs of strain gauges situated at the inlet or mandrel entrance face, mid–thickness and outlet or mandrel exit face positions through the plate thickness. Each pair of gauges were orientated in the tangential and axial directions at the outer radius ($r=b$). Their measurements are presented in figure 7.3a showing the least compressive tangential stresses close to the hole edge at the mandrel exit face. These measurements were in disagreement with FE predictions and X–ray measurements at this position. This is because Özdemir and Edwards (1996 and 1997) used a two–dimensional elastic theory to convert the measured strains to residual stresses which does not allow the calculation of through–thickness distributions.

The ability to measure the through–thickness residual stresses has recently been criticised by Smith et al. (1998) using a FE benchmark of the material removal process on axisymmetric simulations. They concluded that it is only possible to obtain the average residual stress through–thickness using a conventional Sachs formulation. Only limited agreement was obtained between FE predictions and Sachs calculations when trying to predict the surface effect using either the plane stress or generalised plane strain Sachs formulation.

Pip position for split–sleeve cold expansion

After the cold expansion of a hole using the split–sleeve method, a small 'pip' is left at the hole edge coinciding with the position of the split in the sleeve. The least compressive tangential residual stress is thought to be generated at the pip, so installation procedures suggest the alignment of the pip with the loading direction. Several studies looked at this effect but only one study has been found that uses the Sachs boring method.

In addition to the studies presented above, Özdemir et al. (1994) located three strain gauges at three different angular positions in order to measure the angular variation in residual stresses around the hole. Based on average through–thickness residual stresses they found a tensile tangential stress at the pip position and a maximum compressive stress for the position perpendicular to it. Their results are presented in figure 7.4. The results obtained are in disagreement with those obtained by the X–ray method (Cook and Holdway ,1993), where surface tangential residual stresses were the most compressive at the pip position. The reason for this is the inappropriate use of the axisymmetric Sachs formulation to measure angular effects such as the pip.

7.2. X–ray diffraction.

X–ray diffraction analysis is a non–destructive technique for the measurement of near–surface residual stress. This surface residual stress can be quite different to those at the mid–thickness of the specimen. The depth of penetration is limited to less than 100 μm in most metals. The technique is based on the diffraction of X–rays by the parallel planes of the crystal (grain) lattices of the sample. Plastic strains are generally the result of dislocation motion and/or the disruption of the lattice. As a result, the strains measured are elastic strains and the residual stresses are calculated using Hooke's law. A well–defined grain size is required, and if a large grain material is examined very irregular peaks are obtained as described by Dietrich and Potter (1977). They also mentioned that heating the specimens can modify the grain size, but this can lead to an undesired residual stress relaxation. Specimens also need to be polished in order to get a mirror flat surface. Cook and Holdway (1993) ground surfaces mechanically after cold expansion removing any out–of–plane deformation caused by the cold expansion and reaming processes. They also carried out investigations of the effect of X–ray beam size and edge effects related to measurements close to the hole for example.

The literature has many examples of measurements of autofrettaged and cold expanded residual stresses using this technique. Su et al. (1986) used X–ray measurements on axisymmetrically cold expanded high strength steel fastener holes and compared the results to simple analytical solutions. The plates examined were 40 mm wide with a central hole of diameter 6 mm and thickness 4 mm and therefore plane stress theory was used. They measured the presence of reverse yielding and the influence of the Bauschinger effect. They also developed a new analytical model to take these effects into account.

Again, X–ray has been used to study the effect of various parameters in the cold expansion process. The results studying the effect of degree of cold expansion, pip position in split–sleeve cold expansion and the through–thickness effect are described next.

Degree of cold expansion:

Ball and Lowry (1998) carried out a more detailed study of cold expansion in Al 2124–T851 aluminium alloy for different thicknesses, for different hole positions close to the plate edge and for the degree of cold expansion. They compared measurements with analytical and elastic–plastic FE models. Large grain size and texturing were noticed, both of which are characteristic of wrought 2000 series aluminium alloys which have been solution heat–treated, cold worked (rolled and stretched) and artificially aged. Few details were provided about the effect of the degree of cold expansion. Two ratios of 3% and 5% were studied measuring a mean tolerance for the tangential residual stress of ±30.3 MPa for a 3% cold expansion and ±33.1 MPa for a 5% cold expansion. With such large errors they could not find a significant difference between both interference ratios as expected close to the hole edge. They concluded that X–ray was not a viable technique because the combination of large grain sizes and texturing introduced significant inaccuracies in the calculated stress.

Pip position for split–sleeve cold expansion

Cook and Holdway (1993) and Holdway et al. (1994a) used the X–ray diffraction $\sin^2\Psi$ method on 5 mm thick 8090–T8771 aluminium lithium alloy with an unreamed 6.31 mm (approximately 1/4”) hole diameter. The same procedure was repeated by Holdway et al. (1994b) for an Al 7050–T76 aluminium alloy. The cold expansion used the pre–lubricated split–sleeve method developed by FTI. Their results for the exit face are shown in figure 7.5 and can be compared to results shown in figure 7.4 using Sachs boring. They found more compressive tangential residual stresses on the mandrel exit face compared to the entrance face, in particular close to the hole edge ($r/a < 1.3$). The pip effect was examined by checking three different positions: at the pip or position of the split–sleeve ($\theta=0^{o}$), at 90 degrees normal to the pip, and opposite the pip ($\theta=180^{o}$). They found the highest compressive stress at the pip position and the least compressive at the opposite position. The difference found was slightly less than 10% which was not the case for results found by Özdemir and Edwards (1996) using the conventional Sachs boring technique.

The residual stress distribution in cold expanded holes is highly dependent on the position through–thickness as shown by the FE studies in part A of this thesis. The X–ray provides reliable surface measurements for non–axisymmetric distributions even within the large scatter associated with grain and beam size, surface finishing and distance to the hole edge.

Through–thickness effect

Although X–ray diffraction is limited to near surface measurements, the combination of cutting techniques and X–ray has allowed through–thickness effects to be studied. Pintschovius et al. (1986) used X–ray diffraction on the electropolished face of a 25 mm thick ring, cut out of the centre of a steel autofrettaged tube. The correction to measure the original residual stress distribution was a combination of X–ray measurements and calculation of residual stress relaxation due to the cutting out process. Discrepancies between measurements and analytical models were found where models did not include the Bauschinger effect and other effects such as decarburization of the surface layer.

For cold expanded holes in thin sheets of aluminium alloys several studies were found in the literature. For example Priest et al. (1994) found a good comparison between FE axisymmetric predictions and X–ray measurements for the entrance face of split–sleeve cold expanded Al 2024–T351 samples. The measurements were carried out for entrance and exit faces at 90 degrees from the pip while the axisymmetric FE used a uniform displacement of the hole edge and therefore only the free surface effect was predicted. In other words, the effect of a mandrel pulled through the hole on distributions near entrance and exit faces was not modelled.

Özdemir et al. (1994) and republished in Özdemir and Edwards (1996) carried out X–ray diffraction measurements on a cold expanded hole in a 7050–T76 aluminium alloy. Their results are shown in figure 7.6 for entrance and exit faces. They also found more compressive residual stresses at the exit face compared to the entrance face, while this technique produced no information about the distribution between these two free faces.

7.3. Other methods.

7.3.1. Neutron diffraction

The neutron diffraction technique can be thought of as a perfect solution for measuring residual stress distributions. It is quite similar to X–ray diffraction and therefore can be used as a non–destructive technique, but it can penetrate deeper into the material. The depth of penetration can be several centimetres (Yelon and Ross, 1986) which is sufficient for most of the plate thicknesses used in the aircraft industry. A description of precise measurements of internal residual stresses and applications are given by Edwards et al. (1994), including measurements for a cold expanded hole in a mild steel plate. The high cost of the technique, and the restriction to a few neutron sources makes it difficult to use. Once more the grain size plays an important role, particularly where a steep stress gradient exists. For most aluminium alloys, a resolution of ±15 MPa can be expected (Webster, 1991 and Smith et al., 1988).

For autofrettaged tubes, measurements by Pintschovius et al. (1986) for steel and by Bourke et al. (1991) for a low–alloy cracked steel were produced in axial, radial and tangential directions. Their results were in agreement with boundary integral method predictions. Hermann (1994) studied the distribution in axisymmetric roller burnished cold expanded aluminium alloy 8090, Al–Li 8090 and 2091. The measurements were dependent on the crystal orientation chosen for the diffraction, underestimating residual stresses in the vicinity of the hole. They also commented on the negative influence of textured materials for accuracy of neutron measurements.

Several researchers have used neutron diffraction to measure split–sleeve residual stresses. Residual stresses in Al 7050 alloy were measured by Edwards and Özdemir (1991), Özdemir et al. (1994) and Edwards and Wang (1996). A mask was used to reduce the sampling volume to 1 mm^3 as the main concern about measurements was the high stress gradients in the radial direction near the hole edge. They managed to produce contour plots of tangential residual stresses as a function of radius and thickness position through interpolation using a correction for boundary conditions. However, due to difficulties associated with texture and the acquisition of a stress free lattice spacing, the measurement of absolute values of stress were considered to be too difficult. For this reason, and the small sample volume analysed, relatively long counting periods were needed to measure adequate diffraction peaks. They finally compared their neutron measurements for the centre of the plate (Mid–thickness) with Sachs measurements obtaining a good agreement.

Ezeilo et al. (1994) used FE, analytical and neutron diffraction techniques to measure and predict the residual stress field in an Inconel 718 plate at room temperature. The measured and predicted residual stresses were in good agreement. Unfortunately they examined the residual stress distribution for only one angular position, so that it is not possible to compare these results with those obtained from

Sachs and X–ray methods. They also measured the relaxation of residual stresses when samples were subjected to a cyclic fatigue loading from 0 to 1/3 of the monotonic yield stress. The cyclic yield stress was found to decrease about 20% after 105,000 cycles. The residual stresses were found to be redistributed by about the same magnitude, obtaining once more a good agreement between FE simulations and experimental measurements. Their results are presented in figure 7.7 for before and after cyclic relaxation.

7.3.2. Slit angle separation

A cutting method is described next to measure residual stresses in autofrettaged tubes at the inner and outer surfaces. The method is based on the measurement of the opening of a slit introduced in the tube. A reference has been found were the tangential residual stress was measured as a function of degree of expansion, before and after heat treatment. Throop et al. (1981) analysed the relaxation of autofrettaged residual stresses in steel pipes with temperatures reaching 517°C in the inside of the pipe with cooling on the outside face. Their results are shown in figure 7.8 for both inner and outer surfaces of the tube before and after the heat treatment as a function of degree of expansion. This was described as the proportion of plasticity introduced in the pipe in percent. The tangential residual stresses on the inside were a function of the degree of expansion. Unfortunately the heat treatment produced a larger relaxation of more compressive residual stresses. They concluded that relaxation was an important effect, leading to small differences in bore residual stresses between 50% and 100% overstrain autofrettage.

7.3.3. Crack compliance:

Another cutting method is described next based on fracture mechanics where a crack is introduced in the sample and the residual stresses calculated from displacements measured close to the crack tip. This method is called the crack compliance or successive cracking technique.

Legatt et al. (1987) used an incremental slot extension through–thickness to predict the residual stresses through–thickness of a welded joint. This technique allowed the determination of the distribution of residual stresses through–thickness for a constant stress in the welding direction.

Kang and Seol (1996) measured residual stresses in discs obtaining good agreement with sectioning methods. Smoother results can be obtained using influence functions from analytical (FE) simulations (Schindler and Landlot, 1996). Residual stresses in steel rings, hardened by carburization and quenching, were measured by Prime et al. (1999) and compared to FE predictions. To compensate for edge effects and obtain a correct boundary condition they also used X–ray measurements. The profile of tangential residual stress was quite similar to those obtained by cold expansion and good agreement was obtained between experiments and FE simulations.

The crack compliance method has also been used for measurement of residual stresses around split–sleeve cold expanded holes. Lim et al. (1998) analysed 2 mm thick plates of Al 6061–T6 with a central hole of diameter 6.225 mm after cold expansion. The crack compliance method was used by the crack extension up to 10 mm of two cracks at 90 and 270 degrees from the pip position of the split–sleeve. Their results are shown in figure 7.9 and compared to Nadai's analytical model. They measured compressive tangential stresses well over the yield stress near the hole edge and reverse yielding was not detected. This was a consequence of the small number of steps used in the radial direction which could not represent the steep stress gradient.

7.3.4. Concentric rings:

This destructive method is based in the cutting of concentric discs with strain gauges on the top surface. The residual stress is calculated from the strain change using plane stress conditions.

Mack (1962) used this method together with the Sachs method to measure residual stresses in steel discs. He found a good agreement between both techniques concluding that the concentric method required little machining time and only two sets of strain measurements per disc. These advantages were offset by the need for many strain gauges and the danger of introducing plastic strains during the cutting. Therefore the Sachs boring method was preferred.

7.3.5. Centre hole drilling:

Another destructive technique similar to Sachs boring is the centre hole drilling technique, where a strain rosette is attached to the surface of the sample before the drilling of the hole. From the strain change, measured residual stresses at the position of drilling are calculated as a function of drilling position through–thickness. A complex analysis based on FE parameters is needed to relate strains and stresses (Liu and Schajer, 1997, Petrucci and Zuccarello, 1998 and Rasouli et al., 1998). The method is limited to measurement of residual stresses up to one half of the yield stress if they are biaxial, or up to one third of the yield stress if uniaxial, to guarantee elastic behaviour. The measurements in depth were limited to one diameter, as further down, the strain change was too small.

Tait and Newberry (1996) measured cold expanded holes in Al 2024–T3 aluminium alloy with a 6 mm hole diameter and a 2.2 mm thick section. The cold expansion was applied by means of an oversized mandrel with degrees of expansion of 4% and 6%. Air abrasive centre hole drilling was used to create perpendicular sides of the hole from the inlet face. This technique was used in five steps in the radial direction. Residual stresses were calculated for those five different radial positions and compared to analytical models. Unfortunately the measurements were not carried out in an incremental through–thickness scheme which could provide useful information about through–thickness variations of residual stresses.

7.3.6. Etching material removal and curvature measurements:

Another destructive technique is the etching and curvature measurement. There are many layer removal and strain measurement techniques available to measure residual stresses. Sachs boring has already been defined and a new technique is described next to become familiar with the methodology. Hospers and Vogelesang (1975) developed a technique to measure residual stresses in thin sheet material. Thin layers are removed by chemical etching, which induce an increasing curvature of the sheet. The initial distribution of the residual stress is derived from curvature measurements. Results were presented for rolled Al 2024–T3 sheet material and shot peened 7079 material. Their results were in agreement with X–ray measurements.

7.3.7. Photoelasticity, Moiré interferometry and holograph methods:

There are several methods based on optical visualisation of surface strains named differently depending on the device used to visualise the strains.

Photoelasticity has been used to determine optimum levels of interference within pin–loaded lugs (Ligenza, 1963 and discussion by Holister, 1963), using an elastic formulation for thick walled cylinders to determine stresses. Leon (1998) used a photoelasticity stress image of a split–sleeve cold expanded hole and compared it to a technique using a mandrel with four splits. The measurements of stresses around the hole were determined though using X–ray diffraction for Al 6061 aluminium alloy with 6.35 mm hole diameter. Photoelasticity was used to analyse the lack of symmetry in residual stress pattern.

Moiré interferometry has been used to measure strains and residual stresses in Al 2024 (Leftheris and Schwarz, 1987). The application to split–sleeve cold expansion for Al 7050–T651 was described by Link and Sandford (1990). The radial displacements were compared for different optical methods including scanning electron micrographs. A holographic technique was used by Sandford and Link (1989) for the same Al 7050–T651 aluminium alloy. The strain measurements were compared to analytical models and the radius of plasticity was calculated.

In all cases, little information about the values of the residual stresses were provided. However, shapes and gradients near the entrance face were practical information obtained from these methods. For example this method has been useful to determine the presence of the pip in split–sleeve cold expanded holes (Link and Sandford, 1990).

7.4. Conclusions.

(i) Sachs boring is a technique for the measurement of residual stresses averaged through–thickness in axisymmetric components. Many measurements are obtained in the radial direction obtaining good accuracy for near hole edge residual stresses. The method can not be used to measure through–thickness and angular variations. FE benchmarks of the boring process can be used to assess the equation for boring from the inside or machining from the outside.

(ii) X–ray diffraction is a technique for measuring near surface residual stresses, although grain sizes for 2000 series aluminium alloys are found to be a problem. X–ray measurements average the area covered by the beam leading to long measurement times to obtain a complete map of residual stresses. Treatment of surfaces is necessary prior to diffraction measurements. Tangential residual stresses measured using X–ray diffraction around cold expanded holes were found to be more compressive near the pip position of the split compared with other locations.

(iii) Neutron diffraction provides a complete 3D mapping of residual stresses for thickness up to a few centimetres. It is an expensive, time consuming technique with limited experimental facilities. The crystallographic plane used in the measurement affects the results, and large measurement scatter can result.

(iv) Crack compliance measures radial distribution of residual stresses in one angular position. The method requires the use of software to solve the residual stresses from tabulated coefficients, and functions of shape and material.

(v) Other cutting methods are available but do not provide more information than Sachs boring.

(vi) Optical methods are suitable only to define the shape of residual stresses.

Chapter 8

A NEW EXPERIMENTAL METHOD TO MEASURE RESIDUAL STRESSES

A new experimental method has been developed to measure non–axisymmetric residual stresses in cylindrical components. This method is based on Sachs boring, a destructive method. The main motivation for this study was that most of the cases of residual stresses around cold expanded holes analysed in this research were non–axisymmetric. Further developments may provide complete three–dimensional measurements.

8.1. Introduction to general method.

Cutting and strain measurement techniques for the measurement of residual stresses are based on the elastic relaxation of residual stresses during the cutting process. Several considerations are needed to relate the strain change to the stress relaxation.

Traditionally, equilibrium of residual stresses in a component was checked using global equilibrium, in other words, the sum of forces and moments in any direction must be zero. However, there are many unrealistic combinations of residual stresses which could guarantee a global equilibrium. Therefore, the conditions for equilibrium of small finite bodies within the component must be studied. In other words, the basis of the development of a cutting method is the equations of equilibrium of stress (Timoshenko and Goodier, 1987 and Meleshko, 1995).

Such equilibrium is expressed in polar co–ordinates as a function of radius (*r*), angle (θ) and axial distance (*z*) as shown in figure 8.1. If body forces are not considered, the equations of equilibrium obtained by summing all the forces acting on the element are expressed through the following system of three differential equations:

$$\left\{\begin{array}{ll} \sum F_r: & \dfrac{\partial\sigma_r}{\partial r}+\dfrac{\sigma_r-\sigma_\theta}{r}+\dfrac{1}{r}\dfrac{\partial\tau_{r\theta}}{\partial\theta}+\dfrac{\partial\tau_{rz}}{\partial z}=0 \\ \sum F_\theta: & \dfrac{1}{r}\dfrac{\partial\sigma_\theta}{\partial\theta}+\dfrac{\partial\tau_{r\theta}}{\partial r}+\dfrac{2\tau_{r\theta}}{r}+\dfrac{\partial\tau_{\theta z}}{\partial z}=0 \\ \sum F_z: & \dfrac{\partial\sigma_z}{\partial z}+\dfrac{\partial\tau_{rz}}{\partial r}+\dfrac{\tau_{rz}}{r}+\dfrac{1}{r}\dfrac{\partial\tau_{\theta z}}{\partial\theta}=0 \end{array}\right\} \tag{8.1}$$

The aim of an experimental method for measuring residual stresses is to determine the six components of stress expressed in equation 8.1 but for this we need to find more relations.

The Sachs boring procedure assumes elastic unloading, or elastic relaxation of residual stresses, during the removal of cylindrical layers of material. Therefore six relations between the components of strain are expressed through six differential equations, called the conditions of compatibility. Extra relations are then found between stresses and strains using Hooke's law.

The cutting procedure imposes new boundary conditions as the new circular edge of radius *d* becomes stress free in the radial direction. The procedure is shown in figure 8.2, where a cylindrical layer of material is removed at radius *d*, leading to the release of the stresses acting on this face.

The strain change produced from such a relaxation is measured at the face with radius $r=b$, where the following components of strain can be measured: $\Delta\varepsilon_{\theta\theta}$, $\Delta\varepsilon_{zz}$ and $\Delta\varepsilon_{z\theta}$. This can be generalised for any radius $r = d$, where the boring is carried out, from *a* to *b* and therefore a new set of equations is found. The stresses released at *d* (σ_{rr}, $\tau_{r\theta}$ and τ_{rz}.) are equal to the original residual stresses, and therefore relations between the strains and residual stresses can be found as a function of radius *r*, through–thickness position *z* and angle θ, as follows:

$$\begin{Bmatrix} \Delta\varepsilon_{\theta\theta}(r,z,\theta) = f_{\theta\theta}(\sigma_{rr}(r,z,\theta),\tau_{r\theta}(r,z,\theta),\tau_{rz}(r,z,\theta)) \\ \Delta\varepsilon_{z\theta}(r,z,\theta) = f_{z\theta}(\sigma_{rr}(r,z,\theta),\tau_{r\theta}(r,z,\theta),\tau_{rz}(r,z,\theta)) \\ \Delta\varepsilon_{zz}(r,z,\theta) = f_{zz}(\sigma_{rr}(r,z,\theta),\tau_{r\theta}(r,z,\theta),\tau_{rz}(r,z,\theta)) \end{Bmatrix} \tag{8.2}$$

In order to find the relation between stress and strain, complicated analyses are needed. By assuming elastic unloading behaviour, Hooke's law is used at the measurement position, $r=b$, to find the strain change.

The combination of equations 8.1 and 8.2 allow the solution of six components of stress. However, in order to solve differential equations, the initial conditions must be known. These are obtained from known boundary conditions:

$$\begin{Bmatrix} \textit{Hole} & \textit{edge}: & \sigma_{rr}(a,z,\theta) = \tau_{r\theta}(a,z,\theta) = \tau_{rz}(a,z,\theta) = 0 \\ \textit{Measuring} & \textit{edge}: & \sigma_{rr}(b,z,\theta) = \tau_{r\theta}(b,z,\theta) = \tau_{rz}(b,z,\theta) = 0 \\ \textit{Entrance} & \textit{face}: & \sigma_{zz}(r,h/2,\theta) = \tau_{z\theta}(r,h/2,\theta) = \tau_{rz}(r,h/2,\theta) = 0 \\ \textit{Exit} & \textit{face}: & \sigma_{zz}(r,-h/2,\theta) = \tau_{z\theta}(r,-h/2,\theta) = \tau_{rz}(r,-h/2,\theta) = 0 \end{Bmatrix} \tag{8.3}$$

The major difficulty is to find the unique relation between stress and strain expressed in equation 8.2 for any combination of a, b, h. It is complicated to solve the system for three variables r, z and θ. Therefore, both stress and strain are analysed using common stress functions studied extensively in the literature (Michell, 1899, Tinpe, 1923, Melan, 1932, Sternberg and Sadowsky, 1949, Greenwood, 1989, and Steinberg, 1994). These functions are used to split the solutions into systems of only one variable. These stress functions also solve the compatibility conditions. As a first approximation, a Fourier analyses using a series expansion is used assuming that both stresses and strains are distributed sinusoidally in θ for any distribution in r and z as follows:

$$\sigma,\varepsilon(r,z,\theta)=\sum_{m=0}^{\infty}\left[\sum_{n_c=0}^{\infty}\sigma,\varepsilon^{n_c m}(r)cos(n_c\theta)+\sum_{n_s=0}^{\infty}\sigma,\varepsilon^{n_s m}(r)sin(n_s\theta)\right]f^m(z) \qquad (8.4)$$

The experimental technique uses a least squares error approximation to obtain the Fourier coefficients. This technique is based on the measurement of a number of strain readings for "*n_reading*" positions and calculate "*n_coefficient*" Fourier coefficients using a pseudo-inverse matrix solution (Garcia-Granada, A.A., 1996). A least square method is obtained when the number of Fourie coefficients is less than the number of reading positions (*n_coefficient* < *n_reading*).

The stress solution of each strain coefficient represents a particular case of the stress state. For the coefficients where $m=0$ there is no variation in the axial (z) direction, while for coefficients where $n_c=n_s=0$ there is no variation with angle.

8.2. Conventional Sachs boring technique ($n_s=n_c=m=0$).

The residual stress field surrounding a cold expanded hole can be calculated using different experimental methods as described in the literature review. The Sachs boring method is widely used where an axisymmetric residual stress distribution is assumed. Following the notation used in equation 8.4 implies the use of only one coefficient in the Fourier development without any angular variation ($n_c=n_s=0$) and without through–thickness variation ($m=0$).

Three topics have been investigated using the Sachs boring technique. First, the relaxation related to disc extraction, secondly the validity of elastic unloading conditions and finally the use of through–thickness measurements within a conventional formulation.

Disc extraction

The purpose of this study was to find the error due to disc extraction prior to Sachs boring. In order to study the disc extraction in detail, axisymmetric FE models were used for two different outer radii: small discs of radius b = 16 mm and large discs of radius b = 50 mm. Both were cold expanded with uniform radial displacement of the hole edge and using Al 2650 in a kinematic hardening material model. The disc of outer radius b = 16 mm was extracted from the samples of greater outer radius b = 50. Similar simulations were repeated using two–dimensional large square plates (50 x 50 mm). These were first expanded and then a circular disc was extracted of outer radius b = 16 mm.

The results of the axisymmetric simulations are shown in figure 8.3a. The original outer radius of the cold expanded disc was 50 mm. A disk of b=16 mm was extracted. Disc extraction revealed that stress redistribution, close to the hole edge was 36 MPa and 18 MPa at the outer surface of the disc (r = b = 16 mm). The values plotted in figure 8.3b correspond to the mid–thickness position. This redistribution can be calculated using the modified Sachs equations presented in appendix A as equation A.4 for plane stress. To achieve this the tangential strain at the inner radius (r=a) must be measured before and after the disc extraction.

Similar results of relaxation were obtained for two–dimensional models. In both cases equation A.4 was able to calculate such small relaxation.

Elastic relaxation

The aim of this study was to check the relaxation of residual stresses in order to assure the validity of elastic unloading. To do this FE simulations of Sachs boring were carried out. The boring process was simulated by removing cylindrical layers of FE from the inside of the hole. A small plastic stress distribution was observed when removing the layers within the region of reversed yielding. The two areas, elastic and plastic unloading, are shown in figures 8.4a for radial and 8.4b for tangential residual stresses during the boring process. The plastic redistribution is not included in the Sachs formulation where an elastic unloading is assumed. However, the resulting errors between the FE residual stress and the residual stress calculated from FE boring strains are small. This is due to the location of measurements, far from the hole edge, and therefore within the region of elastic relaxation. The strain is a consequence of stresses in equilibrium from the boring location to the outer disc, and therefore elastic unloading is still acceptable. A complete redistribution of stresses was observed when the radius of removal *d* is greater than 2.4 times the hole radius *a*.

Through–thickness measurements

The aim of this study was to check the validity of conventional Sachs formulation to measure residual stress distribution as a function of thickness position, as a similar technique known as deep hole drilling has been modified to measure these through–thickness variations (García–Granada et al., 1998b). This is similar to the study reported by Smith et al. (1998). FE simulations were carried out using an axisymmetric model with combined hardening rules for Al 2650 and non–linear spring elements to simulate the cold expansion process as described in section 4.1.2. This was done to obtain a realistic through–thickness distribution and therefore, a more realistic Sachs boring stress relaxation. The relaxed tangential and axial strains were recorded in the FE analysis at the outer radius during the simulation of Sachs boring. These strains are shown in figure 8.5a for three different locations through–thickness: entrance, mid–thickness and exit face. The conventional Sachs formulation, given in equation A.1 of appendix A, was used to calculate the residual stresses from the strains. The results are compared to the original FE residual stresses in figure 8.5b for those three positions through–thickness.

It was concluded, as in Smith et al. (1998), that conventional Sachs boring equations were able to predict only residual stress averaged through–thickness. The method was not able to calculate for example the small compressive tangential residual stresses near the entrance face.

8.3. Description of new method: Garcia–Sachs (m=0).

The complete measurement of any residual stress distribution in axisymmetrical components, such as discs or pipes, would imply a development of all the infinite coefficients in the Fourier analyses expressed by equation 8.4. As this is impossible, an approach was first examined to obtain two–dimensional solutions assuming a constant distribution of residual stresses across the thickness of the component. Therefore, the analysis considers a residual stress distribution that varies only as a function of angle and radius only.

The strain must be measured at different angular positions to determine the angular variation. From the strain data, Fourier coefficients of strain can be determined in order to determine the number of parameters involved in the calculation and the relevance of each of the coefficients. Independent analyses for each coefficient provides new Fourier coefficients for the residual stresses. Finally, the residual stress distribution must be calculated by adding all the coefficients and taking into account the angular variation as described in equation 8.4.

The detailed analyses for the calculations are published in García–Granada et al. 2000a, together with an FE benchmark for the measurement of residual stresses around cold expanded holes after the application of external uniaxial load and creep. Another FE benchmark is presented in García–Granada et al., 1999b for the measurement of residual stresses around a hole in a plate which was subjected to plastic loading. The FE benchmarks are necessary to demonstrate the validity of the method. This is because the FE residual stresses are known, and therefore from the same simulation it is possible to generate the strains corresponding to material removal. If the method is correct, then the original FE stresses will be generated from the boring FE strains. Also, the method can be improved with several practical aspects studied in more detail. This includes the influence of disc size, number of coefficients and the mathematical algorithms required for solving the stresses.

FE benchmark

The aim of this FE benchmark was to generate a non–axisymmetric residual stress distribution and simulate the boring process. For a straight forward FE benchmark, it was decided to represent a plate containing a hole of radius a=3 mm within a plate of width and height 50 mm and thickness h=6 mm. Two–dimensional elements assuming plane stress conditions and combined hardening laws for Al 2650 were used as described in part A of this thesis. The plate was loaded to a stress of $\sigma_{app} = 0.58\sigma_y'$ = 250 MPa. This caused yielding near the hole edge due to the presence of the stress concentration. Then the sample was unloaded and residual stresses were generated in the vicinity of the hole. A disc of radius b=16 mm was extracted from the plate, leading to a small relaxation of the residual stresses near the hole edge.

The boring procedure was simulated by removing successive cylindrical layers of elements at increments of radius 0.2 mm from inside the hole. The tangential strain change was obtained as a function of the boring radius r at selected positions around the circumference of the disc.

The residual stresses generated after the disc extraction were symmetric (mirror symmetry) with respect to the axes x (θ = 0°, loading direction) and y (θ = 90°).

However, the residual stress field exhibited angular dependence. That is the residual stresses were non–axisymmetric. There were high compressive tangential residual stresses near the hole edge at $\theta = 90°$ which became tensile just after 1 mm from the hole edge. Radial and shear stresses were small compared to tangential stresses.

The tangential strain change obtained at $r=b=16$ mm during the simulated boring process is shown in figure 8.6a for three angular positions. The strains exhibited a non–axisymmetric distribution. The strains were fitted using a Fourier analysis as described by equation 8.4 using the first five cosine terms, from $n_c = 0$ to $n_c = 4$ (with $n_s = 0$ and $m = 0$).

Based on the Fourier strains, and using equations shown in the appendix for each coefficient, the residual stresses were calculated. The Fourier analysis allows the residual stresses to be obtained for any angular position. The calculated stresses using the new procedure and the conventional Sachs method are compared to the original FE residual stresses. In figure 8.6b the tangential residual stresses are shown with excellent agreement between FE stresses and the stresses calculated with the new method. The new method is capable of measuring not only the angular variation but the steep radial gradient in the residual stress close to the hole edge.

The calculations were repeated using the conventional Sachs method as in Özdemir and Edwards (1996). These calculations were made assuming an axisymmetric stress distribution even knowing that the boring strain was a function of angle. The residual stresses were therefore calculated from the conventional equation A.3 for each strain independently. These results are also shown in figure 8.6b and do not agree with the FE original residual stress distribution.

In figure 8.7a the radial residual stresses at $\theta=0°$ and in 8.7b the shear residual stresses at $\theta=45°$ are shown. Again there is good agreement between the original FE stresses and the stresses calculated from the relaxed FE strains using the new method.

In this case the new method was able to determine shear stress, while the conventional Sachs assumes that, as a consequence of axisymmetry, it is zero. However shear stresses were predicted to be zero at $\theta=0°$ and 90 degrees as a consequence of y and x symmetries respectively.

Experimental measurements using this Fourier approach to the Sachs method are also published for several applications and these are described briefly in Chapter 9.

8.4. Conclusions.

(i) The Sachs boring technique has been modified to allow the measurement of non–axisymmetric residual stresses in cylindrical components.

(ii) The new Garcia–Sachs method has been validated using FE benchmarks before their application to experimental measurements.

(iii) The current state of the method allows the measurement of residual stresses averaged through–thickness of the component.

(iv) The use of conventional Sachs formulation to measure through–thickness variations would produce significant errors.

(v) The use of the conventional Sachs formulation to measure non–axisymmetric distributions would generate significant errors.

(vi) Redistribution of residual stresses due to disc extraction gives rise to a small error in the measurement with Sachs. However, this redistribution can be calculated.

(vii) For a cold expanded hole, the redistribution of stresses during boring was mainly elastic, with only local plasticity generated close to the hole edge. This effect introduced only small errors in the calculations.

Chapter 9
COMPARISON FE WITH EXPERIMENTS

Experimental measurements using the new Garcia–Sachs method are compared to FE predictions for several cases studied during this research. Complementary additional X–ray measurements are provided to demonstrate the free surface effect. The first case examines residual stress measurements around split–sleeve cold expanded holes where the presence of the split generated non–axisymmetric distributions, which the conventional Sachs was not able to measure. Cold expanded residual stresses, redistributed after compressive loading, after creep, and after tensile loading and creep were also examined. The method was also applied to non–cold expanded holes after the application of external loads and creep to demonstrate its accuracy. In all cases a good agreement between FE and Garcia–Sachs measurements was obtained.

9.1. Split–sleeve cold expansion.

Split–sleeve cold expansion is widely used in aircraft structures to improve fatigue life by introducing compressive residual stresses. The pre–lubricated sleeve is placed into the hole and around the mandrel to reduce surface damage and cracks inside the hole once the mandrel is pulled through. The split in the sleeve is necessary for installation and removal purposes. Different techniques have been examined where four different splits were included in the mandrel (Leon, 1998) or where the sleeve was left in place as an interference fit (Reid, 1997 and Reid et al., 1997).

However, the split–sleeve technique commercialised by FTI is still mostly used and more understanding about residual stress distributions is required. There are conflicting results obtained using various experimental techniques and numerical methods. For example, Cook and Holdway (1993) and Cook et al. (1994), measured the most compressive surface residual stresses with X–ray at the position that corresponds to the position of the split in the sleeve during cold expansion. In addition Leftheris and Schwarz (1987) measured the largest tangential strain at the position of the split, and Link and Sandford (1990) also noted the greatest amount of expansion occurred at the split position. Furthermore, fatigue testing by Stack and Stephens (1989) showed that cracks started to grow from a location at 180° to the split when the load was applied at 90° to the split. On the other hand, similar crack growths were observed for both positions normal to the split when the load direction was aligned with the split. However, Stack and Stephens (1989) showed that the difference in fatigue life with two different split–sleeve locations was negligible.

In contrast, Edwards and Wang (1996) used neutron diffraction at only one angle and the conventional Sachs method to measure the angular variation of the residual stresses. They obtained the least compressive tangential residual stress at the pip. Similar results were obtained by Özdemir and Edwards (1996), where the maximum compressive stress was measured using the conventional Sachs method at $\theta = 90°$ from the split in the sleeve position. A modified Sachs technique (Lambert, 1954) was available at the time to measure antisymmetric stresses left by plastic bending, but Özdemir and Edwards (1996) did not take into account such angular variations even explicitly in their paper.

In this section, X–ray measurements described in Lacarac (2000) are compared to the FE predictions described in section 4.1. The X–ray measurements were made at the entrance and exit faces. These results illustrate the variation of the residual stresses through–thickness of the cold expanded samples. Measurements using the Garcia–Sachs method, also described in Lacarac (2000), are compared to residual stresses averaged through–thickness for different angular positions. The use of conventional Sachs is also criticised. Only the Garcia–Sachs measurements will be briefly described, as these results are published elsewhere (García–Granada et al., 1999a).

A disc of inner radius $a = 3$ mm, outer radius $b = 16$ mm and thickness $h = 6$ mm was split–sleeve cold expanded. The material used was aluminium alloy Al 2650 as described in chapter 3. Five strain gauges were bonded at $\theta=0^\circ$, 45°, 90°, 135° and 180° to the edge of the disc at a radius $b=16$ mm to measure the tangential strain changes. The material was bored out using a feed rate of 1 mm/sec in radial increments of 0.05 mm. A micrometer was used to measure the hole diameter corresponding to each strain reading. A Fourier analysis was carried out on the measured strains to obtain five Fourier coefficients. For each coefficient of strain the corresponding stress coefficient was determined using a plane stress assumption together with the equations given in appendix A. The stress coefficients were finally added together to generate the measured residual stress distributions as a function of angle.

The results for $\theta = 90^\circ$ are shown in figure 9.1a and compared to the averaged stress through–thickness from axisymmetric models using three different hardening models described in chapter 4. An error bar for Sachs' measurements is shown in figure 9.1a. This error bar is obtained from recalculation of residual stresses based on measurements errors for the strain reading of ± 1 µm/m and errors in the measurement for small radius of $\pm 1\mu\text{m}$. A good agreement was obtained for the combined hardening model, which included Bauschinger effect considerations. The FE analysis did not include the effect of the split–sleeve. Surface X–ray residual stress measurements are shown in figure 9.1b also for $\theta = 90^\circ$ and are compared to results from the combined hardening axisymmetric model. Once more a good agreement was obtained.

On the other hand the results obtained from the Garcia–Sachs and conventional Sachs methods were not in agreement. This is shown in figure 9.2a where the split sleeve position showed a maximum compressive stress using Garcia–Sachs while it was the least compressive using the conventional Sachs formulation. This was done to compare results with other researchers (Özdemir and Edwards, 1996, Edwards and Wang, 1996). Using the conventional Sachs method should be avoided to predict angular variations of residual stresses.

To support the measurements obtained from the application of the Garcia–Sachs, extra measurements were carried out using the X–ray diffraction method for entrance and exit faces at different angular positions. The results are shown in figure 9.2b. At the entrance face the most compressive tangential residual stress was found at the split position ($\theta = 0^{\circ}$).

The variation of residual stresses close to the position of the split–sleeve should be considered as a local effect. Therefore the Fourier analysis, as used in the current Garcia–Sachs method, is not able to describe accurately such a local effect in detail. The results must be interpreted as an indication of the trend of the real residual stress state.

9.2. Redistribution of cold expansion residual stresses after application of external compressive load.

In the last section residual stresses in the vicinity of cold expanded holes in Al 2650 have been measured. In this section the influence of remote or external loading is quantified. A major concern is the possibility of removing compressive residual stresses by redistribution after the application and removal of uniaxial compressive loads. In aircraft lower wing structures this effect must be investigated as the fatigue life, during flying conditions, could be modified after just one landing.

Armen et al. (1984) studied such redistribution using two–dimensional FE analyses. Different compressive loads were remotely applied obtaining a relaxation of the compressive tangential residual stresses near the hole edge in the direction normal to the applied load ($\theta=90^{\circ}$). The new residual stress distribution was non–axisymmetric but no experimental results were obtained to verify this. In addition, they calculated fatigue crack growth using weight functions developed by Grandt (1975) using FE stresses and following the equations developed by Bell and Creager (1975). In their conclusions they stated that omitting the effects of remote compressive loads on the residual stresses around cold expanded holes will result in unconservative crack growth life predictions.

In this section, residual stress measurements using the Garcia–Sachs method on cold expanded holes in Al 2650 aluminium alloy are compared to FE predictions. A plate of 100 mm width and 6 mm thickness containing a central hole was first cold expanded and then reamed to obtain a hole radius a=3.175 mm (1/8"). The plate was then subjected to a uniaxial compressive load of $\sigma_{app} = 0.38\sigma_y' = -162$MPa in the $\theta=0^{\circ}$ direction. Finally, the external load was removed and a disc of outer radius b=16 mm was extracted from the plate. Strain gauges were attached to the outer radius in the tangential direction before commencing the boring out procedure. More details about the experimental procedure are given by Lacarac (2000).

The experimental results are compared to FE predictions in figure 9.3a for $\theta=0^{\circ}$ (loading direction) and in figure 9.3b for $\theta=90^{\circ}$ (normal to loading direction). The FE stresses were obtained from three–dimensional simulations presented in chapter 4.

The FE stresses are averaged through–thickness. The original FE axisymmetric stress distribution from cold expansion is also shown to illustrate the extent of relaxation of the residual stress.

Good agreement between the measurements and simulation is obtained. There is an important reduction of the compressive tangential residual stresses near the hole edge in the direction normal to the loading. As described in chapter 4, the area in compression remained similar to the original cold expansion residual stresses. The residual stress was non–axisymmetric, and therefore the conventional Sachs method should not be used to calculate residual stresses.

9.3. Relaxation of cold expansion residual stresses due to creep.

Creep relaxation of cold expansion residual stresses has been a major issue in this research. In this section an evaluation of cold expansion residual stresses after creep stress relaxation is reported.

Little previous work has been reported about the relaxation of residual stresses in aluminium alloys. Bonnafé et al. (1996) studied age creep forming residual stresses and their interaction with buckling and welds in Al 2219 alloys. Stress relaxation was evaluated through tests performed at different temperatures, but no information was provided about how to model such creep relaxation. Brinksmeier et al. (1994) summarised the reasons for residual stress relaxation as a consequence of quasi–static loading, cycling loading and annealing at higher temperatures. They showed the relaxation of shot–peened residual stresses for SAE 4140 at 450^{o}C for different periods of time. Once again, little detail was given about the modelling.

In this section, the creep relaxation of residual stresses in cold expanded discs of Al

2650 aluminium alloy is presented. A disc of inner radius a=3 mm, outer radius b=16 mm and thickness h=6mm was split–sleeve cold expanded and then placed in a furnace for 1000 hours at 150°C. Once removed from the furnace, strain gauges were attached to the sample on the outer face before commencing the Sachs boring–out process. The strain readings were analysed and residual stresses, averaged through–thickness, were calculated using the Garcia–Sachs method. For completeness, X–ray diffraction was used to measure surface residual stresses at the position normal to the pip (θ=90°). The details of the experiments and procedures are given by Lacarac (2000). The FE studies were presented in chapter 5.

The tangential residual stress measurements and FE predictions averaged through–thickness are compared in figure 9.4a. The figure also shows the initial axisymmetric FE prediction for cold expansion residual stresses. Good agreement was found between FE predictions and experiments. The FE simulations predicted larger final compressive tangential residual stresses near the hole edge. This could be a consequence of the inaccurate creep model not taking into account the influence of large prior plasticity at this position. In any case, this relaxation was smaller when compared to the application of a compressive load studied earlier. This can not be generalised, as creep would be more important at higher temperatures and relaxation due to compressive loading less important for smaller compressive loads.

Results at the entrance and exit faces are shown in figure 9.4b, with X–ray measurements and FE predictions compared for the position normal to the split (θ = 90°). The relaxation occurred everywhere except near the entrance face where original residual stresses were already small. Good agreement was found between FE predictions and X–ray measurements.

9.4. Redistribution of cold expansion residual stresses due to external load and creep.

The lower wing skins of supersonic aircraft are subjected to tensile loads and high temperature during flight conditions. It was decided to analyse the relaxation of residual stresses from cold expansion with the application of external loads.

Plates containing a central hole were cold expanded and then placed on a creep rig where they were heated up to 150°C. Once the temperature was stable, the sample was subjected to a uniaxial external load equivalent to $\sigma_{app} = 0.38\sigma_y' = 162$MPa in the $\theta=0^{o}$ direction for 1000 hours. Then the sample was unloaded and cooled down to room temperature. Next, a disc of outer radius b=16 mm was extracted from the plate and strain gauges bonded at different angular positions in the tangential direction. The residual stresses were calculated using the Garcia–Sachs equations for plane stress. For completeness, X–ray diffraction was used to measure surface residual stresses at the position normal to the pip ($\theta=90^{o}$). More details about the experimental procedure and experimental results are given by Lacarac (2000). The FE results were presented in chapter 5.

Tangential residual stresses averaged through–thickness of the component measured using the Garcia–Sachs method and FE predictions are shown in figure 9.5a. The original axisymmetric FE prediction of the residual stresses is also shown to illustrate the degree of relaxation. Good agreement was obtained between predictions and measurements except for positions close to the hole edge in the direction normal to the loading. In this position FEA predicted larger compressive tangential residual stresses at about 70 MPa more compressive than the measurement. Several reasons could justify such a disagreement. These include the creep modelling, split–sleeve effect and disc extraction. Both the FE and experimental measurements revealed an angular variation of residual stresses, with the most compressive residual stresses near the hole edge at $\theta=90^\circ$.

Surface stresses measured with X–ray are compared to FE predictions in figure 9.5b for entrance and exit faces. Reasonable agreement was found. The FE residual stresses were more compressive than the X–ray results near the exit face, but were nevertheless within the large error bars of X–ray measurements. In this case smaller stress relaxation near the exit face was found when compared to creep relaxation without external load.

9.5. Generation of residual stresses around non–cold expanded holes due to external load and creep.

The benefit of cold expansion residual stresses should be always checked against non–cold expanded holes. The effects of load and temperature should be analysed for non–cold expanded holes since there is a possible generation of either beneficial or detrimental residual stresses in the process.

Plates containing a central hole (non–cold expanded) were placed on a creep rig where they were heated up to 150°C. Once the temperature was stable the sample was subjected to a uniaxial external load equivalent to $\sigma_{app} = 0.38\sigma_y' = 162\text{MPa}$ in the $\theta=0^\circ$ direction for 1000 hours. Then the sample was unloaded and cooled down to room temperature. Next, a disc of outer radius b=16 mm was extracted from the plate and strain gauges bonded at different angular positions in the tangential direction. The residual stresses were calculated using Garcia–Sachs equations for plane stress. More details about the experimental procedure are given by Lacarac (2000). The comparison between FE and experimental results is given by Lacarac et al. (1999).

Tangential residual stresses were developed as a consequence of localised plastic and creep strains during loading and creep. Then the load was removed. The tangential residual stresses are shown as a function of radius in figure 9.6a for the loading direction and in figure 9.6b for the position normal to the loading direction ($\theta = 90^o$). Good agreement was found between the Garcia–Sachs measurements and the FEA predictions. Once more FEA predicted larger compressive tangential residual stresses than the experimental measurement close to the hole edge. The accuracy of the modelling of creep behaviour is questionable for high loads, particularly where power–law creep is no longer valid. No prior plasticity was present in this case before creep relaxation. Further considerations about the transition from 150°C to room temperature must be taken into account as it was not instantaneous and the relaxation of stresses may occur. Beneficial compressive tangential stresses were introduced in the direction normal to the applied load.

Once more, the use of the conventional Sachs method provided erroneous results. Sachs measurements are also included in figure 9.6a and b, and obtained a tensile tangential residual stress for the position normal to the loading direction. This is contrary to the FE results and the Garcia–Sachs measurements.

9.6. Generation of residual stresses around non–cold expanded holes due to external load and plasticity.

A similar simulation and experiment to the last section was produced for plates containing a central hole (non–cold expanded) subjected to a high uniaxial external load at room temperature to produce localised plasticity. The applied load was $\sigma_{app} = 0.7\sigma_y' = 300$MPa in the $\theta=0^o$ direction. The sample had a hole radius $a = 3$ mm, thickness $h = 6$ mm in a plate 22 mm wide and more than 100 mm in height. Then the sample was unloaded to generate the residual stresses, a disc of outer radius b=10 mm was extracted from of the plate and strain gauges bonded at different angular positions in the tangential direction. The residual stresses were calculated using the Garcia–Sachs equations for plane stress. More details about the procedure are given by García–Granada et al. (2000b).

The Sachs boring process was also simulated using FE analysis and the predicted strains compared to those measured with experiments in figure 9.7a for three angular positions. The Fourier coefficients were calculated from the measured strains. Results are shown in figure 9.7b and compared to the FE predictions.

Tangential residual stresses originated as a consequence of plastic strains during loading. Then the load was removed. The tangential residual stresses are shown as a function of radius in figure 9.8a for the loading direction (θ=0°) and in figure 9.8b for the position normal to the loading direction (θ=90°). Good agreement was found between the Garcia–Sachs measurements and the FEA predictions. Once more FEA predicted larger compressive tangential residual stresses close to the hole edge.

However, experiments attempting to measure non–axisymmetric residual stresses using the conventional Sachs method provided significant errors. Sachs measurements are also included in figure 9.8a and b, and reveal tensile tangential residual stresses for the position normal to the loading direction. Again this is contrary to the Garcia–Sachs measurements and the FEA predictions.

9.7. Conclusions.

(i) Several experimental applications of the new Garcia–Sachs method have been presented. Using this technique good agreement between experimental results and FE predictions was found.

(ii) The conventional Sachs boring method produced significant errors when used to measure non–axisymmetric residual stress distributions.

(iii) X–ray was used to measure surface stresses and the Garcia–Sachs method was used for stresses averaged through–thickness with plane stress assumptions.

(iv) Measurement of the tangential residual stresses around split–sleeve cold expanded holes revealed higher compressive stresses at the position of the split using both the X–ray and Garcia–Sachs methods.

(v) The application of compressive loads relaxed the compressive tangential residual stress in the position normal to the applied load. Good agreement was found between FE predictions and the Garcia–Sachs measurement method.

(vi) Creep relaxation of residual stresses at 150°C was studied with and without external loading. Predictions revealed greater relaxation for the second case, which was partially confirmed by experimental measurements.

(vii) Introduction of residual stresses around non–cold expanded holes was predicted using FE analysis and measured using the Garcia–Sachs method. Two examples, where residual stresses were a consequence of either creep or plasticity, were examined. Compressive tangential stresses were generated and are beneficial in the direction perpendicular to the applied load.

Chapter 10
Conclusions and Further Work.

In this thesis, the effect of cold expansion on a new aluminium alloy has been investigated. The split–sleeve method was used to cold expand 6 mm thick plates and discs of Al 2650 containing a central hole, 6 mm in diameter. Several tests were carried out to characterise the material behaviour of Al 2650 at both room temperature and 150°C. FE simulations were undertaken to predict residual stresses arising from the cold expansion process before and after high temperature exposure, with and without the application of external loads. Predictions for crack growth in the presence of residual stresses were presented. A methodology was presented, so that the benefits of cold expansion, compressive loading and creep can be reliably accounted for in fatigue damage tolerant analyses. Predicted residual stresses were compared to experimental measurements using X–ray diffraction and a new approach based on the Sachs boring technique. In this Chapter, conclusions based on this study and recommendations for further work are given.

10.1. Concluding comments

The numerical results and analyses presented in the previous chapters led to the following conclusions, listed in order of appearance within this thesis:

1. Analytical models are capable of describing one–dimensional axisymmetric cold expansion residual stresses as a function of radius. Complicated iterative (numerical) analyses are required to match the Bauschinger effect which predicted

less compressive tangential residual stresses near the hole edge in comparison to other plasticity models. However these models do not provide information about through–thickness and angular distributions arising from the mandrel pulled through and split in the sleeve respectively.

2. The Al 2650 stress–strain response was determined from tensile tests at low strain rates. The results showed a similar behaviour when tested in the longitudinal and transversal directions of rolling. An important Bauschinger effect was also revealed, which was approximated by a combined hardening model. However, this model was not available for two–dimensional analyses (plane stress and plane strain) were the best approximation for material behaviour was kinematic hardening under plane stress assumptions.
3. The Al 2650 cyclic behaviour was tested using strain controlled cyclic tests. The results showed a small softening, or relaxation of maximum stress. This softening is matched in the combined hardening but ignored in the linear kinematic hardening model. However, the effect of cyclic relaxation was not considered in the FE simulations as other effects, such as creep, were of greater importance.
4. The creep behaviour of Al 2650 was tested at several temperatures by means of strain accumulation tension tests with several applied external loads plus stress relaxation tests with different initial applied strains. The experimental study considered the effect of prior plasticity. A primary creep power–law, with time hardening integration, was used to model creep in the FE analyses.
5. Axisymmetric FE simulations showed a through–thickness distribution where the compressive tangential stresses were very small at the entrance (inlet) face and near to the hole edge. There were small variations in the through–thickness direction far from the entrance face. The Bauschinger effect was modelled and consequently lower compressive tangential residual stresses were obtained when

compared to isotropic and kinematic models.

6. Two–dimensional models demonstrated that far field tensile uniaxial loads, even beyond one third of the yield stress, applied to cold expanded holes did not introduce additional plasticity as a combination of stress concentration and compressive residual stresses. The same simulation was repeated using three–dimensional models where cold expanded holes yielded near the entrance face and hole edge, where the compressive tangential residual stresses were smaller.
7. The application of compressive external loads redistributes and relaxes the residual stresses in the position normal to the loading direction. The tangential residual stress became tensile near the hole edge after the application of high compressive external loads.
8. The creep relaxation of residual stresses has been simulated successfully using FE analyses. Creep relaxes the tangential stresses near the hole edge. The relaxation was greater when no external load was applied. The relaxation did not affect the tangential residual stress distribution near the entrance face.
9. Stress intensity factors were evaluated from FE simulations of cracks of various lengths together with different residual stress distributions. Methods such as the *J*–integral, HRR stress fields and crack tip opening displacement (CTOD) were used to calculate the stress intensity factor (*K*). The *J*–integral calculation was path independent for non–cold expanded holes but path dependent for cases containing residual stresses. Through–thickness and corner cracks were examined using three–dimensional models and compared to two–dimensional models with the same CTOD, radial and angular mesh distribution. The results showed that there was a benefit of cold expansion when crack closure was obtained, and therefore a zero effective stress intensity factor was provided. This was not only a function of crack length and applied load but also a function of through–thickness position.

10. A prediction of crack opening was presented as a function of crack length and applied external load. The prediction was able to determine crack opening starting from the crack tip, followed by opening from the hole edge to obtain complete crack opening. This was also predicted from FE and experimental work.
11. The effect of creep on crack tip stresses was also studied. With the application of external load, crack tip stresses, *J*–integral and crack opening all increased with time as creep strains accumulated around the crack tip. For cold expanded holes the accumulation of creep strains did not allow crack closure to take place.
12. Fatigue crack growth was calculated from the stress intensity factors at different crack lengths using a Paris law equation. In all cases, cold expansion was predicted to give lower crack growth rates even after creep relaxation, when compared to non–cold expanded samples.
13. Fatigue life was predicted from the fatigue crack growth calculations using conventional S–N diagrams representing the number of cycles to failure as a function of applied nominal stress range. Longer lives were predicted for cold expanded specimens. For low applied stress ranges, the effective stress intensity factors were zero, and therefore crack arrest was also predicted. From two–dimensional simulations the longest life was predicted for cold expanded holes, then for cold expanded and crept with the application of external load, then for cold expanded and crept without external load. The shortest life was predicted for non–cold expanded holes and slightly longer for cold expanded holes after the application of compressive loads.
14. A new method based on Sachs boring for measuring two–dimensional non–axisymmetric residual stresses was developed. Several FE benchmarks were undertaken to demonstrate the validity of the Garcia–Sachs method. The conventional Sachs can not be used for measuring non–axisymmetric distributions.

15. Several experiments on cold expanded holes were carried out to compare with FEA predictions. A split–sleeve cold expanded hole was measured obtaining more compressive residual stresses near the pip of the sleeve position. These results were supported by X–ray surface measurements. Cold expanded holes after the application of creep, with and without external load, and cold expanded holes after the application of compressive load were also measured. In all cases a good agreement was found between the measurements and the predictions.
16. Further applications to non–cold expanded holes were examined with the Garcia–Sachs method. Two experiments were compared to FEA predictions for holes subjected to high loads to produce plasticity in the vicinity of the hole, and for holes subjected to load and high temperature to produce creep strain in the vicinity of the hole. In both cases a good agreement was found.

10.2. Recommendations for future work

Opportunities for future work can be identified in three main areas in this work: material identification, FE simulations and experimental residual stress measurements.

10.2.1. Experimental studies of Al 2650 aluminium alloy

1. Cold expansion is carried out at high strain rates. The literature suggests that the visco–elastic–plastic material properties would be different to those obtained at low strain rates. Further investigations should be undertaken to obtain the stress–strain behaviour as a function of strain rate, followed by the visco–elastic relaxation of residual stresses.

2. The Bauschinger effect is thought to be a consequence of large deformations in the axial direction as a consequence of the rolling process. Therefore, an accurate determination of the back–stress needs to be measured from tension–compression tests of specimens manufactured in the through–thickness direction. The thickness of the plate was only 15 mm and therefore a more detailed study is needed about how to carry out these tests with micro–specimens.
3. Creep has been measured for different temperatures. However the temperature was always constant throughout the test. More studies are required to simulate the transition between room temperature and higher temperatures (heating up) and the influence on creep strain accumulation combined with stress relaxation.
4. Creep strain accumulation tests were carried out in tension. More testing in compression would provide a strain correction taking into account the change of cross–section during testing, and therefore, producing better curve fitting to a creep power–law.

10.2.2. Finite elements studies

1. Three–dimensional simulations are required to simulate the effect of the opening of the split–sleeve while the mandrel is pulled through the hole. For this simulation it is believed that the friction between the sleeve and the hole edge may play an important role.
2. Application of external loads was simulated as remote stresses, while in reality the hole is meant for load transfer by means of the fasteners. Open holes were a conservative case for fatigue life prediction of cold expanded holes but this is not necessarily true for cases when creep is present. The influence of compressive loading should also be revised with the influence of the fastener.
3. Cracks have always been introduced in the model once the residual stresses were

present. Further studies of fatigue crack growth need to be undertaken to simulate the change of the fatigue crack front, redistribution of residual stresses during the growth and influence of the loading ratio (*R*). In these cases the influence of hold time at high temperature can also be studied obtaining more detailed fatigue and creep crack growth behaviour.

10.2.3. New experimental approach to Sachs boring

1. The formulation provided by Sachs for the measurement of 2D axisymmetric residual stresses has been extended to measure non–axisymmetric distributions. However this new method only measures stresses averaged through–thickness of the component. FE shows an important through–thickness variation, therefore a further study is required to obtain an approach able to measure a complete three–dimensional residual stress distribution.
2. The method may be extended to measure residual stresses minimising the damage to the samples. This would be achieved by avoiding the disc extraction and therefore measuring the strain change on entrance and exit faces directly. New formulation would be needed with a similar approach to the centre hole drilling technique.

REFERENCES

ABAQUS; (1999) "ABAQUS User's Manual, Version 5.8" *Hibbit, Karlson and Sorensen Inc.*, 1080 Main Street, Pawtucket, RI 02860–4847, U.S.A.

ABAQUS User Subroutines; (1997) "ABAQUS Course on Subroutines, 11/6/97" *Hibbit, Karlson and Sorensen Inc.*, Warrington, U.K.

Aktaa, J; and Schinke, B.; (1997) "Unified modelling of time dependent damage taking into account an explicit dependency on back–stress" *International Journal of Fatigue*, Vol.19, N.3, pp.195–200.

Anderson, A.T.; (1995) "Fracture Mechanics; Fundamentals and applications." *CRC Press*, London, U.K.

Armen,H.; Levy,A.; and Eidinoff,H.L.; (1984) "Elastic–plastic behaviour of cold worked holes" *Journal of Aircraft*, Vol.21, No.3, pp.193–201.

Arora, P.R.; and Simha, R.Y.; (1996) "Analytical and experimental evaluation of cold working process for strain hardening materials." *Engineering Fracture Mechanics*, Vol.53, No.3, pp.371–385.

Ashby, M.F.; and Frost, H.J.; (1982) "Deformation Mechanisms. The plasticity and creep of metal and ceramics." *Pergamon Press,* U.K.

ASTM; (1992) "Annual book of ASTM Standards, Metals–Mechanical testing." *ASTM* Vol. 03.01, 1916 Race Street, Philadelphia, PA 19103–1187, USA.

Atkinson,L.V.; Harley,P.J.;Hudson,J.D.; (1989) "Numerical Methods with Fortran 77" *International Computer Science Series.*

Ball, D.L.; (1994) "Elastic–plastic stress analysis of cold expanded fastener holes" *Fatigue and Fracture of Engineering Materials and Structures*, Vol.18, No.1 1995, pp. 47–63.

Ball, D.L.; and Lowry, D.R.; (1998) "Experimental investigation on the effect of cold expansion of fastener holes" *Fatigue and Fracture of Engineering Materials and Structures*, 1998, Vol.21, No.1, pp.17–34.

Bauschinger, J.; (1886) "Ueber die Veränderungen der Elastizitätsgreze und der

Festigkeit des Eisens und Stahls durch Strecken, Quetschen, Erwärmen Abkühlen und durch Oftmals Wiederholte Belastung" *Mitt: Mech–Tech Lab., XIII* München, Germany.

Becker, A.A.; Plant, R.C.A.; and Parker, A.P.; (1993) "Axial cracks in pressurised eroded autofrettaged thick cylinders" *International Journal of Fracture*, Vol. 63, pp.113–134.

Beeston, J.M.; and Burr, T.K.; (1979) "In–reactor stress relaxation of type 348 stainless steel in–pile tube" *Stress Relaxation Testing*, ASTM STP 676, Alfred Fox Ed., ASTM, 1979, pp.155–170.

Bell, P.D.; and Creager, M.; (1974) "Crack growth for arbitrary spectrum loading" *Air Force Federal Defence Laboratory, AFFDL–TR–74–129*, October 1974.

Bernard, M.; Bui–Quoc, T.; and Burlat, M.; (1995) "Effect of re–coldworking on fatigue life enhancement of a fastener hole" *Fatigue and Fracture of Engineering Materials and Structures*, Vol.18, No.7/8 1995, pp. 765–775.

Biscaya, J.M. de A.; (1971) "Influence of plastic prestrain on the creep behaviour of an Al 2.5%Cu, 1.25% Mg alloy" *MSc Thesis* London University Imperial college, UK.

Blankenship, C.P. Jr.; and Kaisand,L.R.; (1996) "Elevated temperature fatigue crack propagation behaviour of an Al–Li–Cu–Mg–Ag–Zr alloy" *Scripta Materialia*, Vol.34,, No.9, pp.1455–1460.

Bonnafé,J.P.; Destandau,C.; and Fougeras,J.; (1996) "Age creep forming process modelling and experimentation in aluminium alloys. Validation on arianne 5 main tank bulkheads." *Proceedings of the Fourth European Conference on Residual Stresses*, Cluny en Bourgogne, France, 4–6 June 1996, pp. 823–828.

Bourke, M.A.M.; MacGillivray, H.J.; Webster, G.A.; and Webster, P.J.; (1991) "Residual stress distribution in cracked autofrettaged tubing" *Proceedings of the NATO Advanced Research Workshop on Measurement of Residual and Applied Stress using the Neutron Diffraction*, Oxford, UK, 18–22 March 1991, pp. 481–493.

Boyle, J.T.; and Spence, J.; (1983) "Stress analysis for creep" *Butterworths*, Southampton, U.K.

Brinksmeier,E.; Scholtes,B.; and Wohlfahrt,H.; (1994) “Residual stresses in advanced surface finishing and joining” *Proceedings of the Fourth International Conference on Residual Stresses*, Baltimore, USA, 8–10 June 1994, pp. 579–588.

Carpinteri, A.; Brighenti, R.; and Spagnoli, A.; (1999a) "External longitudinal part–through flaw in an internaly pressurised pipe" *Proceedings of the Seventh International Fatigue Congress*, Beijing, China, 1999, p.2397–2402.

Carpinteri, A.; Brighenti, R.; and Spagnoli, A.; (1999b) "Fatigue behaviour of cracked pipes under rotatory bending" *Proceedings of the Seventh International Fatigue Congress*, Beijing, China, 1999, p.2431–2435.

Chen, K.L.; Kuo, A.Y.; and Shvarts, S.; (1991) "Stress intensity factor solutions for partial elliptical surface cracks in cylindrical shafts" *Proceedings of the 23rd Symposium on Fracture Mechanics*, Texas, USA, 18–20 June 1991, pp.396–416.

Chen, P.C.T.; (1986) “The Bauschinger and hardening effect on residual stresses in an autofrettaged thick–walled cylinder” *Journal of Pressure Vessel Technology*, February 1986, Vol. 108, pp.108–112.

Cook, R.; and Holdway, P.; (1993) “Residual Stresses Induced by Hole Cold Expansion” *Computer Methods and Experimental Measurements for Surface Treatment Effects*, pp.91–100.

Cook, R.; Holdway, P.; and Bowen, A.W.; (1994) “Residual stresses distribution and fatigue properties of aluminium–litium 8090 5 mm. plate containing plain and cold–expanded fastener holes” *Proceedings of the Fourth International Conference on Residual Stresses*, Baltimore, USA, 8–10 June 1994, pp. 1046–1054.

Coppola, T.; Bianchi, J.H. and Bufalini, A.; (1996) “Evaluation of residual stresses in cold drawn tubes” *Proceedings of the Fourth European Conference on Residual Stresses*, Cluny en Bourgogne, France, 4–6 June 1996, pp. 475–483.

Dietrich,G.; and Potter, J.M.; (1977) “Measurements on cold worked fastener holes” *Advances in X–Ray Analysis*, Vol. 20, pp.321–328.

Duprat, D.;Campassens, D.;Balzano, M.; and Boudet, R.; (1996) “Fatigue life prediction of interference fit fastener and cold worked holes.” *International Journal of Fatigue*, Vol.18, No.8, pp.515–521.

Dusi, A.; Novati, G.; Vitali, R.; and Zanotelli, G.L.; (1993) "Fracture propagation using the cohesive crack model with ABAQUS" *ABAQUS users' conference proceedings*, Aachen Germany, 23–25 June 1993,pp.181–190.

Edwards,L.; and Özdemir,A.T.; (1991) "Residual stresses at cold expanded fastener holes" *Proceedings of the NATO Advanced Research Workshop on Measurement of Residual and Applied Stress using the Neutron Diffraction*, Oxford, UK, 18–22 March 1991, pp. 545–553.

Edwards,L.; and Wang,D.Q.; (1996) "Neutron diffraction of the complete 3D residual stress distribution surrounding a cold expanded hole" *Proceedings of the Fourth European Conference on Residual Stresses*, Cluny en Bourgogne, France, 4–6 June 1996, pp. 619–626.

Edwards, L.; Wang, D.Q.; Johnson, M.W.; Wright, J.S.; Priesmeyer, H.G.; Rustichelli, F.; Albertini, G.;Withers, P.J.; and Harris, I.B.; (1994) "Precise measurement of internal stresses within materials using pulsed neutrons, (PREMIS)" *Proceedings of the Fourth International Conference on Residual Stresses*, Baltimore, USA, 8–10 June 1994, pp. 220–229.

Eigenmann,B.; Schulze,V.; and Vöhringer,O.; (1994) "Surface residual stress relaxation in steels by thermal or mechanical treatment" *Proceedings of the Fourth International Conference on Residual Stresses*, Baltimore, USA, 8–10 June 1994, pp. 598–607.

Evans, R.W.; and Wilshire, B.; (1985) "Creep of metals and alloys" *Dotesios Printers Ltd.*, Bradford–on–Avon, Wiltshire., U.K.

Ezeilo, A.N.; Webster, P.S.; Webster, G.A.; Webster, P.J.; (1994) "Influence of cyclic loading on residual stress distribution caused by cold hole expansion" *Proceedings of the Fourth International Conference on Residual Stresses*, Baltimore, USA, 8–10 June 1994, pp.1275–1284.

Fookes, A.J.; (1996) "Creep and creep–fatigue crack initiation and growth in stainless steel" *MSc Thesis*, Department of Mechanical Engineering, University of Bristol, Bristol, U.K.

Forgues, S.A.; Bernard, M. and Bui–Quoc, T.; (1993) "3D axisymmetric numerical analysis and experimental study of the fastener hole coldworking process" *Computer Methods and Experimental Measurements for Surface Treatment Effects*, Computational Mechanics Publications, Southampton, U.K., pp.61–70.

FTI; (1991) "Extending the fatigue life of metals structures" *Materials Testing, Fatigue Technology Inc.*, 150 Andover Park West, Seattle, Washington, U.S.A.

Gallagher,R.H.; (1978) "A review of finite element techniques in fracture mechanics" *Proceedings of the First International Conference on Numerical Methods in Fracture Mechanics*, Swansea, UK, 1978, pp.1–25.

García–Granada, A.A.; (1996) "Deep hole drilling as a method of measuring residual stresses: Theoretical development" *Fourth Year Project, Department of Mechanical Engineering*, University of Bristol, Bristol, U.K.

García–Granada, A.A.; (1998a) "The influence of combined thermal and mechanical cyclic loading in fatigue improvement methods for advanced supersonic transport light alloys" *First Year Report, Department of Mechanical Engineering*, University of Bristol, Bristol, U.K.

García–Granada, A.A.; George, D.; and Smith, D.J.; (1998b) "Assessment of distortions in the deep hole technique for measuring residual stresses" *Proceedings of the 11th International Conference on Experimental Mechanics*, Oxford, U.K., 24–28 August 1998,pp. 1301–1306

García–Granada, A.A.; Lacarac, V.; Smith, D.J.; Pavier, M.J.; (2000c) "3D residual stresses around cold expanded holes after creep" *Journal of Applied Mechanics, Transcations of ASME,* submitted for publication.

García–Granada, A.A.; Lacarac, V.; Smith, D.J.; Pavier, M.J.; (2000b) "A new procedure based on Sachs boring for measuring non–axisymmetric residual stresses: Experimental application" *Journal of Mechanical Sciences,* in preparation.

García–Granada, A.A.; Lacarac, V.; Smith, D.J.; Pavier, M.J.; Cook, R.; and Holdway, P.; (1999a) "3D residual stresses around cold expanded holes in a new creep resistant aluminium alloy." *Proceedings of the 4th International Conference on Computer Methods and Experimental Measurements for Surface Treatment Effects*, pp.103–116, 20–22 September 1999, Assisi, Italy.

García–Granada, A.A.; Pavier, M.J.; and Smith, D.J.; (2000a) "A new procedure based on Sachs boring for measuring non–axisymmetric residual stresses" *Journal of Mechanical Sciences,* Vol. 42 pp.1027–1047.

García–Granada, A.A.; Smith, D.J.; Pavier, M.J.; (1999b) "Analysis for determining non–axisymmetric residual stresses" *Proceedings of the 5th European Conference on Residual Stresses*, 28–30 September 1999, Noordwijkerhout, The Netherlands.

Gincburg, J.C.; (1957) "Stress relaxation in metals" *Mashges*, Moscow, ex–U.S.S.R.

Grandt, A.F.; (1975) "Stress intensity factors for some through–cracked fastener holes." *International Journal of Fracture*, Vol.11, No.2, pp.283–294.

Grandt, A.F.; and Kullgren, T.E.; (1983) "Tabulated stress intensity factor solutions for flawed fastener holes" *Engineering Fracture Mechanics*, Vol.18, No.2, pp.435–451.

Greenwood, J.A.; (1989) "Exact formulae for stress around circular holes and inclusions" *International Journal of Mechanics and Science*, Vol.31, No. 3, pp. 219–227.

Hammouda, M.M.I.; Ahmad, S.S.E.; Seleem, M.H.; and Sallam, H.E.M.; (1998) "Fatigue crack growth due to two successive single overloads" *Fatigue & Fracture of Engineering Materials and Structures*, 1998, Vol.21, pp.1537–1547.

Hermann, R.; (1994) "Three–dimensional stress distribution around cold expanded holes in aluminium alloys" *Engineering Fracture Mechanics*, Vol.48, No.6, pp.819–835.

Hermann, R.; and Moffat, J.; (1991) "Experiments and analysis of the fatigue life improvement in fastener holes of aluminium lithium alloy 2091" *Proceedings of the Sixth International Al–Li conference*, Germany

Hermann, R.; and Reid, C.N.; (1991) "Experimental analysis of the stress distribution around cold expanded holes in thin sheets" *Proceedings on the Third International Conference in Residual Stresses, ICRS 3*, 23–26 July, Tokushima, Japan.

Hills, D.A.; Kelly, P.; Dai, D.N.; and Korsunsky, A.; (1996) "Solution of crack problems: The distributed dislocation techniques" *Kluiver Academic Publications*, The Netherlands.

Hinton,E.; (1980) "NAFEMS introduction to nonlinear finite element analysis" *NAFEMS.*

Holdway, P.; Cook, R.; and Bowen, A.W.; (1994a) "Residual stresses distribution and fatigue properties of aluminium–litium 8090 5 mm. plate containing plain and cold–expanded fastener holes" *Proceedings of the Fourth International Conference on Residual Stresses*, Baltimore, USA, 8–10 June 1994, pp. 1046–1054.

Holdway, P.; Cook, R.; and Bowen, A.W.; (1994b) "Mapping of residual stresses around fastener holes in high strength aluminium alloy" *Surface Engineering*, 1994, Vol.10, No.4, pp. 292–296.

Holister, G.S.; (1963) "Cyclic–stress reduction within pin–loaded lugs resulting from optimum interference fits: Discussion" *Proceedings of the Society of Experimental Stress Analysis*, Vol.20, No.2, pp.222–224.

Hospers, F.; and Vogelesang; (1975) "Determination of residual stresses in aluminium alloy sheet material" *Proceedings of the Society of Experimental Stress Analysis*, Vol.32, No.1, pp.107–110.

Hsu, Y.C.; and Forman,R.C.; (1975) "Elastic–Plastic analysis of an infinite sheet having a circular hole under pressure" *Journal of Applied Mechanics, Transactions of the ASME*, Vol.42, No. 2, pp.347–352.

Huston, R.J.; (1972) "Influence of plastic prestrain on the creep behaviour of an Al 2.5%Cu, 1.25% Mg alloy" *MSc Thesis* London University Imperial college, UK.

Hutchinson, J.W.; (1968) "Singular behaviour at the end of a tensile crack in a hardening material" *Journal of the mechanics and physics of solids*, Vol.16, pp.13–31.

Jahed, H.; and Dubey, R.N.; (1996) "Residual stresses calculation in autofrettage using variable material properties method" *Residual Stresses in Design, Fabrication, Assesment and Repair ASME* 1996, August 1997, Vol. 119, pp.264–273.

Jahed, H.; and Dubey, R.N.; (1997) "An axisymmetric method of elastic–plastic analysis capable of predicting residual stress field" *Journal of Pressure Vessel Technology*, August 1997, Vol. 119, pp.264–273.

Jones, M.R.; Dai, D.N.; Cook, R.; and Rayaprolu, D.B.; (1999) "The analysis of crack growth life from cold expanded holes using the distributed dislocation method" *Proceedings of the Seventh International Fatigue Congress*, Beijing, China, 1999, p.1207–1212.

Jupp, J.A.; and Price, H.J.; (1998) "Transport aircraft – a challenge for aluminium alloys for the 21st century" *The Aeronautical Journal*, Vol.102, N.1014, April1998, pp.181–188.

Kaguchi, H.; and Nikbin, K.M.; (1993) "Evaluation of fracture mechanics parameters using the ABAQUS virtual crack extension and a contour integral techniques" *ABAQUS users' conference proceedings*, Aachen Germany, 23–25 June 1993,pp.289–303.

Kang, K.J.; and Seol, S.Y.; (1996) "Measurement of residual stresses in a circular ring using the successive cracking method" *Journal of Engineering Materials and Technology*, Vol.118, pp217–223.

Kowalenski, Z.L.; Hayhurst, D.R.; and Dyson, B.S.; (1994) "Mechanisms–Based creep constitutive equations for an aluminium alloy" *The Journal of Strain Analysis*, Vol.29 N.4 1994, pp.309–316.

Lacarac, V.; (2000) "The experimental characterisation of residual stresses and fatigue crack growth in the vicinity of cold worked holes in Al 2650." *PhD Thesis, Department of Mechanical Engineering*, University of Bristol, Bristol, U.K.

Lacarac,V.; García–Granada, A.A.; Smith, D.J.; Pavier, M.J.; (1999) "Experimental measurement of non–axisymmetric residual stresses" *Proceedings of the 5th European Conference on Residual Stresses*, 28–30 September 1999, Noordwijkerhout, The Netherlands.

Lambert, J.W.; (1954) "A method of deriving residual stress equations" *Proceedings of the Society of Experimental Stress Analysis*, Vol.12, No.1, pp.91–96.

Lang, M.; and Marci, G.; (1999) "The influence of single and multiple overloads on fatigue crack propagation" *Fatigue & Fracture of Engineering Materials and Structures*, 1999, Vol.22, pp.257–271.

Lazzarin, P.; and Livieri, P.; (1997) "Different solutions for stress and strain fields in autofrettaged thick–walled cylinders" *International Journal of Pressure Vessels and Piping*, Vol. 71, pp.231–238.

Leftheris, B.P.; and Schwarz, R.; (1987) "Residual stresses in 2024–T81 aluminium using caustics and moire interferometry" *Journal of Aircraft*, Vol.24, No.7, pp.474–476.

Leon, A.; (1998) "Benefits of split mandrel coldworking." *International Journal of Fatigue*, Vol.20, No.1, pp.1–8.

Ligenza, S.J.; (1963) "Cyclic–stress reduction within pin–loaded lugs resulting from optimum interference fits" *Proceedings of the Society of Experimental Stress Analysis*, Vol.20, No.1, pp.21–28.

Lillamand, I.; and Barrallier, L.; (1996) "Phenomenological study of thermal relaxation of residual stresses resulting from shot–peening" *Proceedings of the Fourth European Conference on Residual Stresses*, Cluny en Bourgogne, France, 4–6 June 1996, pp. 465–474.

Lim, W.; Yoo, J.; and Choi, S; (1998) "The effects of concurrent cold–expansion and ring–indentation on the growth of fatigue cracks emanating from circular holes." *Engineering Fracture Mechanics*, Vol.59, No.5, pp.643–653.

Lin, X.B.; and Smith, R.A.; (1997) "Stress intensity factors for semi–elliptical internal surface cracks in autofrettaged thick–walled cylinders" *Journal of Strain Analysis*, 1997, Vol. 32, No. 5, pp. 351–363.

Lin, X.B.; and Smith, R.A.; (1998) "Fatigue shape analysis for corner cracks at fastener holes" *Engineering Fracture Mechanics*, Vol.59, No.1, pp.73–87.

Link, R.E.; and Sanford, R.J.; (1990) "Residual strains surrounding split–sleeve cold expanded holes in 7050–T651 aluminum" *Journal of Aircraft*, Vol.27, No. 7, July 1990, pp.599–604.

Liu, Y.; and Hong, Q.; (1994) "On the unloading solution by viscoplastic BEM of axisymmetric pressure vessels with three material hardening models." *International Journal of Pressure Vessels and Piping*, Vol. 58, pp.41–50.

Liu, X.; and Schajer, G.S.; (1997) "More reliable calculations for layer removal residual stress measurements" *Proceedings SEM Conference*, Bellevue, Washington, June 1997, pp.255–256.

Lu, Z.K.; and Weng, G.J.; (1996) “Multiaxial constitutive modeling of aircraft engine materials” *Finite Elements in Analysis and Design*, Vol.23, pp.319–332.

McNeill,W.A.; and Heston,A.W.; (1987) “Coldworking fastener holes – Theoretical analysis, methods of cold working, experimental results.” *Design, Process and Materials Selection, Proceedings of the ASM Conference on Residual Stress,* Cincinnati, Ohio, USA, 27–29 April 1987, pp.193–204.

Mack, D.R.; (1962) "Measurement of residual stress in disks from turbine–rotor forgings" *Proceedings of the Society of Experimental Stress Analysis,* Vol.19, No.1, pp.155–158.

Mann, J.Y.; Sparrow, J.G.; and Beaver, P.W.; (1989) “Fatigue characteristics of joints with holes cold–expanded in a multi–layer stack” *International Journal of Fatigue,* Vol. 11,N. 4,pp. 214–220.

Martínez, S.; (1998) “Elastic–plastic–creep behaviour of Al 2650” *Final Year Project,* Department of Mechanical Engineering, University of Bristol, Bristol, U.K.

Megahed, M.M.; (1990) “Influence of hardening rule on prediction of cyclic plasticity in pressurized thin tubes subjected to cyclic push–pull” *International Journal of Mechanical Sciences,* Vol. 32,N. 8,pp. 635–652

Megahed, M.M.; and Abbas, A.T.; (1991) “Influence of Reverse Yielding on Residual Stresses Induced by Autofrettage” *International Journal of Mechanical Sciences,* Vol. 33,N. 2,pp. 139–150.

Melan, E.; (1932) "Der Spannungszustand der durch eine Einzelkraft im Innern beanspruchten Halbscheibe" *Zeitschrift für angenwandte Mathematik und Mechanik,* Vol.12, 1932, p.343.

Meleshko, V.V.; (1995) "Equilibrium of elastic rectangle: Mathieu–Inglis–Pickett solution revisited" *Journal of Elasticity,* Vol. 40, 1995, pp.207–238.

Metals Handbook; (1987) “Vol. 2. Properties and selection: Nonferrous alloys and Pure” *American Society for Metals (ASM),* Metals Park, OHIO 44073, U.S.A.

Michell, J.H.; (1899) "Determination of stress in an elastic solid" *Proceedings of the London Mathematical Society,* Vol.31, 1899, p.100–124.

Miller, J.A.; (1946) "A fixture for compressive test of thin sheet metal between laminated steel guides" *National Advisory Committee for Aeronautics. Technical note n. 1022*, NACA.

Milligan, R.V.; (1970) "The influence of the Bauschinger effect on reverse yielding of thick–walled cylinders" *Technical Report, WVT–7036, Benet R&E Lab.*, New York, U.S.A.

Moore, T.K.; (1978) "The influence of the hole processing and joint variables on the fatigue life of shear joints" *Air Force Materials Laboratories AFML–TR–77–167* Vol. 1, Wright–Patterson Air Force Base, Ohio, U.S.A.

Nikbin, KM; Smith, DJ; Webster, GA; (1986) "An engineering approach to the prediction of creep crack growth" *Journal of Engineering Materials and Technology*, Vol.108, pp.186–191.

Nishimura, T.; (1978) "Analysis of axially symmetrical residual stresses in bars and tubes" *Proceedings of the Society of Experimental Stress Analysis*, Vol.35, No.1, pp.180–184.

Özdemir,A.T.; Cook,R.; and Edwards,L.; (1993) "Residual stress distributions around cold–expanded holes." *Procedings of the17th Symposium of the Internatinal Committee on Aeronautical Fatigue*, Stockolm, 1993.

Özdemir, A.T.; and Edwards, L.; (1996) "Measurements of the three–dimensional residual stress distribution around split–sleeve cold–expanded holes" *Journal of Strain Analysis*, Vol.31 N.6 1996, pp.413–421.

Özdemir,A.T.; and Edwards,L.; (1997) "Relaxation of residual stresses at cold–worked fastener holes due to fatigue loading" *Fatigue and Fracture of Engineering Materials and Structures*, Vol.20, No.10, pp. 1443–1451.

Özdemir, A.T.; Wang, D.Q. and Edwards, L.; (1994) "Measurements of the three–dimensional residual stress distribution around split–sleeve cold–expanded holes" *Proceedings of the Fourth International Conference on Residual Stresses*, Baltimore, USA, 8–10 June 1994, pp. 1144–1153.

Papanikos, P.; and Meguid, S.A.; (1998) "Three–dimensional analysis of cold expansion of adjacents holes." *International Journal of Mechanical Sciences*, Vol.40, No.10, pp.1019–1028.

Parker, P.A.; (1981) “Linear elastic fracture mechanics and fracture crack growth. Residual stress effect.” *Proceeding of the Twenty–eigth Sagamore army materials research conference entitled residual stress and stress relaxation*, Lake Placid, New York, USA, 13–17 July 1981, pp. 249–269.

Parker, A.P.; Plant, R.C.A.; and Becker, A.A.; (1991) "Fatigue lifetimes for pressurized, eroded, cracked, autofrettaged thick cylinders" *Proceedings of the 23rd Symposium on Fracture Mechanics*, Texas, USA, 18–20 June 1991, pp.461–473.

Pavier, M.J.; Poussard, C.P; and Smith, D.J.; (1995) “A finite element simulation of cold working process for fastener holes” *Journal of Strain Analysis*, Vol.32, N.4, pp287–300.

Pavier, M.J.; Poussard, C.P; and Smith, D.J.; (1998) “Finite element modelling of the interaction of residual stress with mechanical load for a crack emanating from a cold worked fastener hole” *Journal of Strain Analysis*, Vol.33, N.4, pp275–289.

Pavier, M.J.; Poussard, C.P; and Smith, D.J.; (1999) "Effect of residual stress around cold worked holes on fracture under superimposed mechanical load" *Engineering Fracture Mechanics*, Vol.63, pp.751–773

Pell,R.A.; Beaver,P.W.;Man,J.Y.; and Sparrow,J.G.; (1989) “Fatigue of thick section cold–expanded holes with and without cracks” *Fatigue and Fracture of Engineering Materials and Structures*, 1989, Vol.12, No.6, pp.553–567.

Petrak, G.J.; and Stewart, R.P.; (1974) “Retardation of cracks emanating from fastener holes” *Engineering Fracture Mechanics*, Vol. 6, 1974, pp.275–282.

Petrucci, G.; and Zuccarello, B.; (1998) “A new calculation procedure for non–uniform residual stress analysis by the hole–drilling method” *Journal of strain analysis*, 1998, Vol. 33, No. 1, pp. 27–37.

Pickard,A.C.; (1986) “The application of 3–dimensional finite element methods to fracture mechanics and fatigue life prediction” *Engineering Materials Advisory Services Ltd.*, printed by Chameleon Press Ltd., London, U.K.

Pintschovius, L.; Macherauch, E.; and Scholtes, B.; (1986) "Determination of residual stresses in autofrettaged steel tubes by neutron and X–ray diffraction"

Proceedings of the International Conference on Residual Stresses, Garmisch–Partenkirchen, Germany, 1986, pp.159–166.

Polmear, I.J.; Pons, G.; Octor, H.; Sánchez, C.; Morton, A.; Borbidge, W.; and Rogers, S.; (1996) "After Concorde: Evaluation of an Al–Cu–Mg–Ag alloy for use in the proposed European SST" *Materials Science Forum*, Vols.217–222 1996, pp.1759–1764.

Poussard, C.G.C.; (1995) "An analysis of residual stresses and fatigue behaviour of cracks emanating from cold worked fastener holes" *PhD Thesis*, Department of Mechanical Engineering, University of Bristol, Bristol, U.K.

Poussard, C.P.; Smith, D.J.; and Pavier, M.J.; (1995) "Analytical and finite element predictions of residual stresses in cold–worked fastener holes" *Journal of Strain Analysis for Engineering Design*, 1995, Vol.30, No.4, pp.291–304.

Priest, M.; (1997) "The experimental characterisation of residual stresses and fatigue crack growth in the vicinity of cold worked holes in Al2024–T351." *PhD Thesis*, Department of Mechanical Engineering, University of Bristol, Bristol, U.K.

Priest, M.; Poussard, C.P.; Pavier, M.J.; and Smith, D.J.; (1994) "An assessment of measured and predicted residual stresses around cold worked holes in Al 2024" *Proceedings of the Fourth International Conference on Residual Stresses*, Baltimore, USA, 8–10 June 1994, pp. 324–332.

Priest, R.; (1980) "Life prediction during creep/fatigue." *PhD Thesis*, Department of Mechanical Engineering, University of Bristol, Bristol, U.K.

Prime, M.B.; Prantil, V.C.; Rangaswamy, P.; and Garcia, F.P.; (1999) "Residual stress measurement and prediction in a hardened steel ring" *Proceedings of the 5th European Conference on Residual Stresses*, 28–30 September 1999, Noordwijkerhout, The Netherlands.

Rasouli Yazdi, S.; Retraint, D.; and Lu, J.; (1998) "Study of through–thickness residual stress by numerical and experimental techniques." Journal of strain analysis, 1998, Vol. 33, No. 6, pp. 449–458.

Reid, L.; Marrese, V.; and Easterbrook, E.T.; (1997) "Residual stress analysis of cold expanded bushings" *Proceedings of the19th Symposium of the International*

Committee on Aeronautical Fatigue, Edinburgh, 18–20 June 1997, pp.871–882.

Reid,L.; (1997) “Terminating repair or resizing of damaged/discrepant holes using expanded bushings” *Proceedings of the USAF Aircraft Structural Integrity Program Conference*, San Antonio, Texas, USA, 2–4 December, 1997

Rice, J.R.; (1968) "A path independent integral and the approximate analysis of strain concentrations by notches and cracks" *Journal of Applied Mechanics*, Vol.35, pp.379–386.

Rice, J.R.; and Resengren, G.F.; (1968) "Plane strain deformation near a crack tip in a power hardening material" *Journal of the Mechanics and Physics of Solids*, Vol.16, pp.1–12.

Rich, D.L.; Impellizzeri, L.F.; (1977) “Fatigue analysis of cold–worked and interference fit fasteners holes” *Cyclic Stress–Strain and Plastic Deformation Aspects of Fatigue Crack Growth, ASTM STP 637*, pp.153–175.

Rudd, J.L.; Hsu, T.M.; and Aberson, J.A.; (1978) "Analysis and correlation of crack growth from interference–fit fastener holes" *Proceedings of the First International Conference on Numerical Methods in Fracture Mechanics*, Swansea, UK, 1978, pp.774–786

Rufin,A.C.; (1993) “Extending the fatigue life of aircraft engine components by hole cold expansion technology” *Journal of Engineering for Gas Turbines and Power*, Vol.115, pp.165–171.

Sachs, G.; (1927) “Der Nachweis Innerer Spannungen in Stange und Rohren” *Zeitschrift für Metalkunde*, Vol.19, pp. 352–357.

Sachs, G.; and Hoffman, O.; (1953) “Theory of Plasticity” *McGraw Hill International Editions*, London, U.K.

Sanford, R.J.; and Link, R.E.; (1989) “Holographic measurements of the elastic–plastic boundary surrounding cold–expanded holes” *Journal of Strain Analysis*, Vol.24, No.2, 1989, pp.103–106.

Savin, G.N.; (1966) “Stress distribution around holes” *Institute of Mechanics Kiev*, ex–USSR, translated by NASA TT F–607.

Segerfröjd, G.; and Blom, A.F.; (1999) "Fatigue behaviour of mechanical joints: a state–of–the–art overview" *Proceedings of the Seventh International Fatigue Congress*, Beijing, China, 1999, p.40–56.

Schindler,H.J.; and Landolt,R.; (1996) "Experimental determination of residual stresses and the resulting stress intensity factors in rectangular plates" *Proceedings of the Fourth European Conference on Residual Stresses*, Cluny en Bourgogne, France, 4–6 June 1996, pp. 509–517.

Sharman, D.J.; Stark, H.L.; and Kelly, D.W.; (1997) "Benchmarking of a destructive technique to determine residual stresses in thick–walled axisymmetric components" *Journal of Strain Analysis*, 1997, Vol. 32, No. 2, pp. 87–96.

Smith, D.J.; Leggatt, R.H.; Webster, G.A.; MacGillivary, H.J.; Webster, P.J.; and Mills, G.; (1988) "Neutron diffraction measurements of residual stress and plastic deformation in an aluminium alloy weld" *Journal of Strain Analysis*, Vol.23, N.4, pp201–211.

Smith, D.J.; Poussard, C.P.; and Pavier, M.J.; (1998) "An assessment of Sachs method for measuring residual stresses in cold worked fastener holes" *Journal of Strain Analysis*, Vol.33, No.4, pp.263–274.

Stacey, A; MacGillivary, H.J.; Webster, G.A.; Webster, P.J.; and Ziebeck, K.R.A.; (1985) "Measurement of residual stress by neutron diffraction" *Journal of Strain Analysis*, Vol.20, N.2, pp93–100.

Stack,C.P.;and Stephens,R.I.; (1989) "Effect of split–sleeve cold–expansion on the fatigue resistance of hot rolled 1020 steel" *International Journal of Fatigue*,Vol.11, N.5, pp.327–334.

Steinberg, L.G.; (1994) "Inverse spectral problems for inhomogeneous elastic cylinders" *Journal of Elasticity*, Vol. 38, 1995, pp.133–151.

Sternberg, E; and Sadowsky, M.A.; (1949) "Three–dimensional solution for the stress concentration around a circular hole in a plate of arbitrary thickness" *Journal of Applied Mechanics*, Vol.20, pp27–380.

Su, X.; Gu,M. and Yan,M.; (1986) "A simplified residual stress model for predicting fatigue crack growth behaviour at coldworked fastener holes" *Fatigue and Fracture of Engineering Materials and Structures*, 1986, Vol.9, No.1, pp.57–61.

Suresh,S.; (1991) "Fatigue of materials" *Cambridge University Press*, U.K.

Tait, R.B.; and Newberry, C.L.; (1996) "Evaluation of residual stresses around cold worked fastener holes using air abrasive hole drilling" *Proceedings of the Fourth European Conference on Residual Stresses*, Cluny en Bourgogne, France, 4–6 June 1996, pp. 203–211.

Throop,J.F.; Underwood,J.H.; and Leger, G.S.; (1981) "Thermal relaxation in autofrettaged cylinders" *Proceeding of the Twenty–eigth Sagamore army materials research conference entitled residual stress and stress relaxation*, Lake Placid, New York, USA, 13–17 July 1981, pp. 205–225.

Timoshenko, S.P.; and Goodier, J.N.; (1987) "Theory of Elasticity" *McGraw Hill International Editions*, London, U.K.

Tinpe, A.; (1923) "Die Airysche Funktion für den Ellipsenring" *Mathematische Zeitschrift*, Vol.17, 1923, p.189–205.

Vörhinger, O.; (1983) "Abbau von Eigenspannungen" *Eigenspannungen, Messung–Bewertung–Entstehung,* Vol.1, p.49–83, 1983

Voyiadjis,G.Z.; Kiousis,P.D.; and Hartley, C.S.; (1985) "Analysis of Residual Stresses in Cylindrically Anisotropic Materials" *Proceedings for the Society of Experimental Mechanics*, Vol. XLII, 1985, pp.145–147.

Wanlin, G.; (1993) "Elastic–plastic analysis of a finite sheet with a cold–worked hole" *Engineering Fracture Mechanics*, Vol.45, No.6, pp.857–886.

Webster, G.A.; (1991) "Role of neutron diffraction in engineering stress analysis" *Proceedings of the NATO Advanced Research Workshop on Measurement of Residual and Applied Stress using the Neutron Diffraction*, Oxford, UK, 18–22 March 1991, pp. 21–35.

Weiss, V.; (1957) "Residual stresses in cylinders" *Proceedings of the Society of Experimental Stress Analysis*, Vol.15, No.2, pp.53–56.

Yelon, W.B.; and Ross, F.K.; (1991) "Neutron diffraction" *Metals Handbook, Materials characterization*, Vol.10, pp.420–426.

PUBLISHED WORK – ABSTRACTS

Journal publications

García–Granada, A.A.; Pavier, M.J.; and Smith, D.J.; 2000a "A new procedure based on Sachs boring for measuring non–axisymmetric residual stresses" *Journal of Mechanical Sciences*, Vol. 42 pp.1027–1047.

Abstract: Sachs boring is an established technique for the measurement of axisymmetric residual stresses in cylindrical components. There are however important cases where non–axisymmetric residual stresses need to be found. In this paper a new procedure is developed to measure non–axisymmetric residual stresses. The essential feature of the new procedure is the use of a Fourier series to represent the residual stresses. The correctness of the new procedure is demonstrated using a finite element simulation where a set of non–axisymmetric residual stresses are determined. Excellent agreement is found between the predicted and measured residual stresses.

García–Granada, A.A.; Pavier, M.J.; and Smith, D.J.; 2000c "Creep relaxation of residual stresses around cold expanded holes" *Journal of Applied Mechanics, Transactions of ASME*, Submitted for publication.

Abstract: The cold expansion of fastener holes in aircraft components is a standard technique to improve fatigue life. There is concern that the beneficial residual stresses arising from cold expansion may relax due to creep, particularly in aircraft subjected to higher temperatures. This paper describes experimental measurement and finite element prediction of cold expansion residual stresses and their redistribution after creep, with and without additional mechanical load.

experimental measurements of near–surface stresses used an X–ray diffraction technique while average through–the–thickness stresses were measured using a new method based on Sachs boring. This new method allowed non–axisymmetric residual stresses to be measured, as was the case when creep relaxation occurred under mechanical load. Axisymmetric and three–dimensional finite element analyses were used to predict the stress distribution through–thickness of the component. a combined hardening material model was adopted to match closely the cyclic properties of the material. Power–law equations were used to the creep behaviour. Good agreement was found between predicted and measured residual stresses for cold expanded samples before and after creep relaxation. Creep relaxation of residual stresses does indeed occur, but some benefit of the cold expansion remains, particularly when creep relaxation is combined with the application of mechanical load.

García–Granada,A.A.; Lacarac, V.D.; Smith, D.J.; Pavier, M.J.; 2000b "A new procedure based on Sachs boring for measuring non–axisymmetric residual stresses : Experimental application" *Journal of Mechanical Sciences,* Vo.42 pp. 1027–1047.

Abstract: A new procedure has been developed based on Sachs boring to measure non–axisymmetric residual stresses in cylindrical components. The new procedure uses a Fourier series to represent the residual stresses. This paper describes an experimental application of the procedure to measure the residual stresses around a hole in a specimen subjected to a uniaxial overload. Good agreement is found between the measured residual stresses and those predicted using a finite element simulation.

Conference proceedings

García–Granada, A.A.; George, D.; and Smith, D.J.; 1998a "Assessment of distortions in the deep hole technique for measuring residual stresses" *Proceedings of the 11th International Conference on Experimental Mechanics*, Oxford, U.K., 24–28 August 1998,pp. 1301–1306

Abstract: The Deep Hole Technique for measuring residual stresses in thick section components is used to determine distributions of residual stresses, through–thickness, of a variety of welded steel components of varying geometric complexity. The technique relies on the measurement of the distortion of a reference hole drilled through the wall thickness. This paper presents recent developments in the analysis of the hole distortion. The measured distortions include diametrical changes in the reference hole, together with changes in height during the trepanning of a column containing the reference hole, and are converted to residual stresses using elasticity theory. FE analyses have also been carried out to determine the influence of near surface conditions for thick walled components. These results are then incorporated into the solution procedure.

García–Granada, A.A., Smith, D.J., and Pavier, M.J.; 1999b "Analysis for determining non–axisymmetric Residual Stresses" *Proceedings of the Fifth European Conference on Residual Stresses (ECRS5), 28–30 September 1999, Delft–Noordwijkerhout, Holland,*

Abstract: The Sachs boring technique is used widely to determine residual stresses in axisymmetric components. An example of such a component is an autofrettaged tube. The residual stress measurement technique is based on material removal from the inside of the cylindrical component and strain measurement at the outer face of the component. Several studies have attempted to use this standard method to determine residual stresses where the measured strains are non–axisymmetric. In this paper a new procedure to measure non–axisymmetric residual stresses is presented. The new method is based on a Fourier analyses of the measured strains. The analysis determines radial, tangential and shear tangential stresses as a function of angle and radial distance. The solutions provided can be applied to plane stress and plane strain conditions. The accuracy of the new method is checked using a FE simulation to generate a non–axisymmetric residual stress distribution. The material removal and strain readings are also simulated. Finally the residual stresses are calculated using both the conventional axisymmetric Sachs analysis and the new Fourier analysis. The new method determines accurately the non–axisymmetric residual stress distributions, while the conventional method provides only an average distribution. The figure below illustrates the tangential residual stress distribution using both techniques.

Lacarac, V.; García–Granada, A.A.; Smith, D.J.; and Pavier, M.J.; 1999 "Experimental measurements of non–axisymmetric Residual Stresses" *Proceedings of the Fifth European Conference on Residual Stresses (ECRS5)*, 28–30 September 1999, Delft–Noordwijkerhout, Holland.

Abstract: The conventional Sachs method and a new method using Fourier analysis are employed to measure non–axisymmetric residual stresses. Two examples of non–axisymmetric residual stresses are presented. The first is a highly non–axisymmetric residual stress distribution around a non–cold expanded hole exposed to creep conditions. The second example deals with residual stresses arising in a cold expanded hole. The two residual stress measurement techniques rely on strain measurements in tangential and/or axial directions at a given radial distance. The

Sachs method assumes that the residual stresses are symmetric, and consequently only one strain gauge is needed. However, for the new method the strain distribution at several angles is required. The angular strain measured, as a result of boring out the hole, for both examples were found to exhibit significant variations. The calculated residual stresses from both techniques are discussed and compared. The error introduced using Sachs method depends on the angular variation of the residual stresses. Not only can the conventional Sachs technique give erroneous residual stress magnitudes, but can also provide residual stresses of the opposite sign. The new method is shown to provide accurate results.

García–Granada, A.A.; Lacarac, V.; Smith, D.J.; Pavier, M.J.; Cook, R.; and Holdway, P.; 1999a "3D residual stresses around cold expanded holes in a new creep resistant aluminium alloy" *Proceedings of the Fourth International Conference on Computer Methods and Experimental Measurements in Surface Treatment (SURF99),* pp. 103–116, 20–22 September 1999, Assisi, Italy.

Abstract: Hole cold expansion is used frequently to enhance the fatigue endurance of components. The cold expansion process introduces compressive residual stress at the periphery of the hole and tensile stress further away. To understand how these residual stresses enhance the fatigue life, it is essential that we have an accurate description of the three–dimensional distribution of the stresses. In this paper we describe the results of experimental studies and finite element analyses used to determine detailed residual stress distributions in a new creep resistant alloy. The near surface residual stresses at the mandrel entrance and exit faces were measured using an X–ray diffraction technique. The results show significant differences between residual stresses at the two faces. The residual stresses are also shown to vary as a function of position around the hole. To take account of this variation a new approach, called the Garcia–Sachs method, was used to measure residual stress averaged through–thickness of the component. For finite element simulations, a combined hardening material model was used to reproduce the Bauschinger effect exhibited by the aluminium alloy. Using this new model, excellent agreement was found between predicted and measured near surface residual stresses. Finally there is also good agreement between the measured mid–thickness residual stress and the FE predictions.

APPENDIX

Appendix A
Garcia–Sachs equations

This appendix presents a collection of equations developed to measure residual stresses. The method is based on the Sachs boring technique and therefore these equations are also included. As explained in Chapter 8, a Fourier analysis was carried out and the conventional Sachs was found to form the first coefficient of the series. For each coefficient, the stress function, the strain measured, the equilibrium equations and finally the solution for residual stresses are given. The solutions are valid for two–dimensional cases where the material constant M is the Young's modulus E for plane stress and $E/(1-\nu^2)$ *for plane strain.*

A.1. Conventional Sachs: n=0

Stress function:

$$\phi^{n=0}(r) = Ar^2 + B\,log(r) \tag{A.1}$$

Strain measured at $r=b$:

$$\Delta\varepsilon_{\theta\theta}{}^{n=0}(r)]_{r=b} = \varepsilon^{n=0} = \frac{\sigma_{rr}{}^{n=0}(r)}{M}\left[\frac{2r^2}{b^2-r^2}\right] \tag{A.2}$$

Solution to radial and shear residual stresses on the disc plus equilibrium equation:

$$\left\{\begin{array}{l} \sigma_{rr}{}^{n=0}(r) = M\left[\dfrac{b^2 - r^2}{2r^2}\right]\varepsilon^{n=0} \\ \tau_{r\theta}{}^{n=0}(r) = 0 \\ \sigma_{\theta\theta}{}^{n=0}(r) = \dfrac{\partial r\sigma_{rr}{}^{n=0}(r)}{\partial r} \end{array}\right\} \tag{A.3}$$

Solution to residual stresses relaxed due to disc extraction. The tangential strain must be measured on the inside of the hole, $r=a$:

$$\left\{\begin{array}{l} \Delta\sigma_{rr}{}^{n=0}(r) = M\left[\dfrac{r^2 - a^2}{2r^2}\right]\Delta\varepsilon_{\theta\theta}{}^{n=0}\,]_{r=a} \\ \Delta\sigma_{\theta\theta}{}^{n=0}(r) = M\left[\dfrac{r^2 + a^2}{2r^2}\right]\Delta\varepsilon_{\theta\theta}{}^{n=0}\,]_{r=a} \end{array}\right\} \tag{A.4}$$

A.2. First cosine/sine coefficient: n=1

Stress function:

$$\phi^{n=1}(r) = \left(Ar^2 + \frac{B}{r}\right) cos/\,sin(\theta) \tag{A.5}$$

Strain measured at $r=b$:

$$\Delta\varepsilon_{\theta\theta}{}^{n=1}(r)]_{r=b} = \varepsilon^{n=1} = \frac{\sigma_{rr}{}^{n=1}(r)}{M}\left[\frac{4br^3}{b^4 - r^4}\right] \tag{A.6}$$

Solution to radial and shear residual stresses on the disc plus equilibrium equation:

$$\left\{\begin{array}{l} \sigma_{rr}{}^{n=1}(r) = M\left[\dfrac{b^4 - r^4}{4br^3}\right]\varepsilon^{n=1} \\ \tau_{r\theta}{}^{n=1}(r) = \pm M\left[\dfrac{b^4 - r^4}{4br^3}\right]\varepsilon^{n=1} \\ \sigma_{\theta\theta}{}^{n=1}(r) = \dfrac{\partial r\sigma_{rr}{}^{n=1}(r)}{\partial r} \pm \tau_{r\theta}{}^{n=1}(r) = \pm\dfrac{\partial r\tau_{r\theta}{}^{n=1}(r)}{\partial r} \pm \tau_{r\theta}{}^{n=1}(r) \end{array}\right\} \tag{A.7}$$

A.3. Second cosine/sine coefficient: n=2

Stress function:

$$\phi^{n=2}(r) = \left(Ar^4 + Br^2 + \frac{C}{r^2} + D\right) cos/\,sin(2\theta) \tag{A.8}$$

Strain measured at $r=b$:

$$\Delta\varepsilon_{\theta\theta}{}^{n=2}(r)]_{r=b} = \varepsilon^{n=2} = \frac{\sigma_{rr}{}^{n=2}(r)\left(b^2 + r^2\right) \pm -\tau_{r\theta}{}^{n=2}(r)b^2}{M}\left[\frac{4r^2}{\left(b^2 - r^2\right)^2}\right] \tag{A.9}$$

Solution to radial and shear residual stresses on the disc plus equilibrium equation:

$$\left\{\begin{array}{l} \sigma_{rr}{}^{n=2}(r) = -M\left[\dfrac{b^2 - r^2}{4r^2}\right]\times \\ \times\left(\varepsilon^{n=2} - 6b^2\left(\dfrac{b^2 - r^2}{r^2}\right)\displaystyle\int_a^r \dfrac{r'\varepsilon^{n=2}}{\left(b^2 - r'^2\right)^2}\partial r'\right) \\ \tau_{r\theta}{}^{n=2}(r) = \pm - M\left[\dfrac{b^2 - r^2}{2r^2}\right]\times \\ \times\left(\varepsilon^{n=2} - 3\left(b^2 + r^2\right)\left(\dfrac{b^2 - r^2}{r^2}\right)\displaystyle\int_a^r \dfrac{r'\varepsilon^{n=2}}{\left(b^2 - r'^2\right)^2}\partial r'\right) \\ \sigma_{\theta\theta}{}^{n=2}(r) = \dfrac{\partial r\sigma_{rr}{}^{n=2}(r)}{\partial r} \pm 2\tau_{r\theta}{}^{n=2}(r) = \pm\dfrac{\partial r\tau_{r\theta}{}^{n=2}(r)}{2\partial r} \pm \dfrac{1}{2}\tau_{r\theta}{}^{n=2}(r) \end{array}\right\} \tag{A.10}$$

A.4. Third cosine/sine coefficient: n=3

Stress function:

$$\phi^{n=3}(r)=\left(Ar^5+Br^3+\frac{C}{r^3}+\frac{D}{r}\right)cos/\,sin(3\theta) \tag{A.11}$$

Strain measured at $r=b$:

$$\begin{aligned}&\Delta\varepsilon_{\theta\theta}{}^{n=3}(r)]_{r=b}=\varepsilon^{n=3}=\\&\frac{\sigma_{rr}{}^{n=3}(r)\left(3b^4+3b^2r^2+3r^4\right)\pm-\tau_{r\theta}{}^{n=3}(r)\left(3b^4+4b^2r^2-r^4\right)}{M}\times\\&\times\left[\frac{2br^3}{\left(b^4+4b^2r^2+r^4\right)\left(b^2-r^2\right)^2}\right]\end{aligned} \tag{A.12}$$

Solution to radial and shear residual stresses on the disc plus equilibrium equation:

$$\left\{\begin{aligned}&\sigma_{rr}{}^{n=3}(r)=-M\left[\frac{\left(b^2-r^2\right)\left(b^4+4b^2r^2+r^4\right)}{12br^3\left(b^2+r^2\right)}\right]\times\\&\times\left(\varepsilon^{n=3}-4\left(\frac{\left(b^4-r^4\right)\left(3b^4+b^2r^2-r^4\right)}{\left(b^4+4b^2r^2+r^4\right)r^2}\right)\int_a^r\frac{\left(b^4+4b^2r'^2+r'^4\right)r'\,\varepsilon^{n=3}}{\left(b^4-r'^4\right)^2}\partial r'\right)\\&\tau_{r\theta}{}^{n=3}(r)=\pm-M\left[\frac{\left(b^2-r^2\right)\left(b^4+4b^2r^2+r^4\right)}{4br^3\left(b^2+r^2\right)}\right]\times\\&\times\left(\varepsilon^{n=3}-4\left(\frac{\left(b^4-r^4\right)\left(3b^4+b^2r^2-r^4\right)}{\left(b^4+4b^2r^2+r^4\right)r^2}\right)\int_a^r\frac{\left(b^4+4b^2r'^2+r'^4\right)r'\,\varepsilon^{n=3}}{\left(b^4-r'^4\right)^2}\partial r'\right)\\&\sigma_{\theta\theta}{}^{n=3}(r)=\frac{\partial r\sigma_{rr}{}^{n=3}(r)}{\partial r}\pm3\tau_{r\theta}{}^{n=3}(r)=\pm\frac{\partial r\tau_{r\theta}{}^{n=3}(r)}{3\partial r}\pm\frac{1}{3}\tau_{r\theta}{}^{n=3}(r)\end{aligned}\right\} \tag{A.13}$$

A.5. Fourth cosine/sine coefficient: n=4

Stress function:

$$\phi^{n=4}(r)=\left(Ar^{6}+Br^{4}+\frac{C}{r^{4}}+\frac{D}{r^{2}}\right)cos/\,sin(4\theta) \tag{A.14}$$

Strain measured at $r=b$:

$$\begin{gathered}\Delta\varepsilon_{\theta\theta}{}^{n=4}(r)]_{r=b}=\varepsilon^{n=4}= \\ \frac{\sigma_{rr}{}^{n=4}(r)\left(2b^{6}+2b^{4}r^{2}+2b^{2}r^{4}+2r^{6}\right)\pm-\tau_{r\theta}{}^{n=4}(r)\left(2b^{6}+b^{4}r^{2}-r^{6}\right)}{M}\times \\ \left[\frac{2b^{2}r^{4}}{\left(b^{4}+2b^{3}r+4b^{2}r^{2}+2br^{3}+r^{4}\right)\left(b^{4}-2b^{3}r+4b^{2}r^{2}-2br^{3}+r^{4}\right)\left(b^{2}-r^{2}\right)^{2}}\right]\end{gathered} \tag{A.15}$$

Solution to radial and shear residual stresses on the disc plus equilibrium equation:

$$\left\{\begin{array}{l}
\sigma_{rr}{}^{n=4}(r)=-M\left[\dfrac{\left(b^{2}-r^{2}\right)\left(b^{4}+2b^{3}r+4b^{2}r^{2}+2br^{3}+r^{4}\right)\left(b^{4}-2b^{3}r+4b^{2}r^{2}-2br^{3}+r^{4}\right)}{8b^{2}r^{4}\left(3b^{4}+4b^{2}r^{2}+3r^{4}\right)}\right]\times \\
\times\left(\begin{array}{l}\varepsilon^{n=4}-30\left(\dfrac{\left(b^{2}-r^{2}\right)\left(2b^{6}+b^{4}r^{2}-r^{6}\right)\left(3b^{4}+4b^{2}r^{2}+3r^{4}\right)}{\left(b^{4}+2b^{3}r+4b^{2}r^{2}+2br^{3}+r^{4}\right)\left(b^{4}-2b^{3}r+4b^{2}r^{2}-2br^{3}+r^{4}\right)r^{2}}\right) \\ \displaystyle\int_{a}^{r}\frac{\left(b^{4}+2b^{3}r'+4b^{2}r'^{2}+2br'^{3}+r^{4}\right)\left(b^{4}-2b^{3}r'+4b^{2}r'^{2}-2br'^{3}+r'^{4}\right)r'\varepsilon^{n=4}}{\left(3b^{4}+4b^{2}r'^{2}+3r'^{4}\right)\left(b^{2}-r'^{2}\right)^{2}}\partial r'\end{array}\right) \\
\tau_{r\theta}{}^{n=4}(r)=\pm-M\left[\dfrac{\left(b^{2}-r^{2}\right)\left(b^{4}+2b^{3}r+4b^{2}r^{2}+2br^{3}+r^{4}\right)\left(b^{4}-2b^{3}r+4b^{2}r^{2}-2br^{3}+r^{4}\right)}{2b^{2}r^{4}\left(3b^{4}+4b^{2}r^{2}+3r^{4}\right)}\right]\times \\
\times\left(\begin{array}{l}\varepsilon^{n=4}-15\left(\dfrac{\left(b^{2}-r^{2}\right)\left(b^{2}+r^{2}\right)\left(b^{4}-r^{4}\right)\left(3b^{4}+4b^{2}r^{2}+3r^{4}\right)}{\left(b^{4}+2b^{3}r+4b^{2}r^{2}+2br^{3}+r^{4}\right)\left(b^{4}-2b^{3}r+4b^{2}r^{2}-2br^{3}+r^{4}\right)r^{2}}\right) \\ \displaystyle\int_{a}^{r}\frac{\left(b^{4}+2b^{3}r'+4b^{2}r'^{2}+2br'^{3}+r^{4}\right)\left(b^{4}-2b^{3}r'+4b^{2}r'^{2}-2br'^{3}+r'^{4}\right)r'\varepsilon^{n=4}}{\left(3b^{4}+4b^{2}r'^{2}+3r'^{4}\right)\left(b^{2}-r'^{2}\right)^{2}}\partial r'\end{array}\right) \\
\sigma_{\theta\theta}{}^{n=4}(r)=\dfrac{\partial r\sigma_{rr}{}^{n=4}(r)}{\partial r}\pm4\tau_{r\theta}{}^{n=4}(r)=\pm\dfrac{\partial r\tau_{r\theta}{}^{n=4}(r)}{4\partial r}\pm\dfrac{1}{4}\tau_{r\theta}{}^{n=4}(r)
\end{array}\right\} \tag{A.16}$$

A.6. General cosine/sine coefficient: n

Stress function:

$$\phi^n(r) = \left(Ar^{n+2} + Br^n + \frac{C}{r^n} + \frac{D}{r^{n-2}} \right) cos/\,sin(n\theta) \tag{A.17}$$

Strain measured at $r=b$:

$$\Delta\varepsilon_{\theta\theta}{}^n(r)]_{r=b} = \varepsilon^n = \frac{\sigma_{rr}{}^n(r)k_1(n,r) \pm \tau_{r\theta}{}^n(r)k_2(n,r)}{M} \tag{A.18}$$

Solution to radial and shear residual stresses on the disc plus equilibrium equation:

$$\left\{ \begin{array}{l} \sigma_{rr}{}^n(r) = M \times f(n,r) \times \left(\varepsilon^n + g_1(n,r) \int_a^r h(n,r')\varepsilon^n \partial r \right) \\ \tau_{r\theta}{}^n(r) = \pm M \times n \times f(n,r) \times \left(\varepsilon^n + g_2(n,r) \int_a^r h(n,r')\varepsilon^n \partial r \right) \\ \sigma_{\theta\theta}{}^n(r) = \dfrac{\partial r \sigma_{rr}{}^n(r)}{\partial r} \pm n\tau_{r\theta}{}^n(r) = \pm \dfrac{\partial r \tau_{r\theta}{}^n(r)}{n \partial r} \pm \dfrac{1}{n} \tau_{r\theta}{}^n(r) \end{array} \right\} \tag{A.19}$$

where k_1, k_2, f, g_1, g_2 and h are functions to be determined for each coefficient.

The equilibrium equation can be solved for both pressure and shear given the following relation:

$$\left\{ \begin{array}{l} \sigma_{rr}{}^n(r) = \pm \dfrac{1}{nr} \displaystyle\int_a^r r' \dfrac{\partial \tau_{r\theta}{}^n(r')}{\partial r'} - \left(n^2 - 1\right) \tau_{r\theta}{}^n(r') \partial r' \\ or \\ \tau_{r\theta}{}^n(r) = \pm n r^{n^2-2} \displaystyle\int_a^r \dfrac{\sigma_{rr}{}^n(r') + r \dfrac{\partial \sigma_{rr}{}^n(r')}{\partial r'}}{r'^{n^2-1}} \partial r' \end{array} \right\} \tag{A.20}$$

TABLES

Table 3.1. Typical properties for general aluminium alloys from Metals Handbook (1987).

Density, δ	2.7 Kg/dm^3
Modulus of Elasticity, *E*	70 GPa
Poissons Ratio, ν	0.33
Shear Modulus, *G*	26 GPa
Thermal expansion	2.4x10^{-5} K^{-1}
Melting Point	620 °C

Table 3.2. Aluminium alloy Al 2650 chemical composition.

	%Cu	%Mg	%Mn	%Si	%Fe	%Ti	%Al
Nominal	2.7	1.65	0.35	0.4	0.1	0.1	remainder
Actual	2.74	1.74	0.34	0.41	0.11	0.09	remainder

Table 3.3. Aluminium alloy Al 2650 tensile properties.

Tensile test at room temperature	E=72 GPa	σ_y=427 MPa	$\sigma_{4\%}$=448 MPa
Tensile test at 150°C	E=72 GPa	σ_y=348 MPa	$\sigma_{4\%}$=359 MPa

Table 3.4. Creep power–law fit for Al 2650.

Power–law creep $\varepsilon_c = C_c e^{-\frac{\Delta H}{RT}} \sigma^{n_c} t^{m_c}$	C_c=4x10^{-11} MPa$^{-n_c}$ s$^{-m_c}$	ΔH=10^5 J mol^{-1}	R=8.316 J mol^{-1} K^{-1}	m_c=0.32	n_c=7.5

Table 3.5. Paris law fit for Al 2650.

Paris law $\frac{\partial c}{\partial N} = C_f (\Delta K)^{m_f}$	C_f=4.928 10^{-8} mm cycle^{-1} (MPa √m)$^{-m_c}$	m_f=3.99

Table 4.1. Parameters for combined hardening model.

$$\dot{\alpha} = C\frac{1}{\sigma_0}(\sigma - \alpha)\dot{\varepsilon}^{pl} - \gamma\alpha\dot{\varepsilon}^{pl}$$

$$\sigma_o = \sigma|_o + Q_\infty\left(1 - e^{-b\varepsilon^{pl}}\right)$$

E **MPa**	ν	$\sigma\vert_0$ **MPa**	**C** **MPa**	γ	**Q$_\infty$** **MPa**	**b**	$\varepsilon^{pl}\vert_0$	$(\alpha\vert_{ox},\alpha\vert_{oy},\alpha\vert_{oz})$ **MPa**
72000	0.33	370	12500	120	–200	0.25	0.2	0,0,–100

Table 6.0. CPU time in seconds for FE calculation SIGINI residual stress map–in technique.

Residual Stress→ Crack type ↓	(a) ncw	(b) cwcp	(c) cwht	(d) cwcr	(e) cw
zero (0 mm) 2dzclsc– P.S.	72	91	550	752	76
2dzclec– P.E.	69	93	510	822	83
very short (0.25 mm) 2dvclsc– P.S.	204	244	863	909	175
2dvclec– P.E.	203	202	687	1136	123
short (1 mm) 2dsclsc– P.S.	200	232	857	979	110
2dsclec– P.E.	197	191	675	1163	120
medium (2 mm) 2dmclsc– P.S.	192	184	809	907	121
2dmclec– P.E.	183	137	642	981	120
long (3 mm) 2dlclsc– P.S.	112	160	823	892	141
2dlclec– P.E.	160	130	640	922	123
extra (4 mm) 2declsc– P.S.	114	175	841	942	150
2declec– P.E.	166	164	670	1008	153
zero (0 mm) 3dzclsc–	8371	12738	21114	33979	12636
corner (0x0 mm)					
veryshort (0.25 mm) 3dvclsc–	28990	22338	83120	107621	24636
corner (1x1 mm) 3dvccsc–	9584	24207	56251	231258	18155
short (1 mm) 3dsclsc–	28941	25306	78939	124080	15478
corner (1x1 mm) 3dsccsc–	12679	16883	61973	171967	21176
medium (2 mm) 3dmclsc–	30260	20750	74036	101537	18005
corner (2x2 mm) 3dmccsc–	15632	22054	56634	148324	13925
long (3 mm) 3dlclsc–	29030	31658	78834	114820	31589
corner (3x3 mm) 3dlccsc–	16109	16019	55293	136700	14813
extra (4 mm) 3declsc–	23111	28410	81788	118639	32966
corner (4x4 mm) 3deccsc–	15728	16021	55556	123903	16446
Crack type ↑ Residual Stress→	(a) ncw	(b) cwcp	(c) cwht	(d) cwcr	(e) cw

Table 6.1a. Veryshort cracks (c=0.25mm): 2D J [MPa mm] and $U_{\theta\theta}$ [μm] for ncw.

position→ σ_{app}↓	J2D P.S.	J2D P.E.	U2D P.S.	U2D P.E.	U3D entr	U3D mid	U3D exit	U3D $\psi=0$	U3D $\psi=45$	U3D $\psi=90$
14.33 MPa	0.01	0.01	0.01	0.01	0.01	0.01	0.01	0.006	0.005	0.007
71.67 MPa	0.40	0.38	0.07	0.05	0.05	0.07	0.05	0.03	0.03	0.03
107.5 MPa	0.98	0.93	0.24	0.22	0.18	0.25	0.18	0.05	0.04	0.08
143.3 MPa	1.87	1.67	0.64	0.59	0.43	0.69	0.43	0.11	0.09	0.15
215.0 MPa	5.50	4.12	3.89	2.70	1.65	3.23	1.65	0.29	0.34	0.39
286.7 MPa	11.88	7.90	10.47	6.28	4.54	6.82	4.54	0.52	0.65	0.69

Table 6.1b. Veryshort cracks (c=0.25mm): 2D J [MPa mm] and $U_{\theta\theta}$ [μm] for cwcp.

position→ σ_{app}↓	J2D P.S.	J2D P.E.	U2D P.S.	U2D P.E.	U3D entr	U3D mid	U3D exit	U3D $\psi=0$	U3D $\psi=45$	U3D $\psi=90$
14.33 MPa	0	0	0	0	0	0	0	0	0	0.001
71.67 MPa	0.09	0	0.04	0.02	0.02	0.03	0.02	0.01	0.01	0.02
107.5 MPa	0.49	0.21	0.13	0.04	0.04	0.07	0.04	0.02	0.02	0.03
143.3 MPa	1.09	0.65	0.34	0.16	0.13	0.22	0.10	0.03	0.03	0.05
215.0 MPa	3.35	2.05	2.09	1.16	0.32	1.31	0.29	0.06	0.08	0.09
286.7 MPa	7.18	4.44	5.79	3.36	0.43	3.18	0.39	0.09	0.11	0.12

Table 6.1c. Veryshort cracks (c=0.25mm): 2D J [MPa mm] and $U_{\theta\theta}$ [μm] for cwht.

position→ σ_{app}↓	J2D P.S.	J2D P.E.	U2D P.S.	U2D P.E.	U3D entr	U3D mid	U3D exit	U3D $\psi=0$	U3D $\psi=45$	U3D $\psi=90$
14.33 MPa	0	0	0	0	0	0	0	0	0	0
71.67 MPa	0	0	0	0	0.02	0	0	0.01	0.01	0.01
107.5 MPa	0.0001	0.0003	0.01	0.01	0.04	0.008	0.006	0.02	0.02	0.02
143.3 MPa	0.19	0.16	0.04	0.03	0.10	0.03	0.03	0.03	0.03	0.03
215.0 MPa	1.38	1.26	0.39	0.30	0.31	0.31	0.13	0.06	0.07	0.08
286.7 MPa	3.95	3.08	2.36	1.82	0.43	1.76	0.30	0.08	0.11	0.11

Table 6.1d. Veryshort cracks (c=0.25mm): 2D J [MPa mm] and $U_{\theta\theta}$ [μm] for cwcr.

position→ σ_{app}↓	J2D P.S.	J2D P.E.	U2D P.S.	U2D P.E.	U3D entr	U3D mid	U3D exit	U3D $\psi=0$	U3D $\psi=45$	U3D $\psi=90$
14.33 MPa	0	0	0	0	0	0	0	0	0	0
71.67 MPa	0	0	0	0	0.01	0	0	0.007	0.006	0.007
107.5 MPa	0	0	0	0	0.03	0	0	0.016	0.016	0.017
143.3 MPa	0.02	0.05	0.01	0.02	0.07	0.01	0.02	0.025	0.025	0.028
215.0 MPa	0.72	0.77	0.13	0.16	0.27	0.12	0.08	0.05	0.06	0.07
286.7 MPa	2.29	2.22	1.00	1.15	0.41	0.86	0.27	0.08	0.10	0.11

Table 6.1e. Veryshort cracks (c=0.25mm): 2D J [MPa mm] and $U_{\theta\theta}$ [μm] for cw.

position→ σ_{app}↓	J2D P.S.	J2D P.E.	U2D P.S.	U2D P.E.	U3D entr	U3D mid	U3D exit	U3D $\psi=0$	U3D $\psi=45$	U3D $\psi=90$
14.33 MPa	0	0	0	0	0	0	0	0	0	0
71.67 MPa	0	0	0	0	0.02	0	0	0.01	0.01	0.01
107.5 MPa	0	0	0	0	0.04	0	0	0.02	0.02	0.02
143.3 MPa	0.0001	0.03	0.001	0.01	0.10	0.001	0.01	0.03	0.03	0.03
215.0 MPa	0.42	0.61	0.08	0.13	0.31	0.06	0.05	0.06	0.07	0.08
286.7 MPa	1.76	1.99	0.69	0.97	0.43	0.61	0.24	0.08	0.11	0.11

Table 6.2a. Short cracks (c=1mm): 2D J [MPa mm] and $U_{\theta\theta}$ [μm] for ncw.

position→ σ_{app}↓	J2D P.S.	J2D P.E.	U2D P.S.	U2D P.E.	U3D entr	U3D mid	U3D exit	U3D ψ=0	U3D ψ=45	U3D ψ=90
14.33 MPa	0.04	0.03	0.05	0.05	0.05	0.056	0.05	0.035	0.035	0.05
71.67 MPa	1.0	0.9	0.6	0.5	0.42	0.56	0.42	0.17	0.17	0.53
107.5 MPa	2.2	2.0	1.6	1.4	1.2	1.5	1.2	0.48	0.5	1.2
143.3 MPa	4.0	3.7	3.4	2.8	2.4	3.1	2.4	0.9	1.0	2.3
215.0 MPa	9.8	8.4	8.9	6.5	6.1	7.3	6.1	2.4	3.4	5.9
286.7 MPa	19.4	15.0	18.3	12.1	12.7	14.3	12.7	5.1	7.7	11.8

Table 6.2b. Short cracks (c=1mm): 2D J [MPa mm] and $U_{\theta\theta}$ [μm] for cwcp.

position→ σ_{app}↓	J2D P.S.	J2D P.E.	U2D P.S.	U2D P.E.	U3D entr	U3D mid	U3D exit	U3D ψ=0	U3D ψ=45	U3D ψ=90
14.33 MPa	0	0	0	0	0	0	0	0	0	0.01
71.67 MPa	0	0	0	0	0.06	0	0	0.05	0	0.17
107.5 MPa	0.07	0	0.1	0	0.17	0.05	0.03	0.12	0.04	0.54
143.3 MPa	0.4	0.07	0.5	0.1	0.48	0.19	0.14	0.21	0.12	0.97
215.0 MPa	3.0	1.6	2.7	1.0	1.44	1.69	0.82	0.69	0.58	1.79
286.7 MPa	7.0	4.9	6.8	3.6	2.21	4.74	1.82	1.17	1.98	2.41

Table 6.2c. Short cracks (c=1mm): 2D J [MPa mm] and $U_{\theta\theta}$ [μm] for cwht.

position→ σ_{app}↓	J2D P.S.	J2D P.E.	U2D P.S.	U2D P.E.	U3D entr	U3D mid	U3D exit	U3D ψ=0	U3D ψ=45	U3D ψ=90
14.33 MPa	0	0	0	0	0	0	0	0	0	0
71.67 MPa	0	0	0	0	0.06	0	0	0.06	0	0.02
107.5 MPa	0	0	0	0	0.15	0	0	0.13	0.04	0.13
143.3 MPa	0.01	0.05	0.1	0.07	0.46	0.09	0.04	0.24	0.12	0.39
215.0 MPa	1.7	1.4	1.2	0.8	1.41	1.00	0.37	0.73	0.49	1.31
286.7 MPa	7.0	4.6	4.7	3.4	2.20	3.78	1.41	1.23	1.64	2.08

Table 6.2d. Short cracks (c=1mm): 2D J [MPa mm] and $U_{\theta\theta}$ [μm] for cwcr.

position→ σ_{app}↓	J2D P.S.	J2D P.E.	U2D P.S.	U2D P.E.	U3D entr	U3D mid	U3D exit	U3D ψ=0	U3D ψ=45	U3D ψ=90
14.33 MPa	0	0	0	0	0	0	0	0	0	0
71.67 MPa	0	0	0	0	0.08	0	0	0.07	0	0.01
107.5 MPa	0	0	0	0	0.17	0	0	0.14	0.06	0.12
143.3 MPa	0.004	0.004	0.01	0.01	0.50	0.001	0	0.28	0.14	0.35
215.0 MPa	1.15	1.04	0.66	0.52	1.47	0.50	0.15	0.78	0.59	1.27
286.7 MPa	4.31	3.76	3.44	2.85	2.16	2.85	0.88	1.28	1.74	2.04

Table 6.2e. Short cracks (c=1mm): 2D J [MPa mm] and $U_{\theta\theta}$ [μm] for cw.

position→ σ_{app}↓	J2D P.S.	J2D P.E.	U2D P.S.	U2D P.E.	U3D entr	U3D mid	U3D exit	U3D ψ=0	U3D ψ=45	U3D ψ=90
14.33 MPa	0	0	0	0	0	0	0	0	0	0
71.67 MPa	0	0	0	0	0.06	0	0	0.06	0	0
107.5 MPa	0	0	0	0	0.15	0	0	0.13	0.04	0.09
143.3 MPa	0	0	0	0	0.4	0	0	0.24	0.12	0.24
215.0 MPa	0.7	0.8	0.3	0.3	1.35	0.2	0.1	0.73	0.48	1.15
286.7 MPa	3.2	3.3	2.7	2.5	2.1	2.2	0.6	1.23	1.53	1.94

Table 6.3a. Medium cracks (*c*=2mm): 2D *J* [MPa mm] and $U_{\theta\theta}$ [μm] for ncw.

position→ σ_{app}↓	J2D P.S.	J2D P.E.	U2D P.S.	U2D P.E.	U3D entr	U3D mid	U3D exit	U3D ψ=0	U3D ψ=45	U3D ψ=90
14.33 MPa	0.05	0.04	0.1	0.1	0.1	0.06	0.1	0.07	0.07	0.13
71.67 MPa	1.3	1.2	1.0	0.8	0.76	0.68	0.76	0.37	0.38	1.25
107.5 MPa	2.8	2.7	2.5	2.0	1.9	1.87	1.9	0.98	0.99	2.77
143.3 MPa	5.2	4.8	4.9	3.8	3.6	3.8	3.6	1.84	1.91	4.76
215.0 MPa	12.4	10.8	11.8	8.6	8.75	9.3	8.75	4.44	5.1	10.3
286.7 MPa	24.0	19.4	23.3	15.7	17.9	18.7	17.9	8.48	10.4	18.1

Table 6.3b. Medium cracks (*c*=2mm): 2D *J* [MPa mm] and $U_{\theta\theta}$ [μm] for cwcp.

position→ σ_{app}↓	J2D P.S.	J2D P.E.	U2D P.S.	U2D P.E.	U3D entr	U3D mid	U3D exit	U3D ψ=0	U3D ψ=45	U3D ψ=90
14.33 MPa	0	0	0	0	0	0	0	0	0	0
71.67 MPa	0	0	0	0	0.05	0	0	0.04	0	0.03
107.5 MPa	0	0.002	0	0	0.19	0	0	0.17	0	0.96
143.3 MPa	0.1	0.04	0.1	0.08	0.46	0.06	0	0.34	0.07	2.08
215.0 MPa	2.1	1.7	1.6	1.1	2.28	0.97	0.38	1.39	0.47	5.1
286.7 MPa	8.6	5.8	7.4	4.5	4.57	4.89	2.27	3.01	2.22	7.99

Table 6.3c– Medium cracks (*c*=2mm): 2D *J* [MPa mm] and $U_{\theta\theta}$ [μm] for cwht.

position→ σ_{app}↓	J2D P.S.	J2D P.E.	U2D P.S.	U2D P.E.	U3D entr	U3D mid	U3D exit	U3D ψ=0	U3D ψ=45	U3D ψ=90
14.33 MPa	0	0	0	0	0	0	0	0	0	0
71.67 MPa	0	0	0	0	0.05	0	0	0.05	0	0
107.5 MPa	0.006	0.003	0.005	0	0.19	0	0	0.18	0	0.17
143.3 MPa	0.2	0.08	0.2	0.1	0.46	0.09	0	0.34	0.12	0.61
215.0 MPa	2.3	1.9	1.9	1.3	2.29	1.17	0.37	1.42	0.60	3.00
286.7 MPa	9.1	6.3	8.3	4.9	4.58	5.45	2.30	3.07	2.32	6.14

Table 6.3d– Medium cracks (*c*=2mm): 2D *J* [MPa mm] and $U_{\theta\theta}$ [μm] for cwcr.

position→ σ_{app}↓	J2D P.S.	J2D P.E.	U2D P.S.	U2D P.E.	U3D entr	U3D mid	U3D exit	U3D ψ=0	U3D ψ=45	U3D ψ=90
14.33 MPa	0	0	0	0	0	0	0	0	0	0
71.67 MPa	0.005	0	0	0	0.08	0	0	0.09	0	0
107.5 MPa	0.02	0.01	0.04	0.01	0.24	0.02	0	0.22	0	0.02
143.3 MPa	0.18	0.10	0.18	0.13	0.56	0.09	0	0.38	0.16	0.33
215.0 MPa	2.33	1.98	2.03	1.38	2.51	1.23	0.26	1.59	0.74	2.22
286.7 MPa	9.14	6.50	8.62	5.17	4.73	5.73	1.85	3.31	2.49	5.25

Table 6.3e. Medium cracks (*c*=2mm): 2D *J* [MPa mm] and $U_{\theta\theta}$ [μm] for cw.

position→ σ_{app}↓	J2D P.S.	J2D P.E.	U2D P.S.	U2D P.E.	U3D entr	U3D mid	U3D exit	U3D ψ=0	U3D ψ=45	U3D ψ=90
14.33 MPa	0	0	0	0	0	0	0	0	0	0
71.67 MPa	0.001	0	0	0	0.05	0	0	0.05	0	0
107.5 MPa	0.01	0.006	0.02	0.004	0.19	0.005	0	0.18	0	0
143.3 MPa	0.07	0.04	0.1	0.07	0.39	0.05	0	0.30	0.11	0.22
215.0 MPa	1.7	1.6	1.4	1.1	2.20	0.81	0.13	1.42	0.55	1.78
286.7 MPa	8.1	5.7	7.5	4.5	4.54	4.77	1.33	3.10	2.13	4.73

Table 6.4a. Long cracks (c=3mm): 2D J [MPa mm] and $U_{\theta\theta}$ [μm] for ncw.

position→ σ_{app}↓	J2D P.S.	J2D P.E.	U2D P.S.	U2D P.E.	U3D entr	U3D mid	U3D exit	U3D ψ=0	U3D ψ=45	U3D ψ=90
14.33 MPa	0.06	0.06	0.16	0.1	0.15	0.16	0.15	0.1	0.1	0.2
71.67 MPa	1.5	1.4	1.3	1.0	1.02	1.21	1.02	0.6	0.6	1.9
107.5 MPa	3.3	3.2	3.1	2.6	2.5	2.9	2.5	1.6	1.4	4.0
143.3 MPa	6.1	5.7	5.9	4.7	4.6	5.3	4.6	2.9	2.6	6.6
215.0 MPa	14.6	12.8	14.3	10.5	11.0	12.1	11.0	6.8	6.5	13.7
286.7 MPa	28.7	23.1	28.6	19.3	22.9	24.1	22.9	12.8	13.2	23.8

Table 6.4b. Long cracks (c=3mm): 2D J [MPa mm] and $U_{\theta\theta}$ [μm] for cwcp.

position→ σ_{app}↓	J2D P.S.	J2D P.E.	U2D P.S.	U2D P.E.	U3D entr	U3D mid	U3D exit	U3D ψ=0	U3D ψ=45	U3D ψ=90
14.33 MPa	0.0001	0.001	0	0	0	0	0	0	0	0
71.67 MPa	0.03	0.03	0.08	0.08	0.04	0.08	0	0.03	0	0.41
107.5 MPa	0.16	0.15	0.2	0.2	0.25	0.23	0	0.22	0	1.07
143.3 MPa	0.9	0.64	0.7	0.5	0.65	0.55	0.03	0.48	0.19	2.61
215.0 MPa	5.0	4.0	5.0	3.4	3.3	3.89	1.00	2.29	1.02	6.85
286.7 MPa	16.3	12.2	17.0	11.0	7.77	12.8	4.95	5.45	3.68	12.3

Table 6.4c. Long cracks (c=3mm): 2D J [MPa mm] and $U_{\theta\theta}$ [μm] for cwht.

position→ σ_{app}↓	J2D P.S.	J2D P.E.	U2D P.S.	U2D P.E.	U3D entr	U3D mid	U3D exit	U3D ψ=0	U3D ψ=45	U3D ψ=90
14.33 MPa	0.004	0.001	0.001	0	0	0.001	0	0	0	0
71.67 MPa	0.07	0.04	0.1	0.1	0.04	0.14	0	0.04	0	0
107.5 MPa	0.25	0.16	0.3	0.2	0.26	0.28	0	0.23	0.03	0
143.3 MPa	1.1	0.7	0.8	0.5	0.68	0.71	0.08	0.5	0.3	0.75
215.0 MPa	5.5	4.2	5.4	3.6	3.49	4.35	1.18	2.3	1.3	4.0
286.7 MPa	16.9	12.5	17.5	11.1	7.93	13.3	5.29	5.5	4.1	9.0

Table 6.4d. Long cracks (c=3mm): 2D J [MPa mm] and $U_{\theta\theta}$ [μm] for cwcr.

position→ σ_{app}↓	J2D P.S.	J2D P.E.	U2D P.S.	U2D P.E.	U3D entr	U3D mid	U3D exit	U3D ψ=0	U3D ψ=45	U3D ψ=90
14.33 MPa	0.02	0.01	0.01	0	0	0.02	0	0	0	0
71.67 MPa	0.14	0.07	0.20	0.13	0.09	0.20	0	0.08	0	0
107.5 MPa	0.39	0.24	0.38	0.28	0.33	0.37	0.02	0.29	0.12	0
143.3 MPa	1.22	0.83	0.95	0.57	0.85	0.88	0.17	0.56	0.37	0.37
215.0 MPa	5.65	4.41	5.70	3.86	3.68	4.68	1.51	2.57	1.58	2.79
286.7 MPa	16.40	12.43	17.3	11.2	8.00	13.37	5.39	5.81	4.49	7.27

Table 6.4e. Long cracks (c=3mm): 2D J [MPa mm] and $U_{\theta\theta}$ [μm] for cw.

position→ σ_{app}↓	J2D P.S.	J2D P.E.	U2D P.S.	U2D P.E.	U3D entr	U3D mid	U3D exit	U3D ψ=0	U3D ψ=45	U3D ψ=90
14.33 MPa	0.01	0.003	0.01	0	0	0.01	0	0	0	0
71.67 MPa	0.12	0.06	0.2	0.1	0.06	0.17	0	0.05	0	0
107.5 MPa	0.35	0.21	0.3	0.3	0.27	0.33	0	0.24	0.06	0
143.3 MPa	0.9	0.63	0.7	0.5	0.61	0.6	0.07	0.48	0.28	0.18
215.0 MPa	4.9	4.0	5.0	3.4	3.33	3.98	0.93	2.28	1.28	2.18
286.7 MPa	16.2	12.2	17.3	11.1	7.91	13.23	4.97	5.52	4.0	6.4

Table 6.5a. Extralong cracks (c=4mm): 2D J [MPa mm] and $U_{\theta\theta}$ [μm] for ncw.

position→ σ_{app}↓	J2D P.S.	J2D P.E.	U2D P.S.	U2D P.E.	U3D entr	U3D mid	U3D exit	U3D $\psi=0$	U3D $\psi=45$	U3D $\psi=90$
14.33 MPa	0.06	0.06	0.21	0.20	0.20	0.21	0.20	0.17	0.16	0.32
71.67 MPa	1.76	1.64	1.58	1.29	1.30	1.50	1.30	0.95	0.81	2.55
107.5 MPa	3.90	3.71	3.73	3.09	3.13	3.47	3.13	2.38	1.88	5.10
143.3 MPa	7.14	6.57	6.95	5.56	5.72	6.30	5.72	4.36	3.35	8.32
215.0 MPa	17.09	14.91	17.0	12.5	13.90	14.70	13.90	10.00	8.21	17.15
286.7 MPa	33.89	27.06	34.5	23.4	28.93	29.82	28.93	18.63	16.7	30.23

Table 6.5b. Extralong cracks (c=4mm): 2D J [MPa mm] and $U_{\theta\theta}$ [μm] for cwcp

position→ σ_{app}↓	J2D P.S.	J2D P.E.	U2D P.S.	U2D P.E.	U3D entr	U3D mid	U3D exit	U3D $\psi=0$	U3D $\psi=45$	U3D $\psi=90$
0 MPa	0.01	0.02	0.05	0.08	0	0.12	0	0	0	0
14.33 MPa	0.03	0.04	0.11	0.13	0	0.18	0	3e–4	0	0
71.67 MPa	0.32	0.34	0.42	0.43	0.22	0.48	0.04	0.26	0.08	0.41
107.5 MPa	0.90	0.79	0.77	0.67	0.49	0.81	0.19	0.54	0.30	1.19
143.3 MPa	2.65	2.22	2.44	1.93	1.61	2.34	0.58	1.31	0.64	3.03
215.0 MPa	9.85	8.11	10.3	7.64	5.35	8.75	3.92	4.86	2.80	8.24
286.7 MPa	24.5	19.3	27.2	19.1	9.97	21.93	10.03	10.89	7.64	15.54

Table 6.5c. Extralong cracks (c=4mm): 2D J [MPa mm] and $U_{\theta\theta}$ [μm] for cwht.

position→ σ_{app}↓	J2D P.S.	J2D P.E.	U2D P.S.	U2D P.E.	U3D entr	U3D mid	U3D exit	U3D $\psi=0$	U3D $\psi=45$	U3D $\psi=90$
0 MPa	0.02	0.02	0.09	0.08	0	0.15	0	0	0	0
14.33 MPa	0.05	0.04	0.16	0.14	0	0.22	0	1e–4	0	0
71.67 MPa	0.43	0.36	0.49	0.44	0.23	0.54	0.07	0.26	0.17	0
107.5 MPa	1.03	0.82	0.87	0.68	0.53	0.95	0.23	0.55	0.38	0.17
143.3 MPa	2.85	2.35	2.63	2.03	1.71	2.54	0.63	1.33	0.76	0.95
215.0 MPa	10.19	8.32	10.59	7.75	5.44	9.02	4.09	4.90	3.14	5.09
286.7 MPa	24.88	19.53	27.43	19.13	10.02	22.14	10.34	10.96	8.05	11.67

Table 6.5d. Extralong cracks (c=4mm): 2D J [MPa mm] and $U_{\theta\theta}$ [μm] for cwcr.

position→ σ_{app}↓	J2D P.S.	J2D P.E.	U2D P.S.	U2D P.E.	U3D entr	U3D mid	U3D exit	U3D $\psi=0$	U3D $\psi=45$	U3D $\psi=90$
0 MPa	0.03	0.02	0.04	0.06	0	0.14	0	0	0	0
14.33 MPa	0.05	0.05	0.12	0.12	0	0.21	0	0	0	0
71.67 MPa	0.42	0.36	0.49	0.45	0.25	0.55	0.17	0.28	0.25	0
107.5 MPa	1.00	0.85	0.84	0.70	0.53	1.01	0.36	0.58	0.48	0
143.3 MPa	2.66	2.27	2.43	1.97	1.71	2.48	0.72	1.37	0.96	0.49
215.0 MPa	9.60	7.98	9.95	7.50	5.44	8.72	4.26	4.92	3.52	3.71
286.7 MPa	23.83	18.86	26.16	18.44	10.02	21.22	10.28	10.89	8.46	9.64

Table 6.5e. Extralong cracks (c=4mm): 2D J [MPa mm] and $U_{\theta\theta}$ [μm] for cw.

position→ σ_{app}↓	J2D P.S.	J2D P.E.	U2D P.S.	U2D P.E.	U3D entr	U3D mid	U3D exit	U3D $\psi=0$	U3D $\psi=45$	U3D $\psi=90$
0 MPa	0.04	0.02	0.13	0.10	0	0.19	0	0	0	0
14.33 MPa	0.08	0.05	0.20	0.16	0	0.26	0	0.001	0	0
71.67 MPa	0.55	0.41	0.56	0.48	0.25	0.59	0.14	0.28	0.21	0
107.5 MPa	1.17	0.92	1.00	0.75	0.50	1.08	0.33	0.56	0.42	0
143.3 MPa	2.65	2.21	2.44	1.93	1.62	2.36	0.58	1.28	0.75	0.22
215.0 MPa	9.83	8.11	10.3	7.69	5.27	8.73	3.79	4.83	3.16	2.92
286.7 MPa	24.46	19.32	27.4	19.25	9.99	22.24	10.06	10.98	8.13	8.55

FIGURES

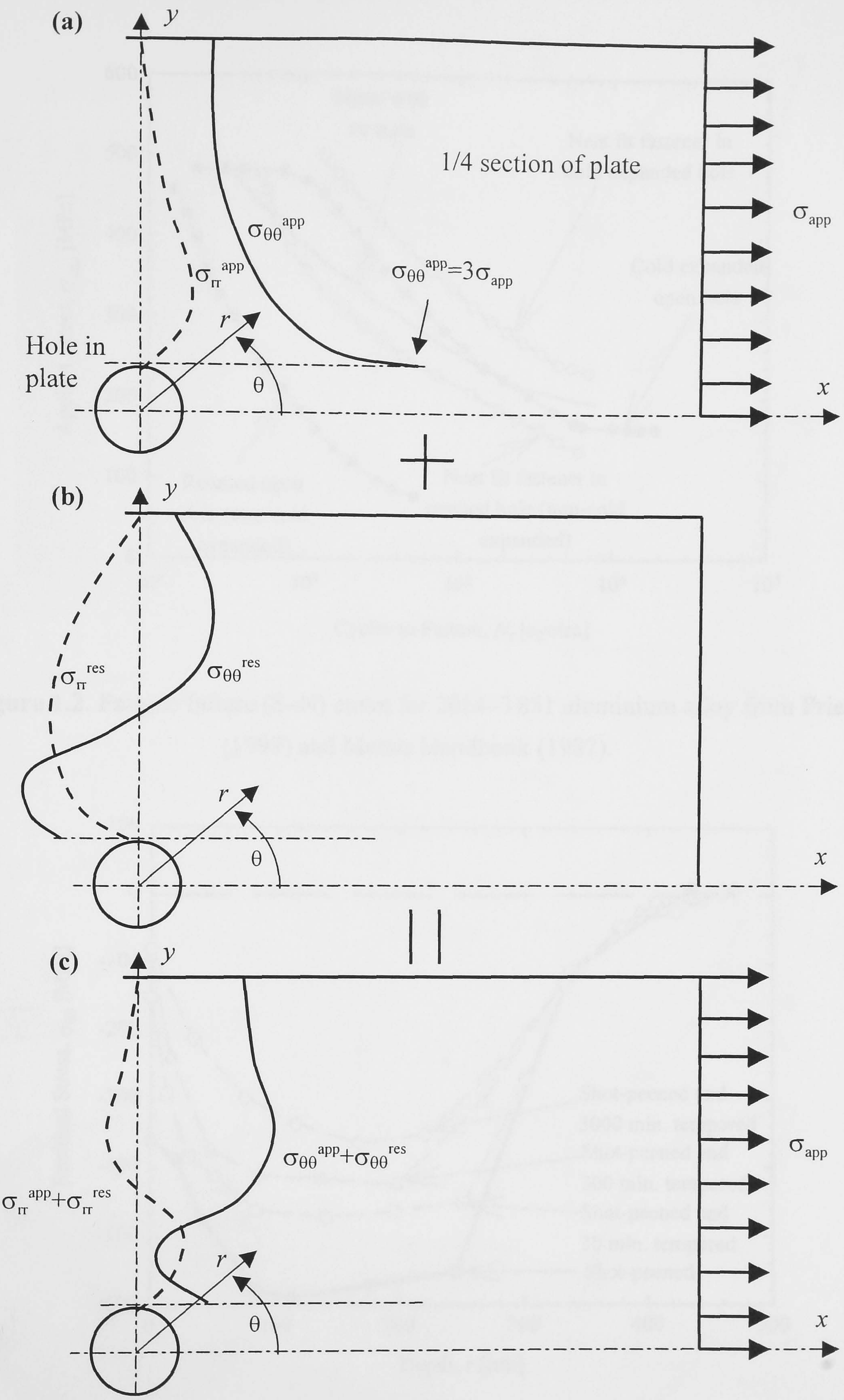

Figure 1.1. Radial stress σ_{rr} and tangential stress $\sigma_{\theta\theta}$ at $\theta = 90°$ on (a) loaded non–cold expanded hole, (b) residual stresses from cold expansion and (c) loaded cold expanded hole.

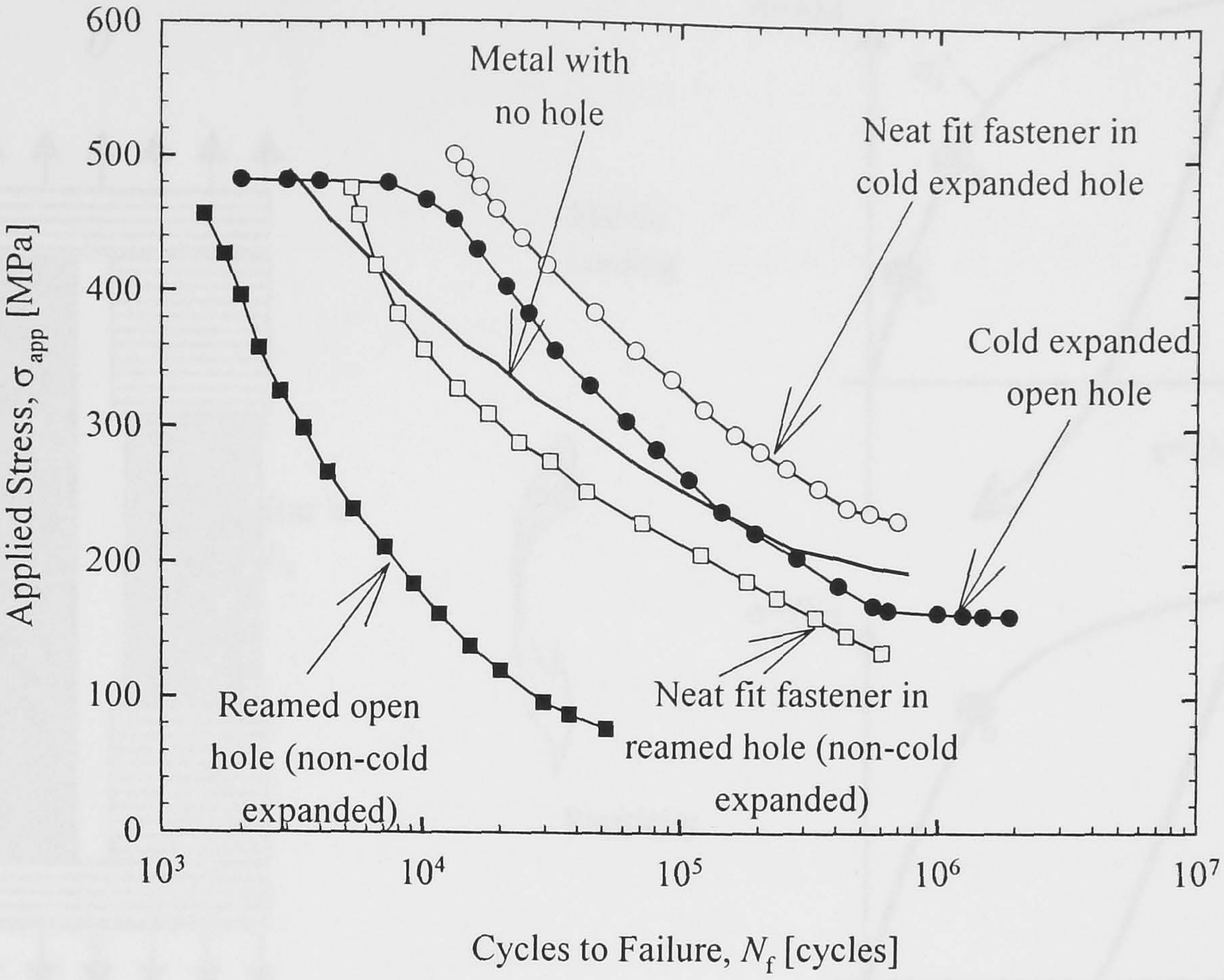

Figure 1.2. Fatigue failure (S–N) curve for 2024–T851 aluminium alloy from Priest (1997) and Metals Handbook (1987).

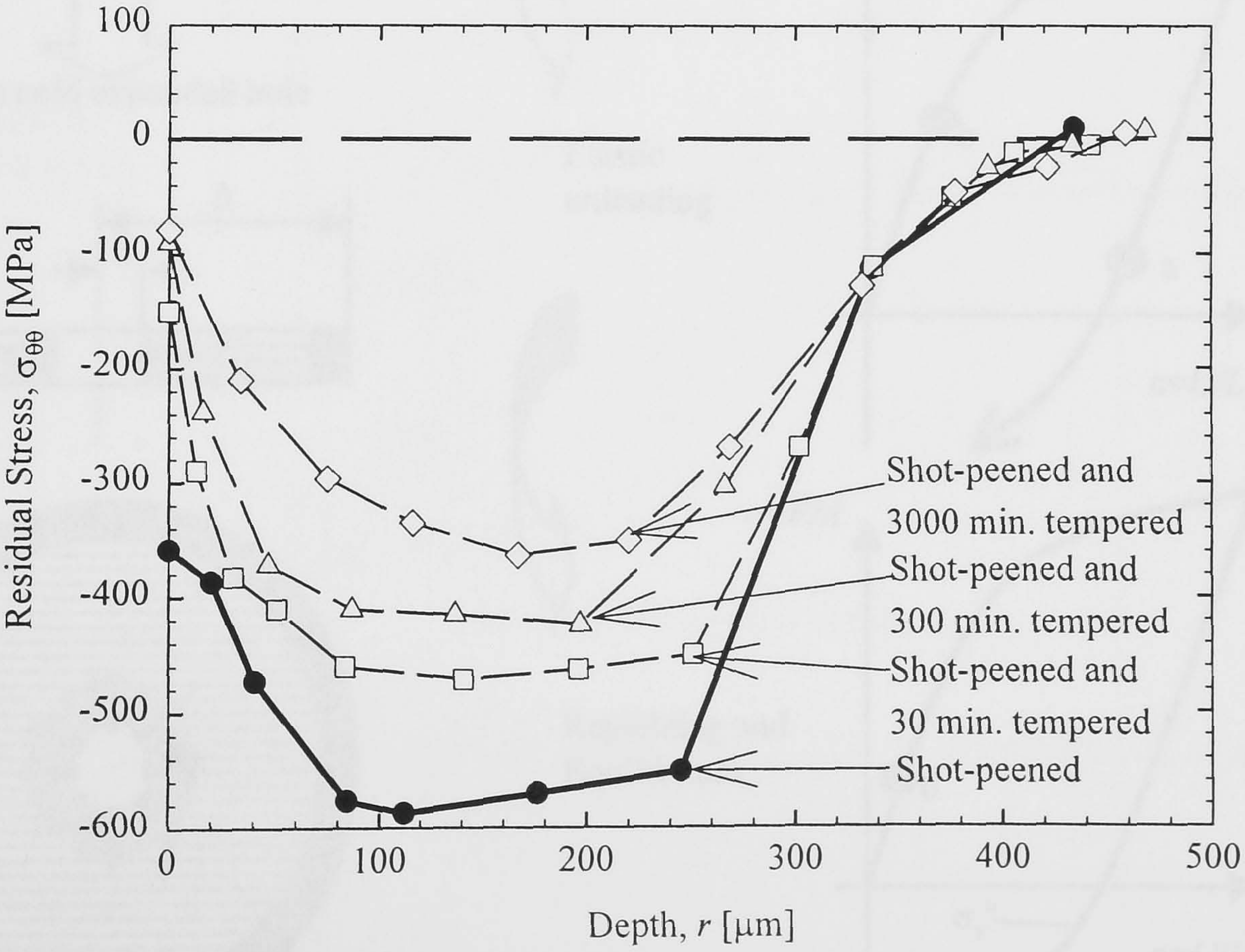

Figure 1.3. Residual stress relaxation in shot–peened steel cylinders at 400°C for different time exposure from Lillamand and Barralier (1996).

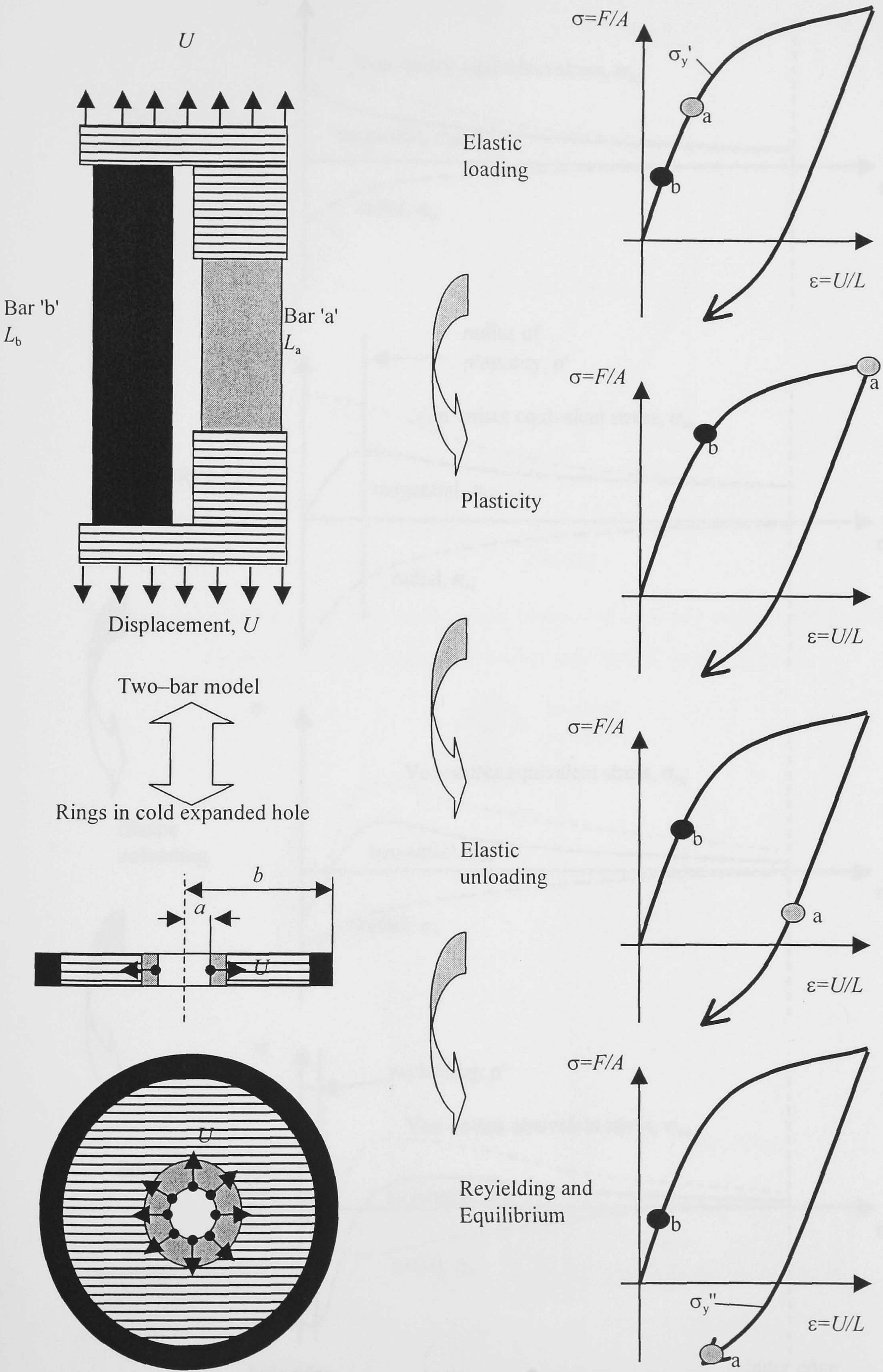

Figure 1.4. Demonstration of the generation of compressive residual stresses using tensile loading of a two–bar model.

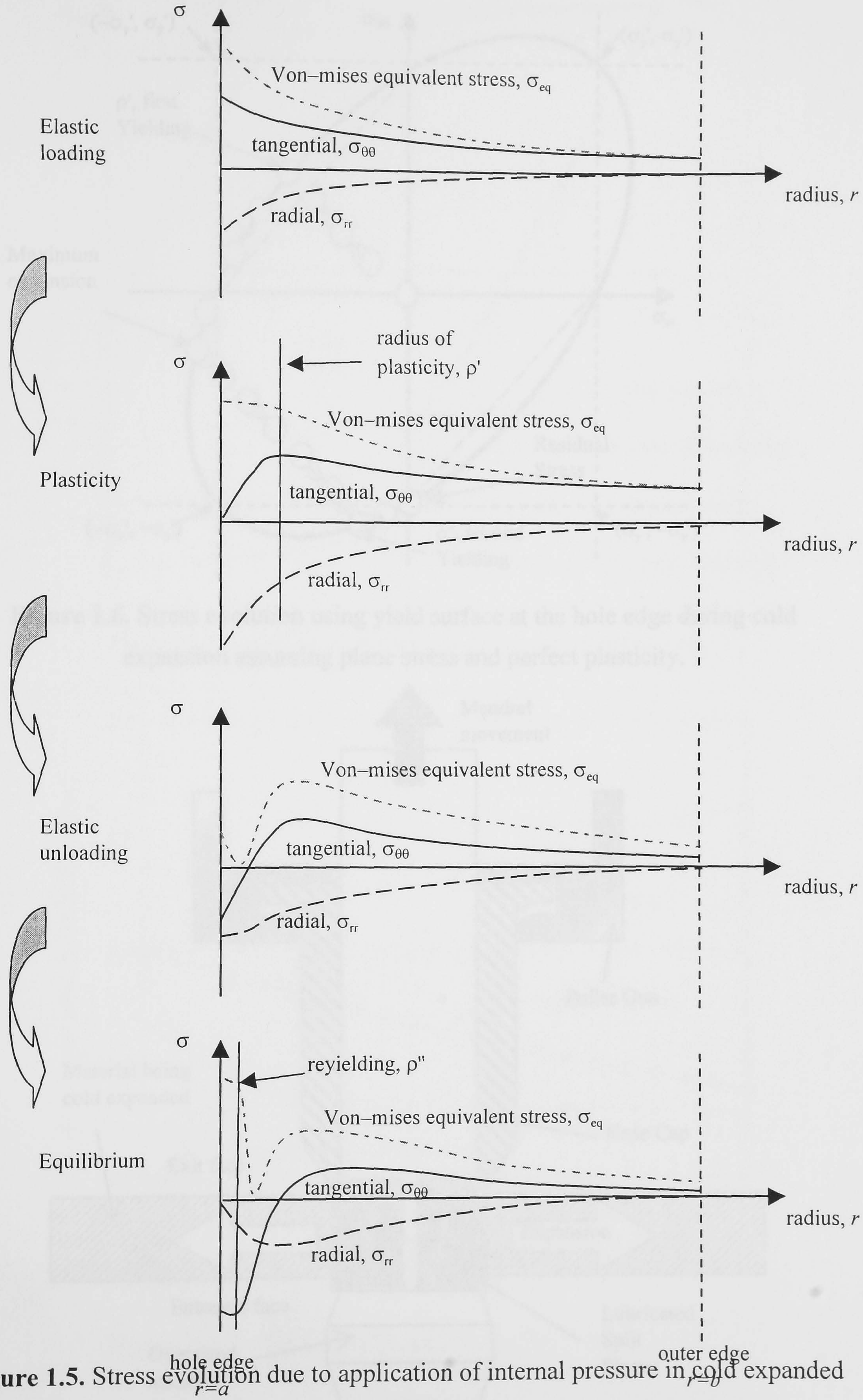

Figure 1.5. Stress evolution due to application of internal pressure in cold expanded discs and tubes.

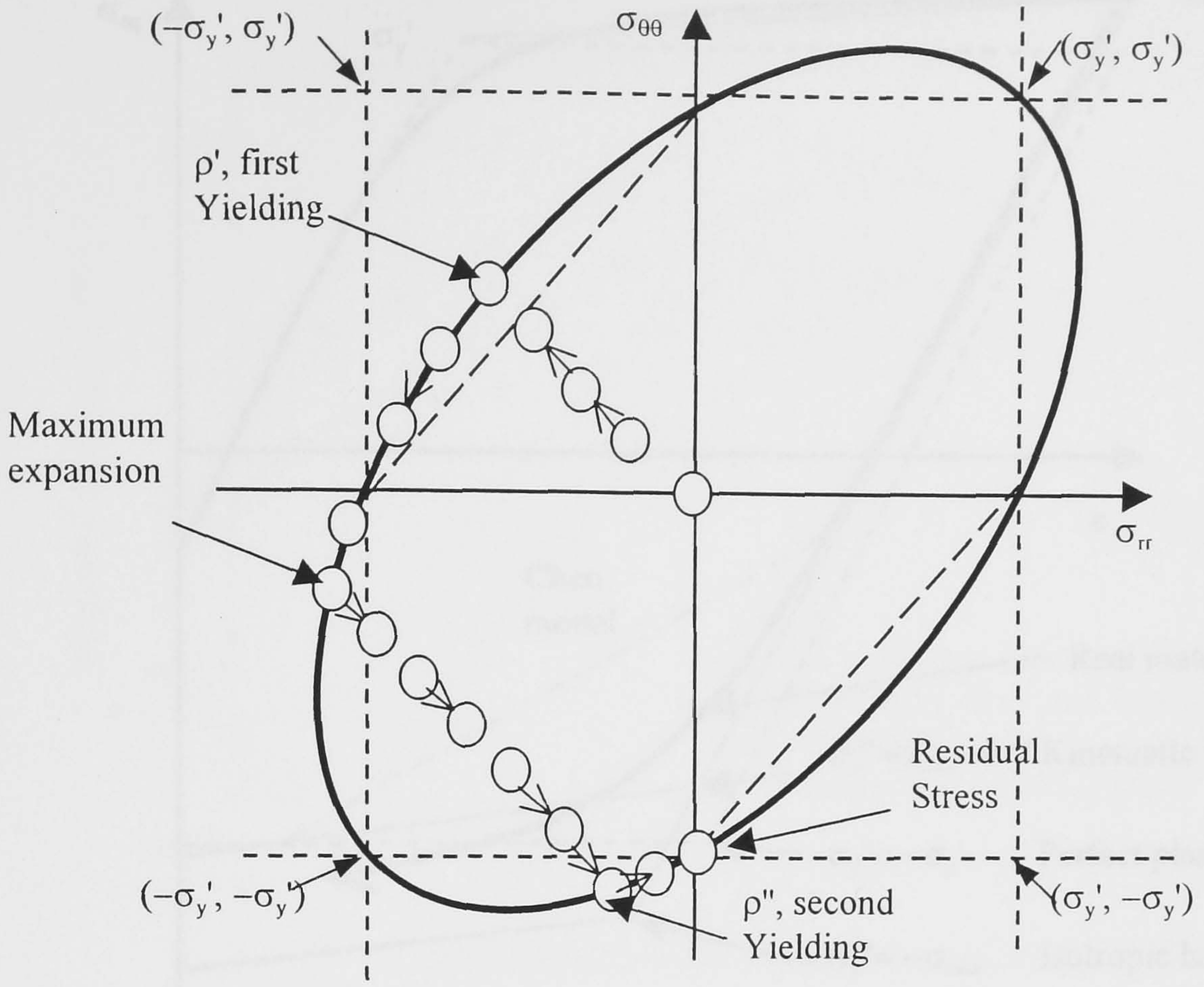

Figure 1.6. Stress evolution using yield surface at the hole edge during cold expansion assuming plane stress and perfect plasticity.

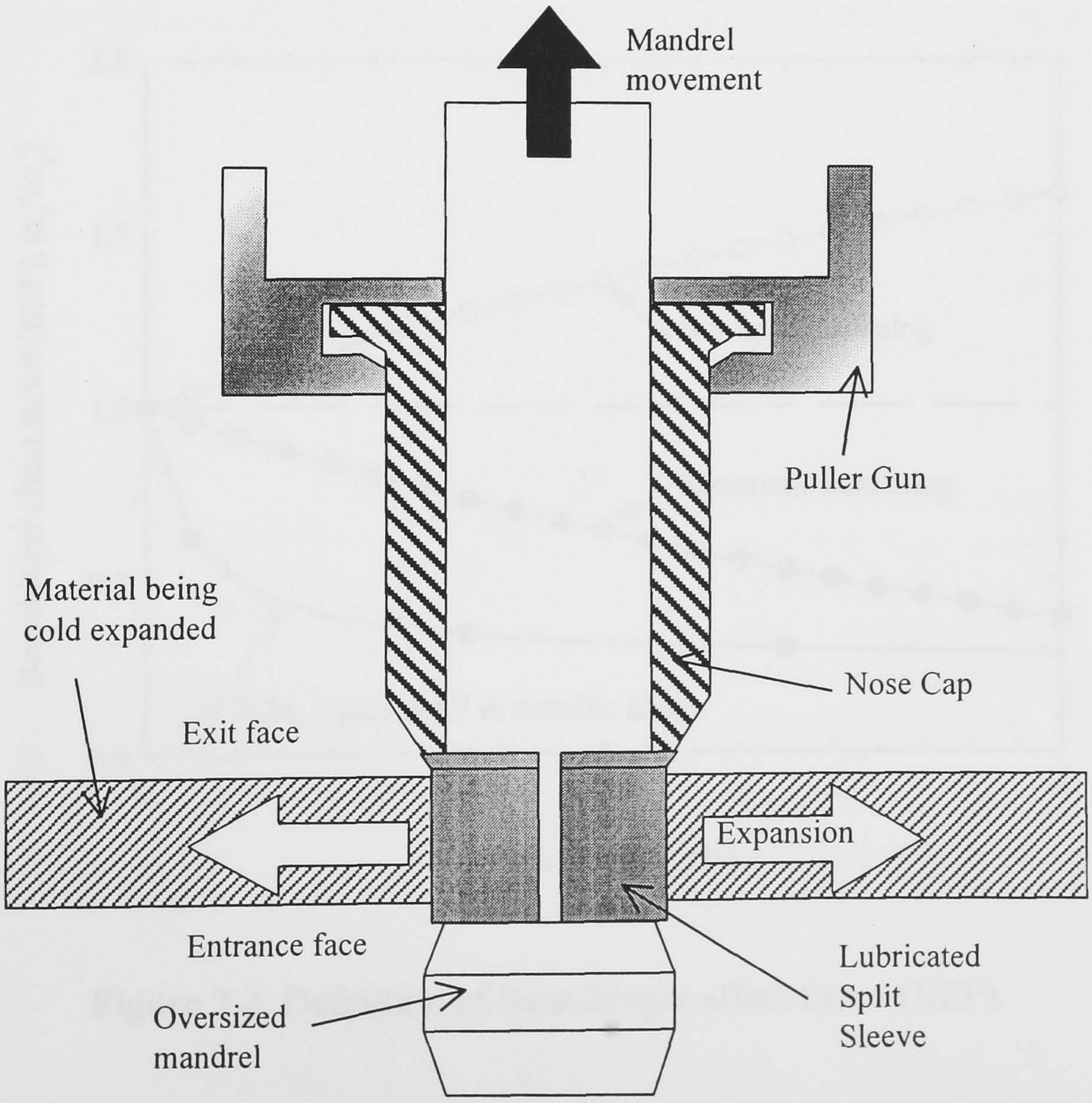

Figure 1.7. A partial section through the FTI split–sleeve cold expansion.

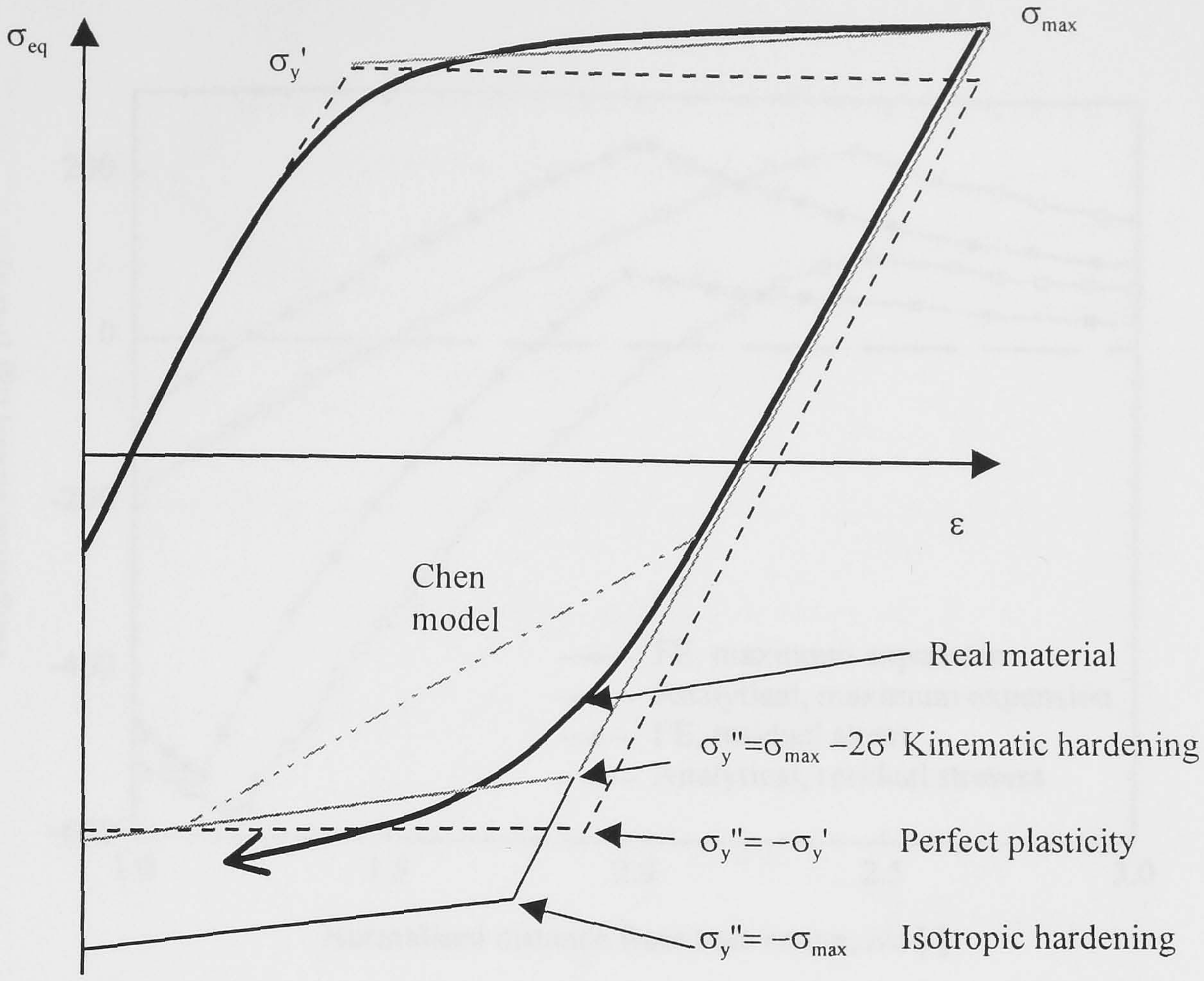

Figure 2.1. Analytical models for stress–strain behaviour.

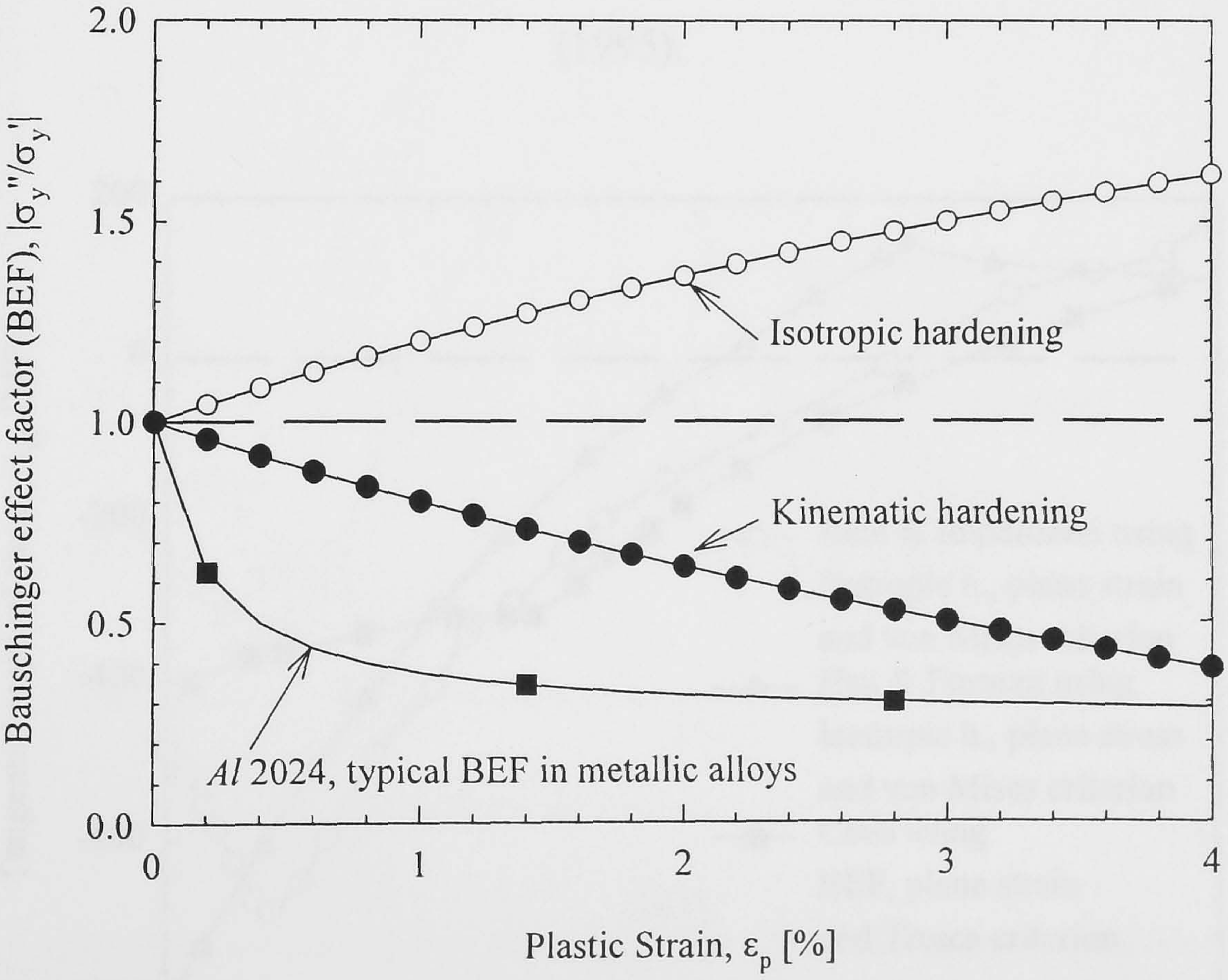

Figure 2.2. Definition of Bauschinger effect factor (BEF).

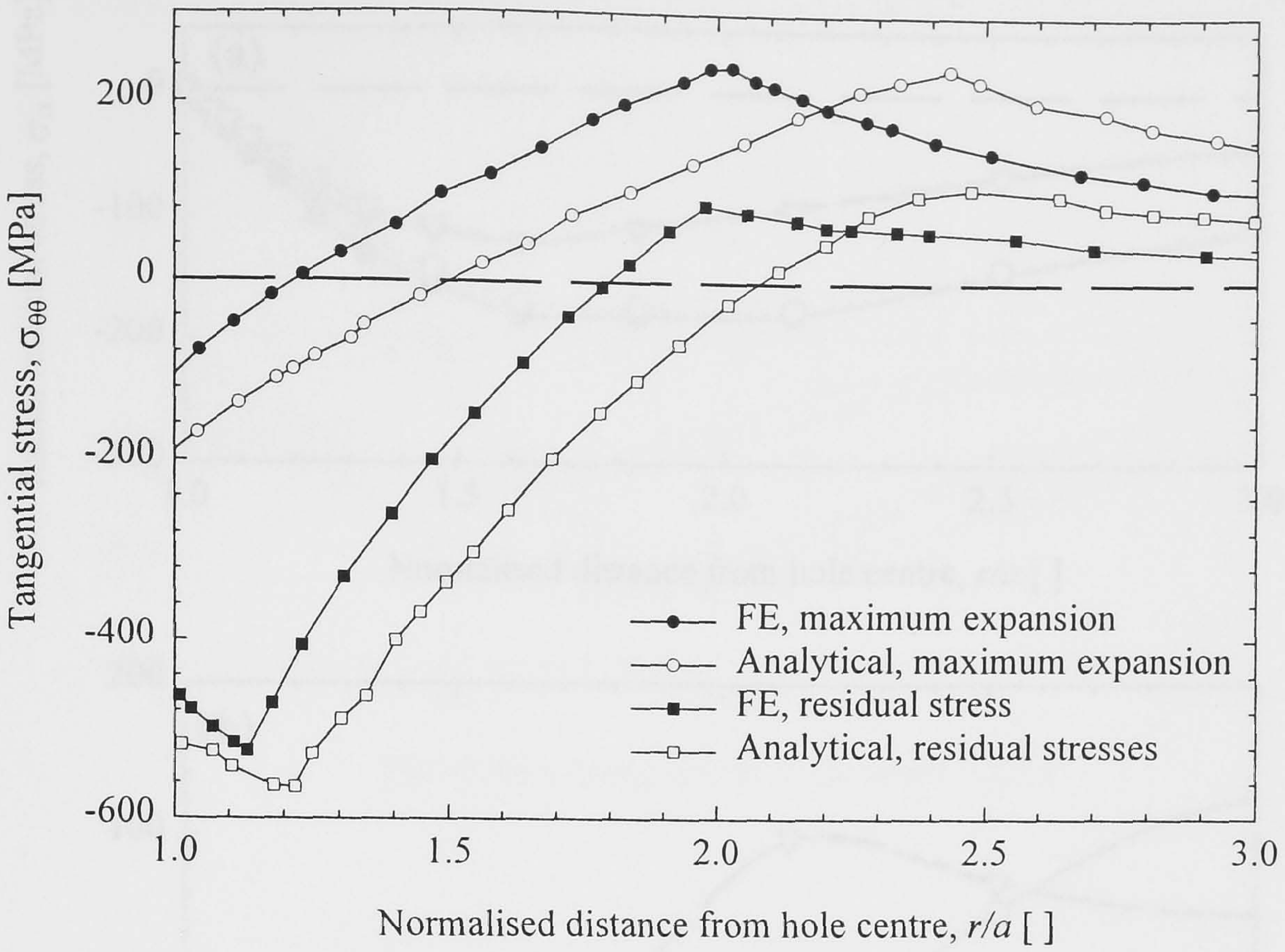

Figure 2.3. Analytical tangential residual stresses around a cold expanded hole from Rich and Impellizzeri (1997) compared with finite element solutions from Pousard (1995).

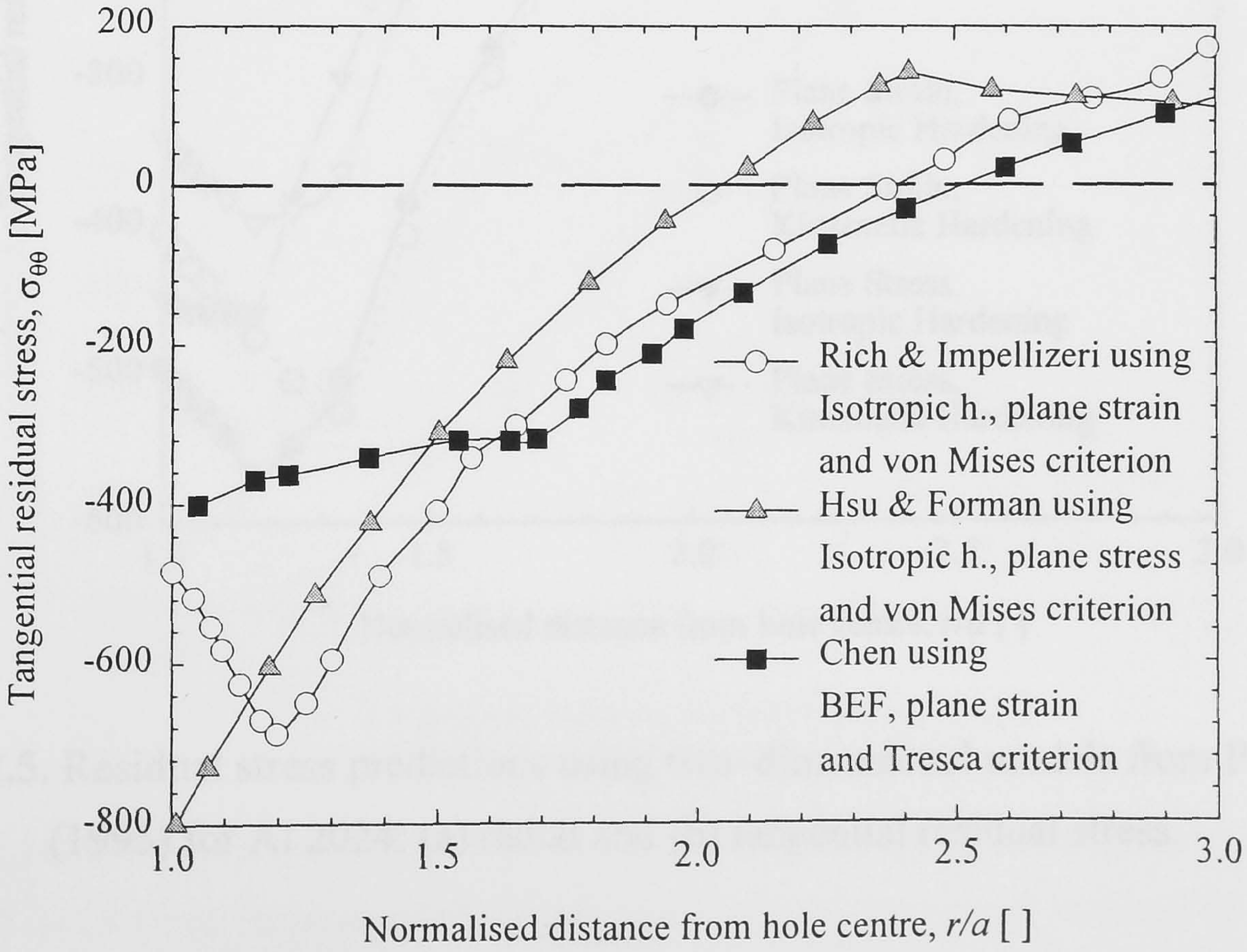

Figure 2.4. Tangential residual stresses around a cold expanded hole using different analytical solutions. (From Poussard, 1995).

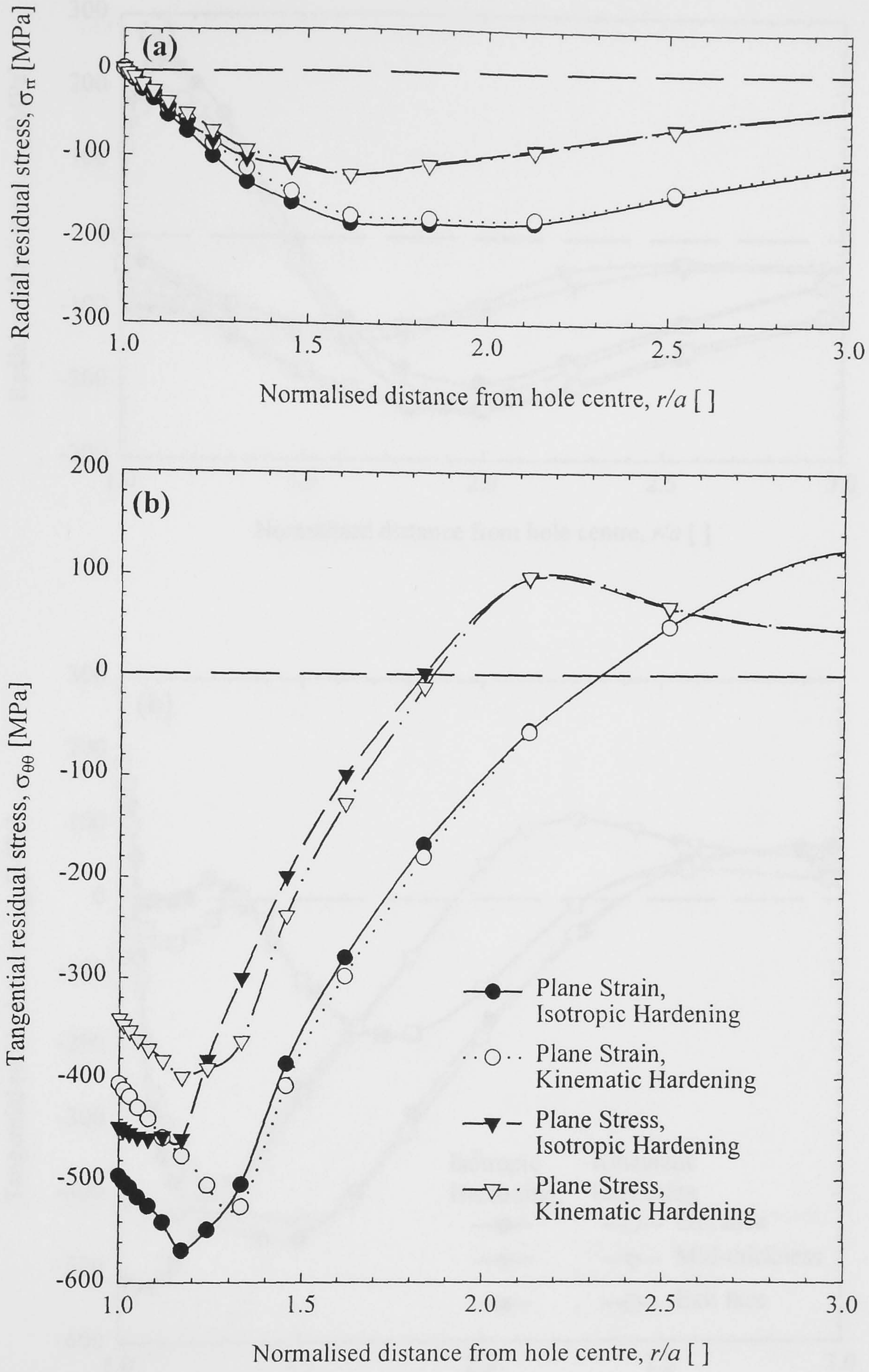

Figure 2.5. Residual stress predictions using two–dimensional models from Poussard (1995) for Al 2024: (a) radial and (b) tangential residual stress.

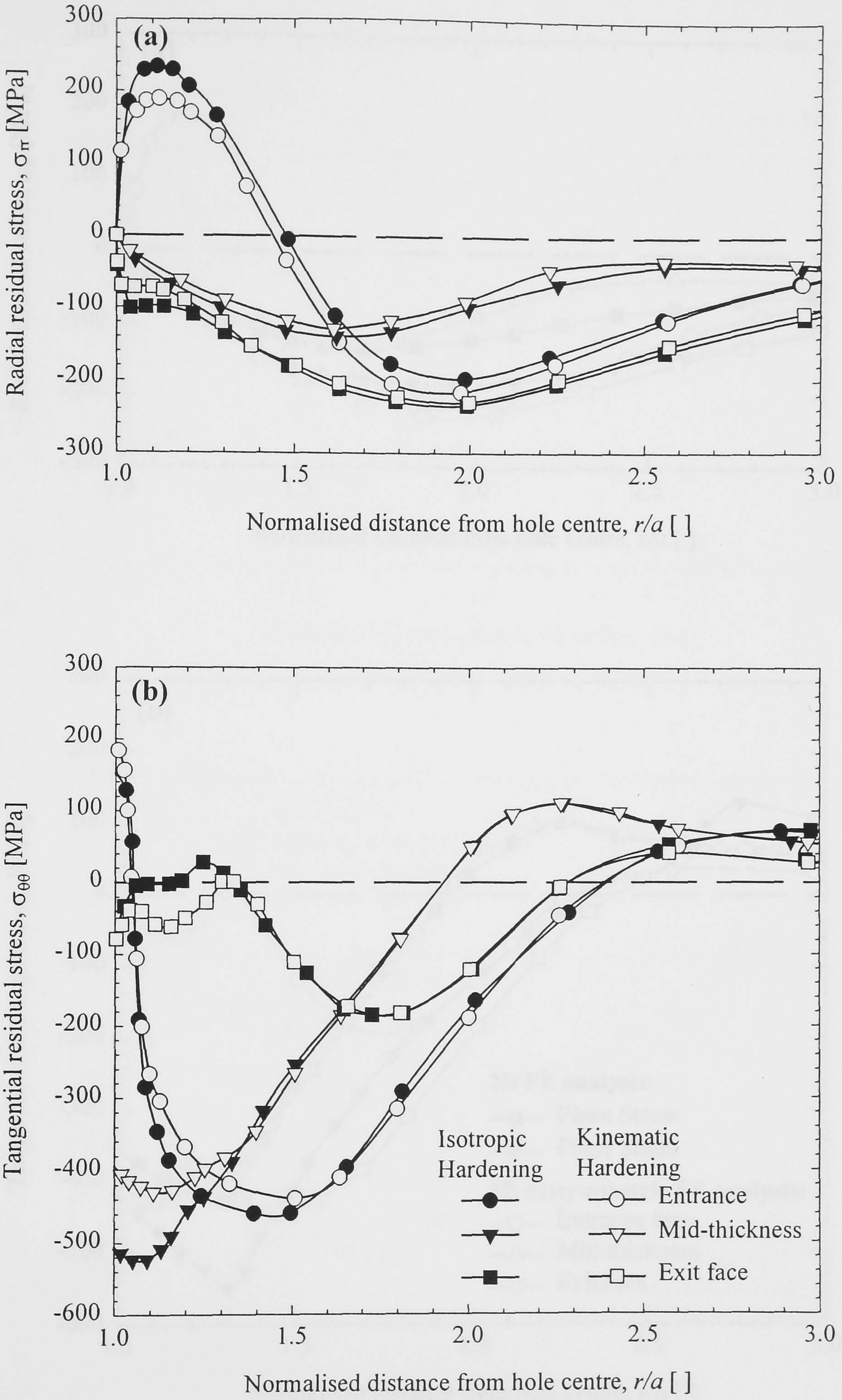

Figure 2.6. Residual stress predictions through–thickness using axisymmetric models in Al 2024 from Poussard (1995): (a) radial and (b) tangential residual stress.

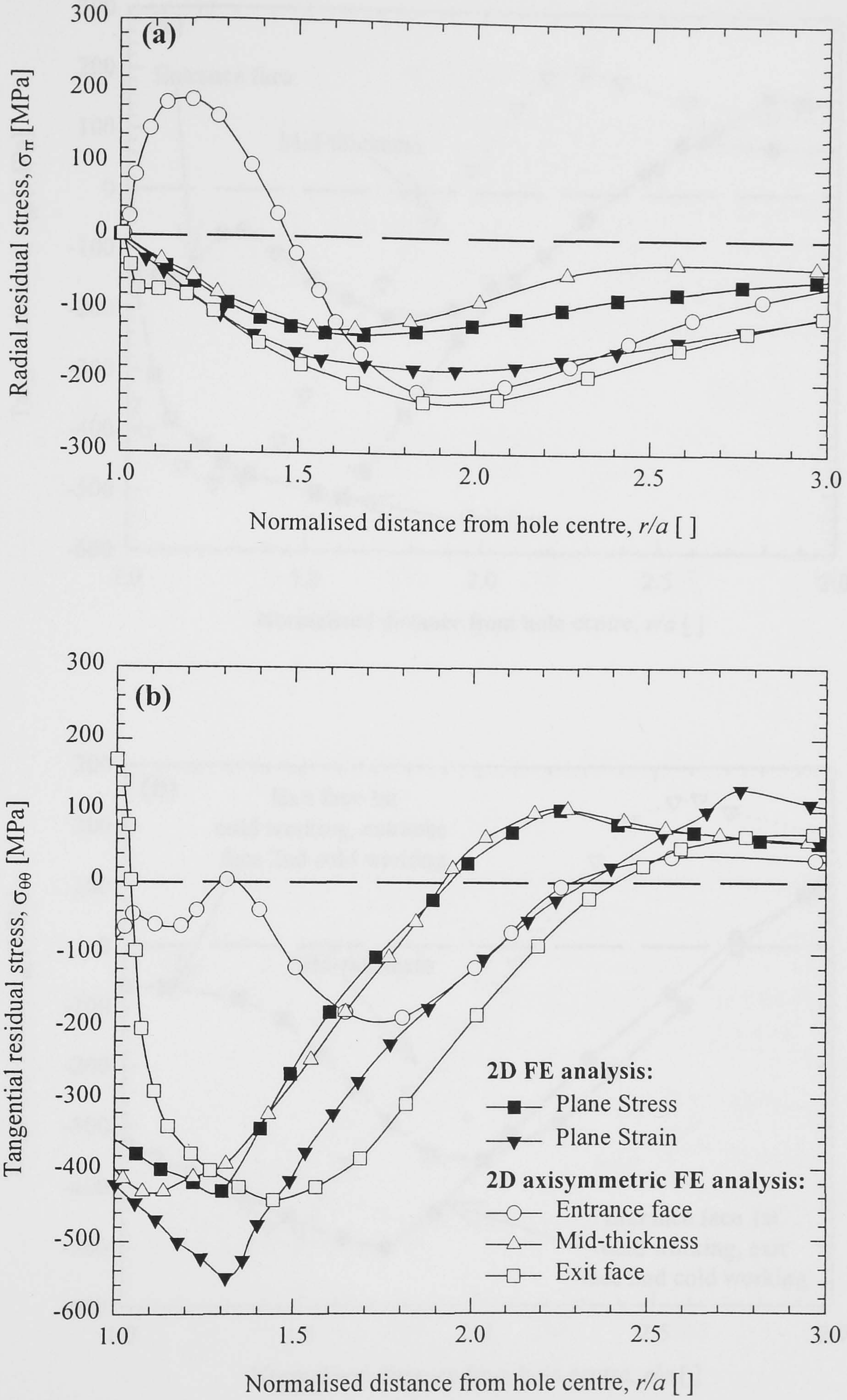

Figure 2.7. Residual stress predictions with kinematic hardening for axisymmetric through–thickness and 2D models from Poussard (1995): (a) radial and (b) tangential residual stress.

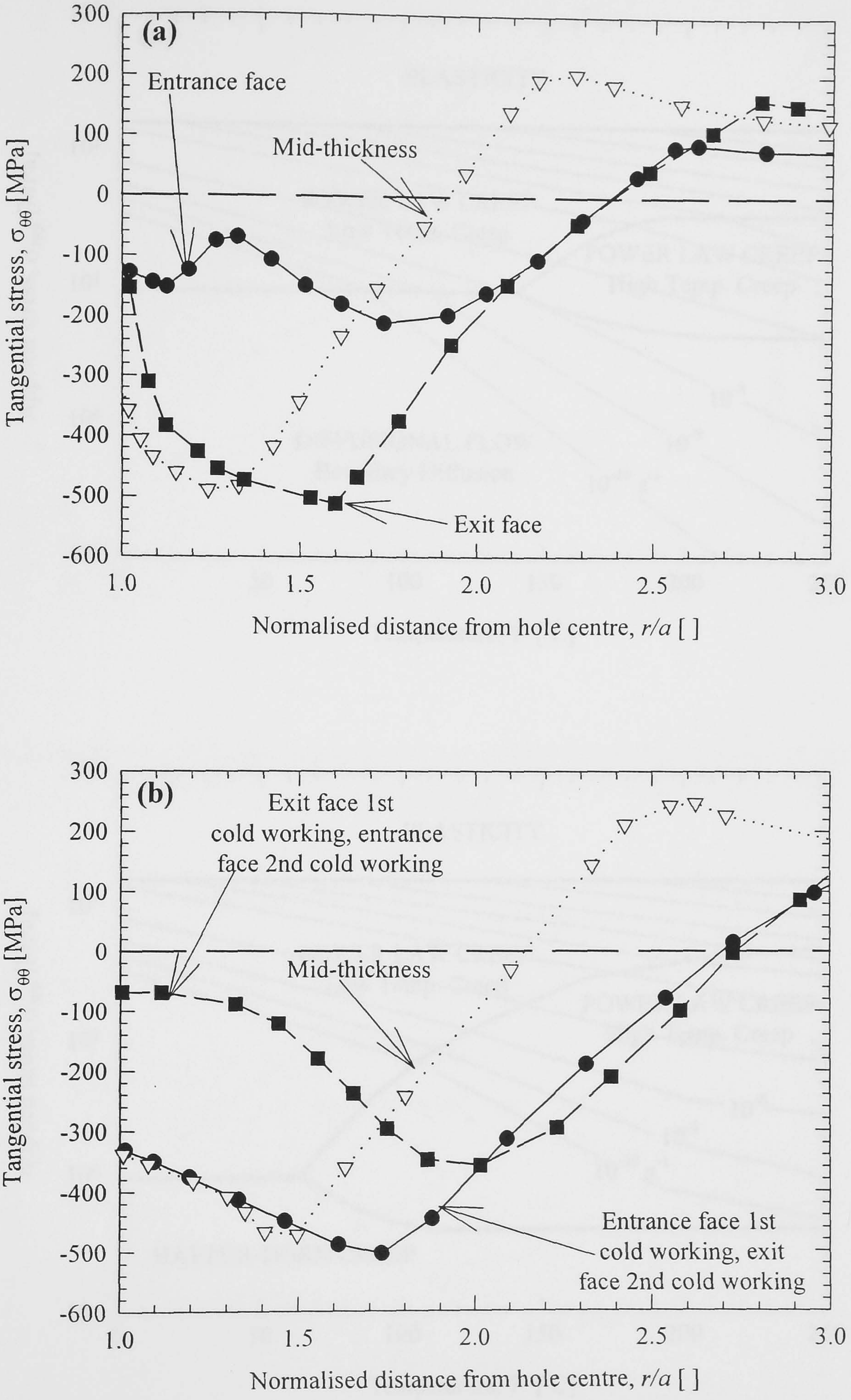

Figure 2.8. Residual stress predictions through–thickness from Bernard et al. (1995): (a) One mandrel pulled and (b) Two mandrels pulled in both directions.

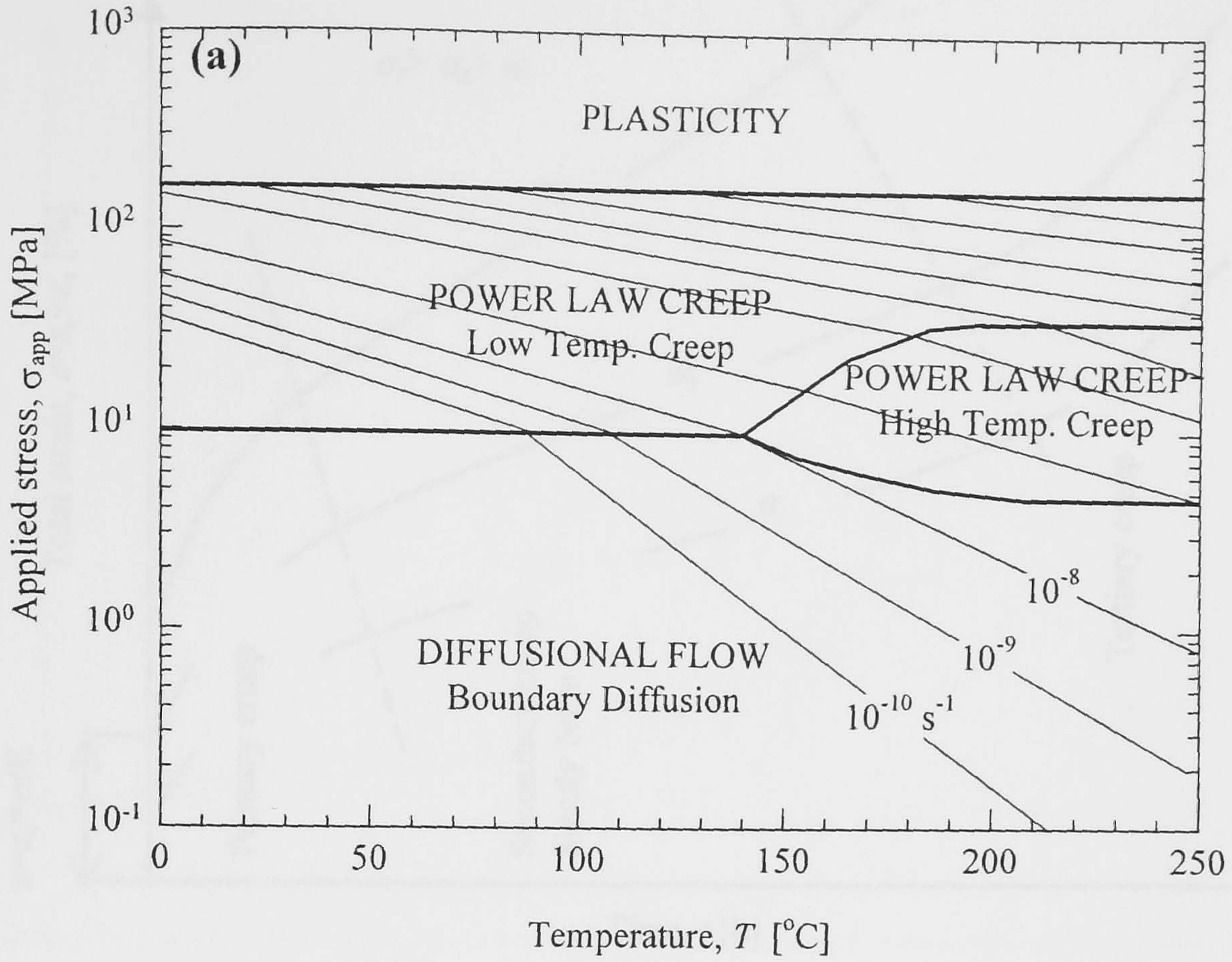

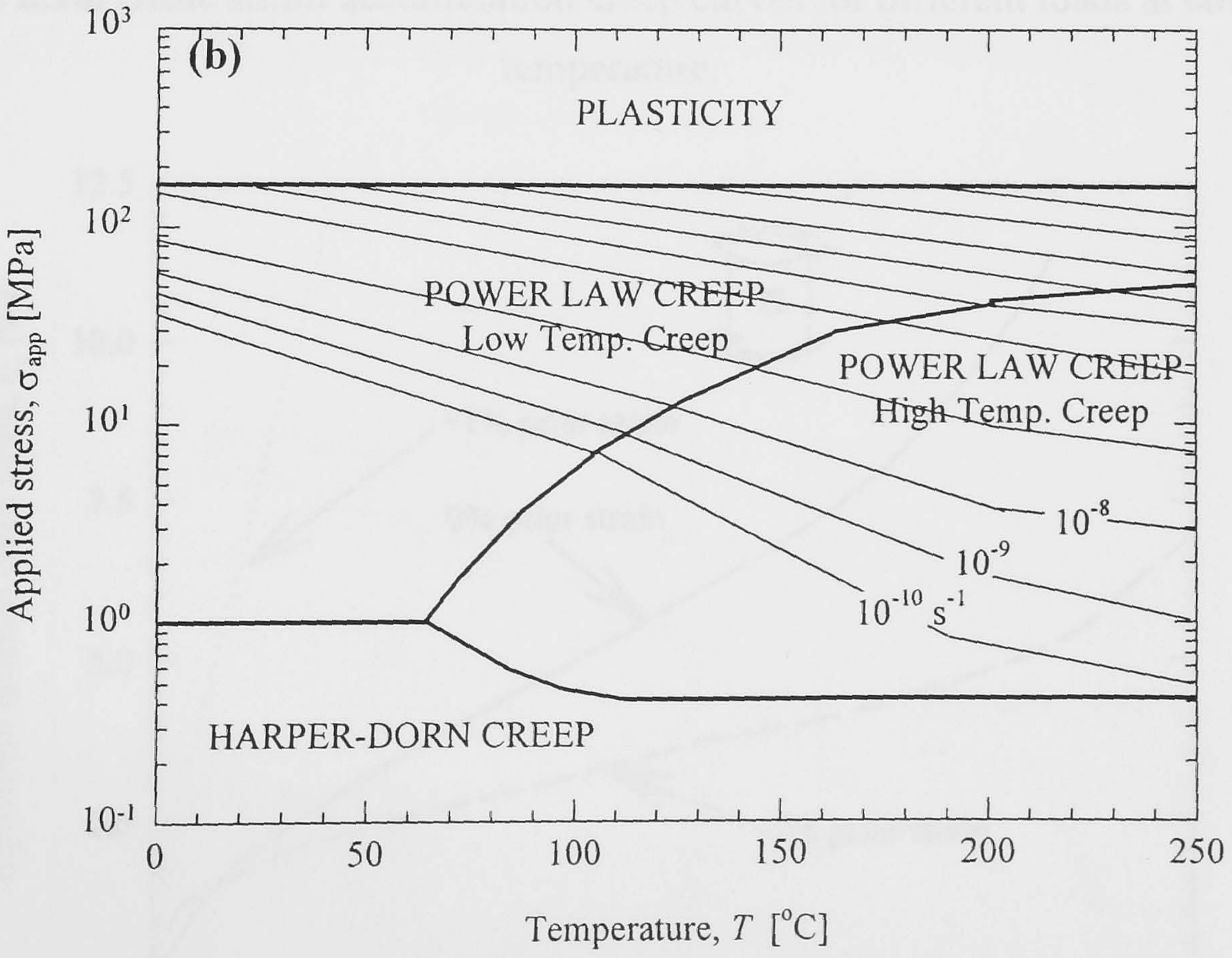

Figure 2.9. Deformation maps with steady state creep rates for pure aluminium from Ashby and Frost (1987) for grain sizes: (a) 10 μm and (b) 1 mm.

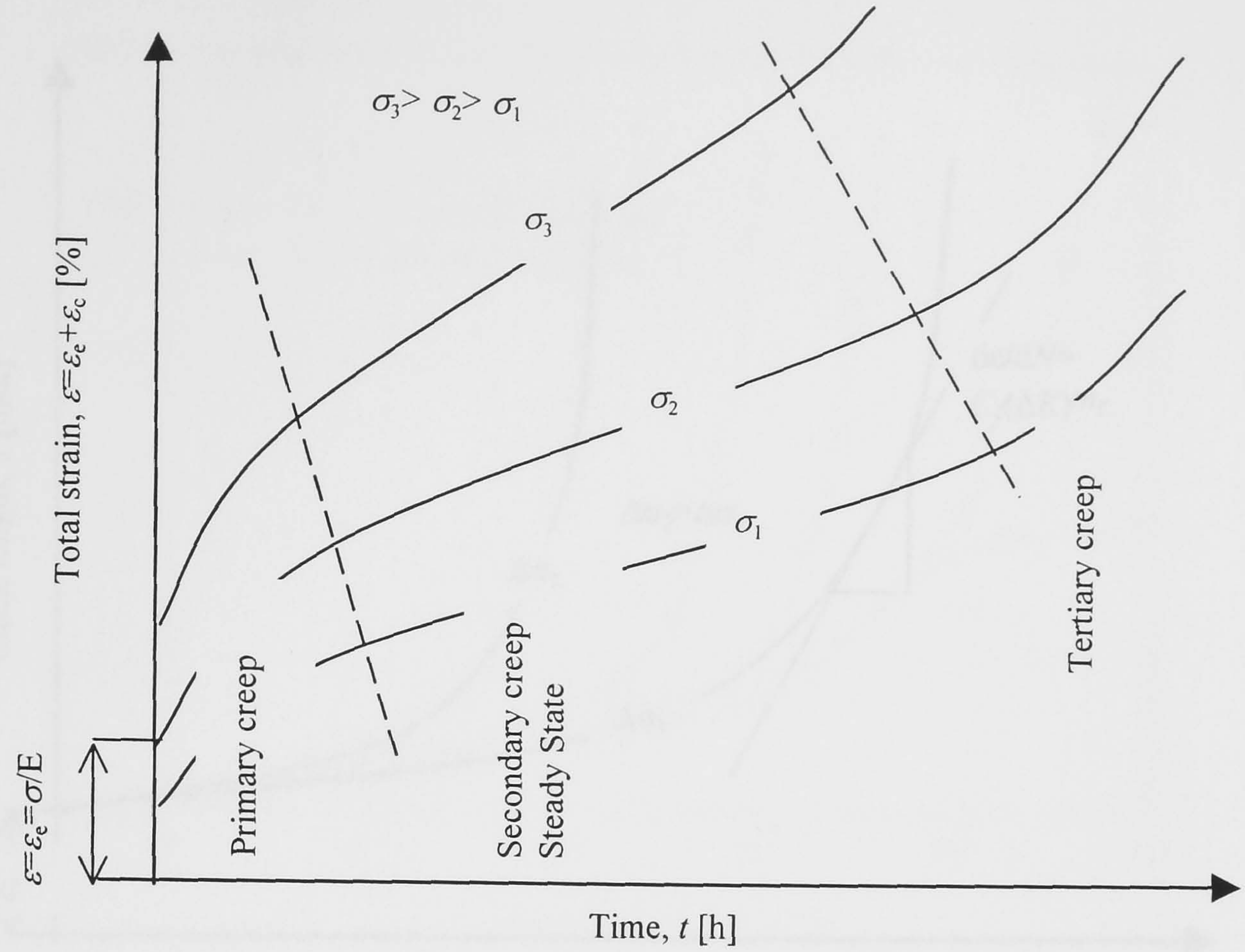

Figure 2.10. Basic strain accumulation creep curves for different loads at constant temperature.

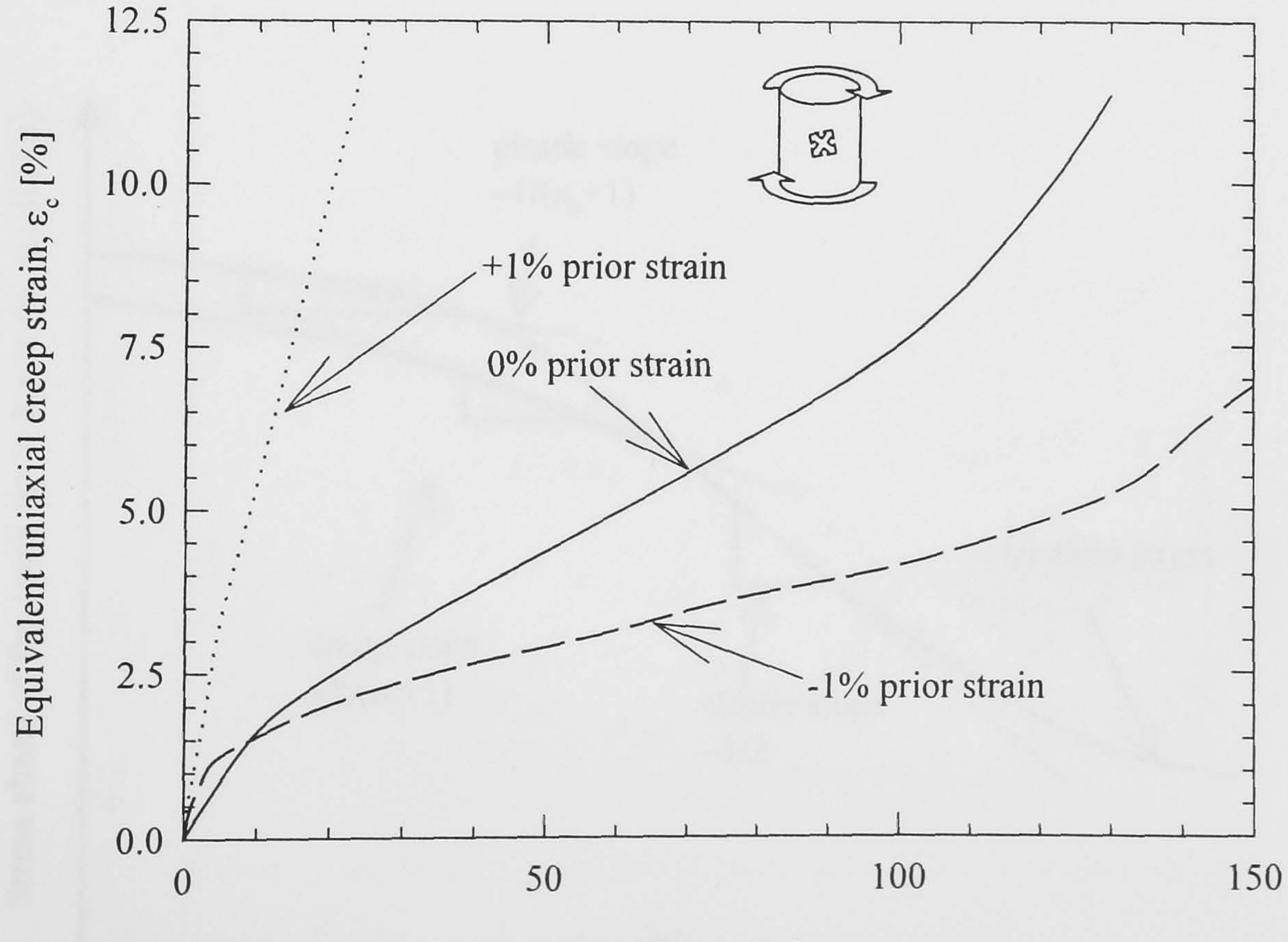

Figure 2.11. Effect of prestrain at 20°C on creep behaviour of the aluminium RR58 alloy for a torsional stress of 128 MPa and 150°C from Biscaya (1971).

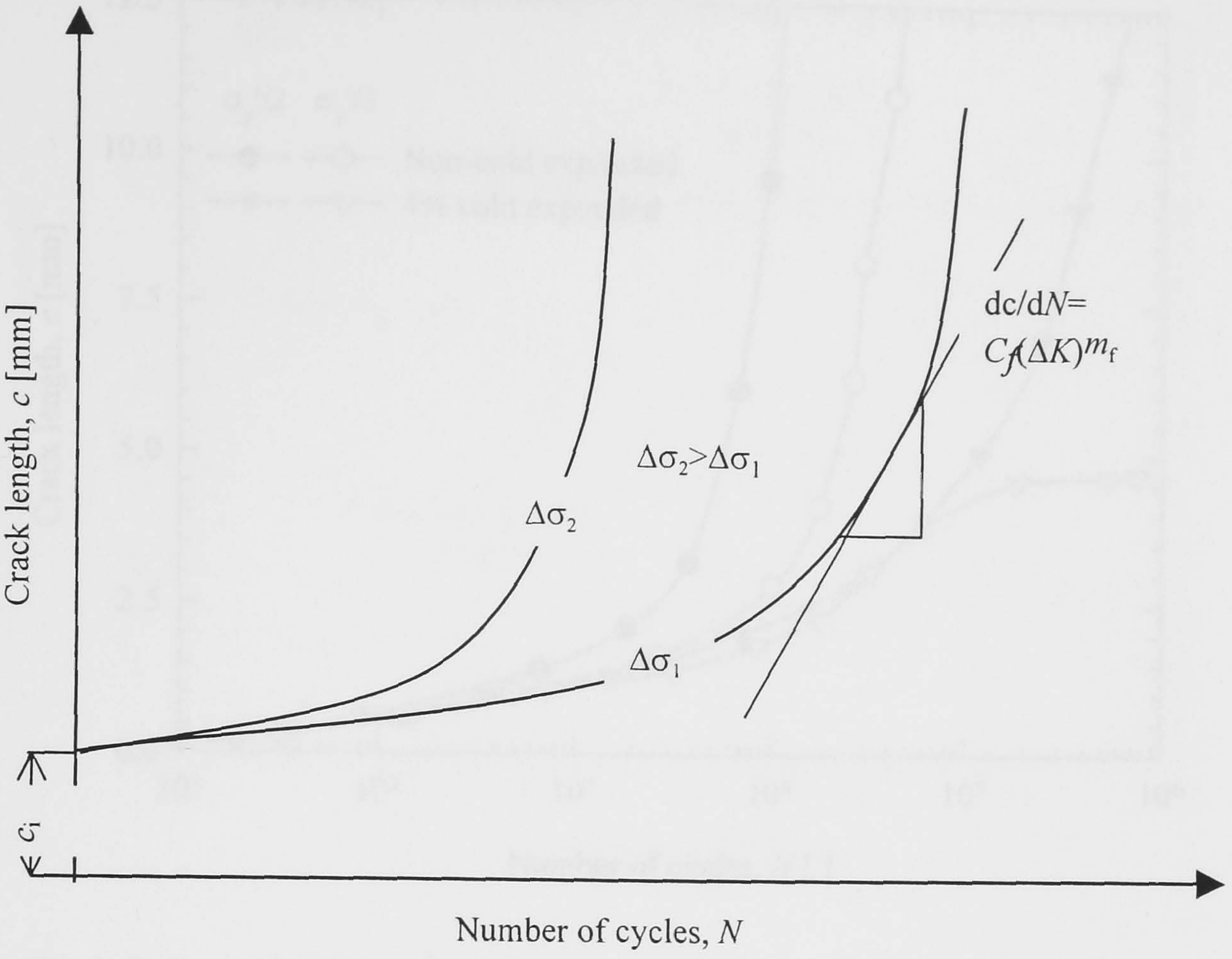

Figure 2.12. Typical fatigue crack growth behaviour in constant amplitude loading from Suresh (1991).

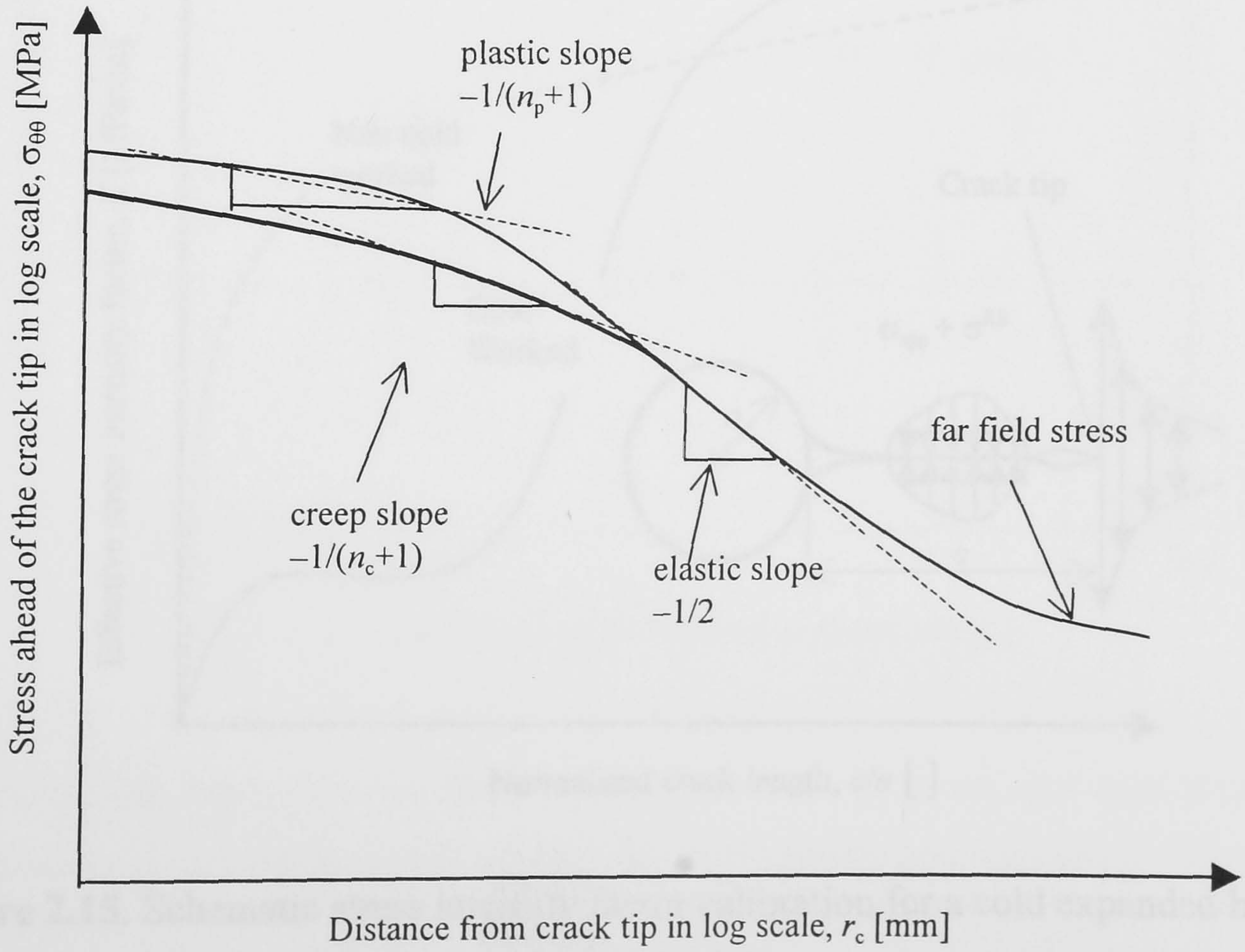

Figure 2.13. Stress distribution ahead of crack tip from Anderson (1995).

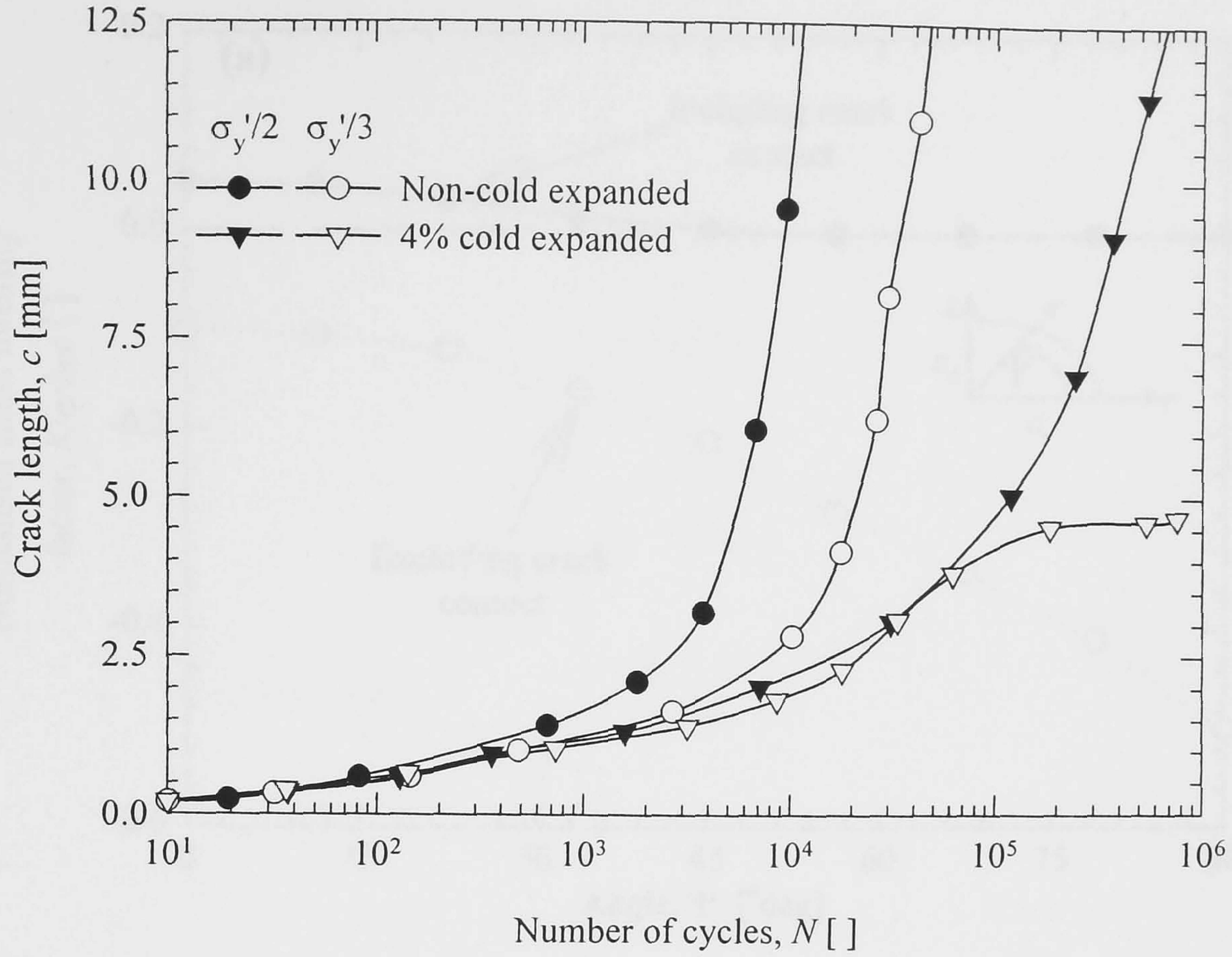

Figure 2.14. Schematic fatigue crack growth improvement due to cold expansion on aluminium alloy Al 2024 from Priest (1997).

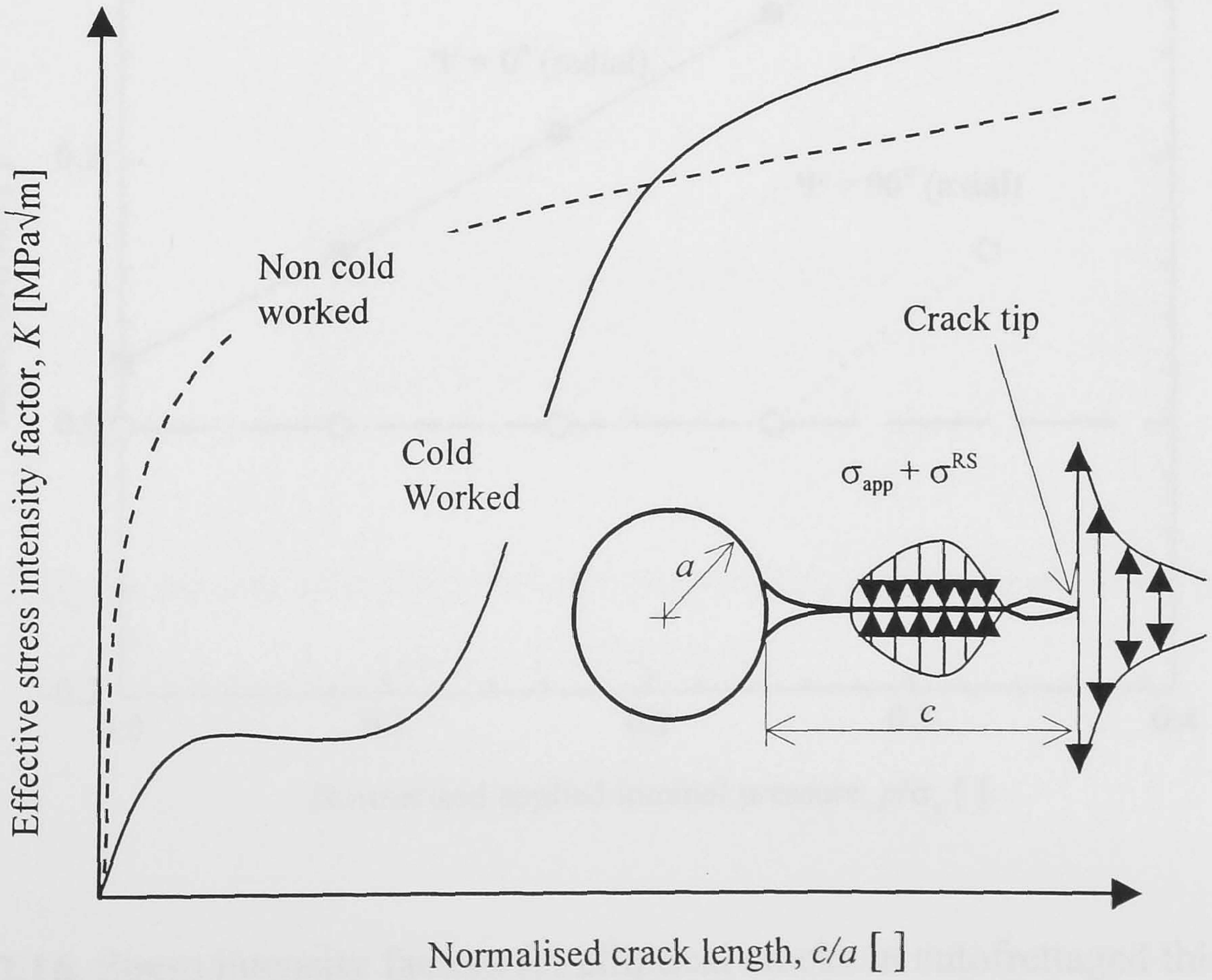

Figure 2.15. Schematic stress intensity factor calibration for a cold expanded hole from Grandt (1975).

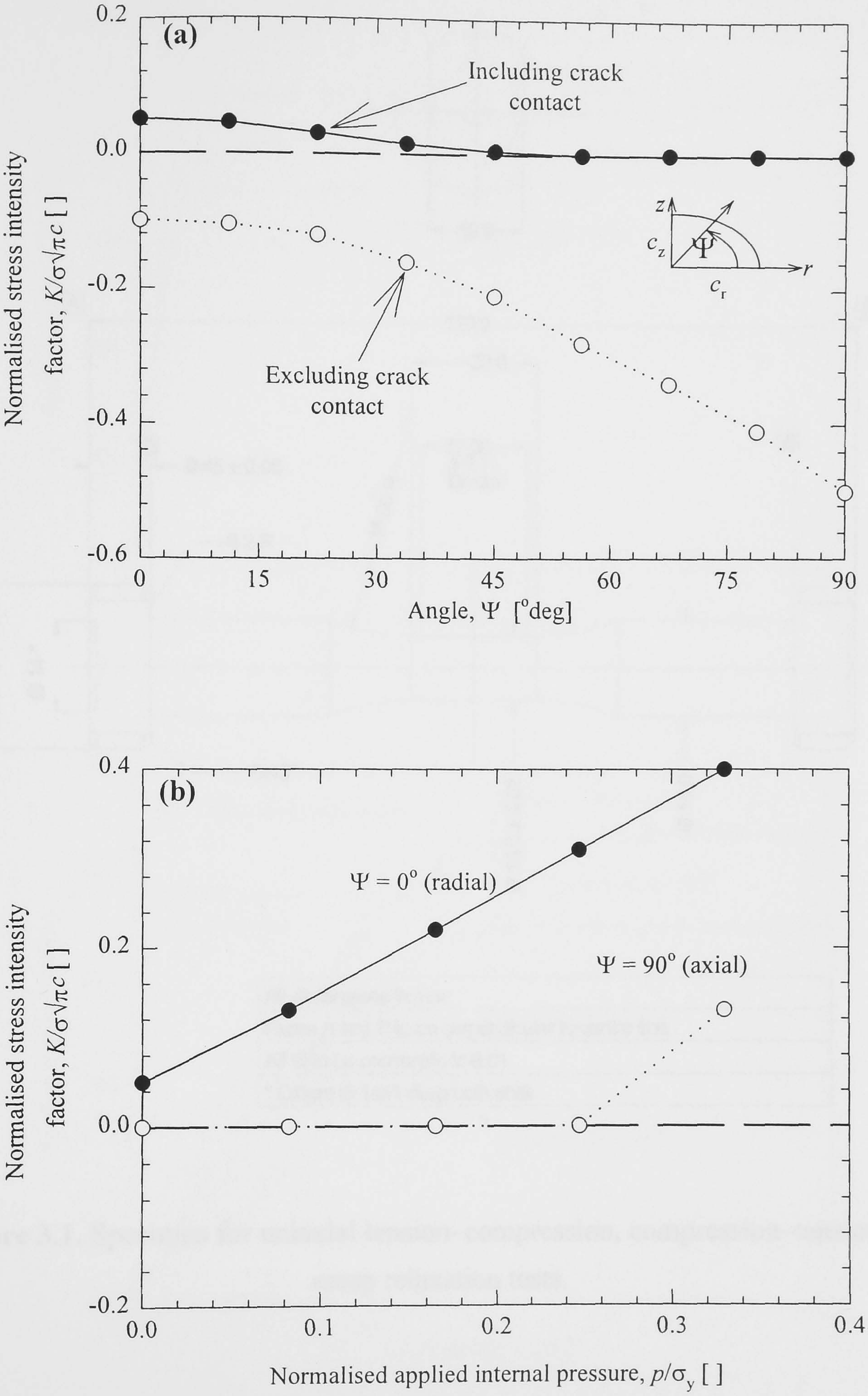

Figure 2.16. Stress intensity factors for elliptical cracks in autofrettaged thick–cylinders from Lin and Smith (1997): (a) crack closure and (b) loading effect.

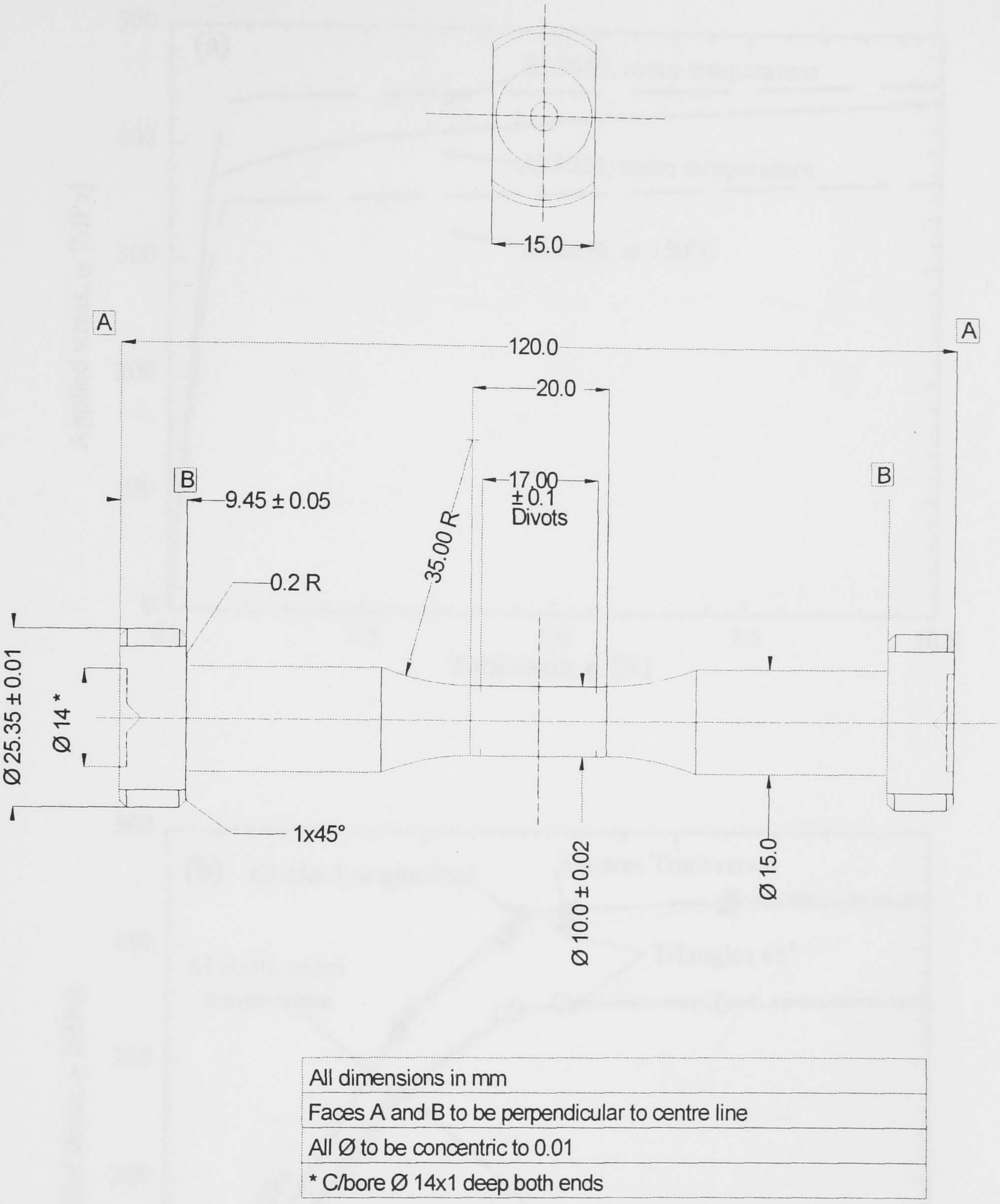

Figure 3.1. Specimen for uniaxial tension–compression, compression–tension and creep relaxation tests.

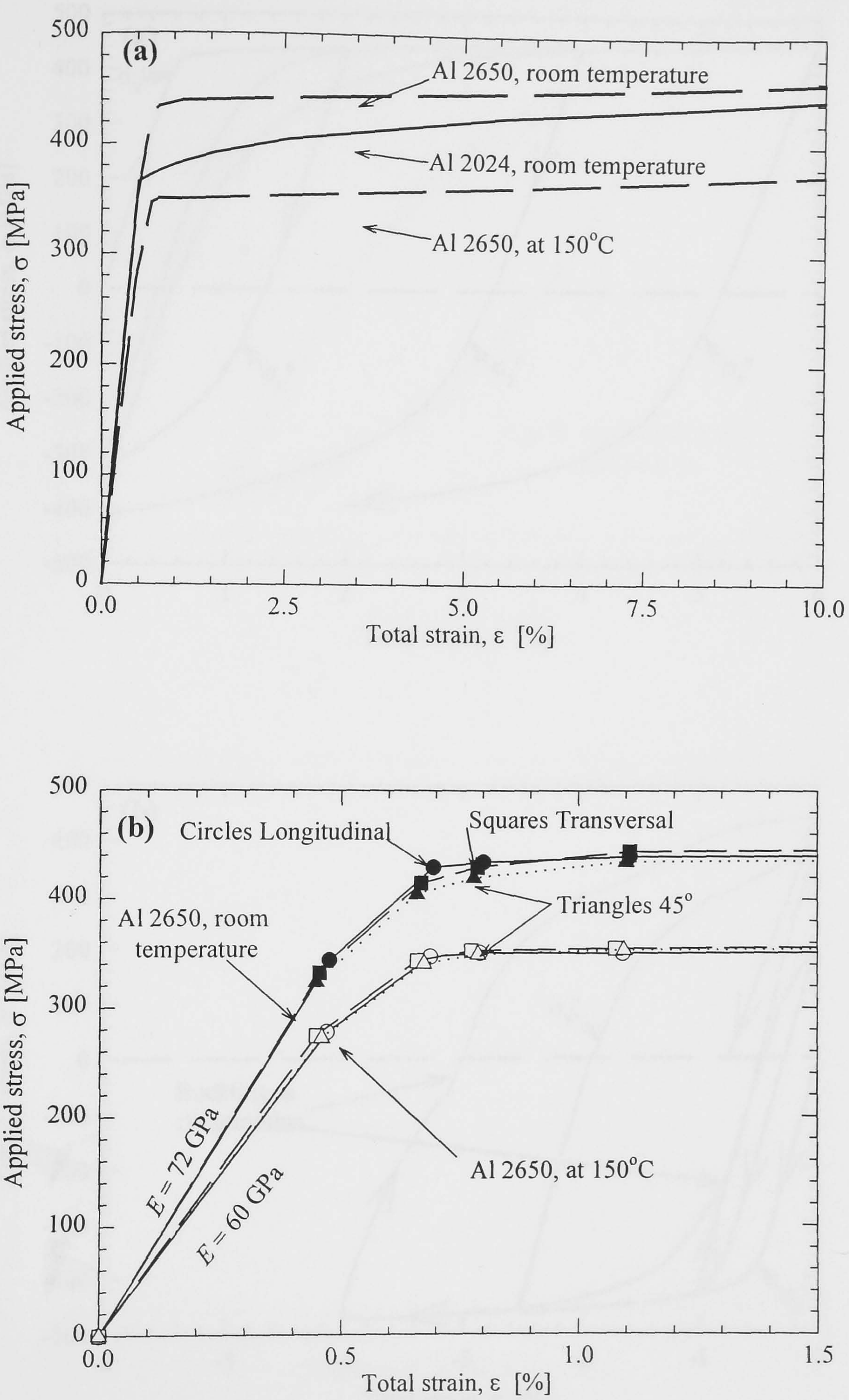

Figure 3.2. Tensile tests for aluminium alloy Al 2650 at room temperature and 150°C (a) Average behaviour compared to Al 2024 and (b) grain orientation effect.

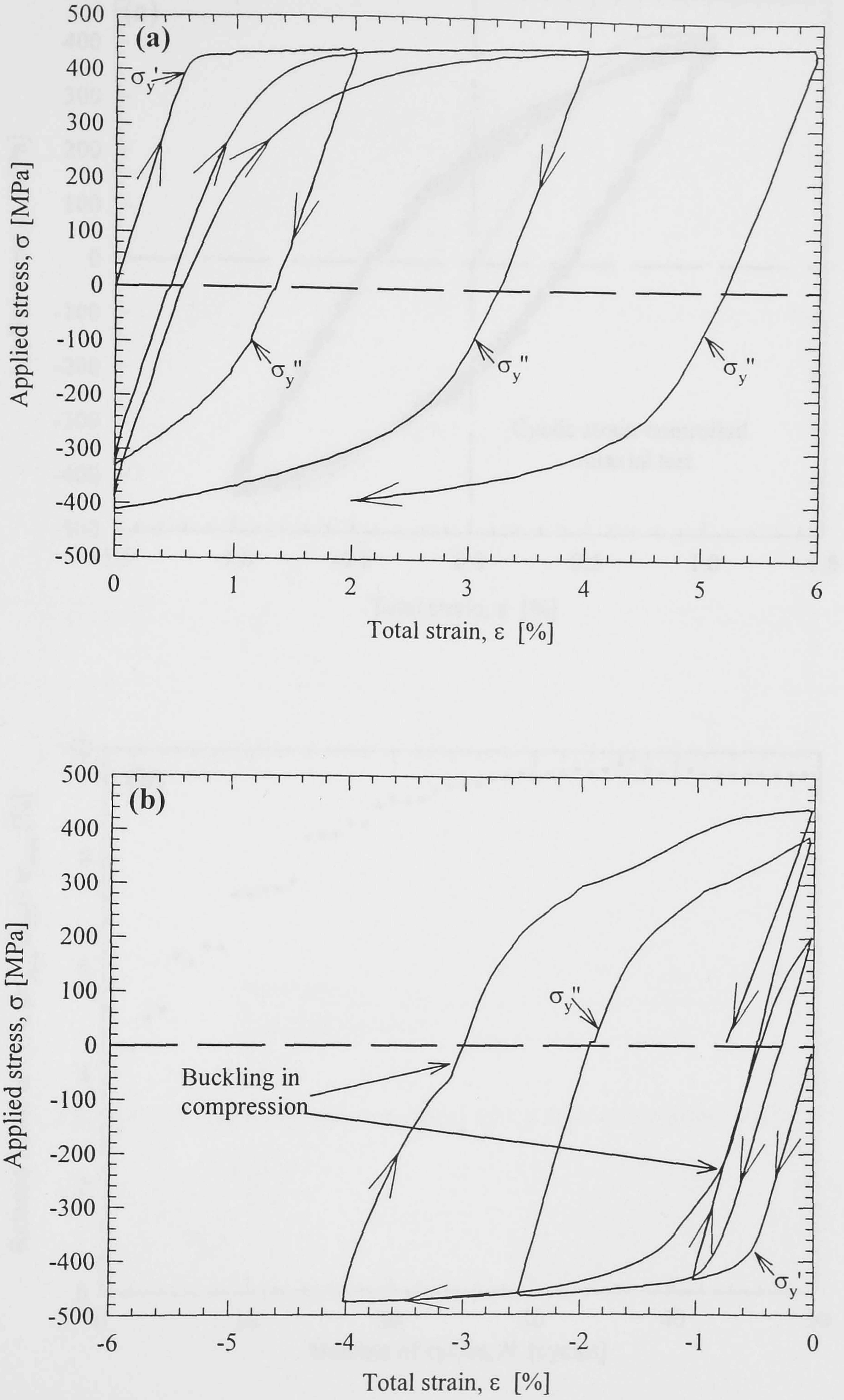

Figure 3.3. Cyclic tests for aluminium alloy Al 2650 at room temperature: (a) tension–compression and (b) compression tension.

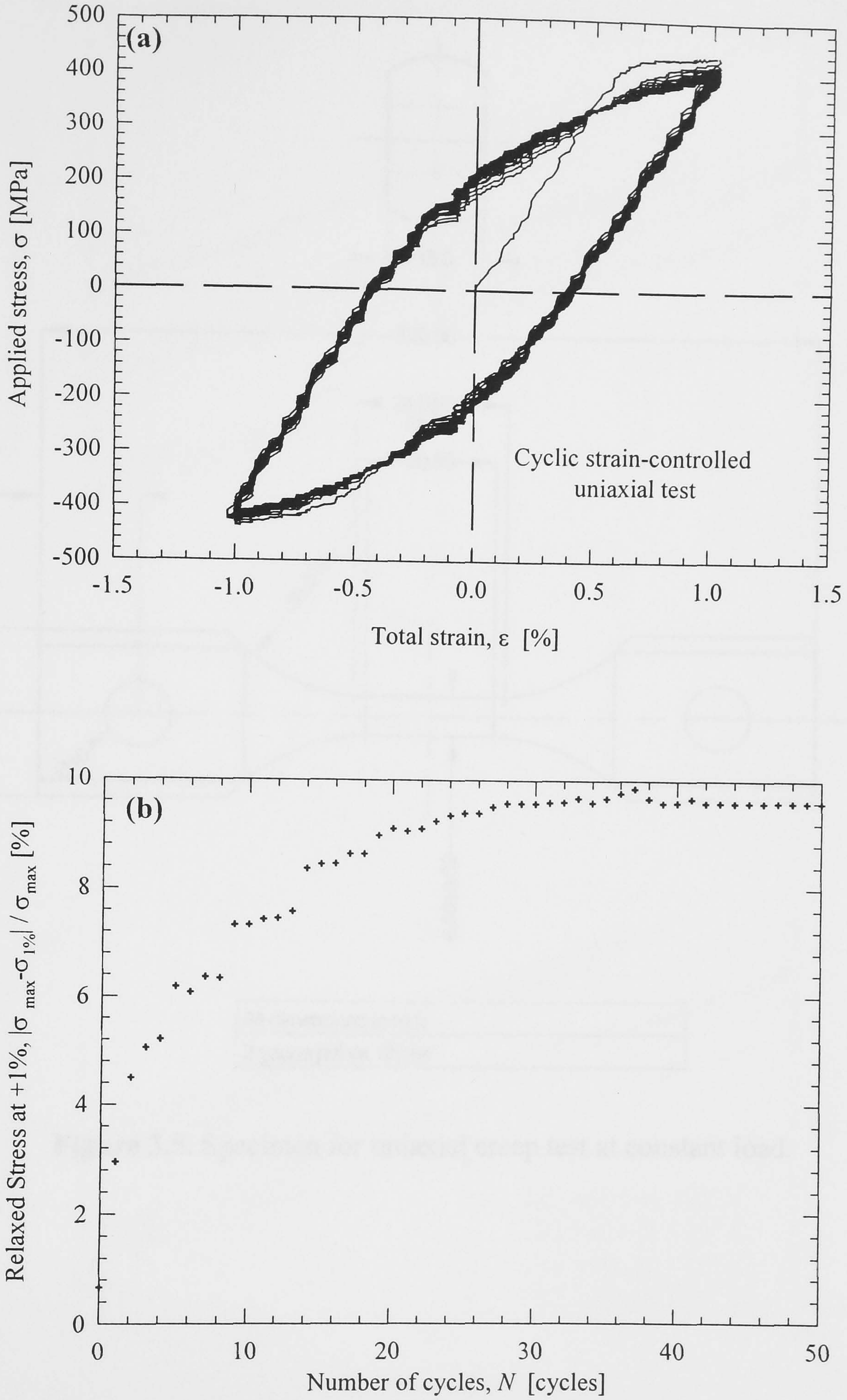

Figure 3.4. Cyclic softening in strain controlled uniaxial test for aluminium alloy Al 2650 at room temperature from Martínez (1998): (a) stress versus strain and (b) maximum stress versus number of cycles.

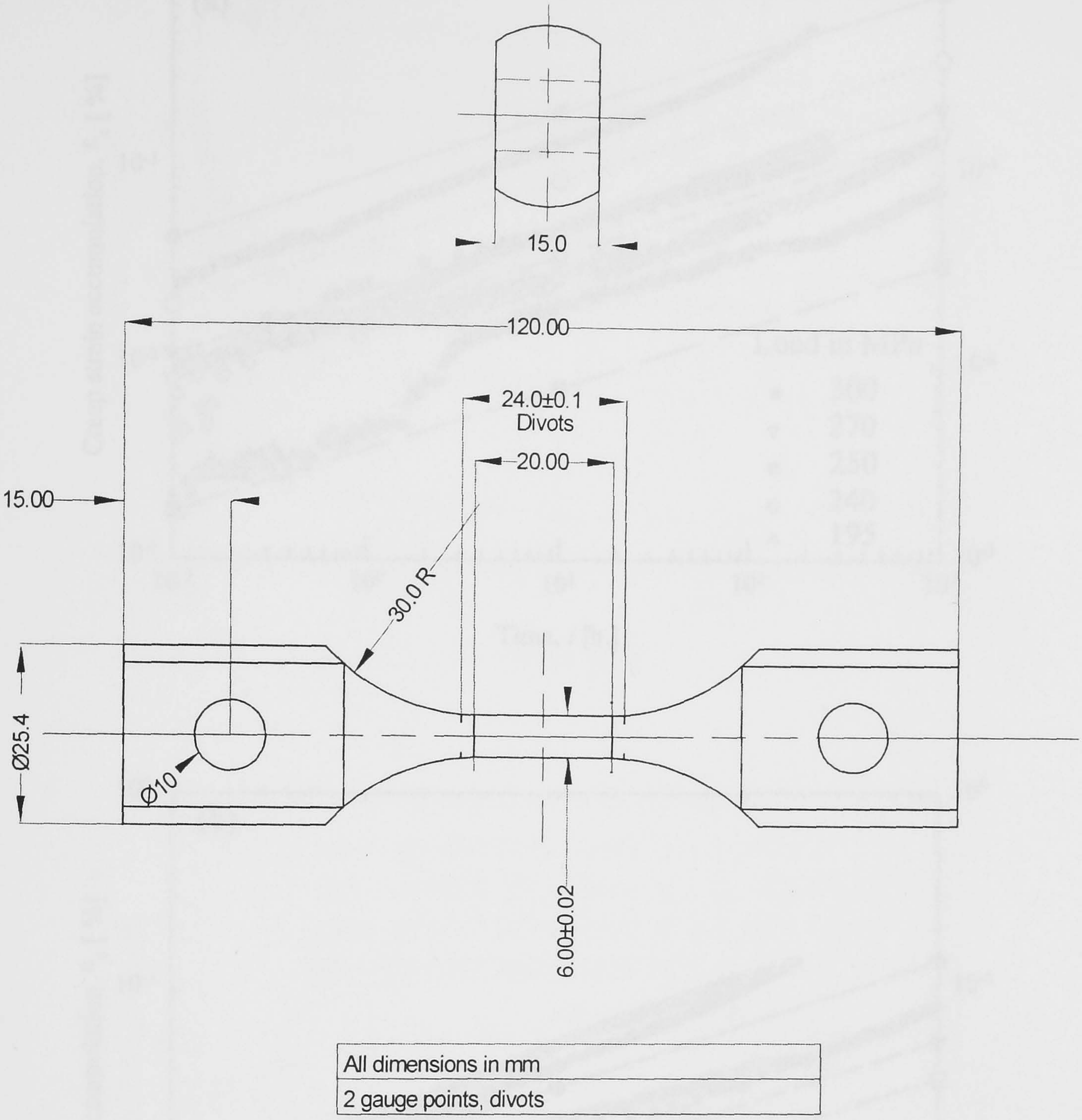

Figure 3.5. Specimen for uniaxial creep test at constant load.

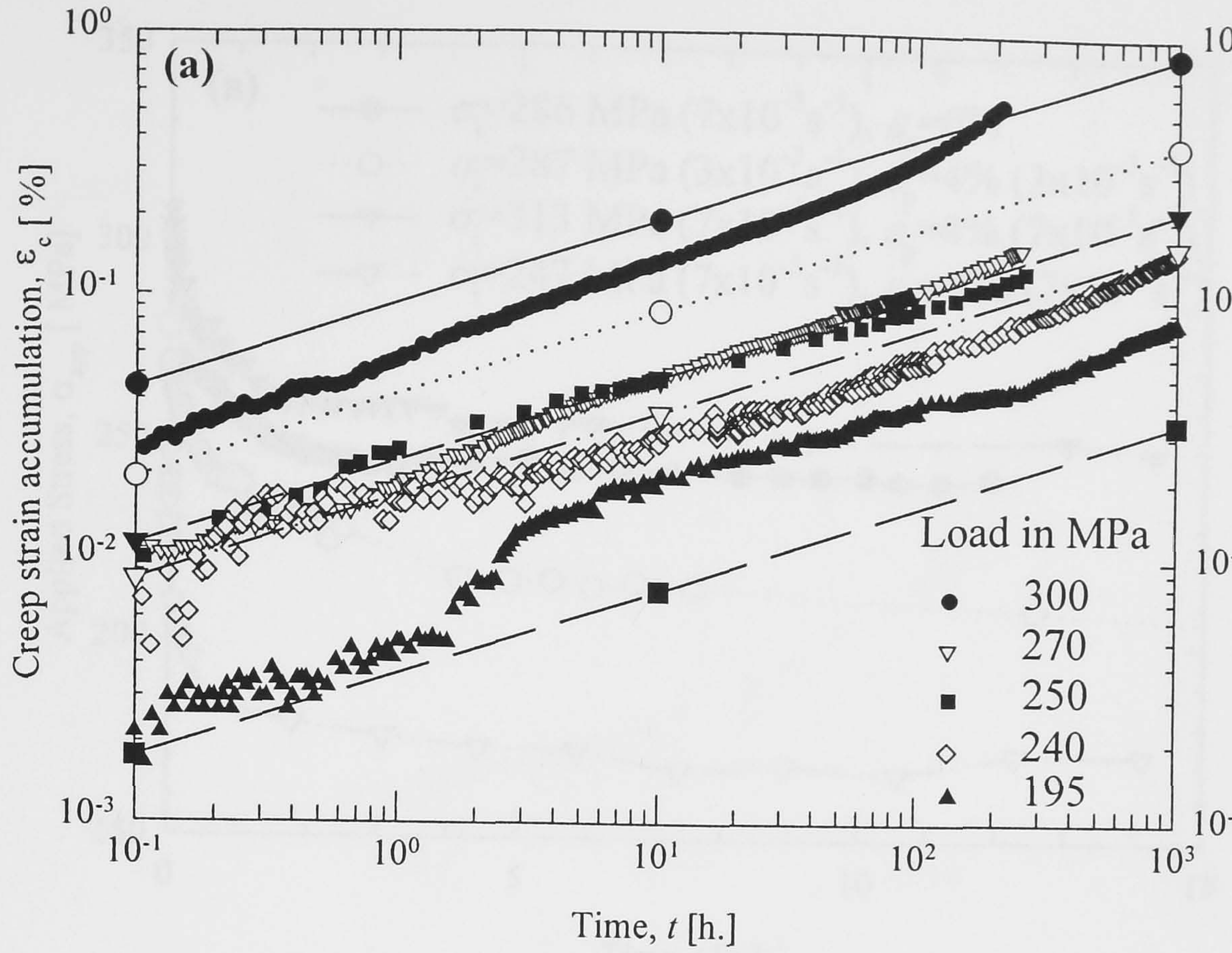

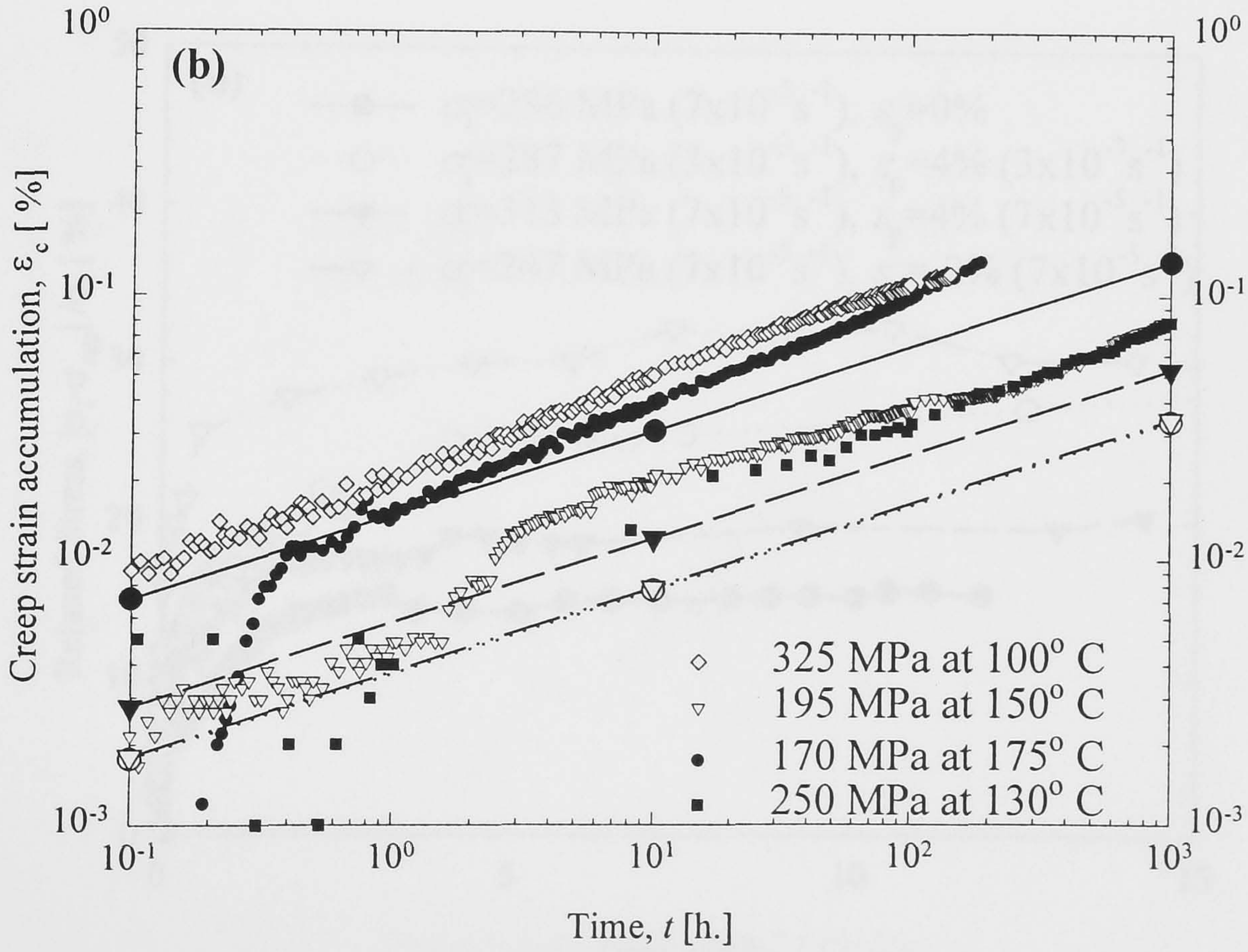

Figure 3.6. Creep strain accumulation tests for aluminium alloy Al 2650 for (a) different loads at 150°C and (b) different temperatures.

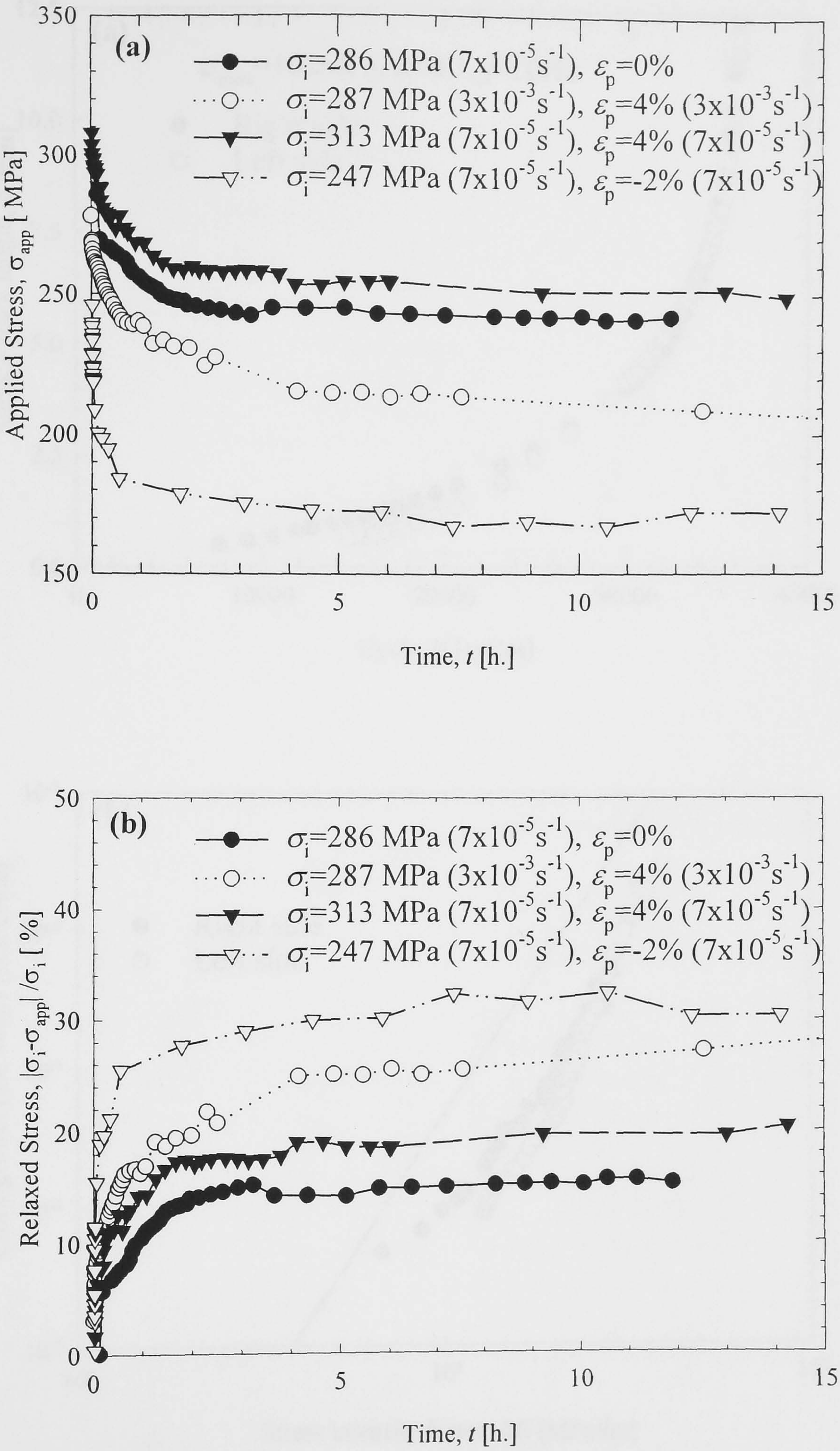

Figure 3.7. Influence of prior plasticity on creep stress relaxation at 150°C for aluminium alloy Al 2650 for (a) absolute applied stress and (b) relative to initial stress from Martínez (1998).

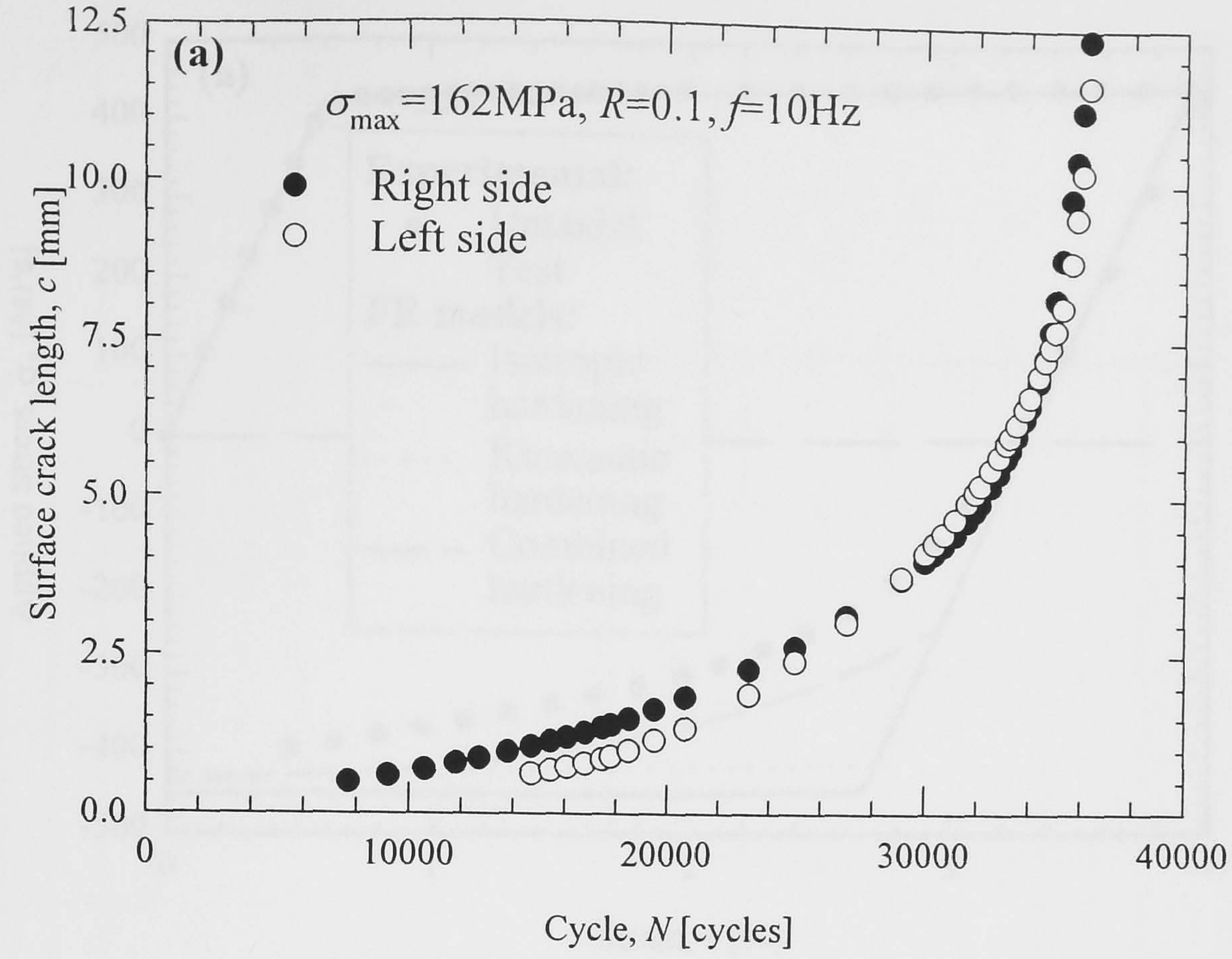

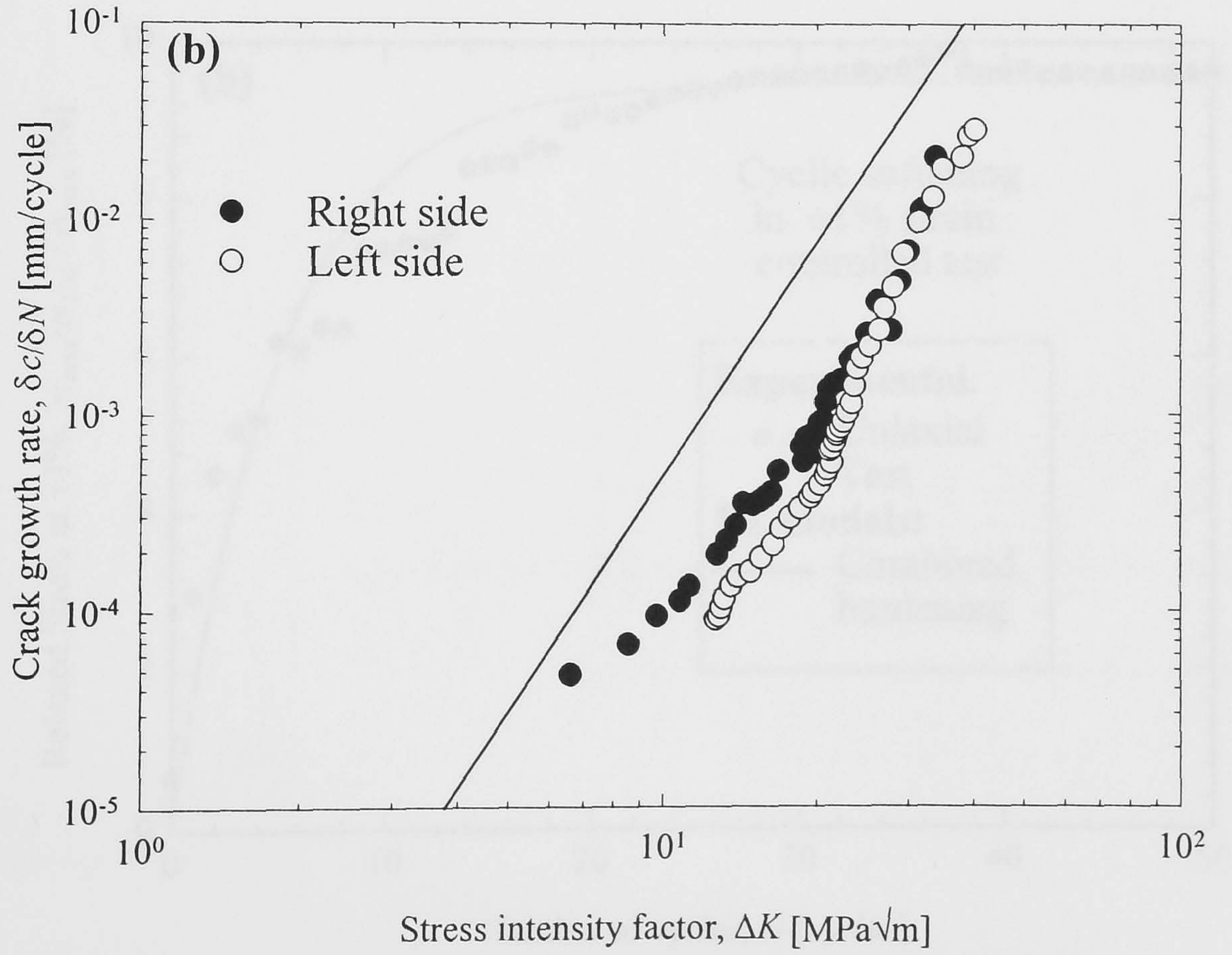

Figure 3.8. Fatigue crack growth for aluminium alloy Al 2650: (a) crack length versus number of cycles and (b) crack growth rate versus stress intensity factor from Lacarac (2000).

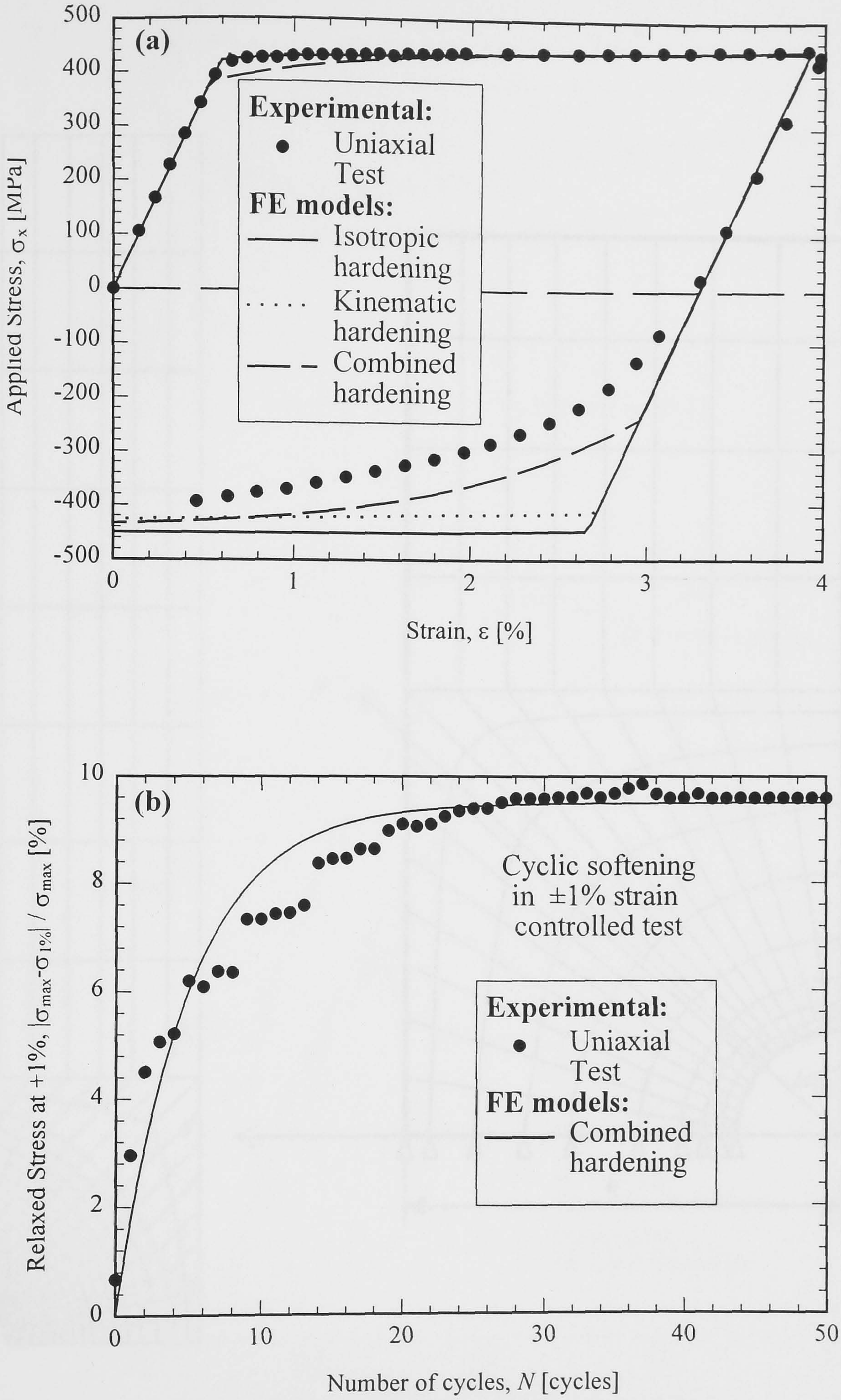

Figure 4.1. Plasticity models used in FE simulations for Al 2650 at room temperature: (a) uniaxial tension–compression test and (b) cyclic softening in ±1% strain controlled test.

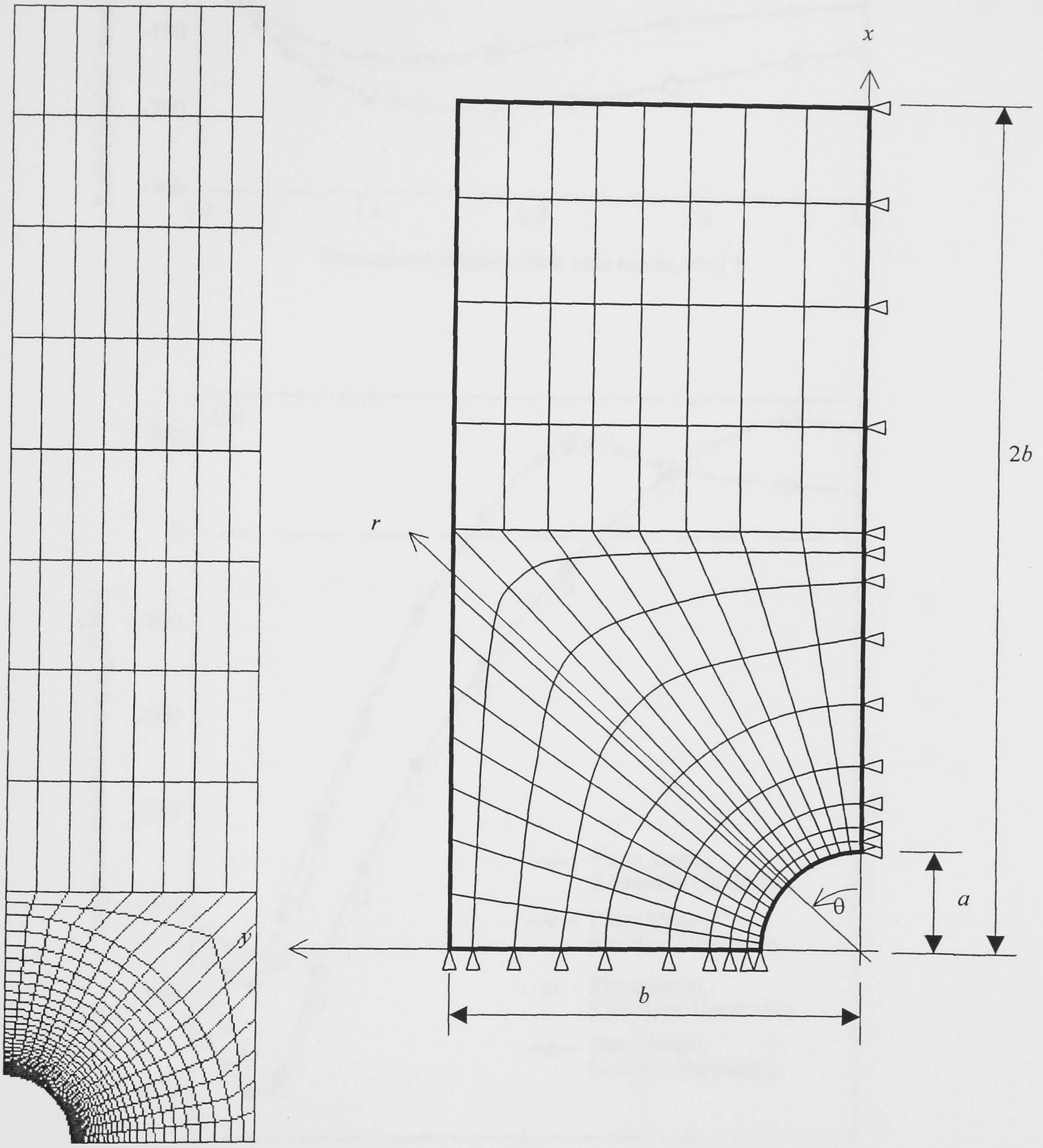

Figure 4.2. FE snapshot and schematic 2D FE mesh used for simulation of cold expansion.

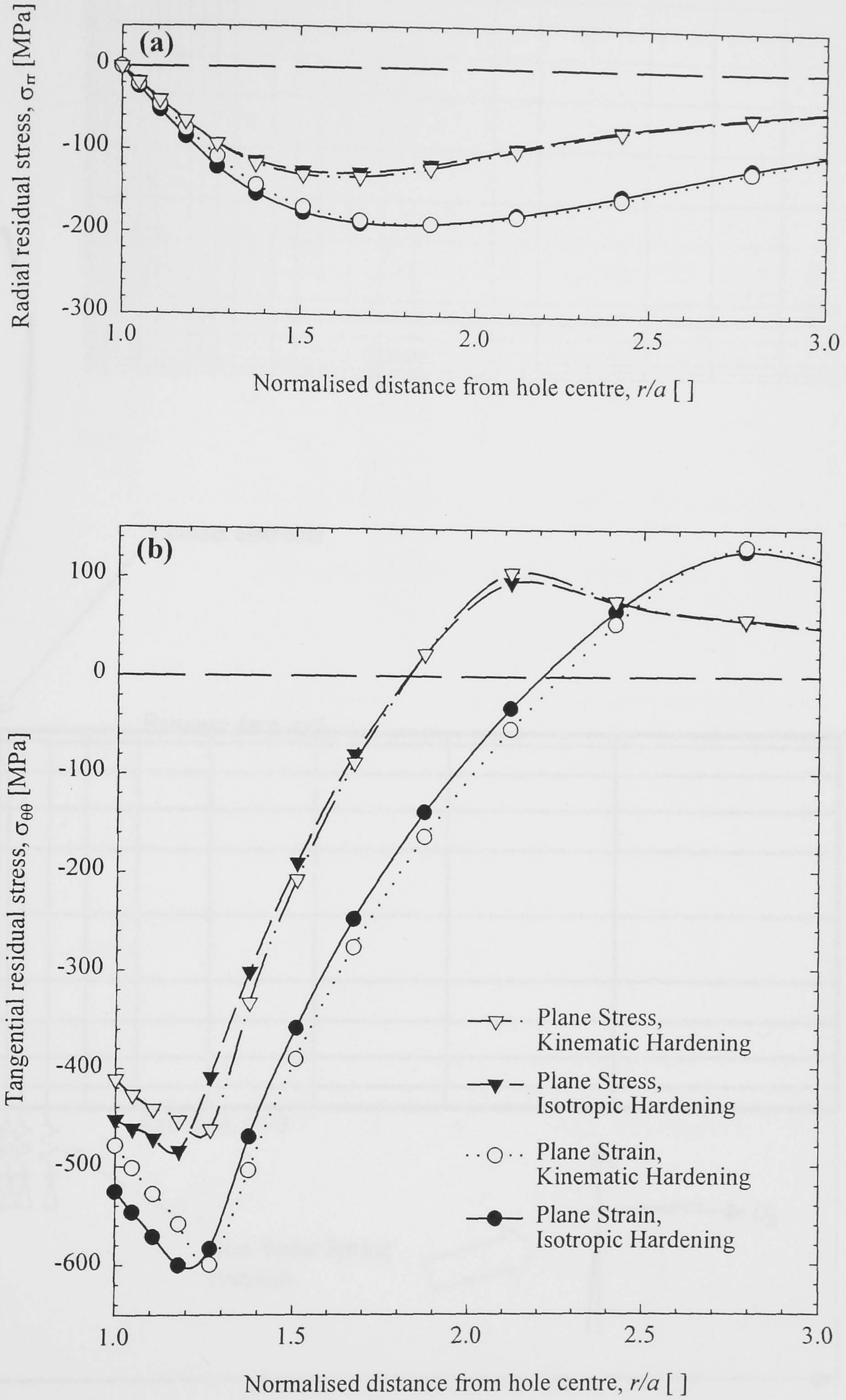

Figure 4.3. Residual stresses obtained from 2D FE simulations for Al 2650 at room temperature: (a) radial and (b) tangential.

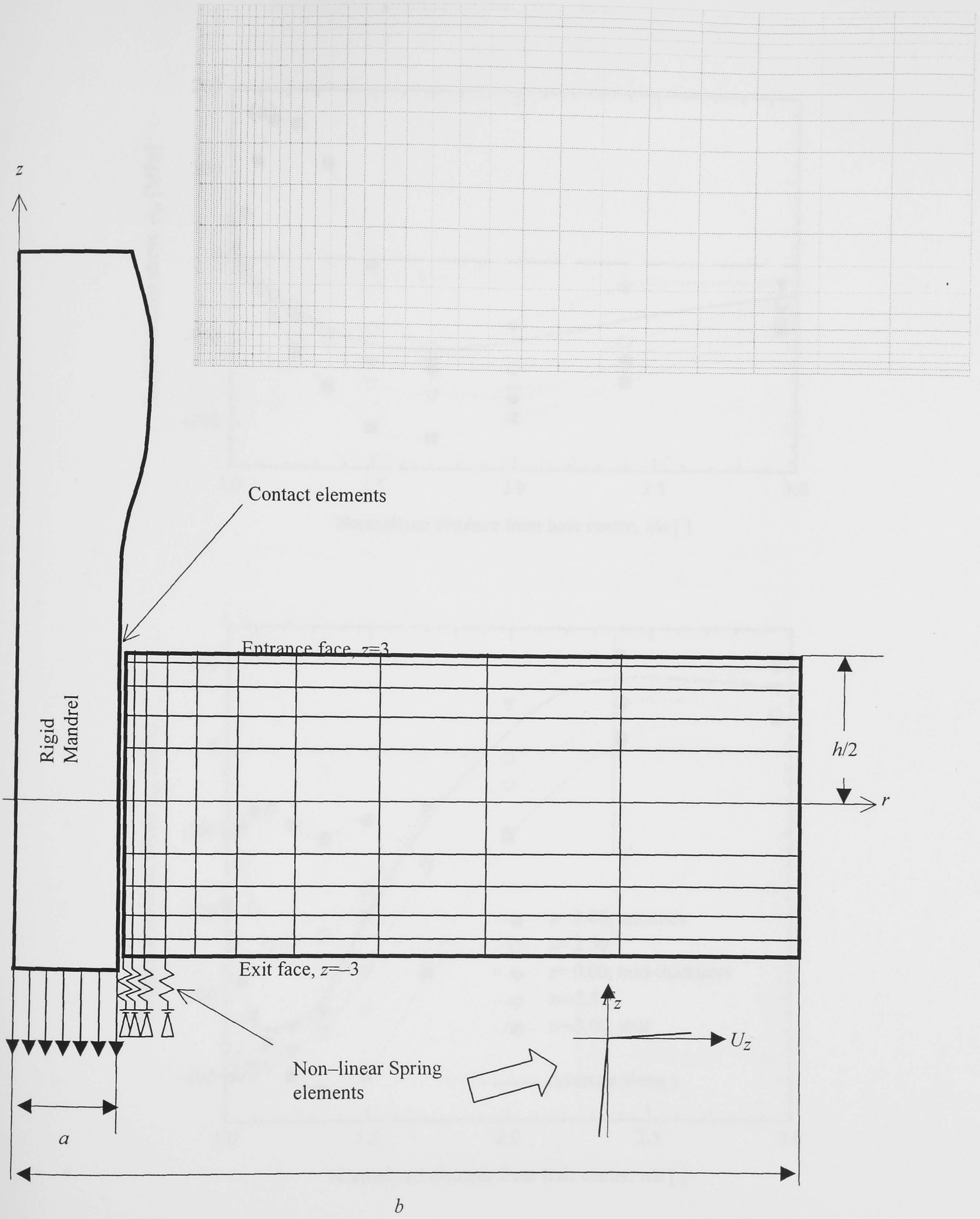

Figure 4.4. FE snapshot and schematic 2D axisymmetric FE mesh used for simulation of mandrel pull through cold expansion.

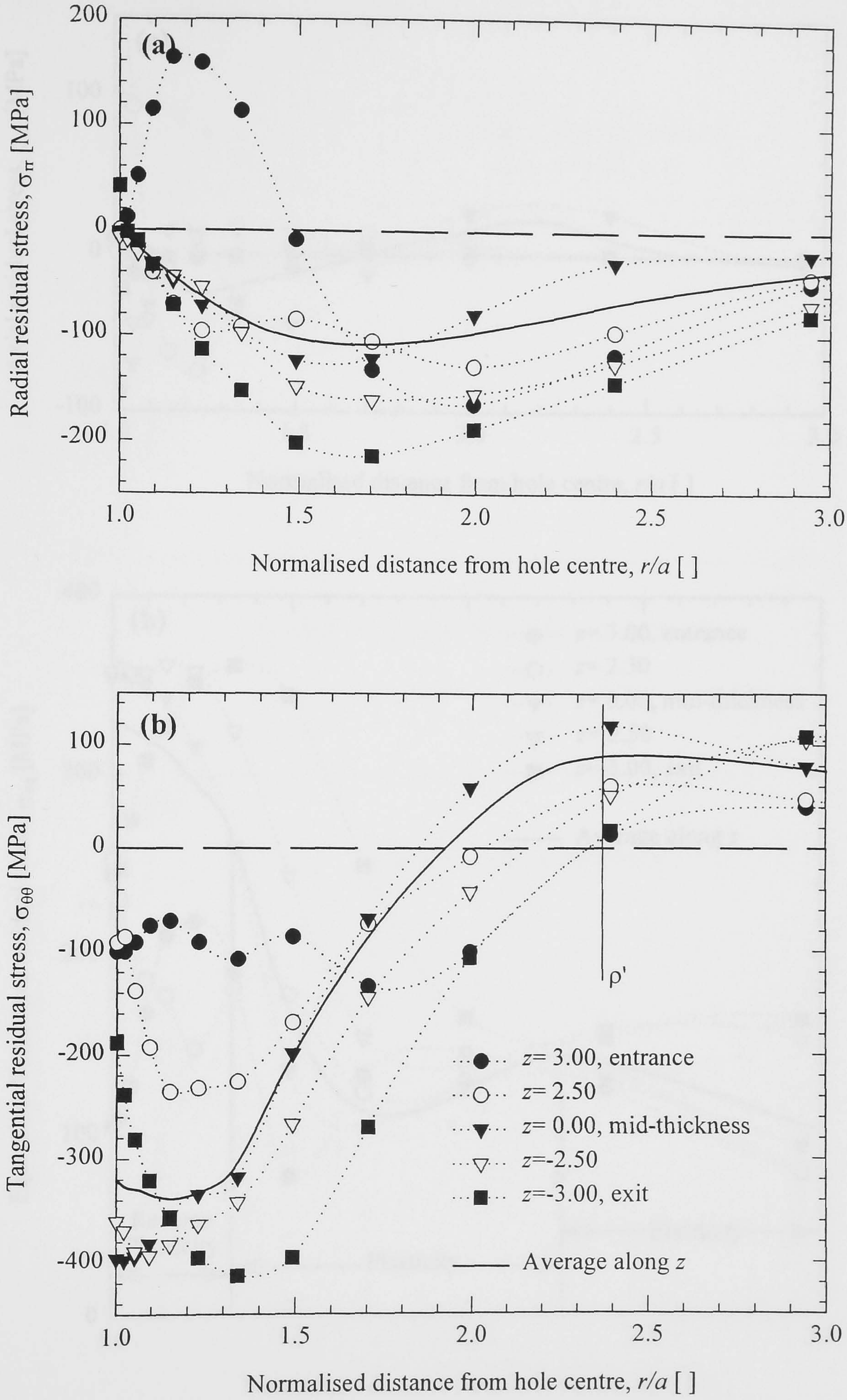

Figure 4.5. Residual stresses as a function of radial position for different through–thickness positions using a 2D axisymmetric, combined hardening FE model: (a) radial stresses and (b) tangential stresses.

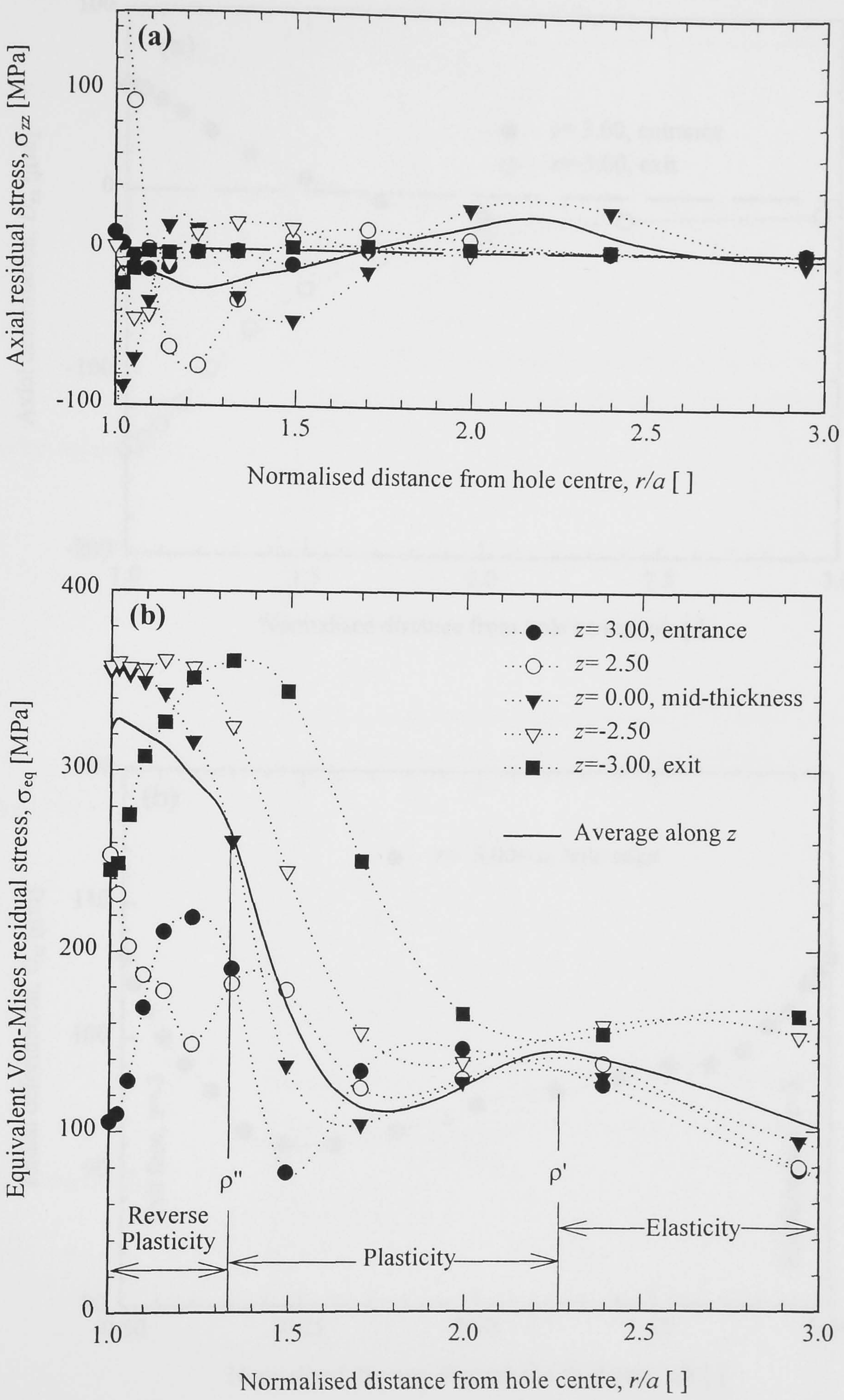

Figure 4.6. Residual stresses as a function of radial position for different through–thickness positions using a 2D axisymmetric, combined hardening FE model: (a) axial stresses and (b) Von–Mises equivalent stresses.

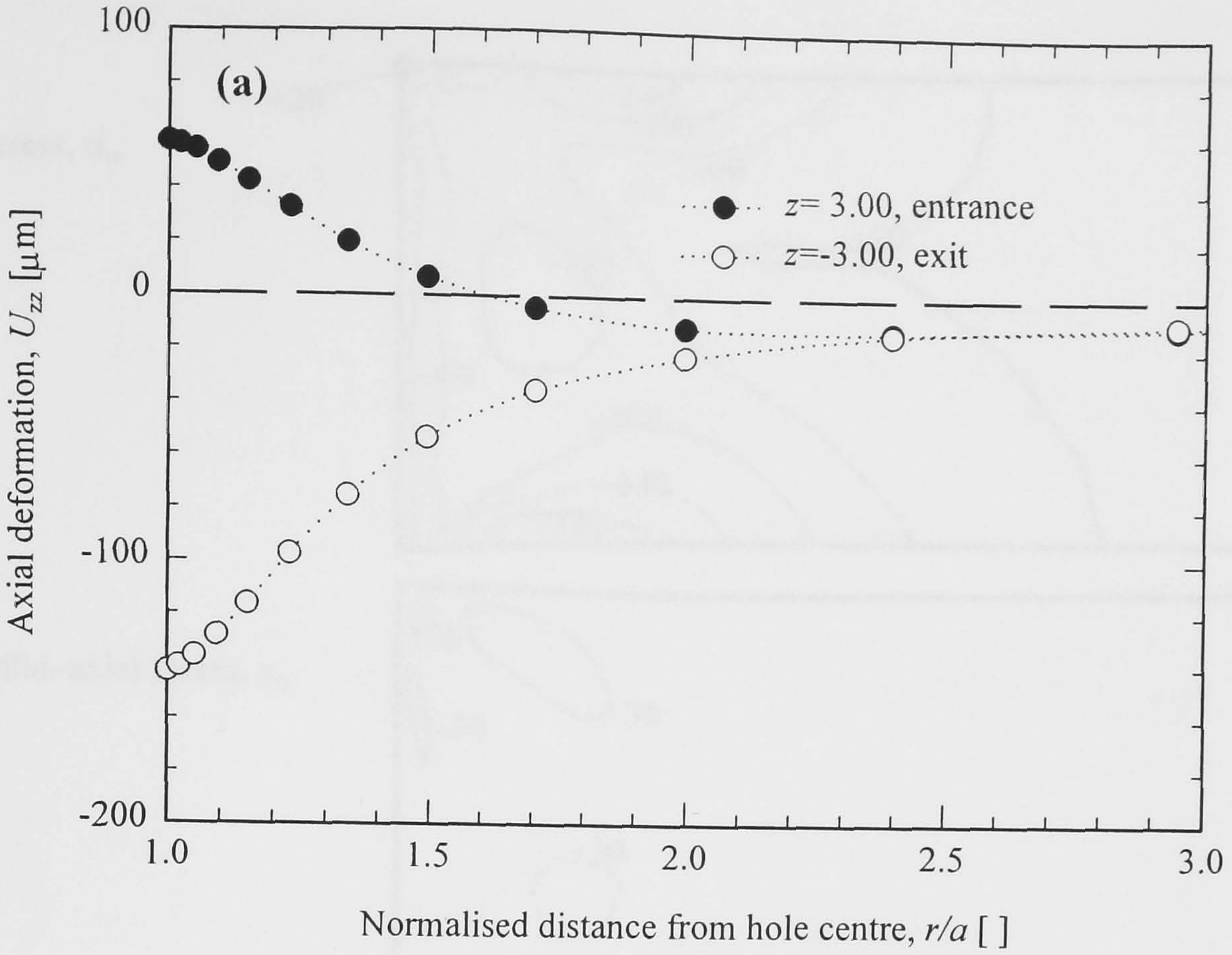

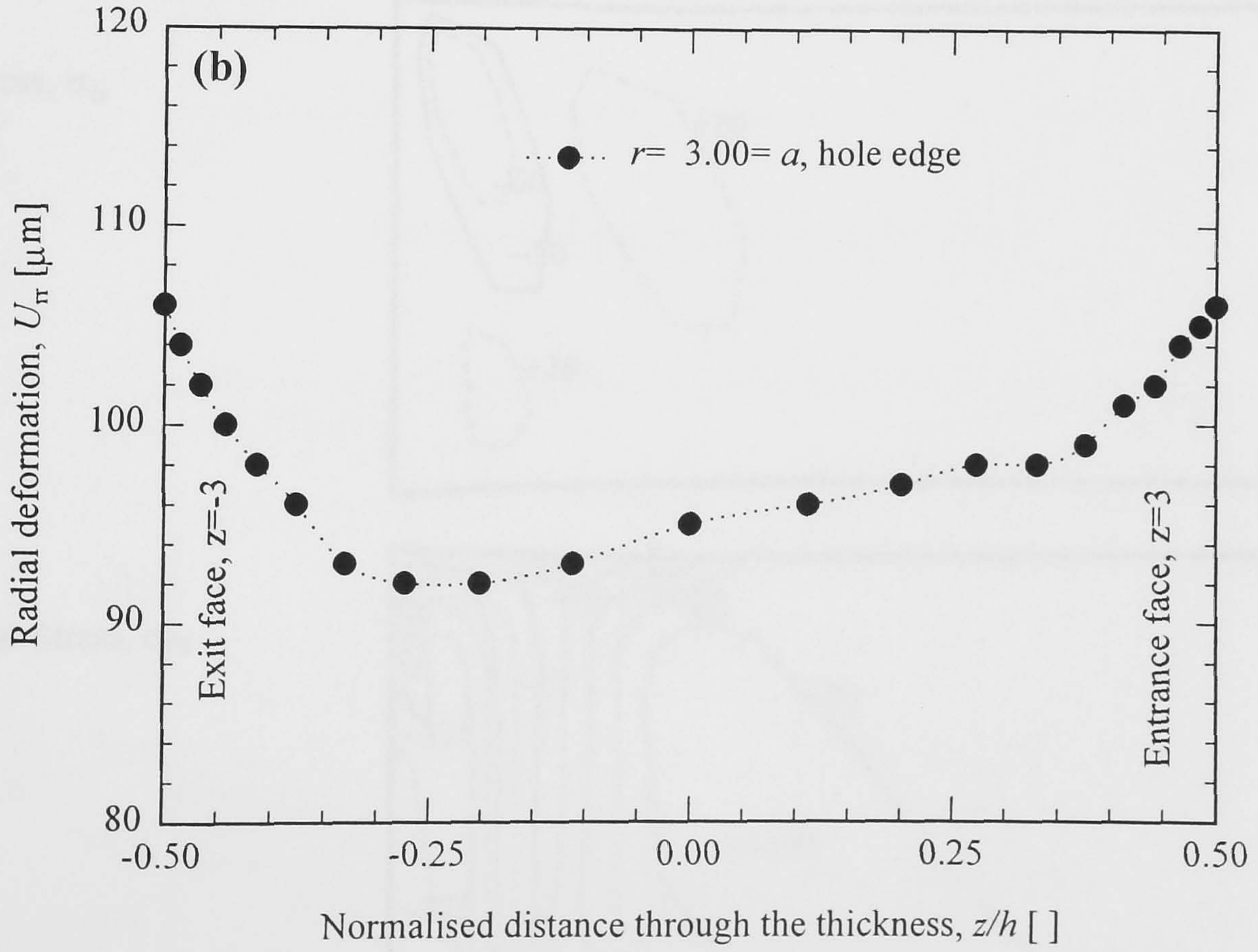

Figure 4.7. Permanent deformations using a 2D axisymmetric, kinematic hardening FE model: (a) axial displacement of entrance and exit faces and (b) radial displacement of the hole edge.

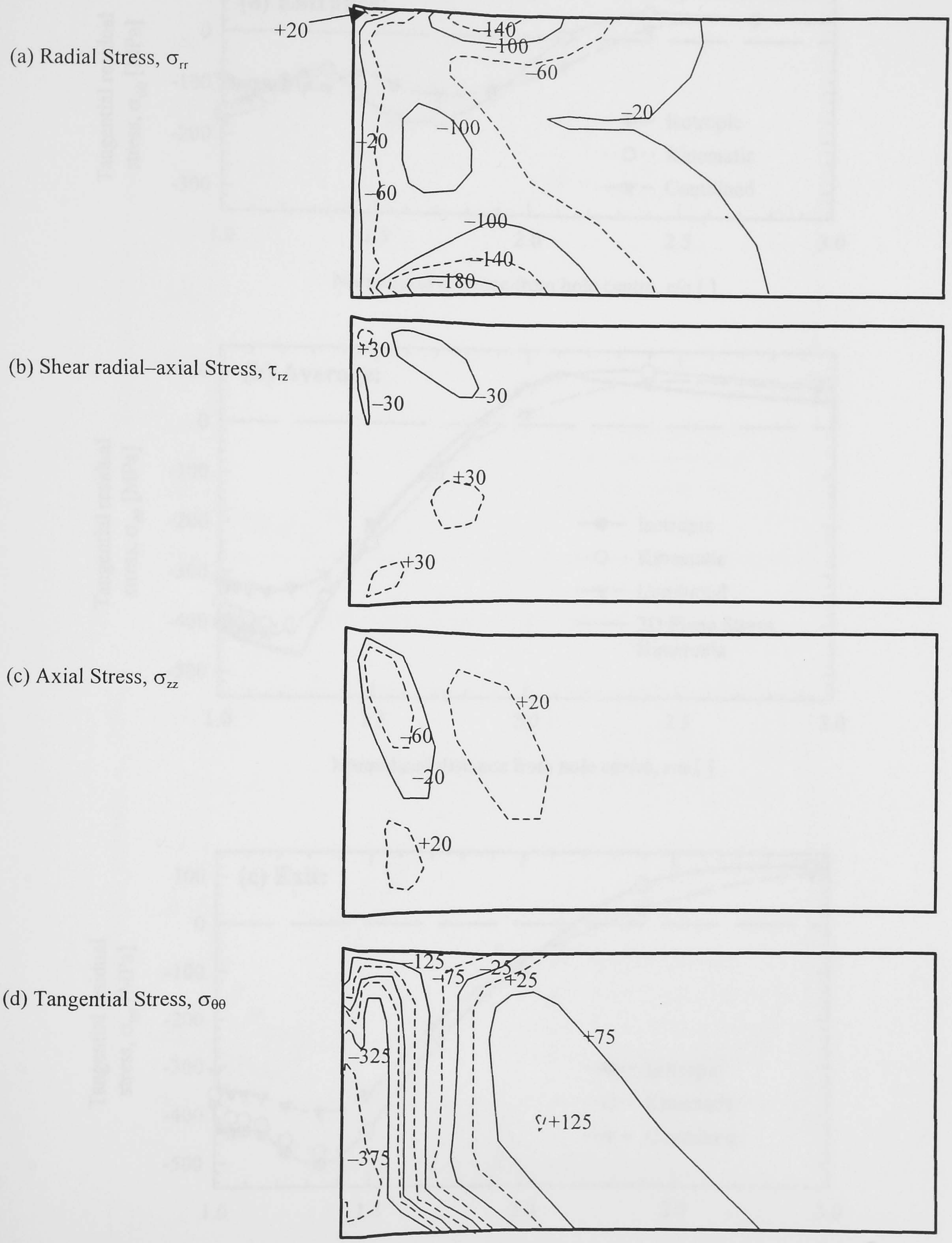

(a) Radial Stress, σ_{rr}

(b) Shear radial–axial Stress, τ_{rz}

(c) Axial Stress, σ_{zz}

(d) Tangential Stress, $\sigma_{\theta\theta}$

Figure 4.8. Finite element simulation of mandrel pulled through (a) radial, (b) shear radial–axial, (c) axial and (d) tangential residual stresses in MPa.

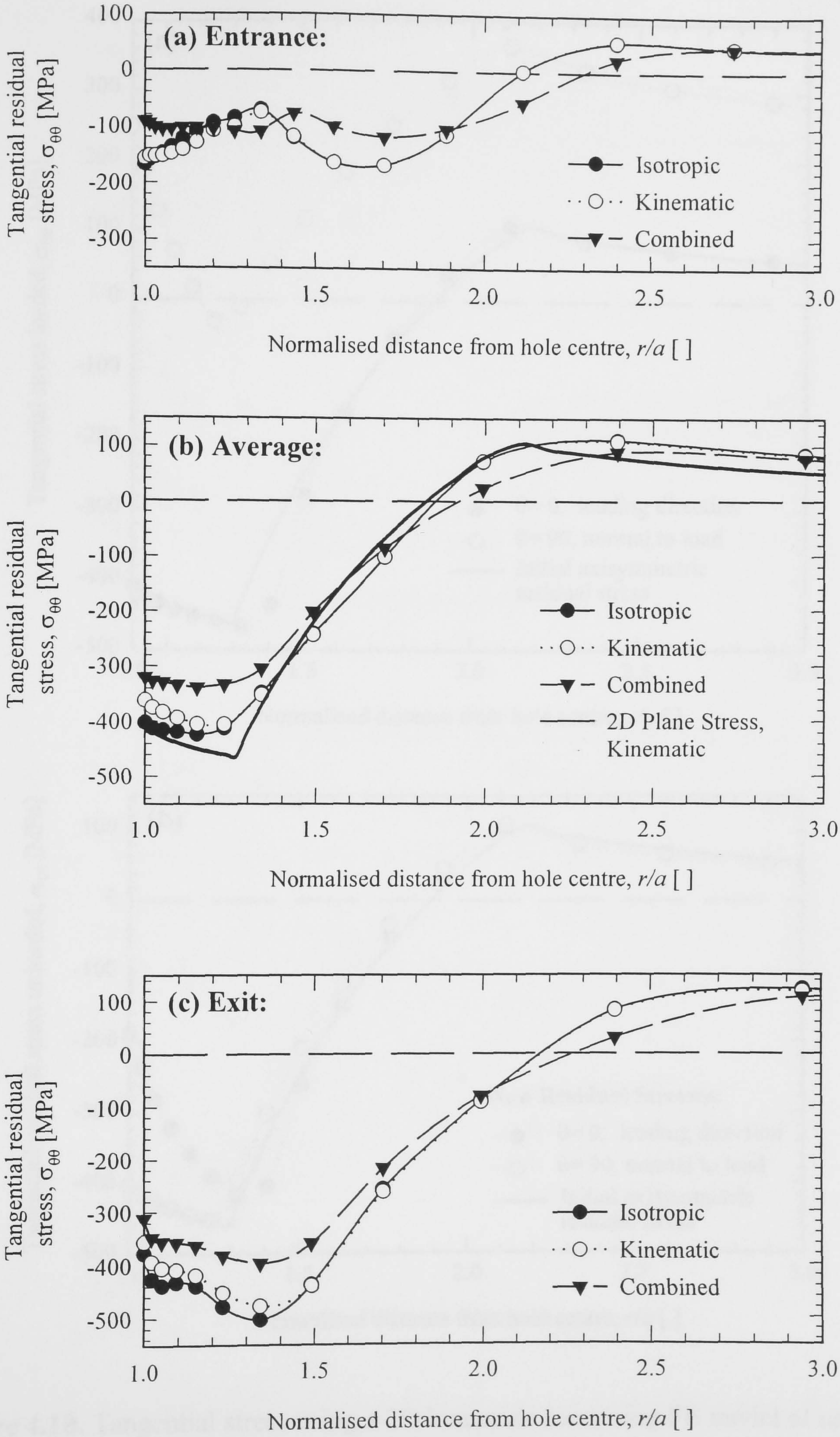

Figure 4.9. Tangential residual stress using a 2D axisymmetric and different hardening FE models for: (a) entrance (b) average through–thickness and (c) exit face.

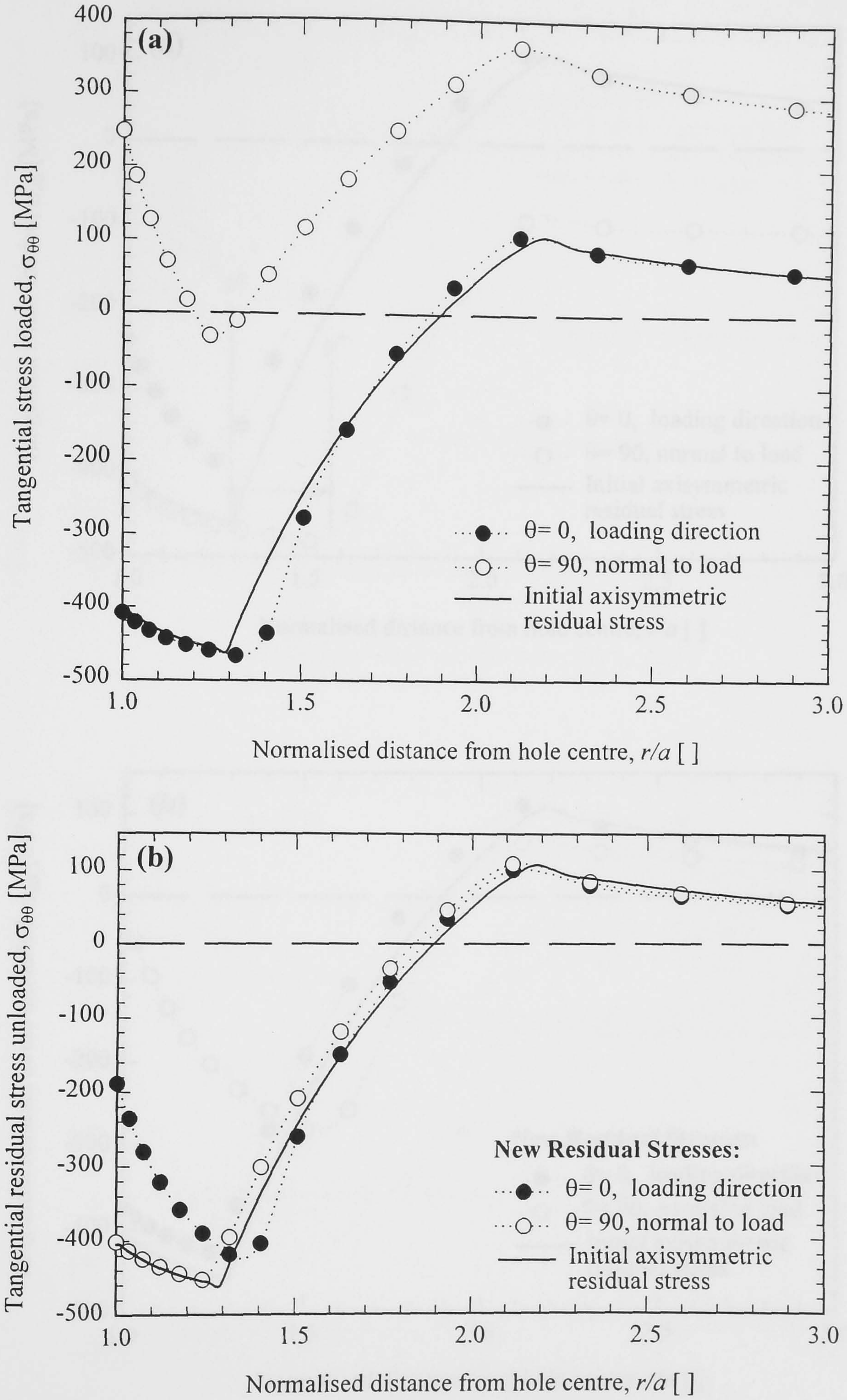

Figure 4.10. Tangential stress using a 2D kinematic hardening FE model of uniaxial tensile load for: (a) loaded and (b) unloaded (new residual stresses) plate.

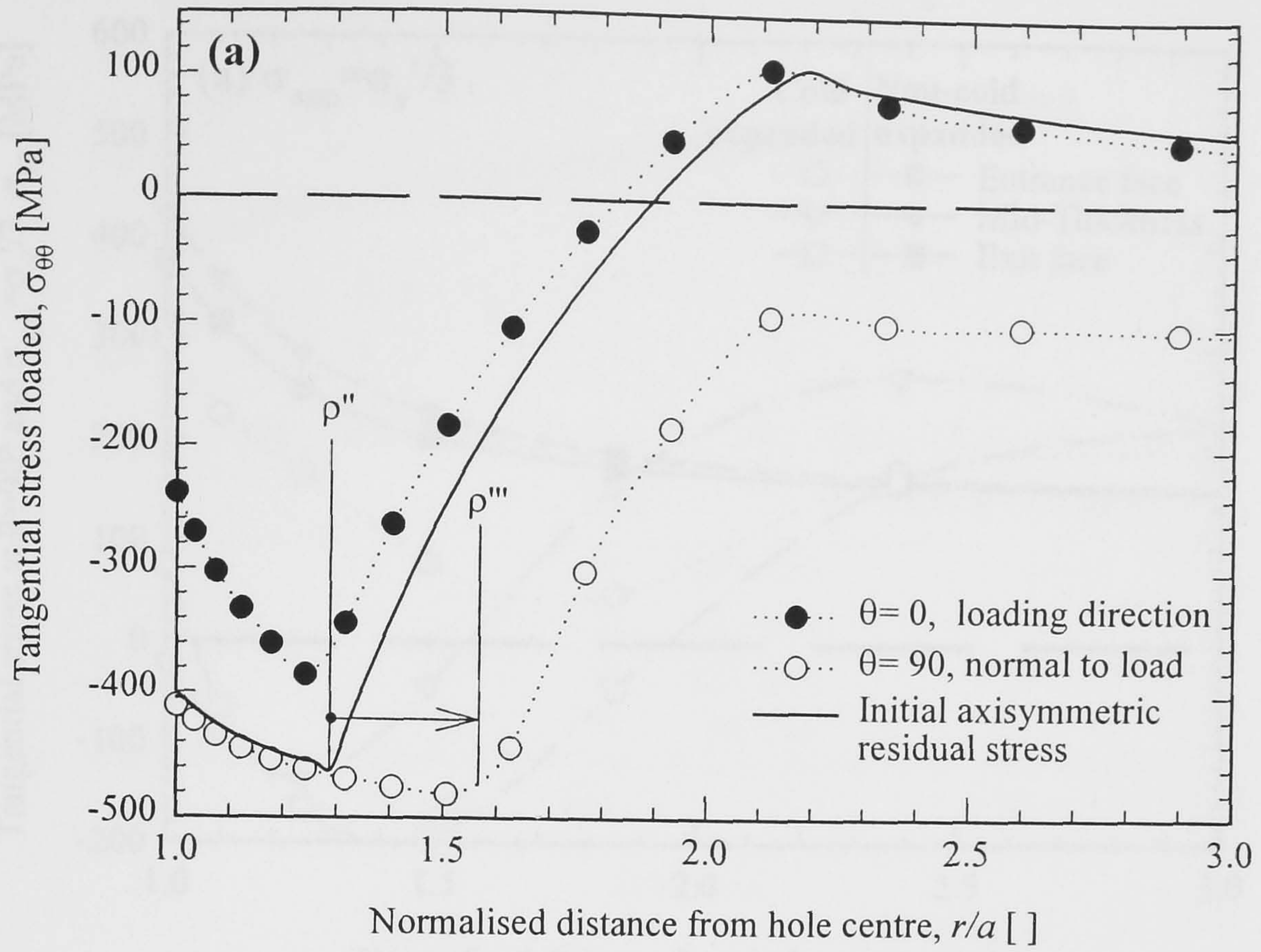

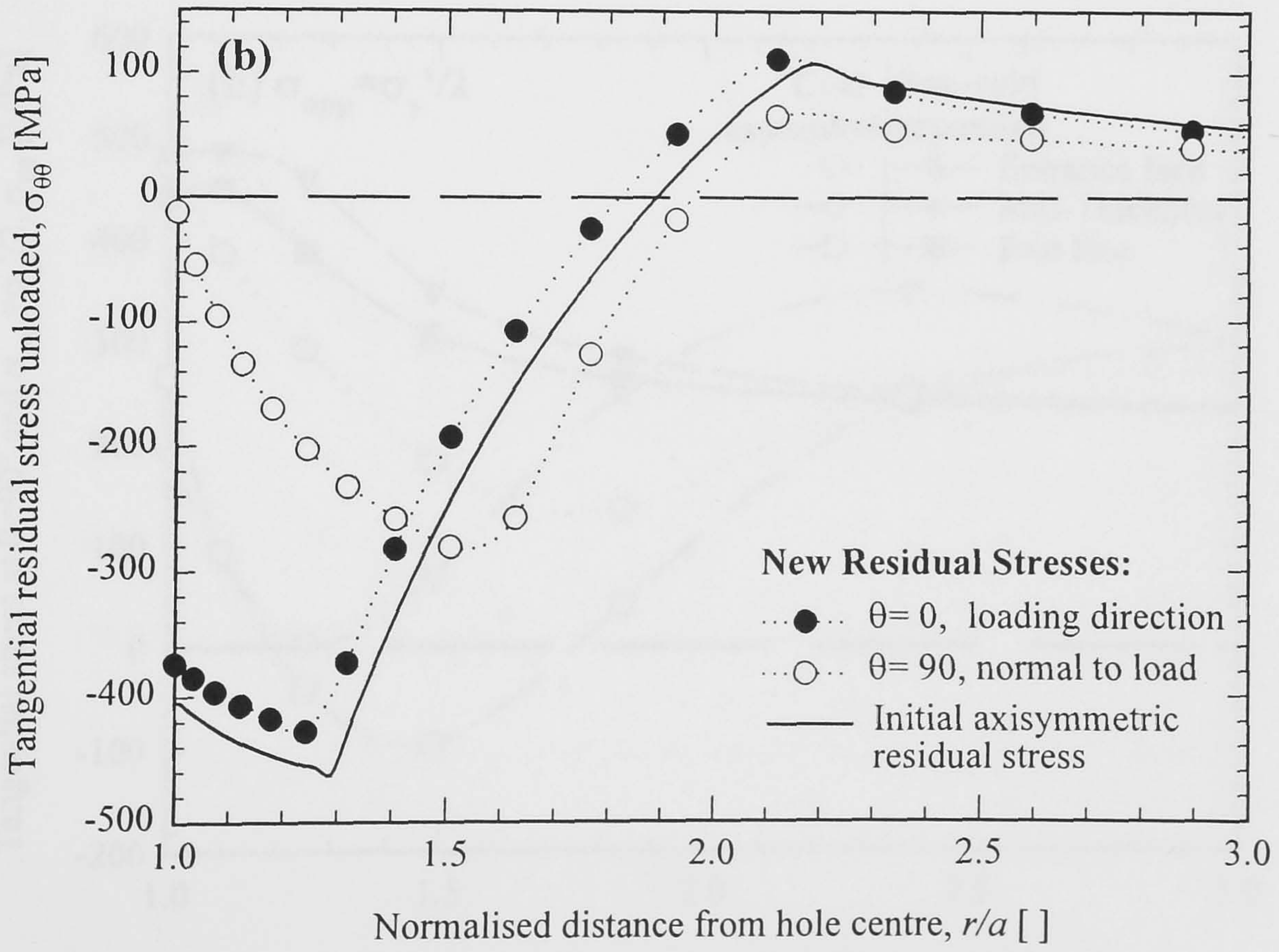

Figure 4.11. Tangential stress using a 2D kinematic hardening FE model of uniaxial compressive load for: (a) loaded and (b) unloaded (new residual stresses) plate.

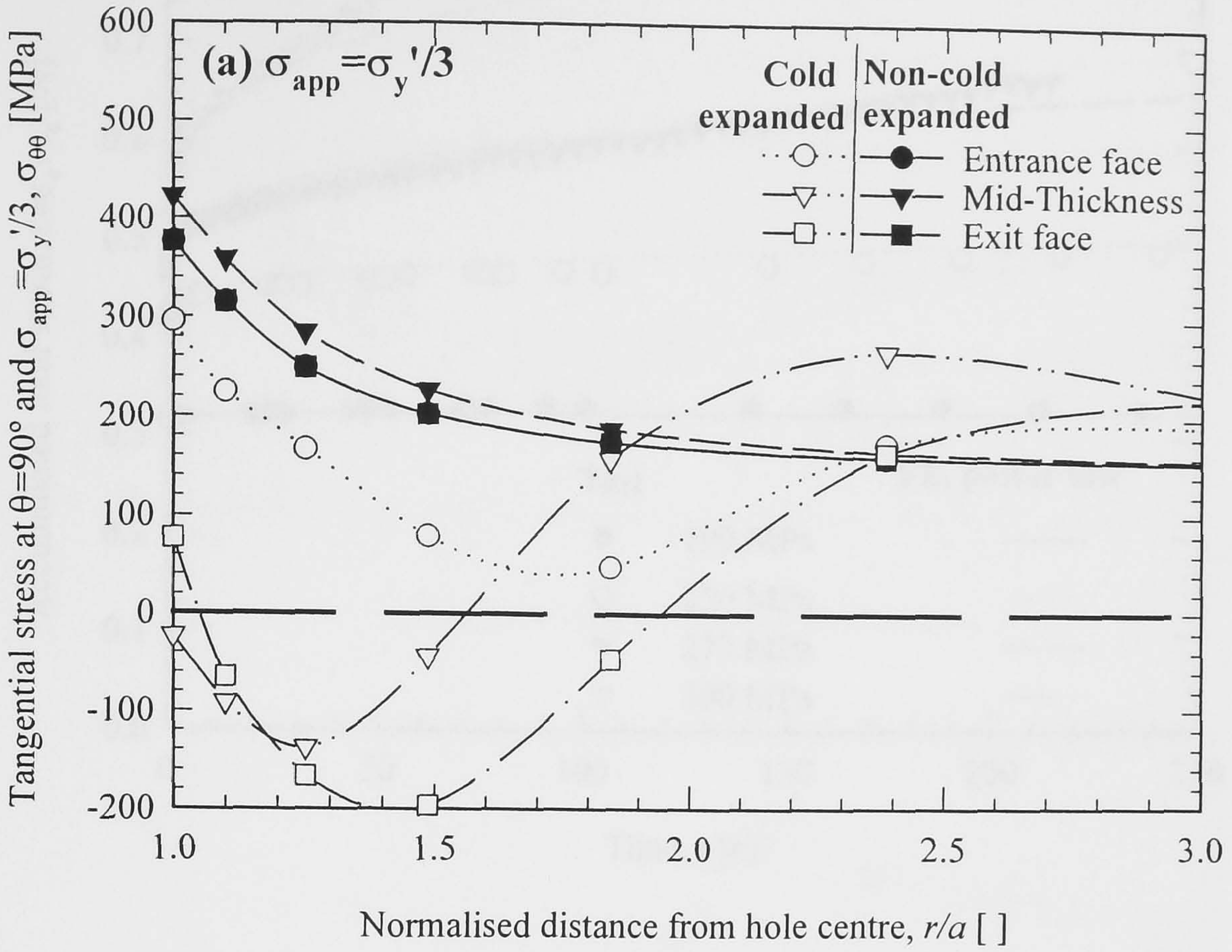

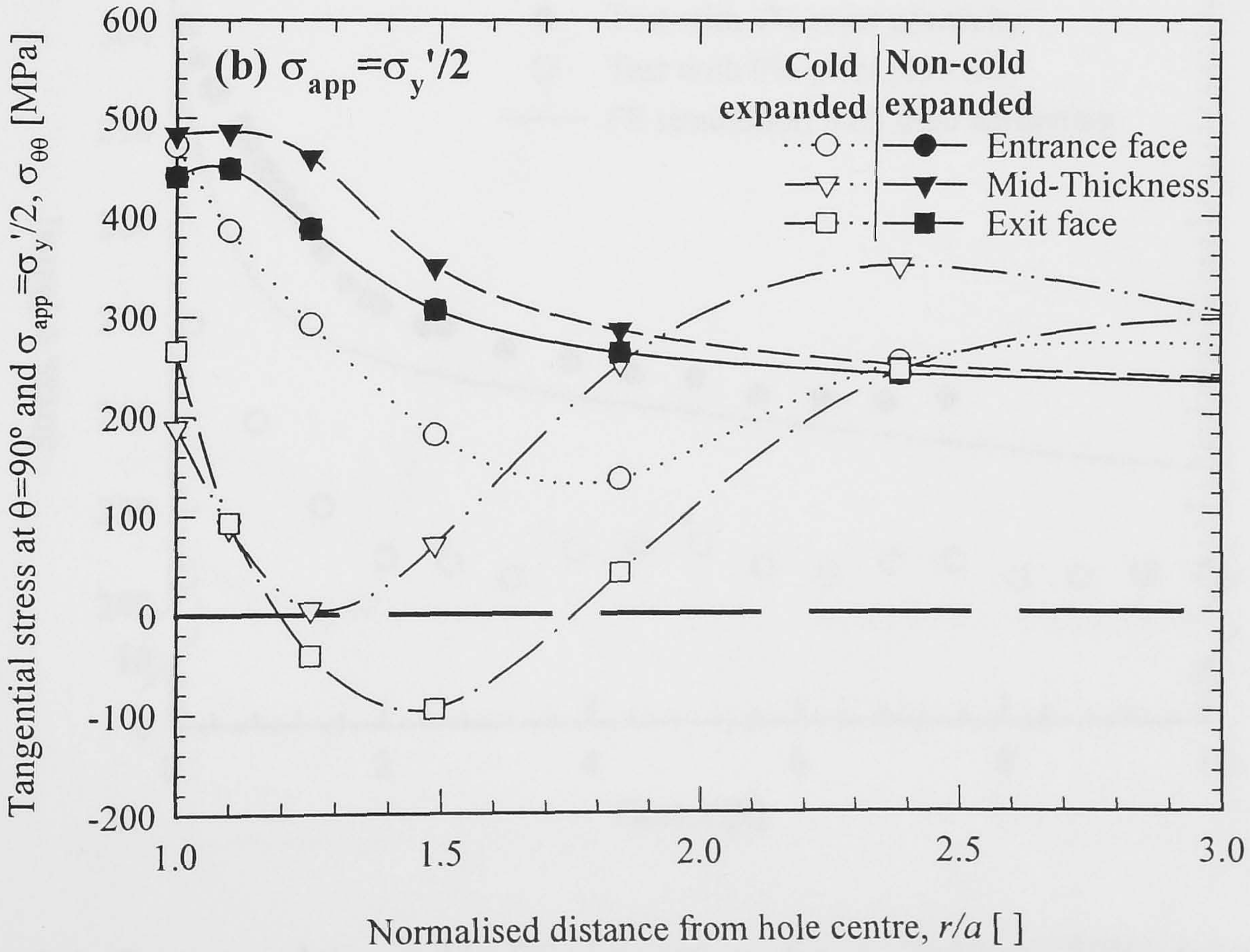

Figure 4.12. Tangential stress for a 3D kinematic hardening FE model of cold expanded and non–cold expanded hole for applied loads: (a) $\sigma_{app}=\sigma_y'/3$ and (b) $\sigma_{app}=\sigma_y'/2$.

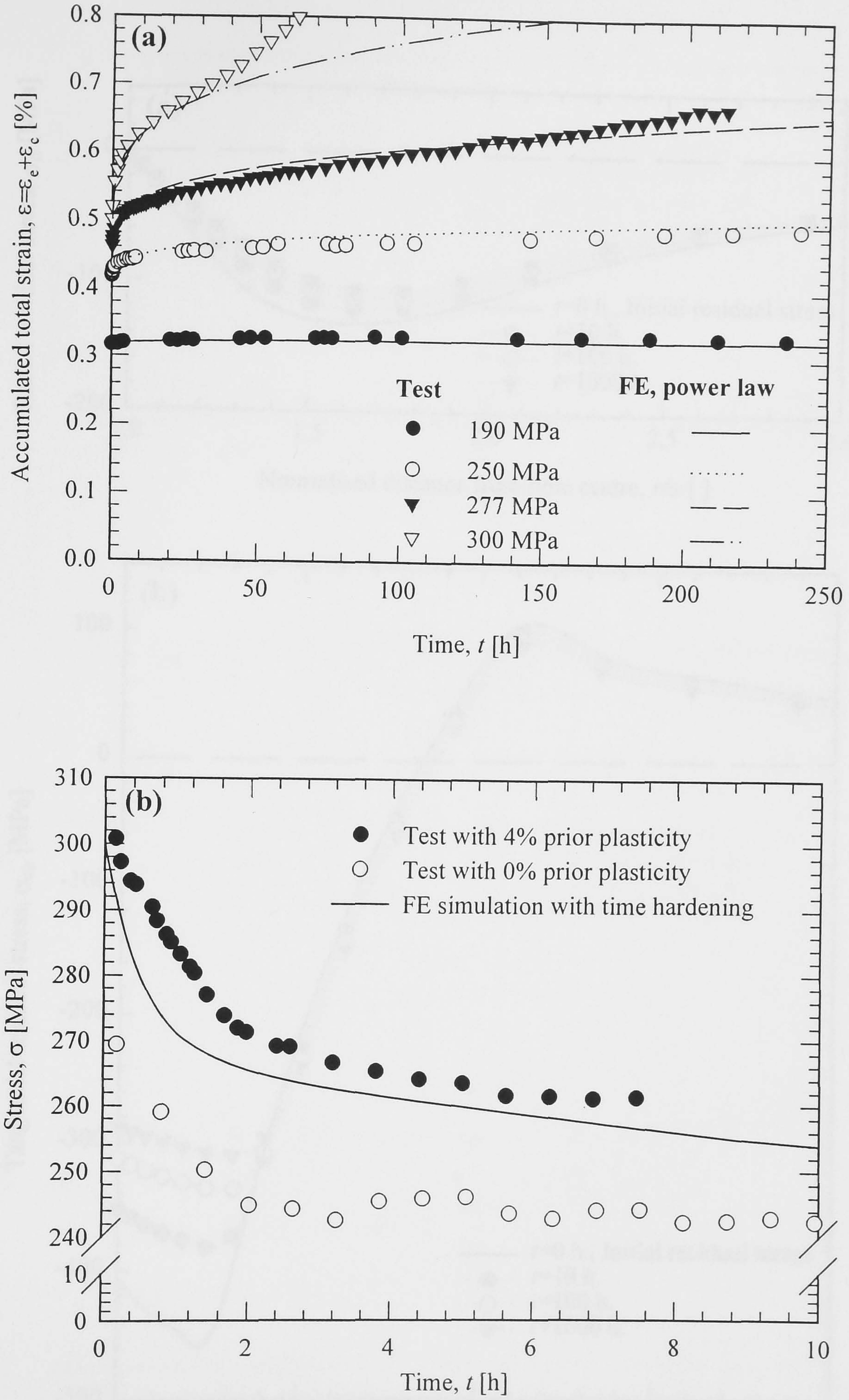

Figure 5.1. Creep models used in FE simulations for Al 2650 at 150°C: (a) constant load and (b) constant strain with influence of prior plasticity.

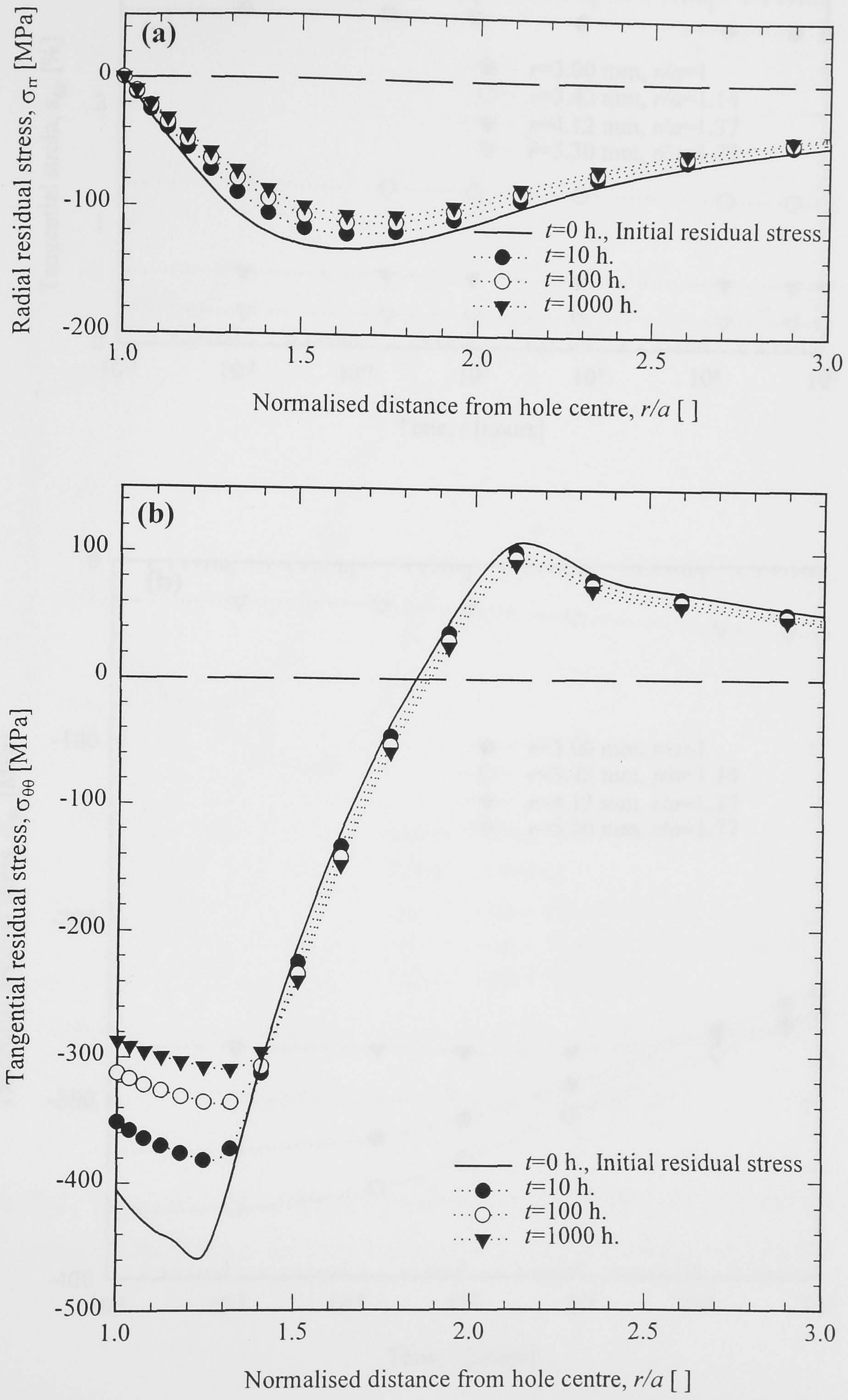

Figure 5.2. Relaxation of (a) tangential and (b) radial residual stresses at 150°C for different exposure times.

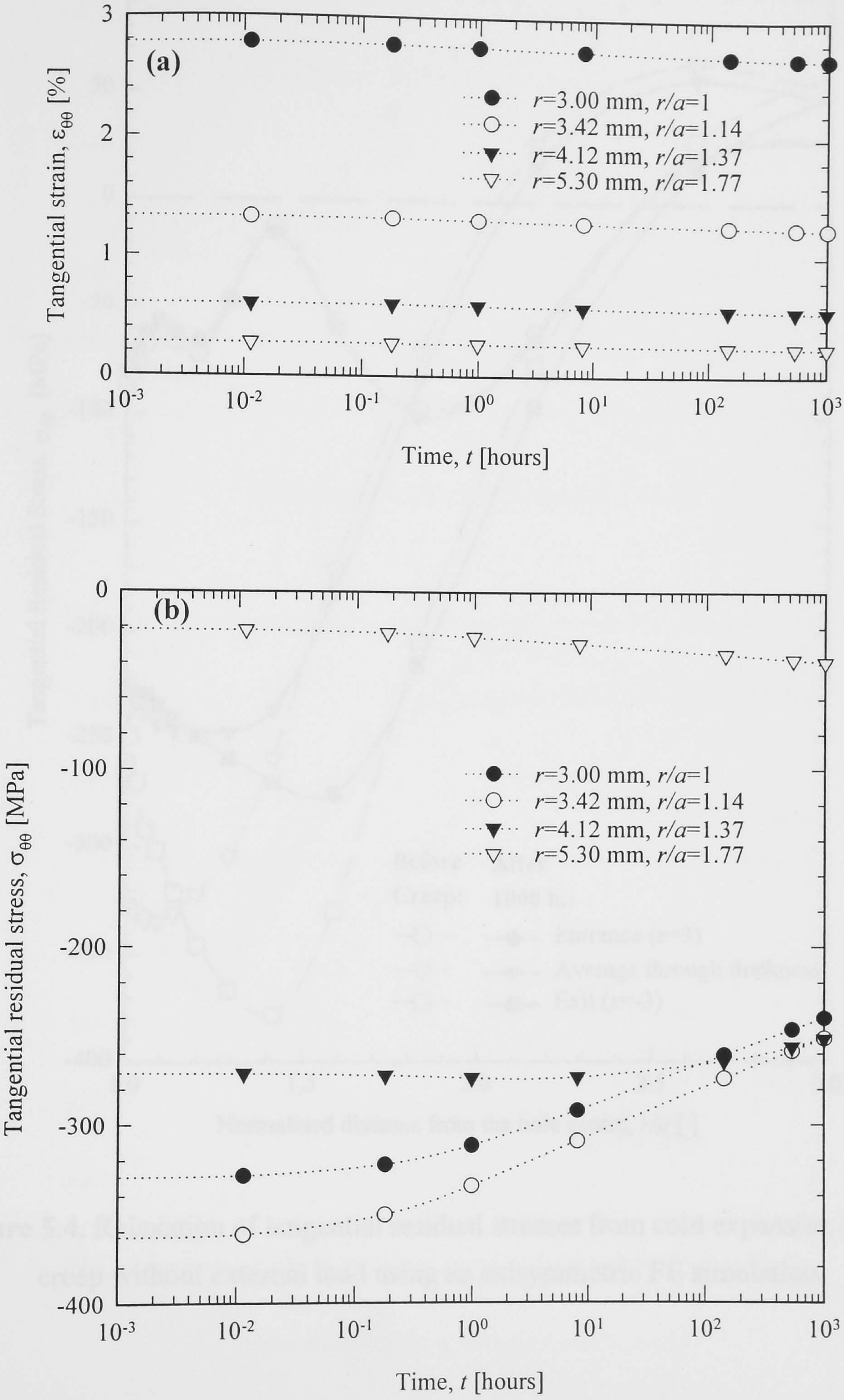

Figure 5.3. Change of (a) tangential strain and (b) tangential residual stress from cold expansion with time due to creep. Results shown for different radial positions.

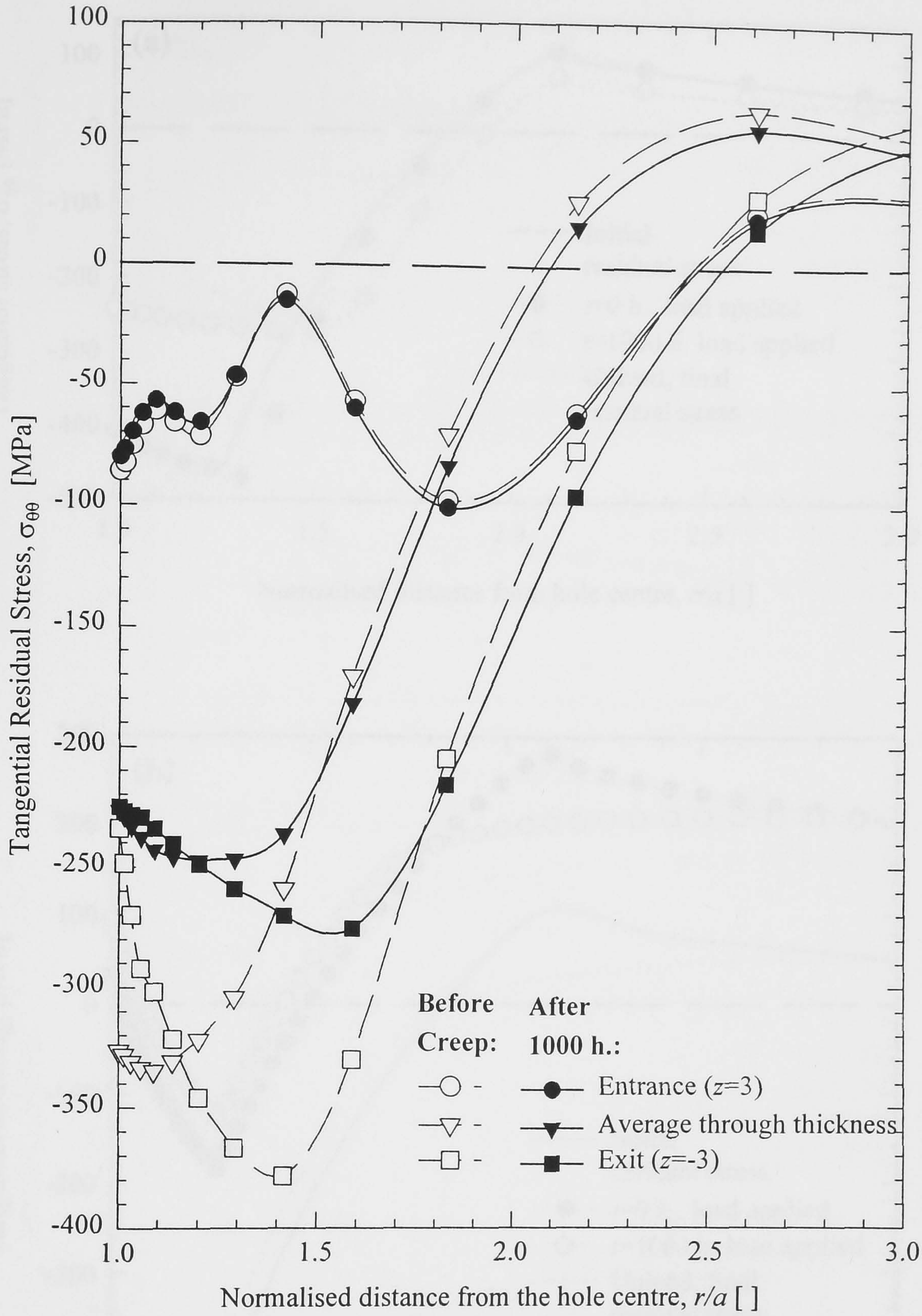

Figure 5.4. Relaxation of tangential residual stresses from cold expansion due to creep without external load using an axisymmetric FE simulation.

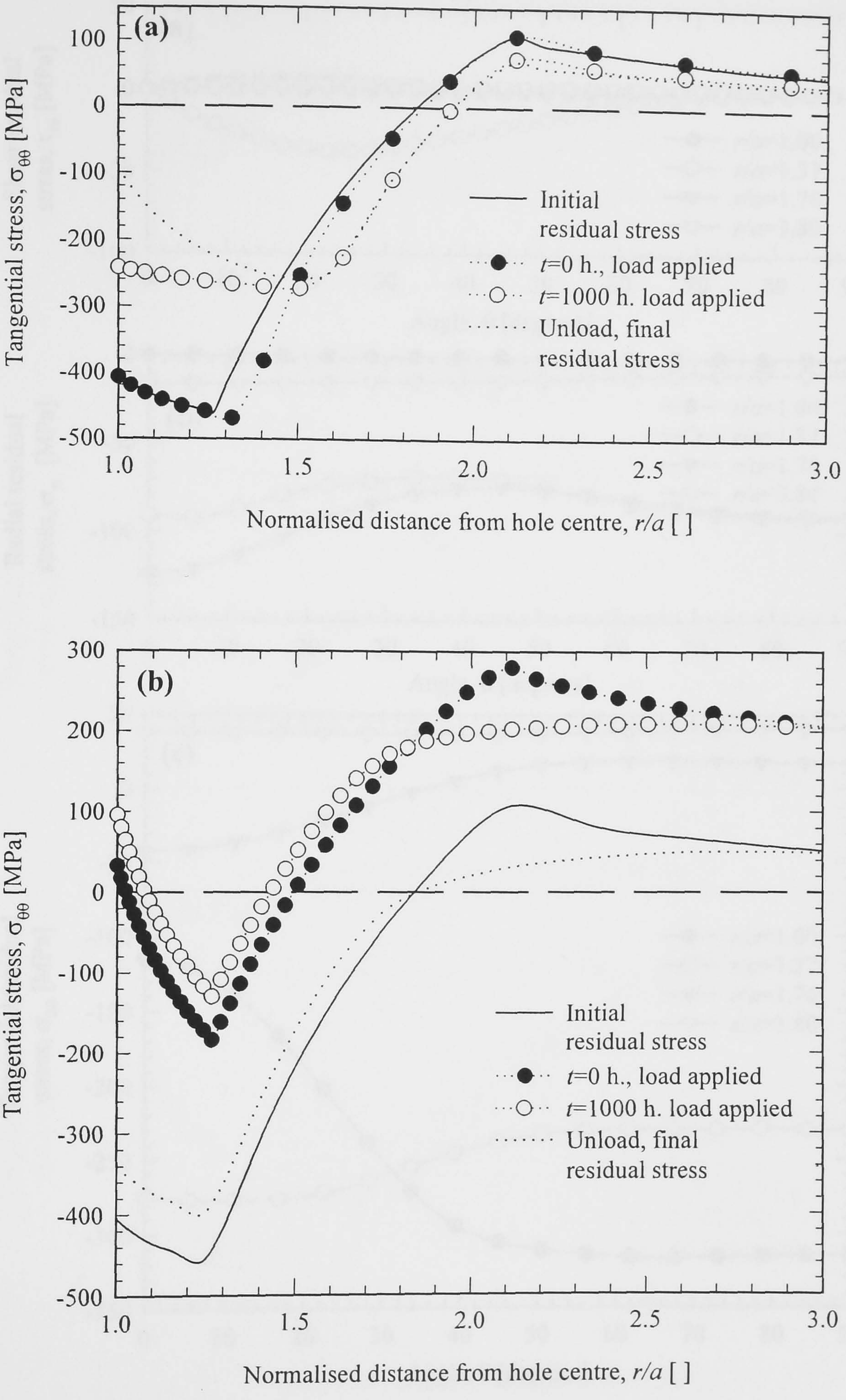

Figure 5.5. Relaxation of residual stresses from cold expansion due to creep with application of uniaxial external load $\sigma_{app} = \sigma_y'/3$: (a) $\theta=0°$ parallel to load and (b) $\theta=90°$, perpendicular to load.

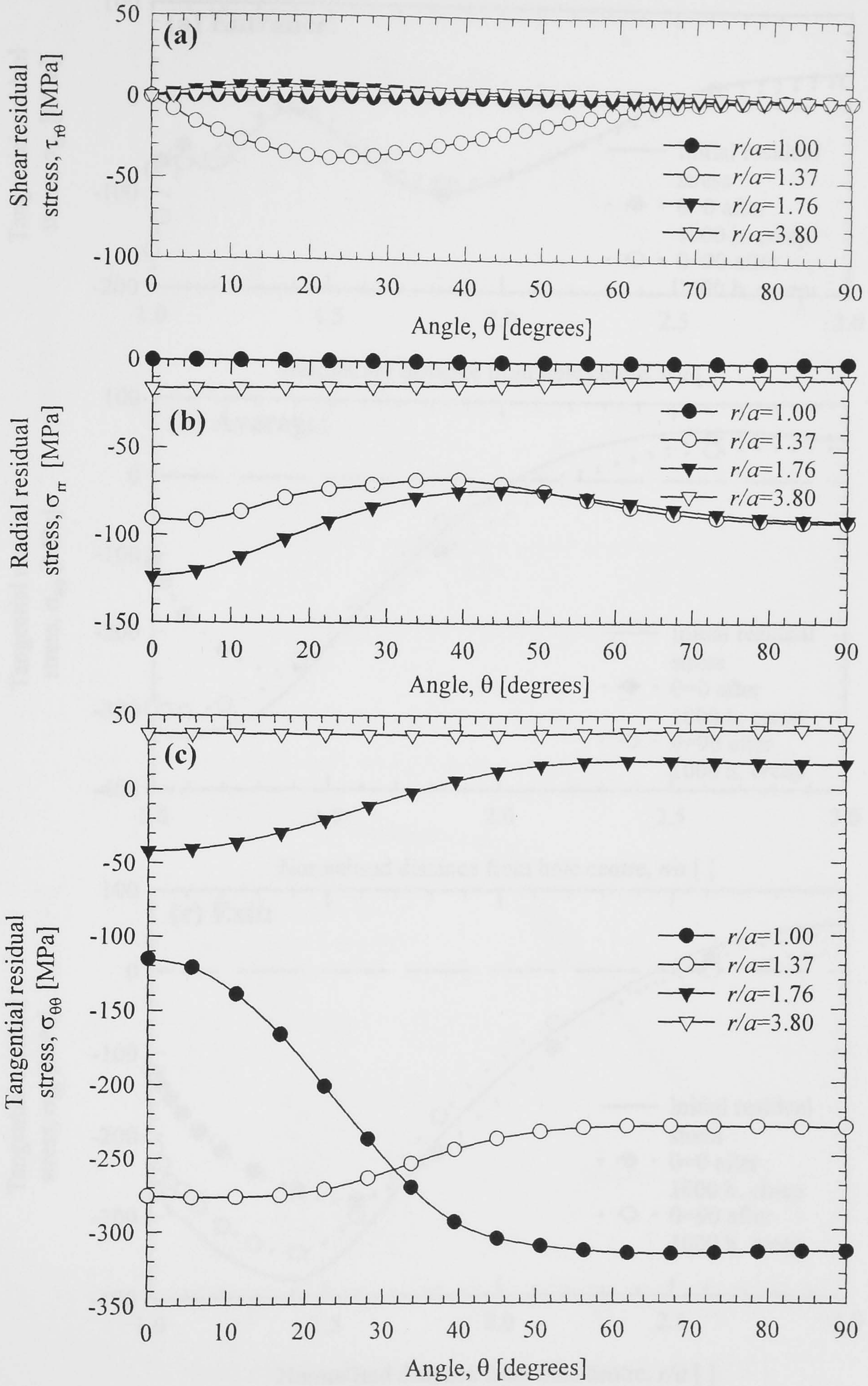

Figure 5.6. Relaxed residual stresses arising from the application of uniaxial external load for 1000 h. at 150 °C with $\sigma_{app} = \sigma_y'/3$ as function of angle: (a) shear, (b) radial and (c) tangential stress.

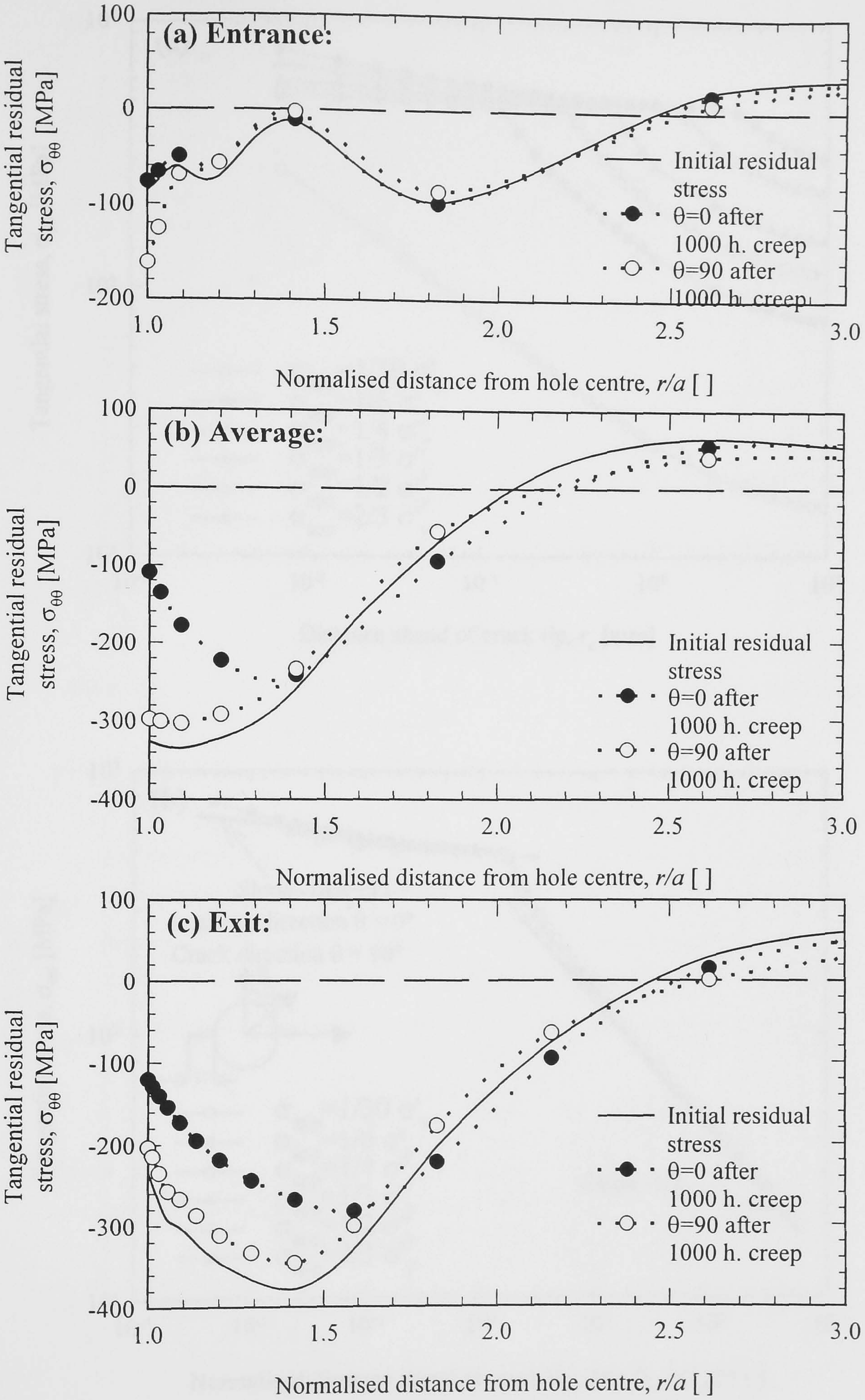

Figure 5.7. Relaxation of tangential residual stresses in 3D models with application of uniaxial external load $\sigma_{app} = \sigma_y'/3$. Results shown as a function of radius: (a) entrance face, (b) average through the thickness and (c) exit face.

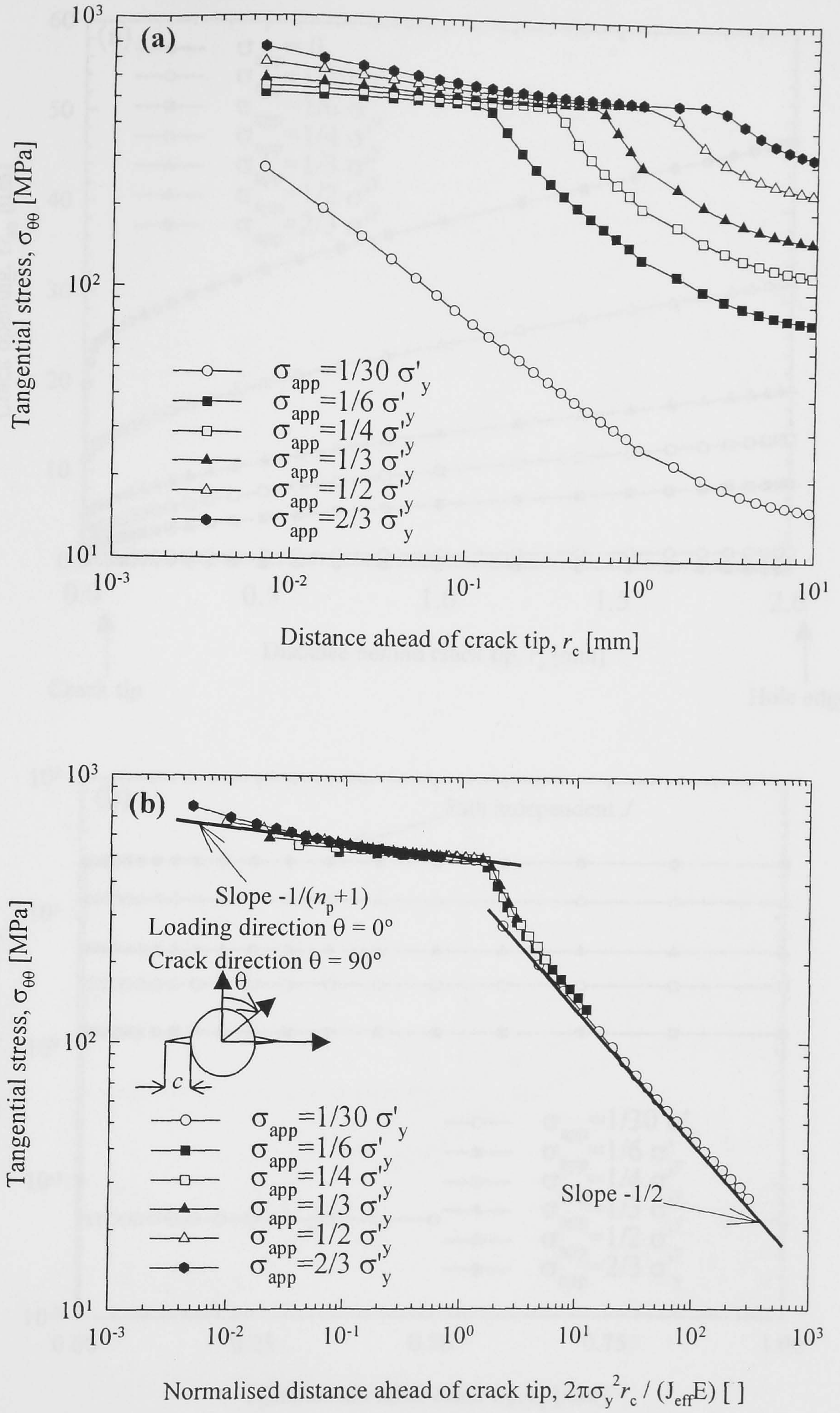

Figure 6.1. Tangential stress ahead of the crack tip for θ = 90° for a non–cold expanded hole using plane stress and kinematic hardening for hole radius *a*=3 mm and crack length *c*=2 mm. Stresses shown (a) versus crack tip distance and (b) versus normalised crack tip distance.

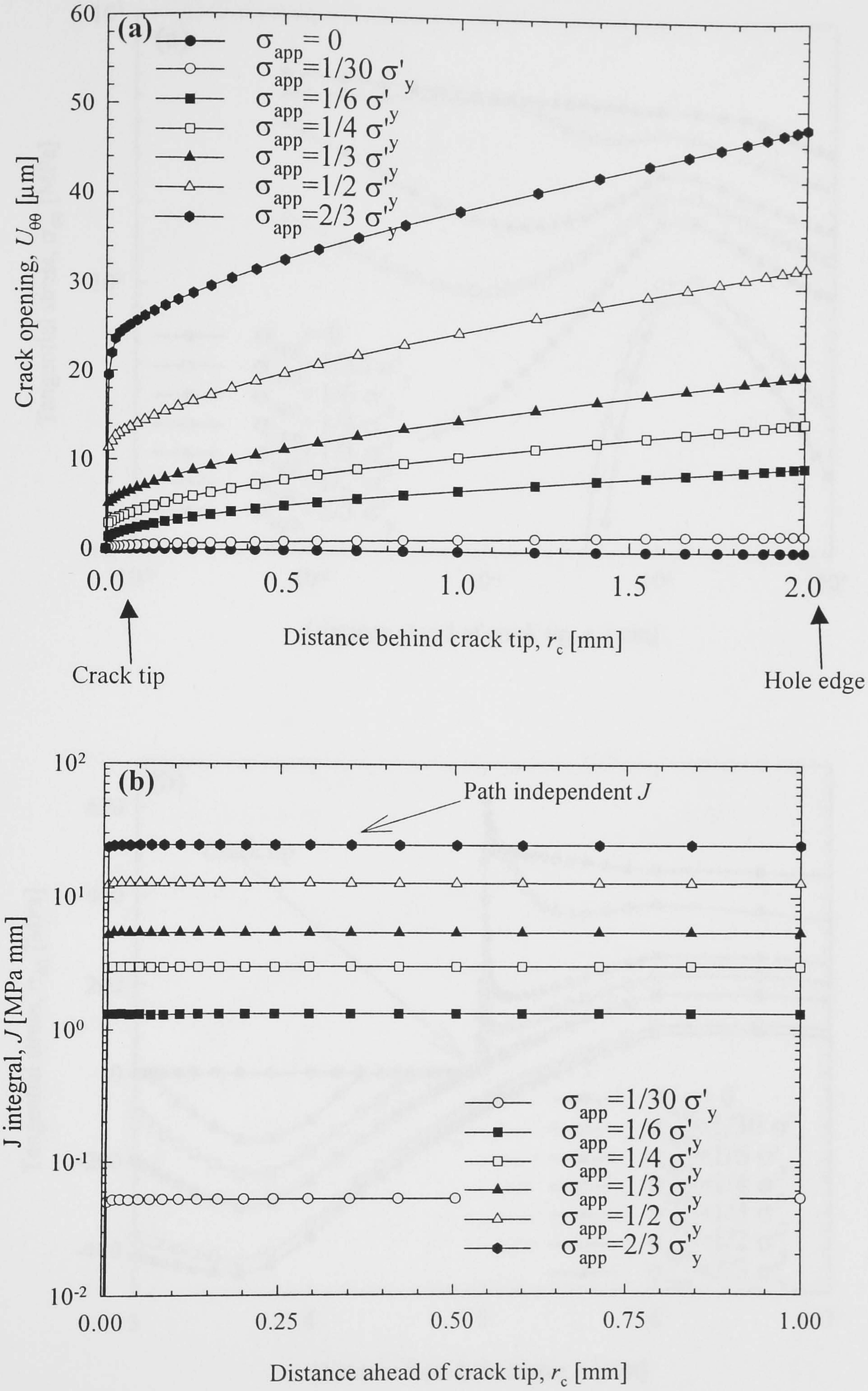

Figure 6.2. FE simulation of through–thickness crack (c=2 mm) using 2D plane stress, kinematic hardening for non–cold expanded holes: (a) crack opening displacement $U_{\theta\theta}$ and (b) J–integral.

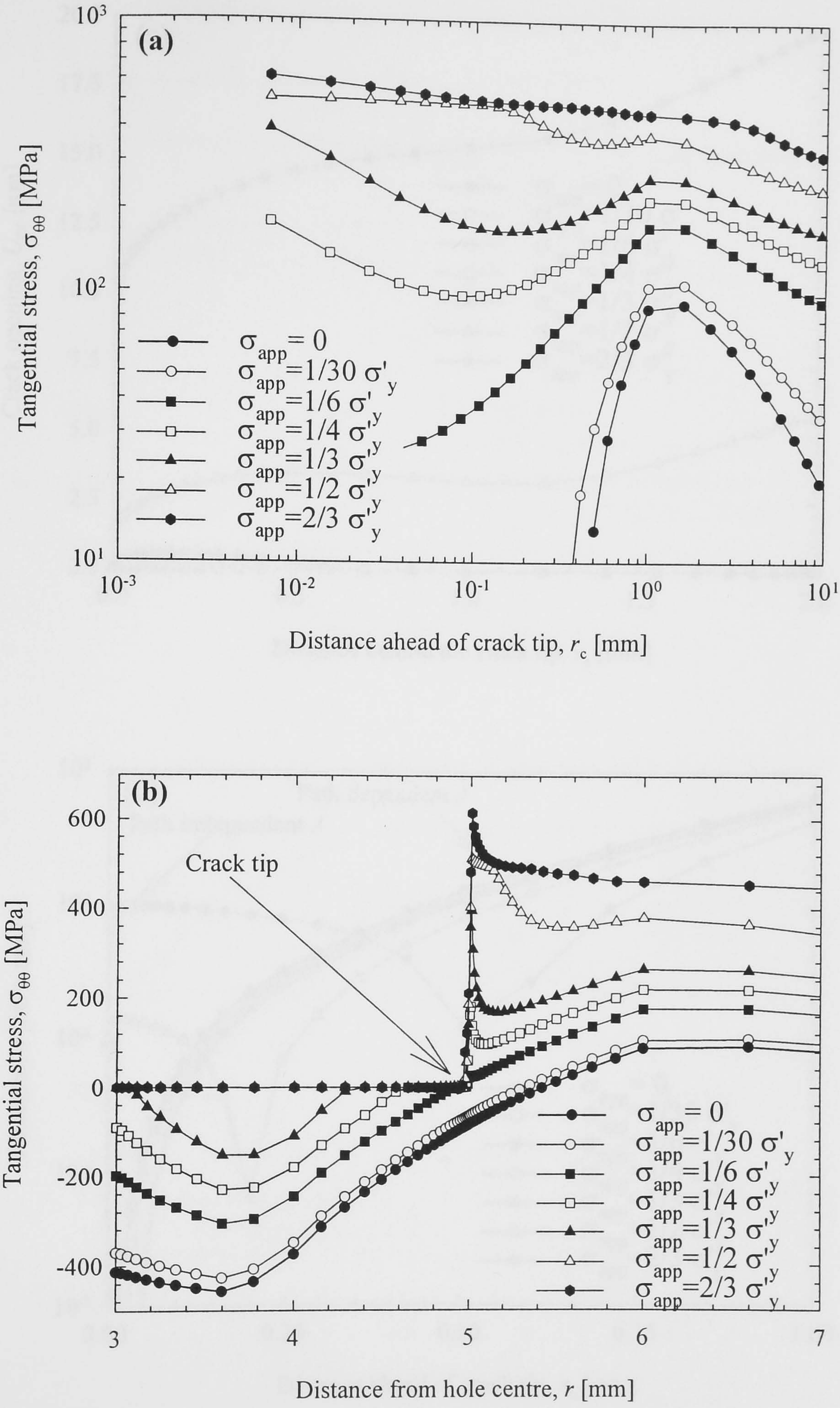

Figure 6.3. Tangential stress ahead of the crack tip for a cold expanded hole in Al 2650 using plane stress and kinematic hardening. Stresses shown for crack direction θ=90° (a) versus crack tip distance in log scale and (b) versus distance from hole centre.

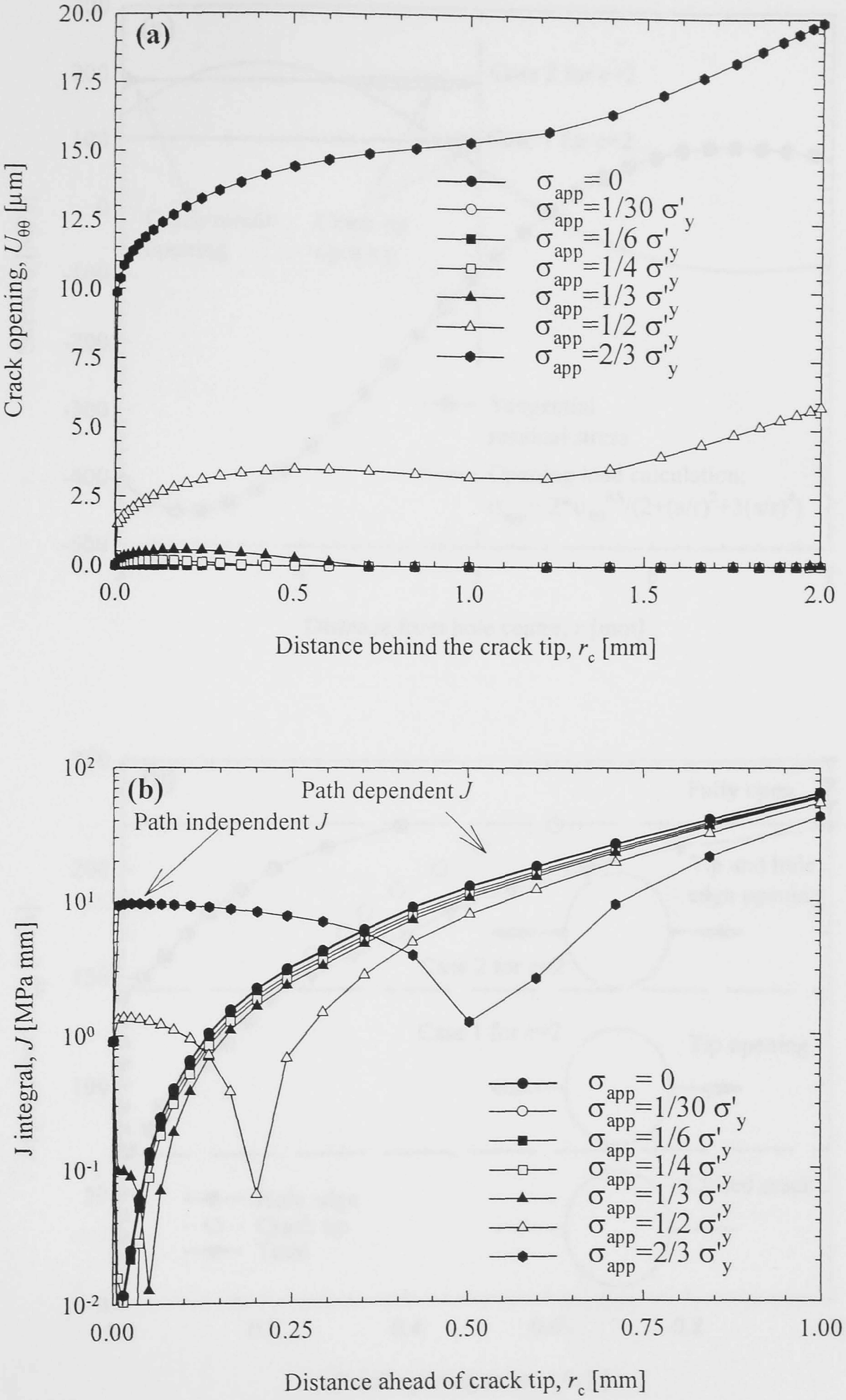

Figure 6.4. FE simulation of through thickness crack in cold expanded holes using 2D plane stress and kinematic hardening (a) crack opening displacement $U_{\theta\theta}$ and (b) *J* integral.

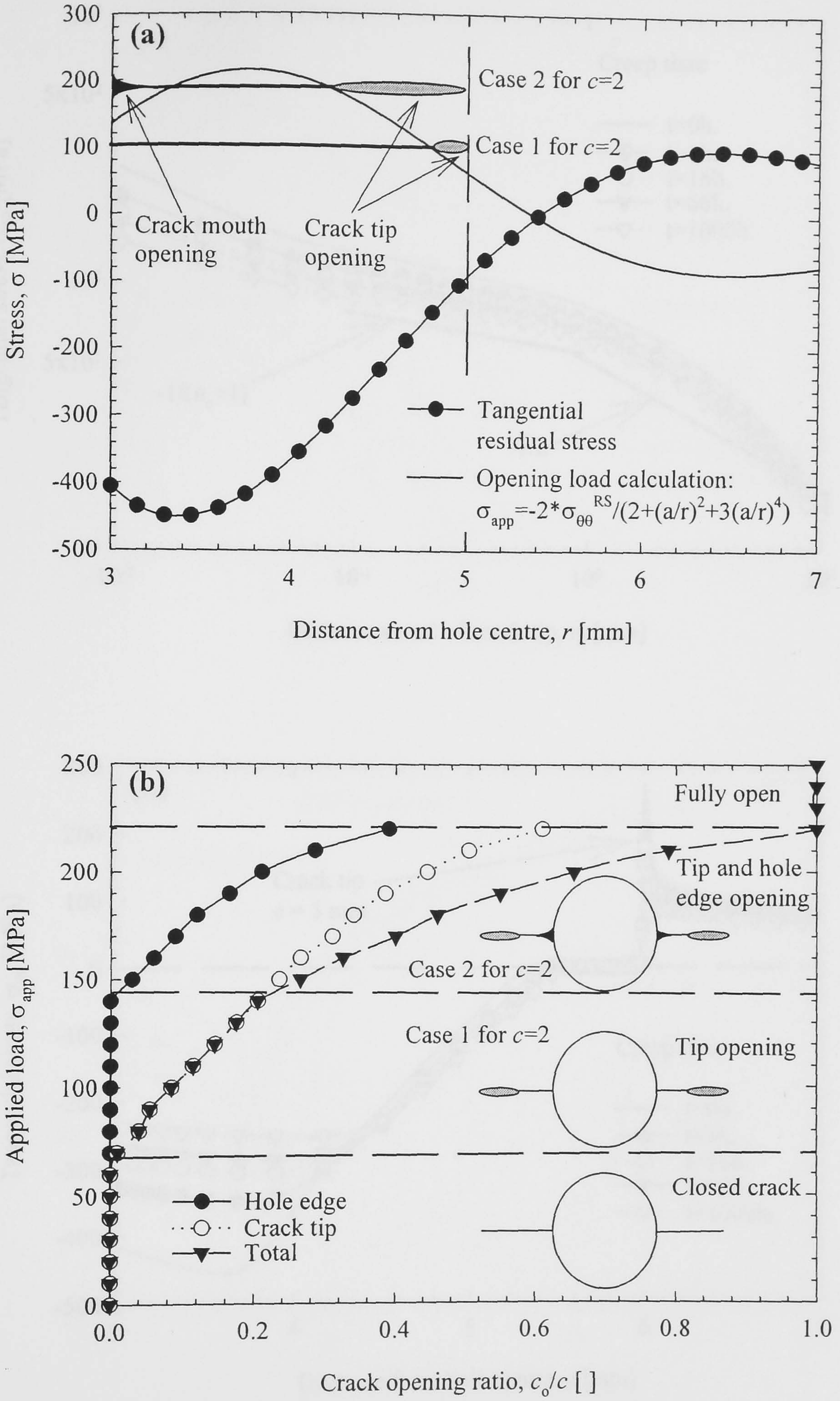

Figure 6.5. Prediction of crack opening in cold expanded holes using 2D plane stress and kinematic hardening material model: (a) load to produce crack opening and (b) crack opening ratio between length of crack which opens and crack length c=2 mm .

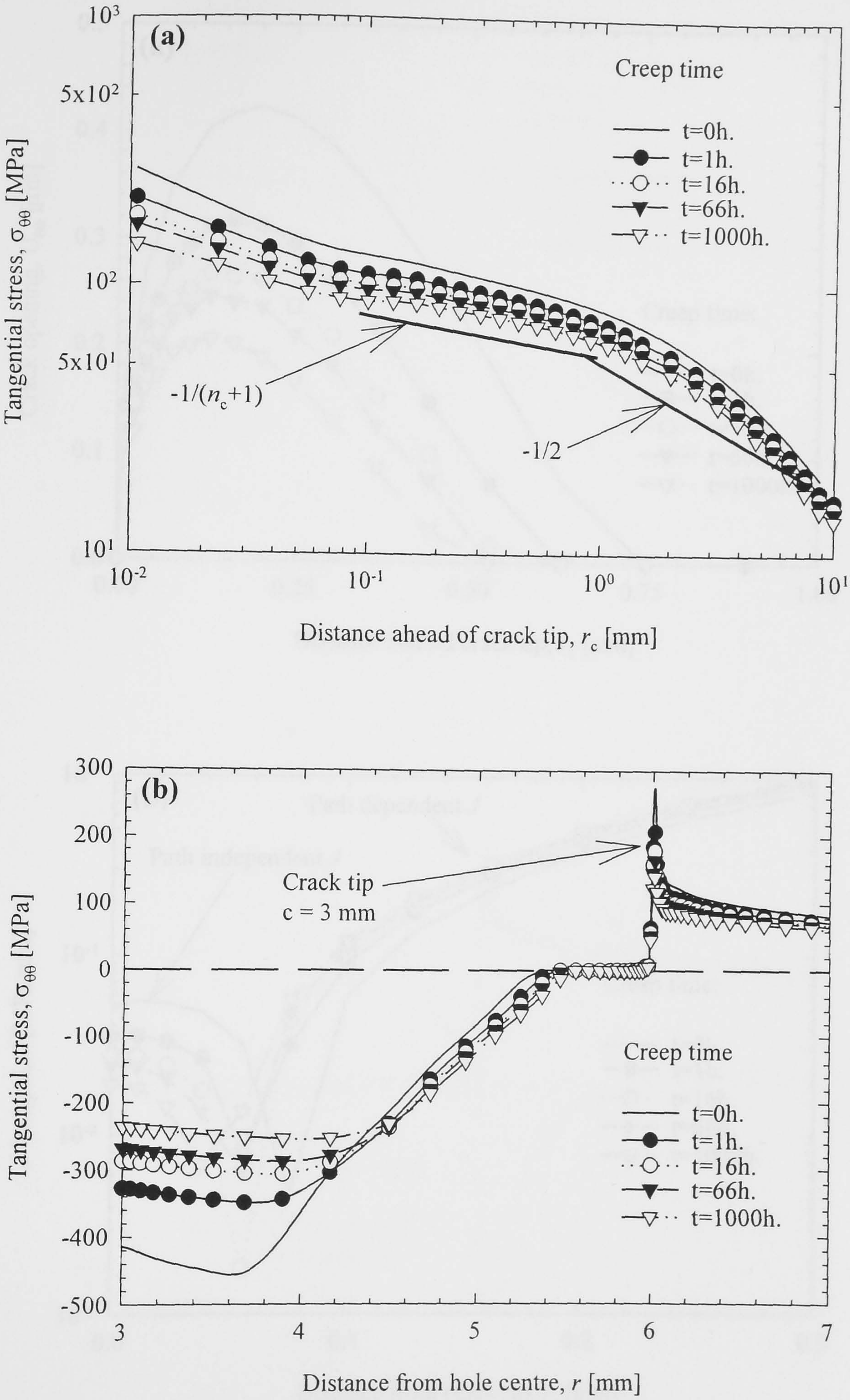

Figure 6.6. Tangential stress ahead of the crack tip for cold expanded hole containing a long crack (c=3 mm) during creep without external load: (a) versus crack tip distance in log scale and (b) versus distance from hole centre.

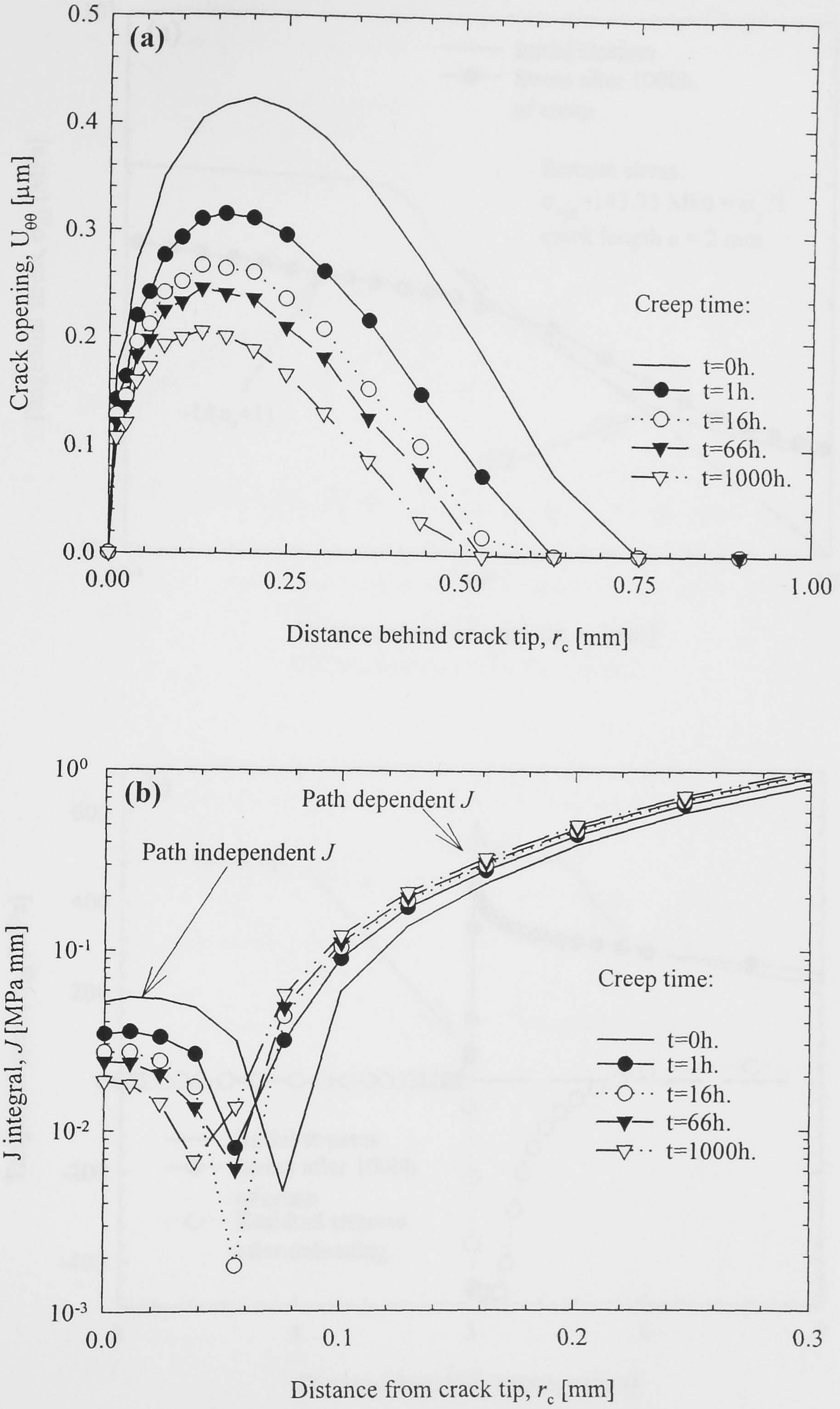

Figure 6.7. FE simulation of a long through–thickness crack (c=3 mm) and creep without external load in cold expanded holes using kinematic hardening (a) crack opening displacement $U_{\theta\theta}$ and (b) J integral.

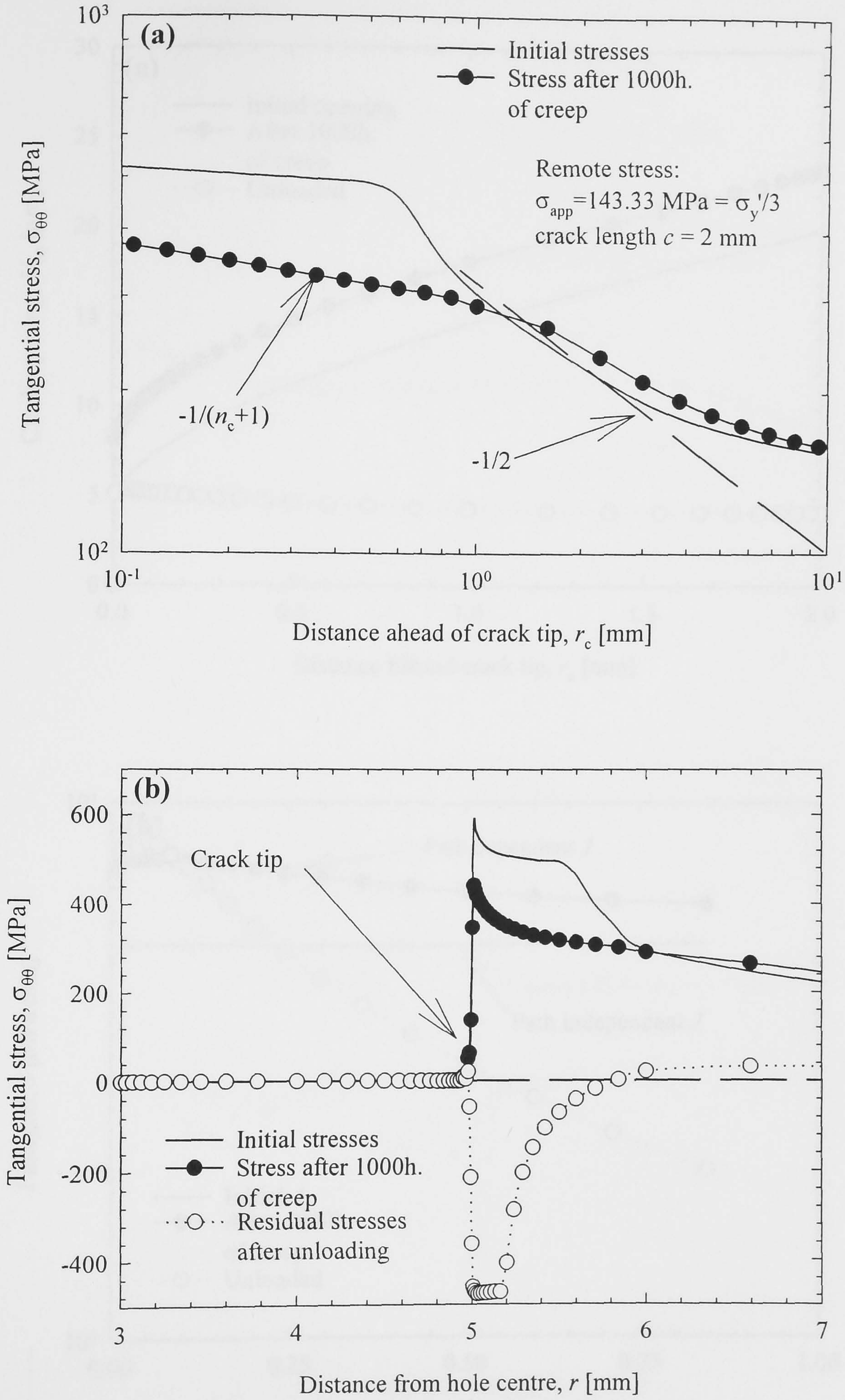

Figure 6.8. Tangential stress ahead of the crack tip for non–cold expanded hole during creep and load: (a) versus crack tip distance in log scale and (b) versus distance from hole centre.

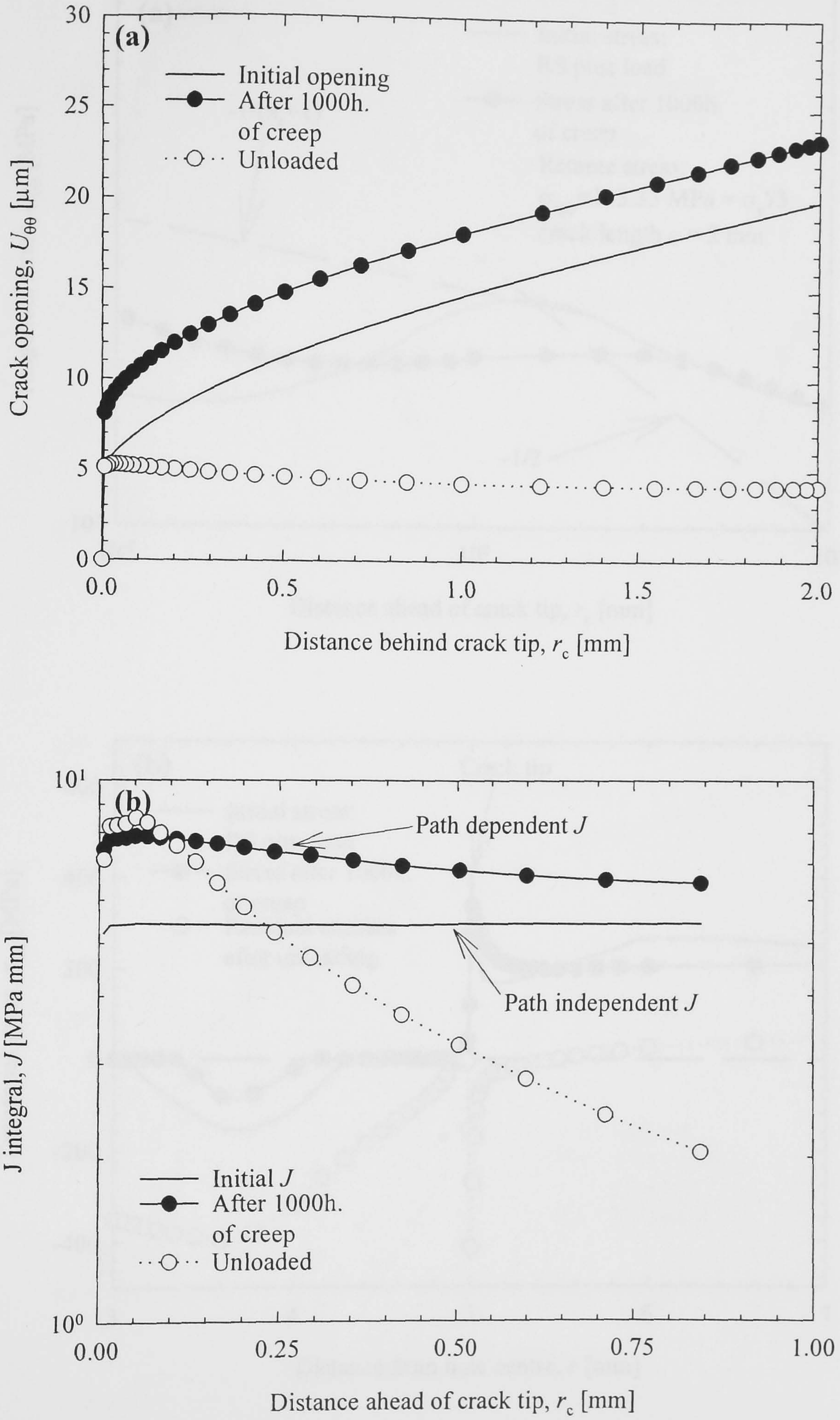

Figure 6.9. FE simulation of a through–thickness crack, with externally applied load and creep in non–cold expanded holes using kinematic hardening (a) crack opening displacement $U_{\theta\theta}$ and (b) J integral.

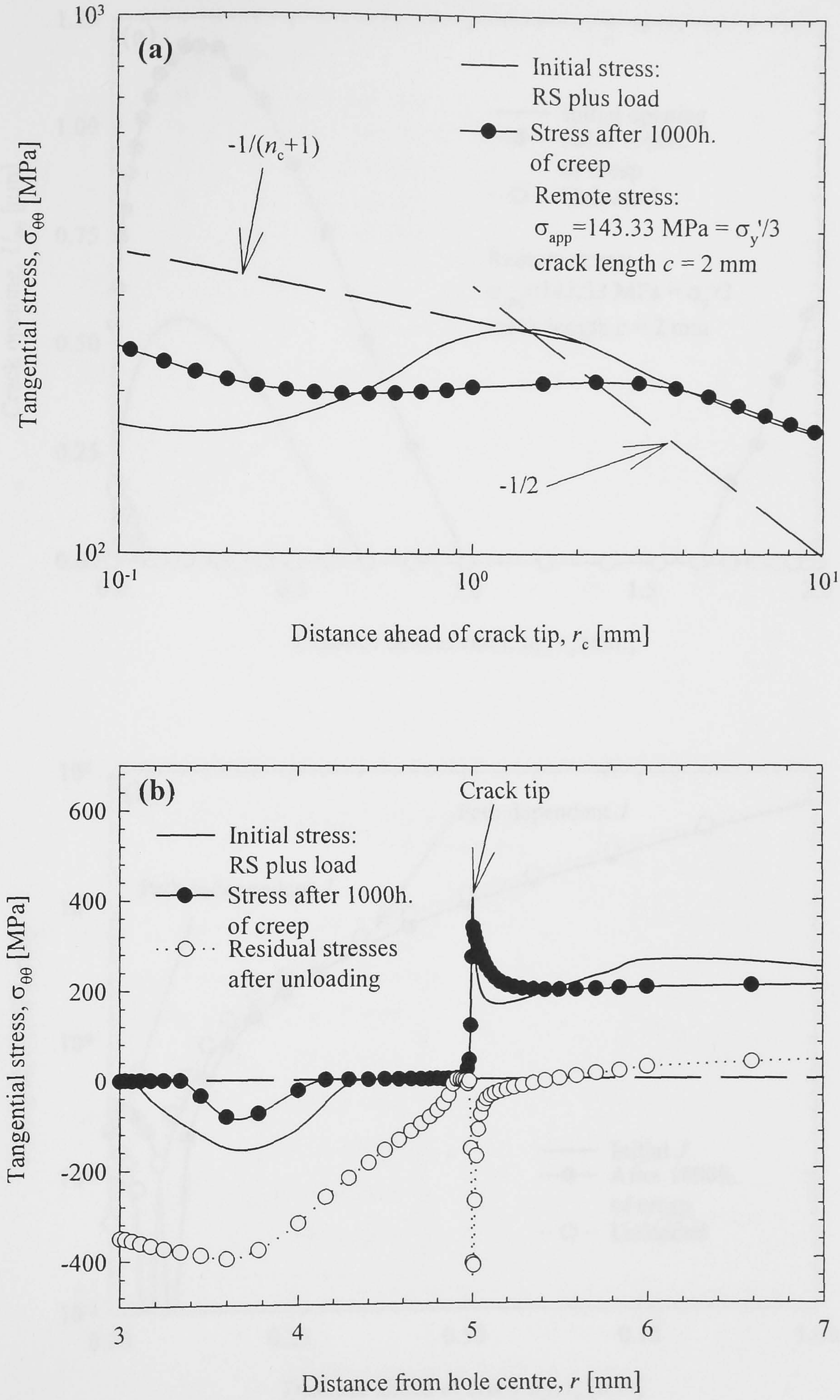

Figure 6.10. Tangential stress ahead of the crack tip for cold expanded hole during creep and load: (a) versus crack tip distance in log scale and (b) versus distance from hole centre.

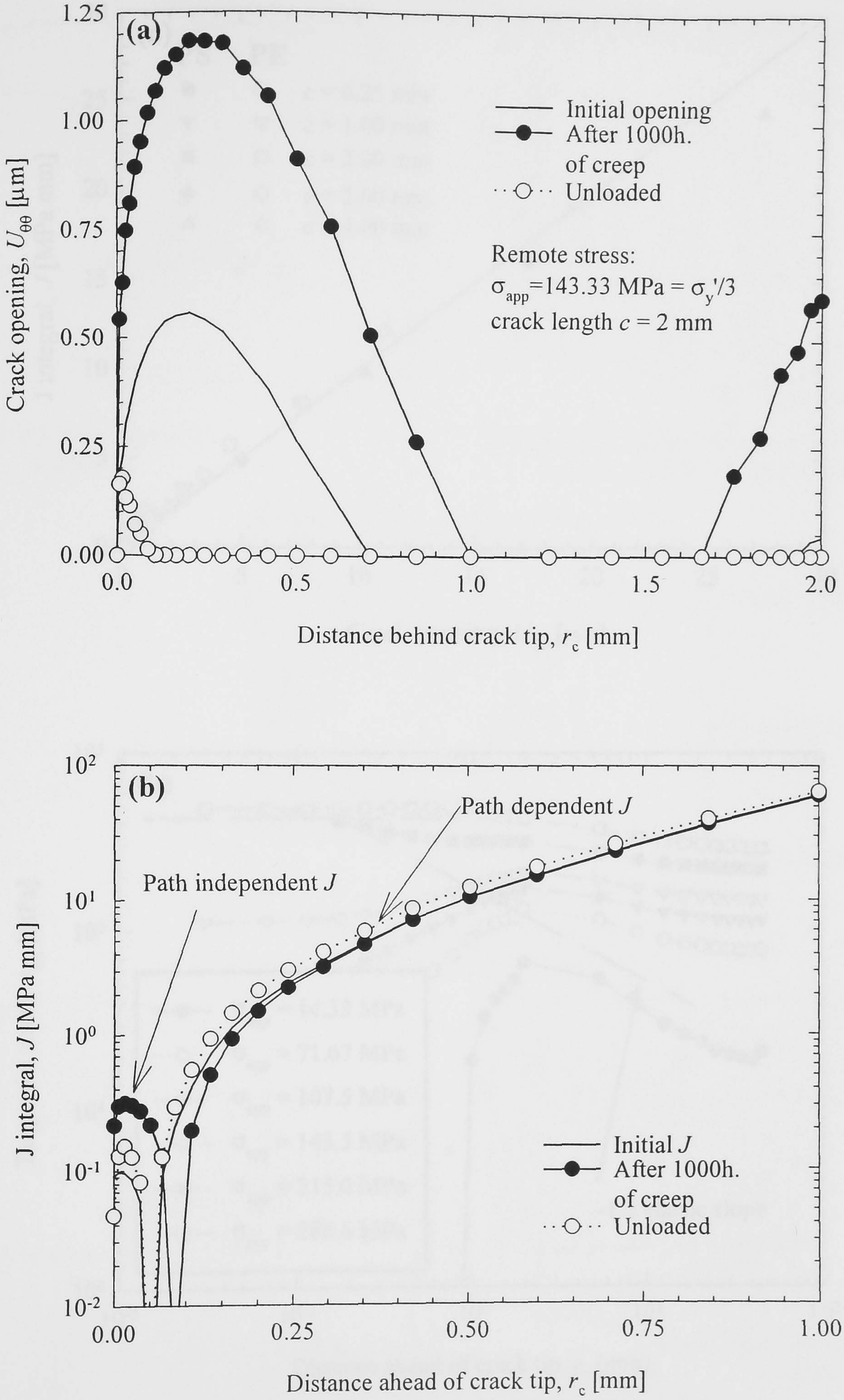

Figure 6.11. FE simulation of through–thickness crack, load and creep in cold expanded holes using kinematic hardening (a) crack opening and (b) *J*–integral.

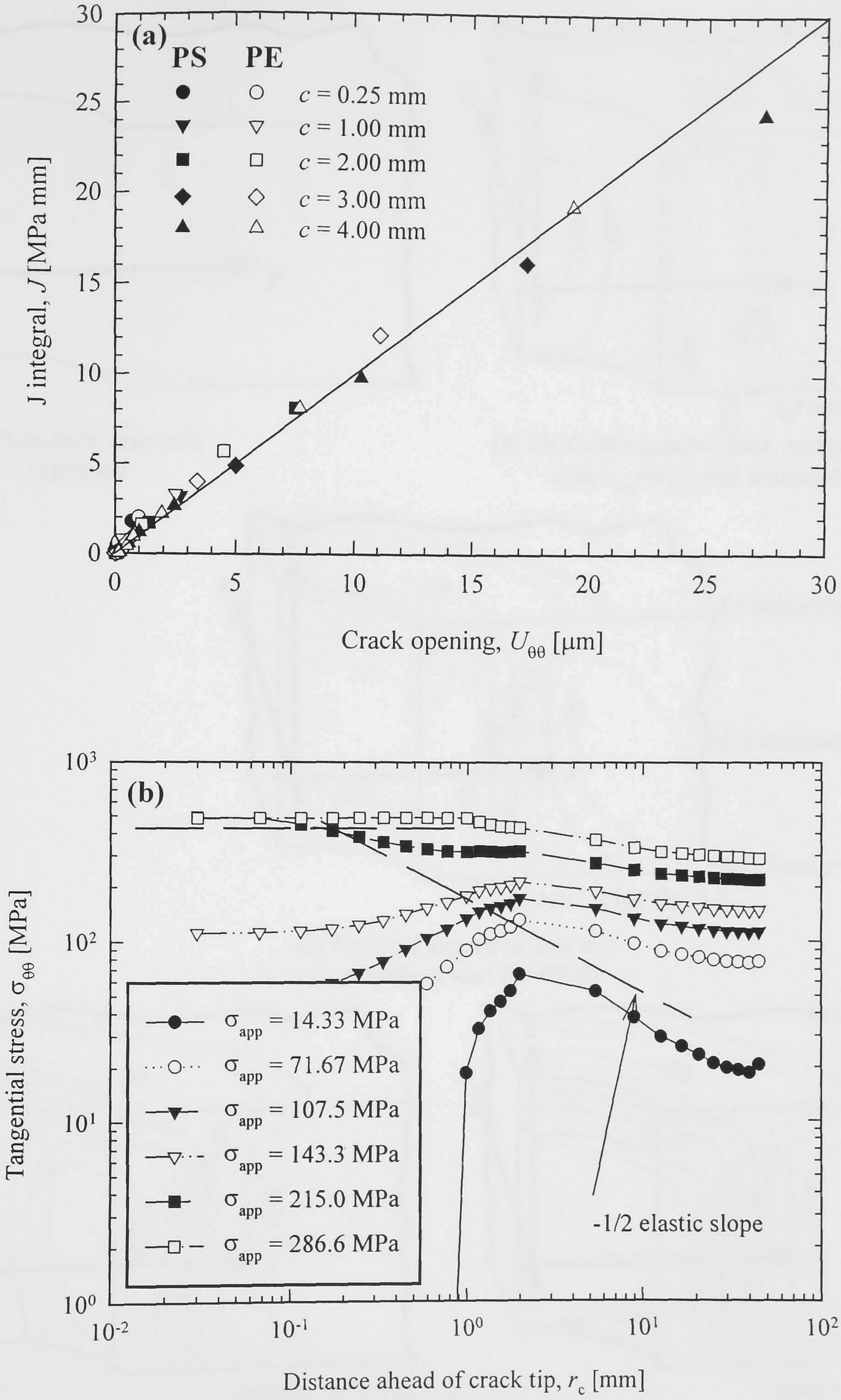

Figure 6.12. Stress intensity factor calibration using 2D plane stress and plane strain in an Al 2650 cold expanded hole. (a) crack opening technique versus ABAQUS *J*–integral and (b) HRR solutions.

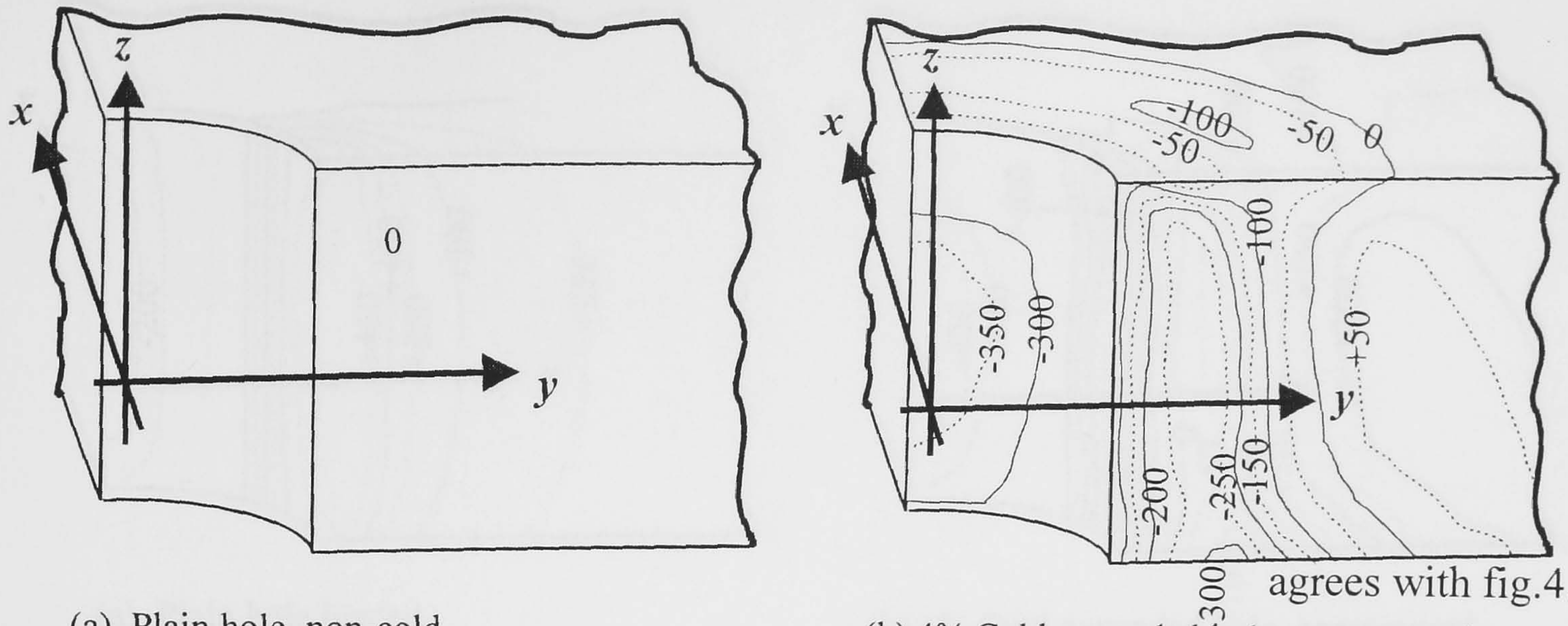

agrees with fig.4.11

(a) Plain hole, non-cold expanded

(b) 4% Cold expanded hole, compressed with $\sigma_{app}=\sigma'_y/3$ and unloaded.

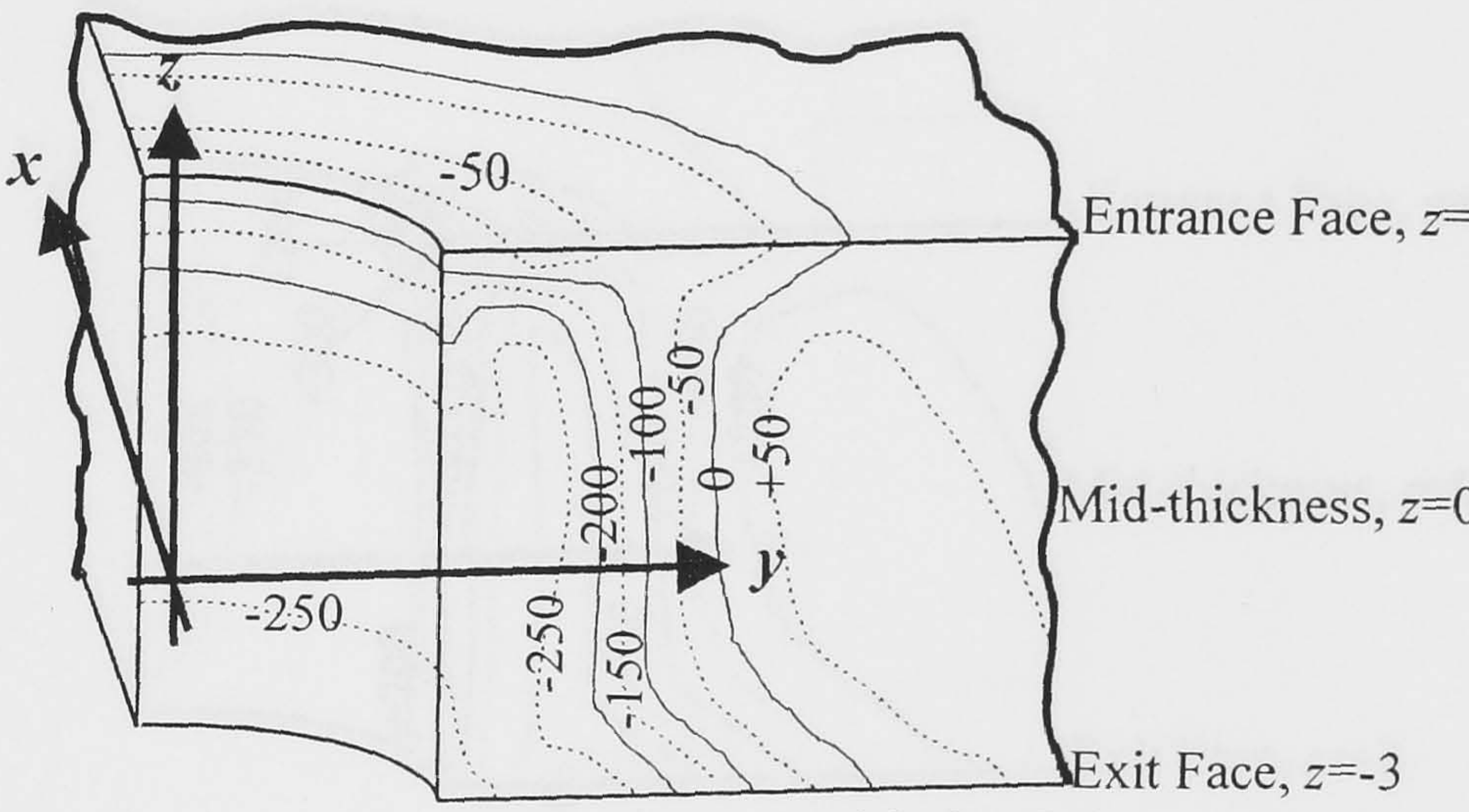

agrees with fig.5.4

(c) 4% Cold expanded hole and crept without load for 1000h.

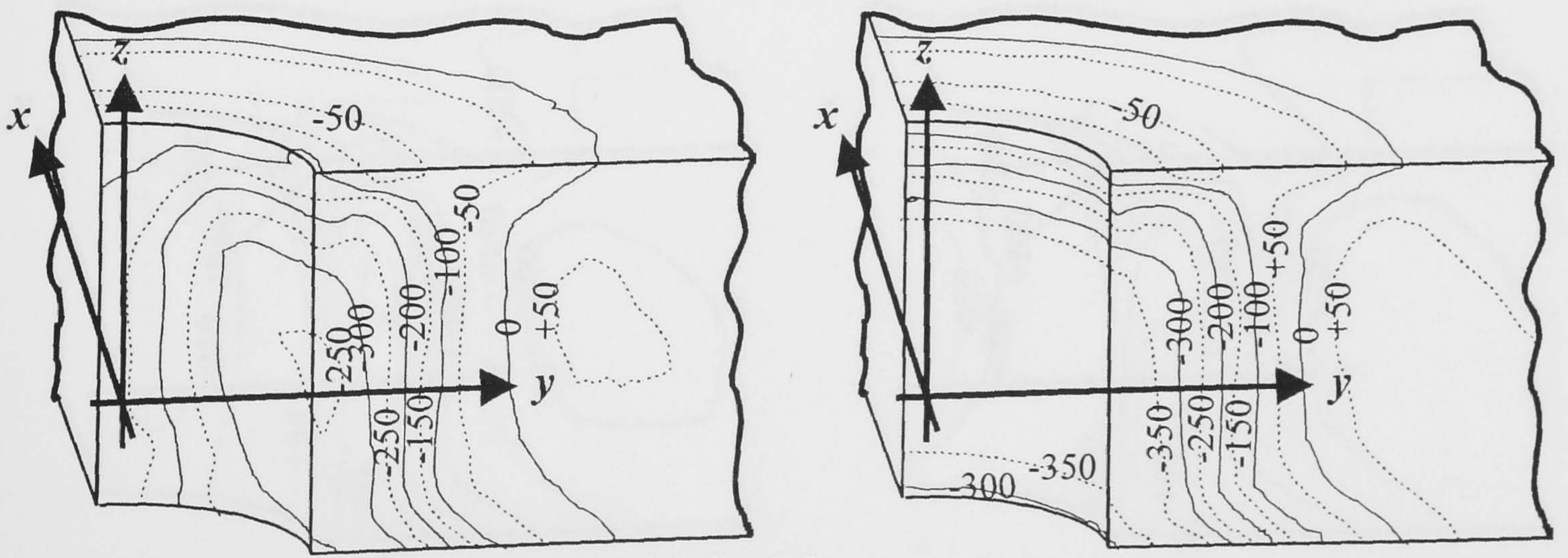

agrees with fig.5.5

agrees with fig.4.5

(d) 4% Cold expanded hole, loaded $\sigma'_y/3$, crept for 1000h. and unloaded.

(e) 4% Cold expanded hole.

Figure 6.13. Tangential residual stresses for $\sigma_{app}=0$, and uncracked models (c=0mm), $\sigma_{\theta\theta}$ [MPa].

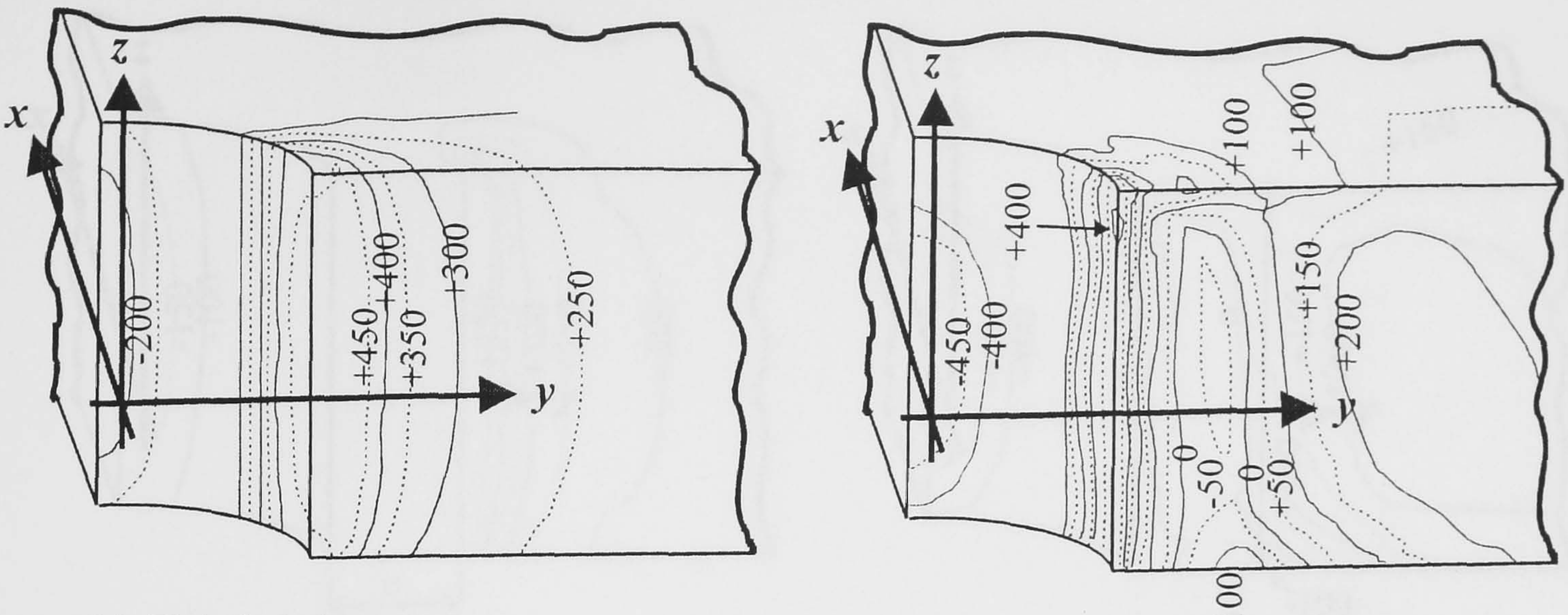

(a) Plain hole loaded

(b) 4% Cold expanded hole, compressed with $\sigma_{app}=\sigma'_y/3$, unloaded and reloaded.

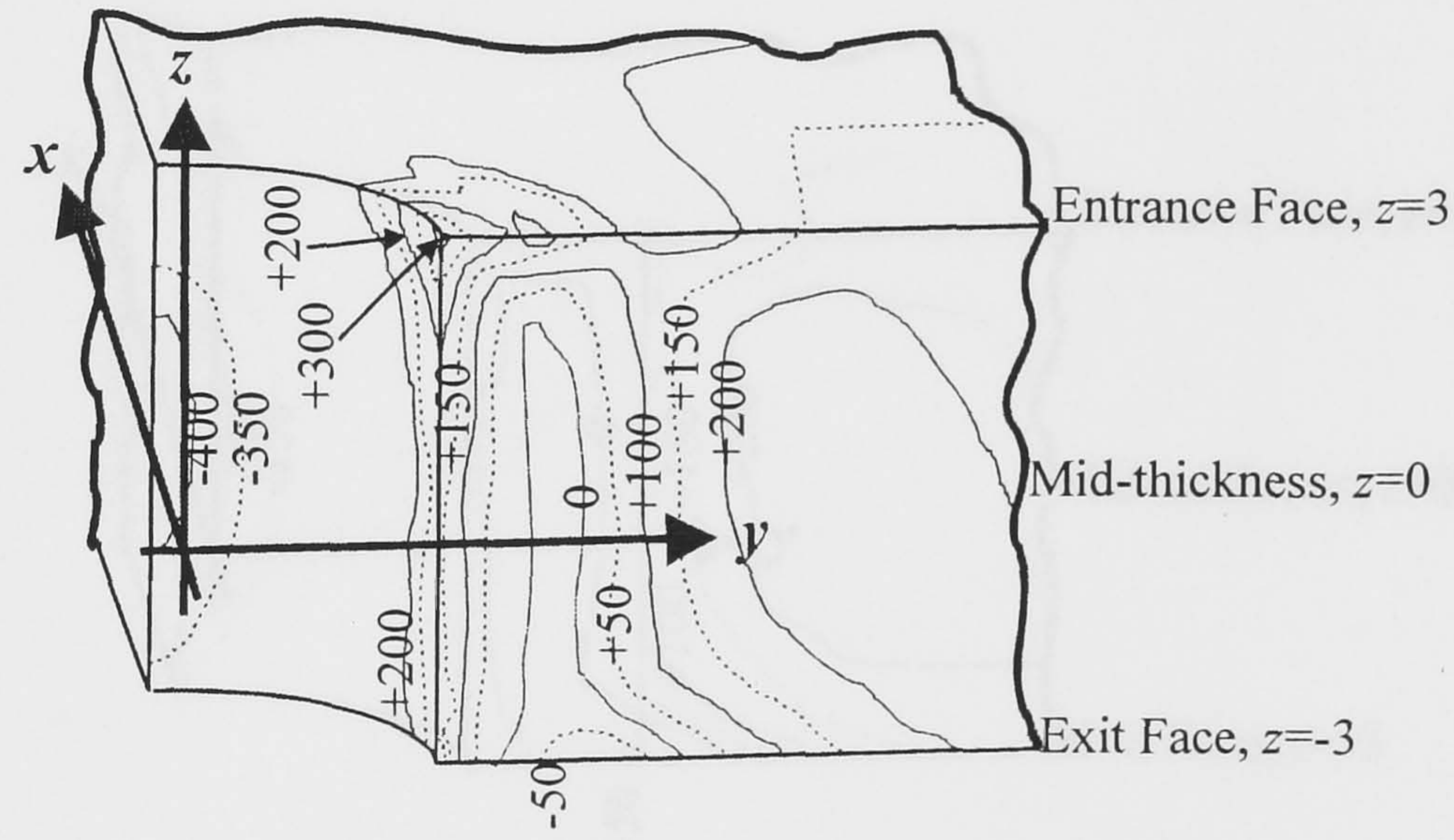

(c) 4% Cold expanded hole and crept without load for 1000h. and loaded with $\sigma_{app}=\sigma'_y/3$

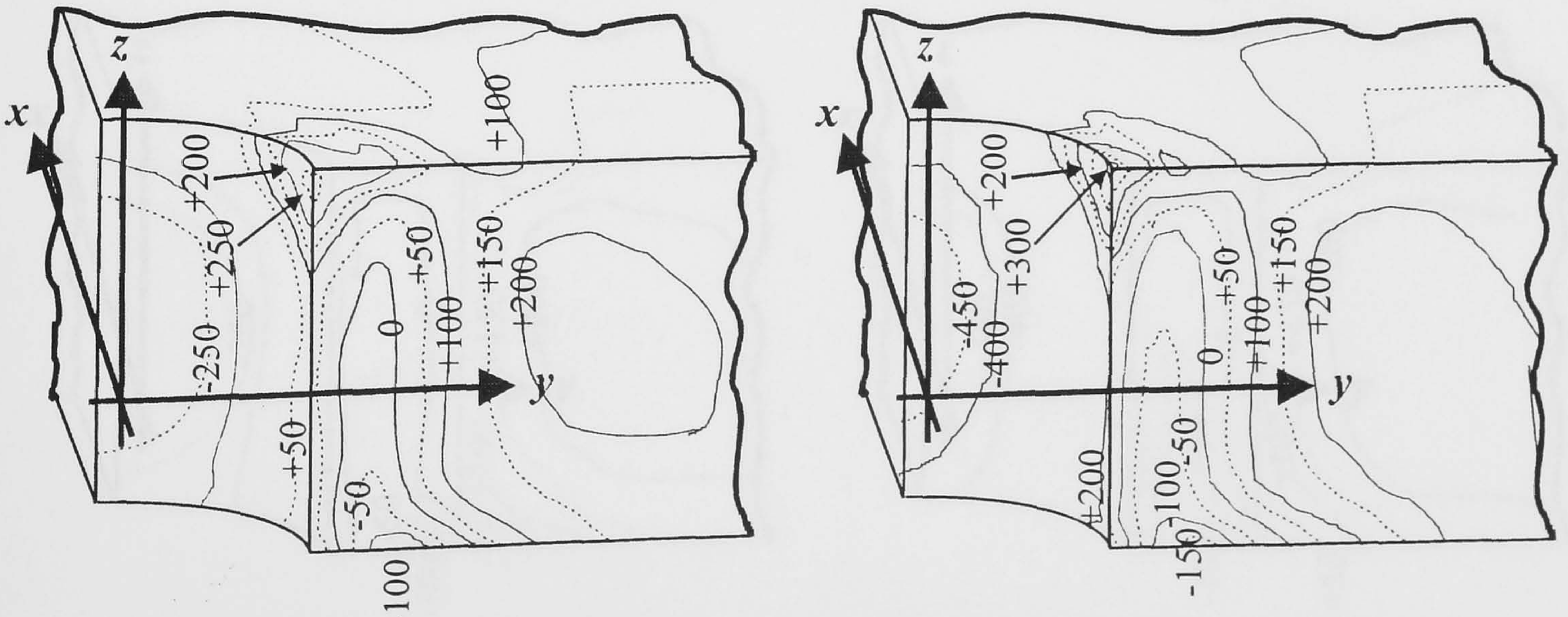

(d) 4% Cold expanded hole, loaded $\sigma'_y/3$, crept for 1000h., unloaded and reloaded at room temperature.

(e) 4% Cold expanded hole, loaded with $\sigma_{app}=\sigma'_y/3$.

Figure 6.14. Tangential stresses for σ_{app}= 143.33 MPa = $\sigma_y'/3$, and uncracked models (c=0mm), $\sigma_{\theta\theta}$ [MPa].

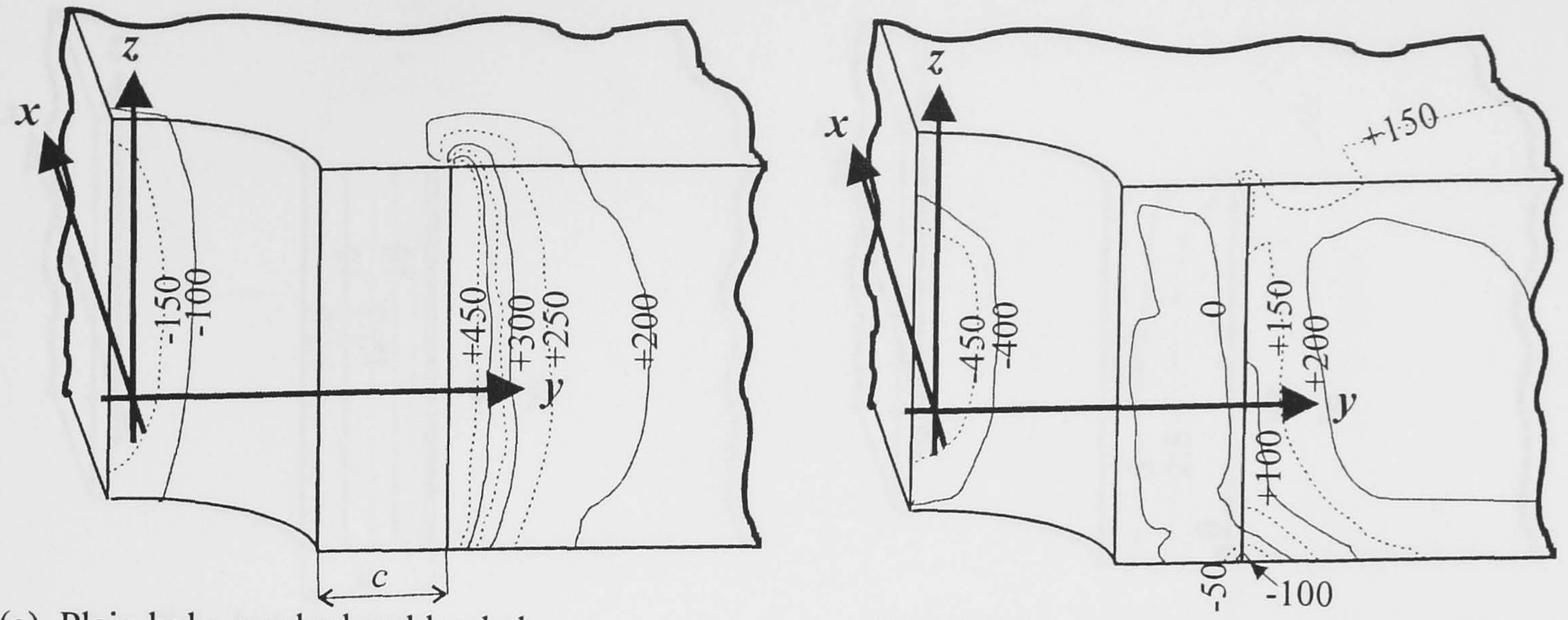

(a) Plain hole, cracked and loaded

(b) 4% Cold expanded hole, compressed with $\sigma_{app}=\sigma'_y/3$, unloaded, cracked and reloaded.

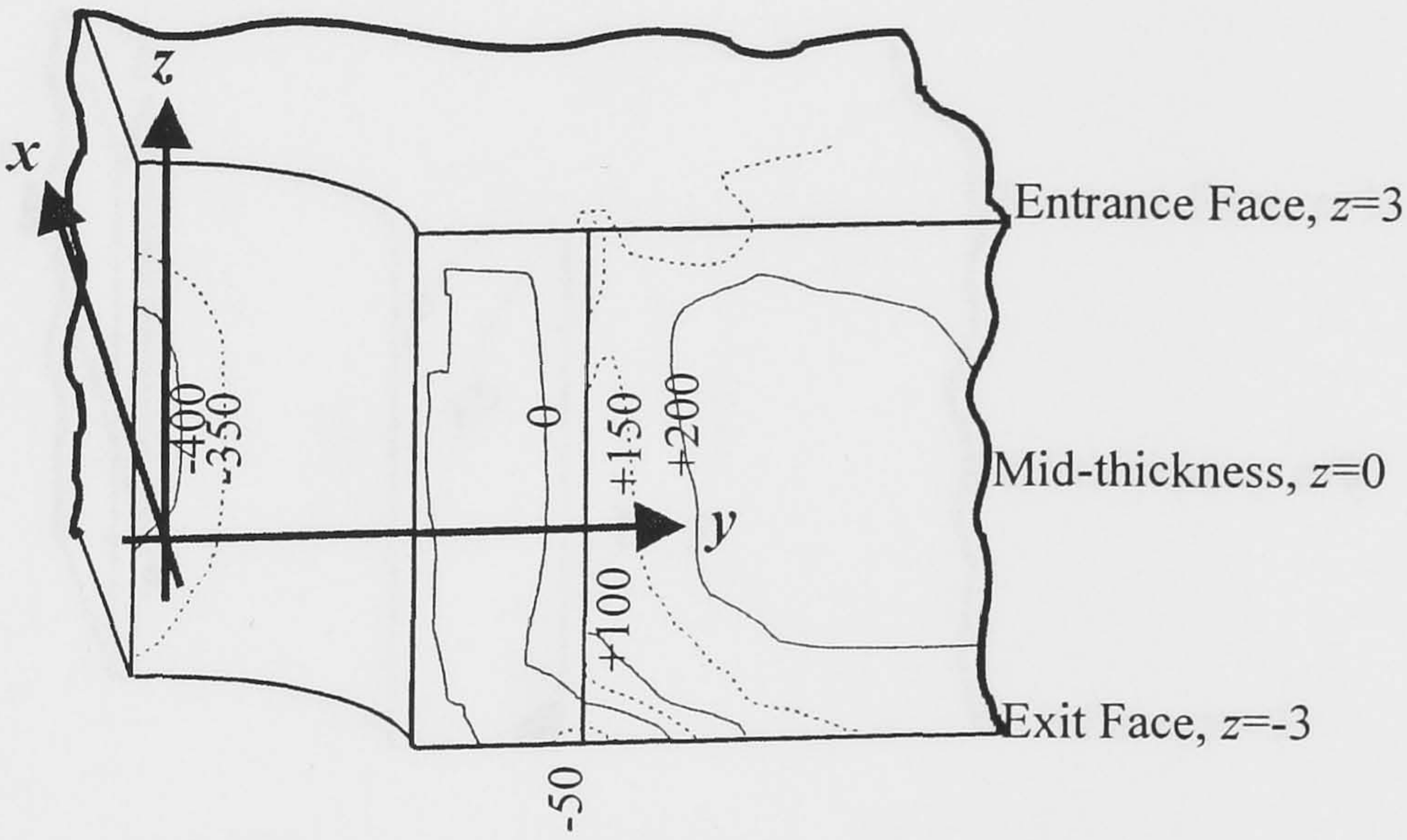

(c) 4% Cold expanded hole and crept without load for 1000h., cracked and loaded with $\sigma_{app}=\sigma'_y/3$

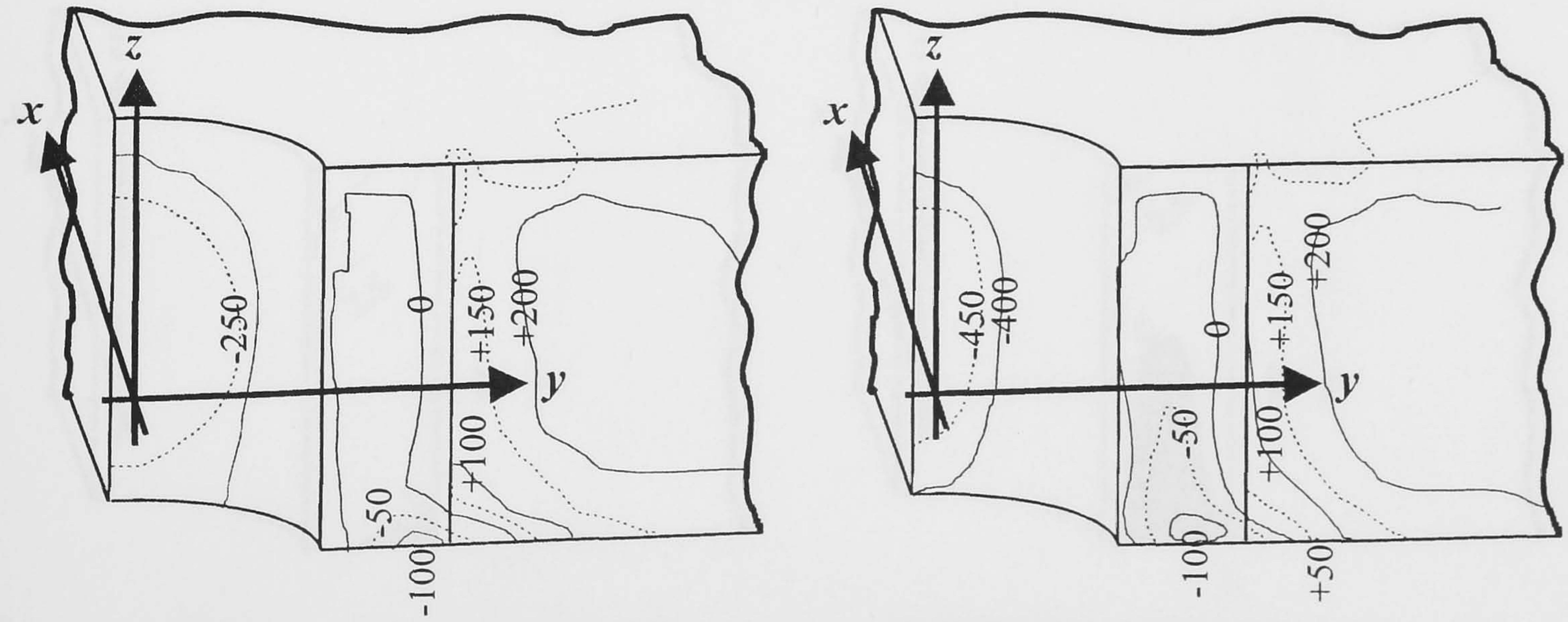

(d) 4% Cold expanded hole, loaded $\sigma'_y/3$, crept for 1000h., unloaded, cracked and reloaded at room temperature.

(e) 4% Cold expanded hole, cracked and loaded with $\sigma_{app}=\sigma'_y/3$.

Figure 6.15. Tangential stresses for σ_{app}= 143.33 MPa = $\sigma_y'/3$, and through–thickness double cracked samples (c=2 mm), $\sigma_{\theta\theta}$ [MPa].

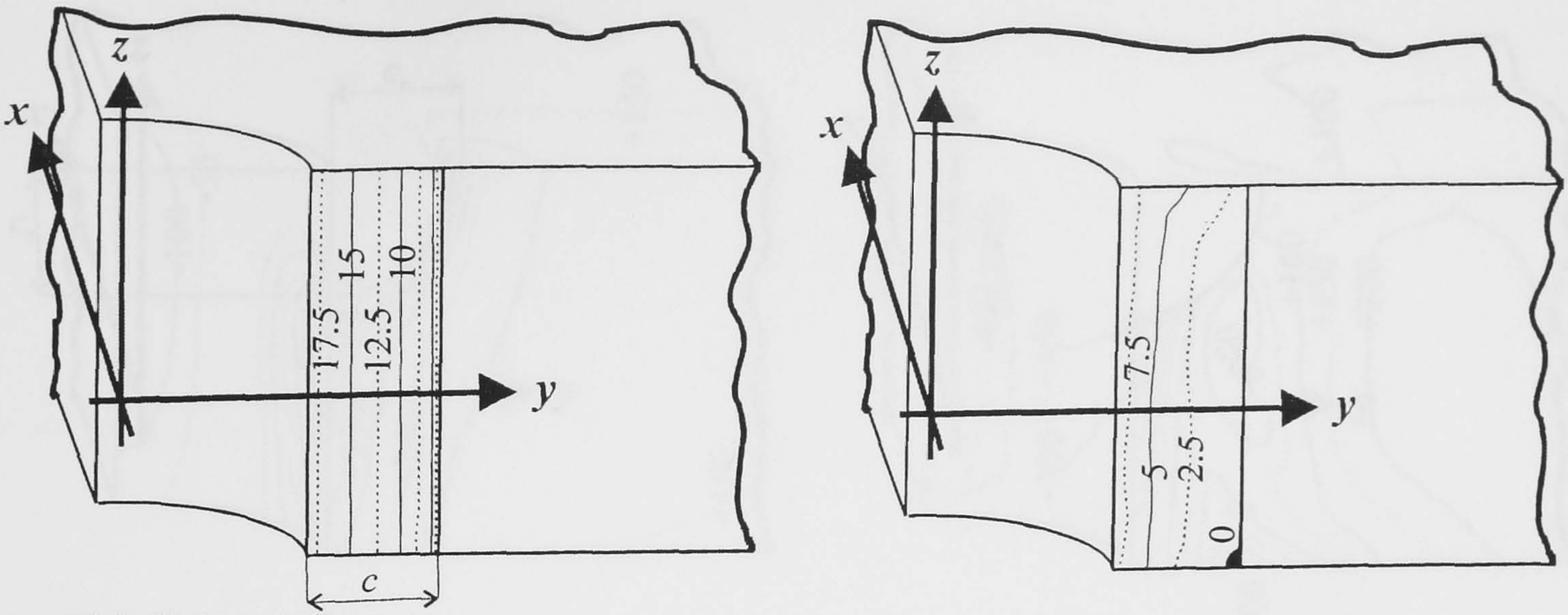

(a) Plain hole loaded

(b) 4% Cold expanded hole, compressed with $\sigma_{app}=\sigma'_y/3$, unloaded and reloaded.

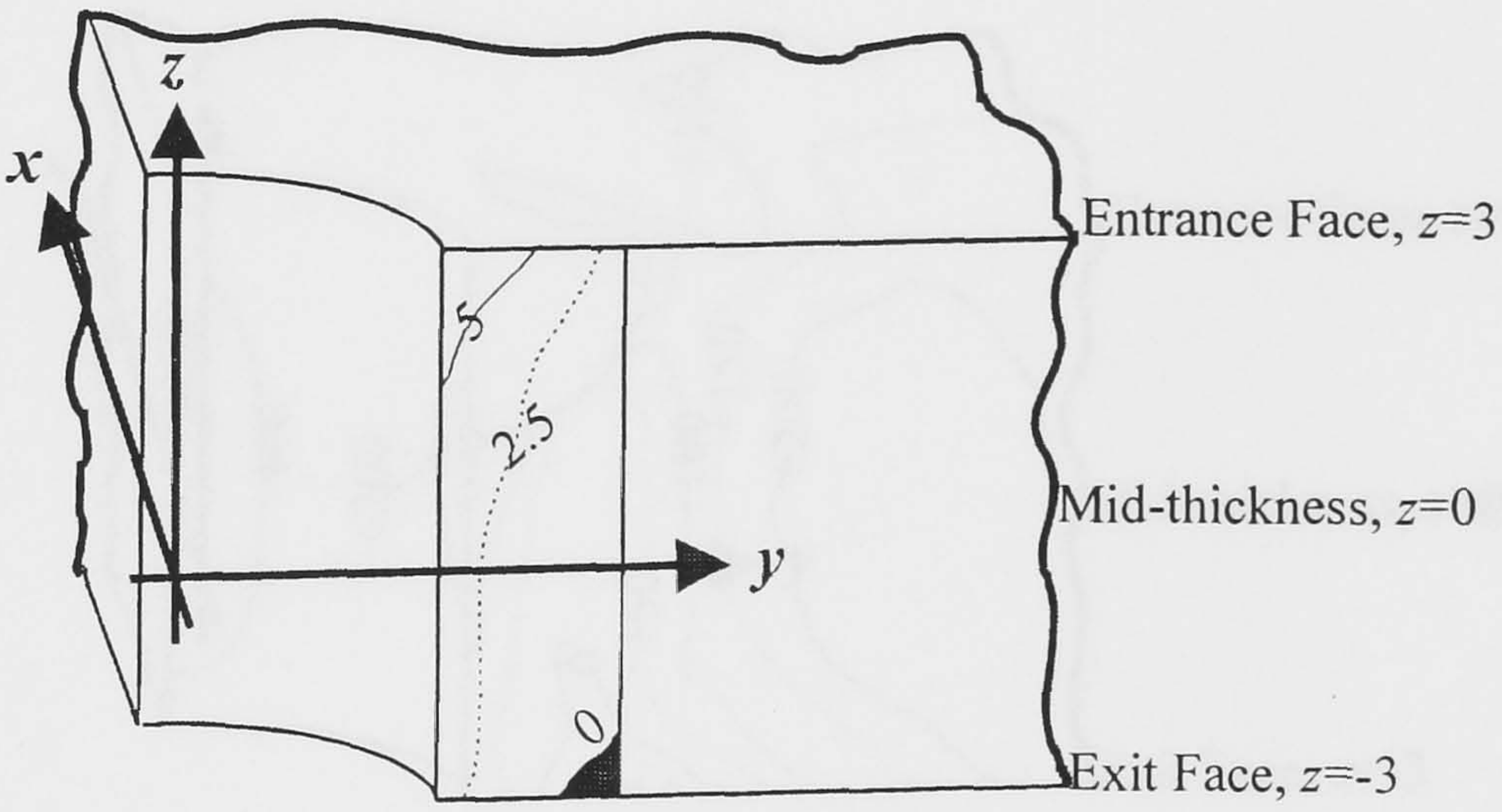

(c) 4% Cold expanded hole and crept without load for 1000h. and loaded with $\sigma_{app}=\sigma'_y/3$

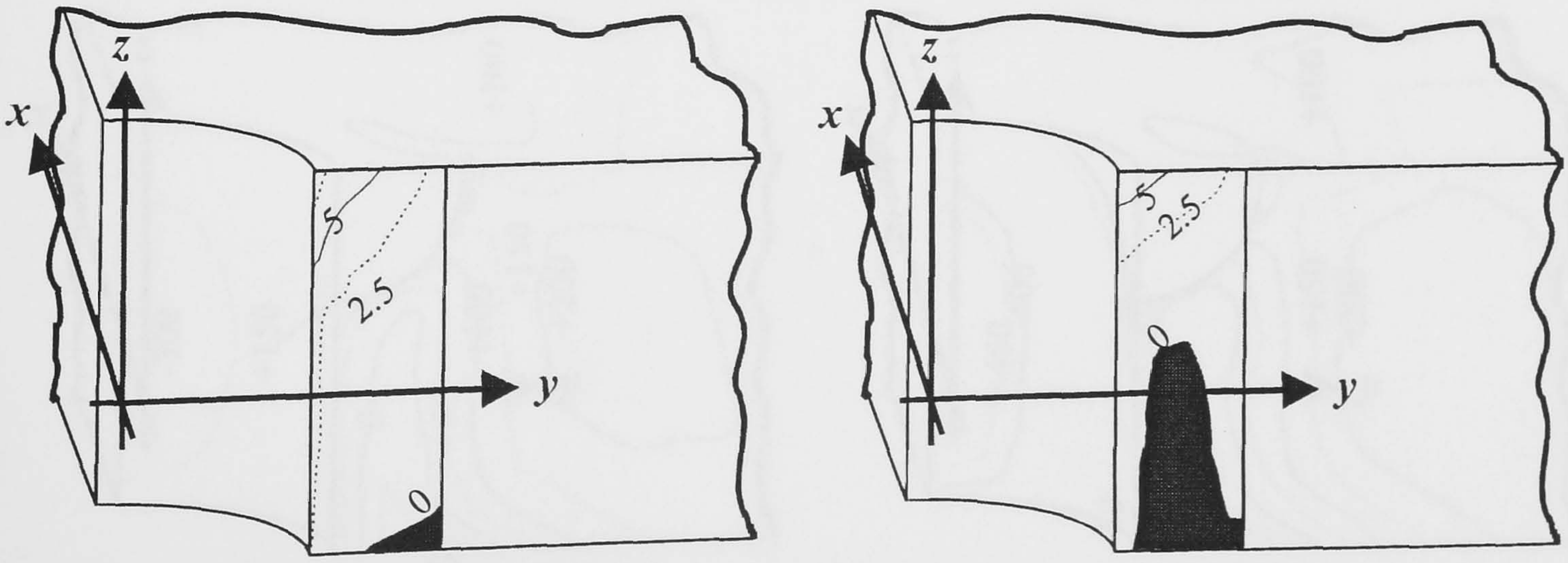

(d) 4% Cold expanded hole, loaded $\sigma'_y/3$, crept for 1000h., unloaded and reloaded at room temperature.

(e) 4% Cold expanded hole, loaded with $\sigma_{app}=\sigma'_y/3$.

Figure 6.16. Crack opening displacement for σ_{app}= 143.33 MPa = $\sigma_y'/3$, and through–thickness double cracked samples (c=2 mm), $U_{\theta\theta}$ [μm].

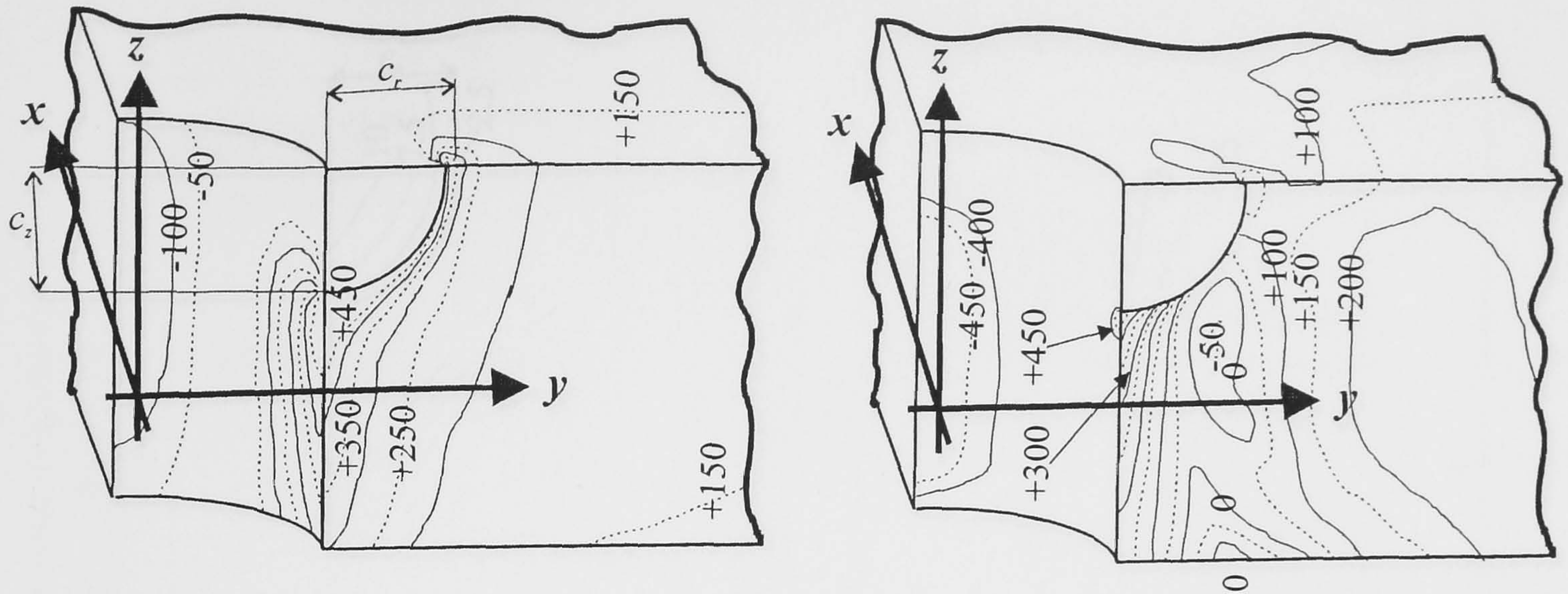

(a) Plain hole, cracked and loaded

(b) 4% Cold expanded hole, compressed with $\sigma_{app}=\sigma'_y/3$, unloaded, cracked and reloaded.

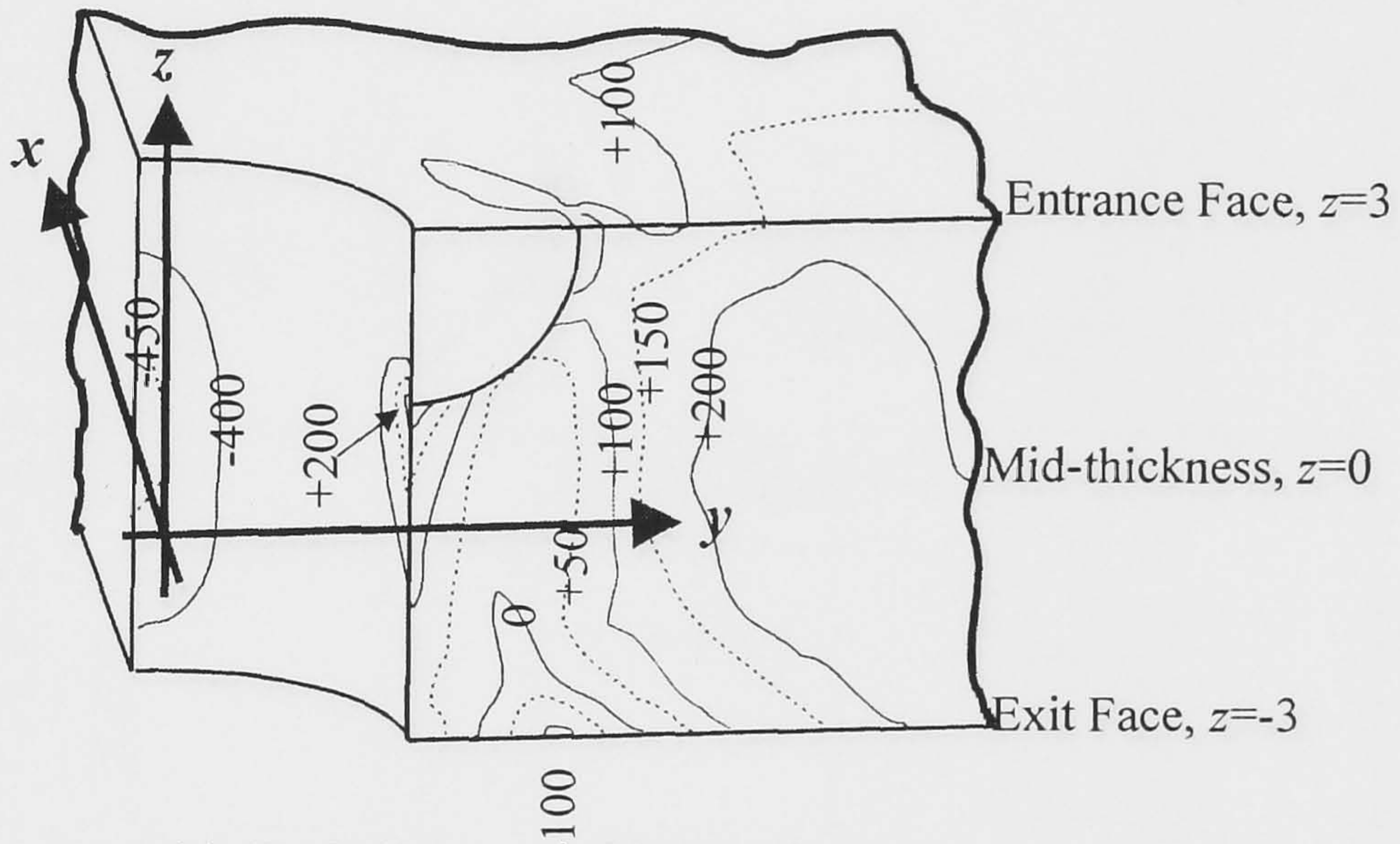

(c) 4% Cold expanded hole and crept without load for 1000h., cracked and loaded with $\sigma_{app}=\sigma'_y/3$

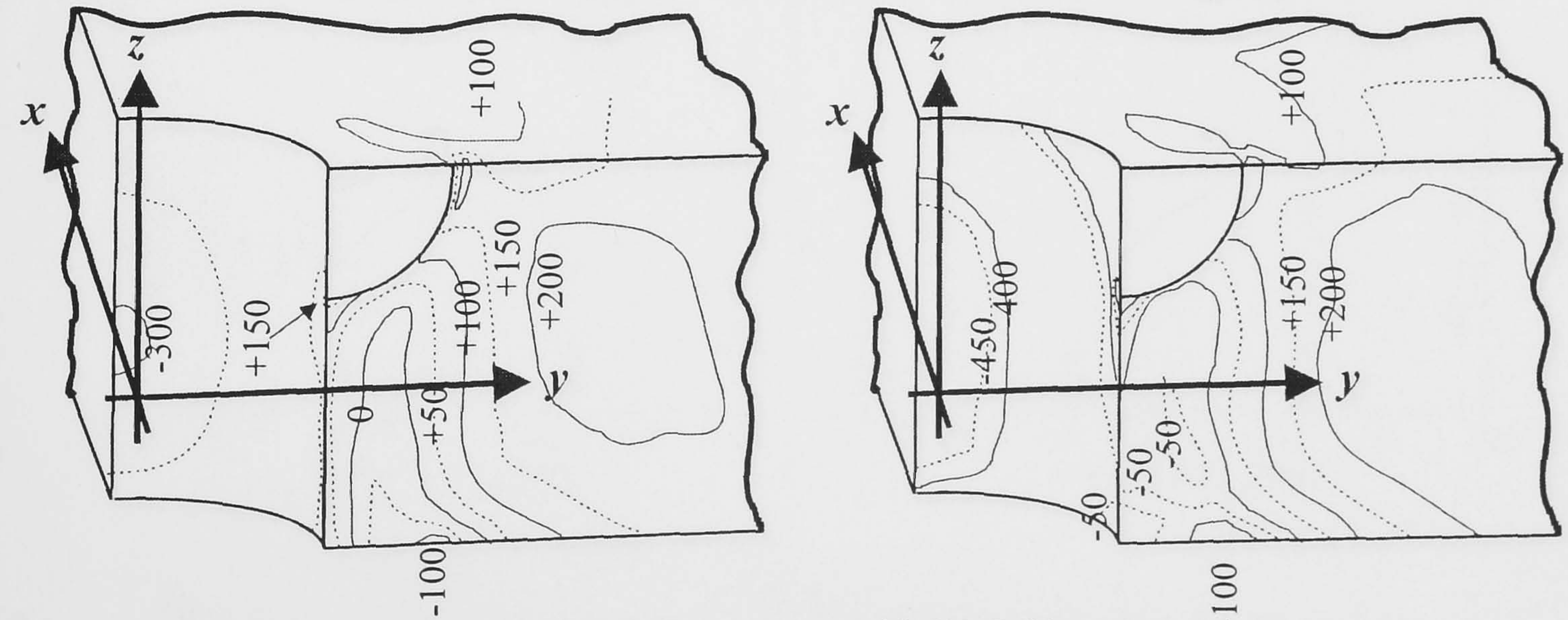

(d) 4% Cold expanded hole, loaded $\sigma'_y/3$, crept for 1000h., unloaded, cracked and reloaded at room temperature.

(e) 4% Cold expanded hole, cracked and loaded with $\sigma_{app}=\sigma'_y/3$.

Figure 6.17. Tangential stresses for σ_{app}= 143.33 MPa = $\sigma_y'/3$, and corner double cracked samples (c_r= c_z =2 mm), $\sigma_{\theta\theta}$ [MPa].

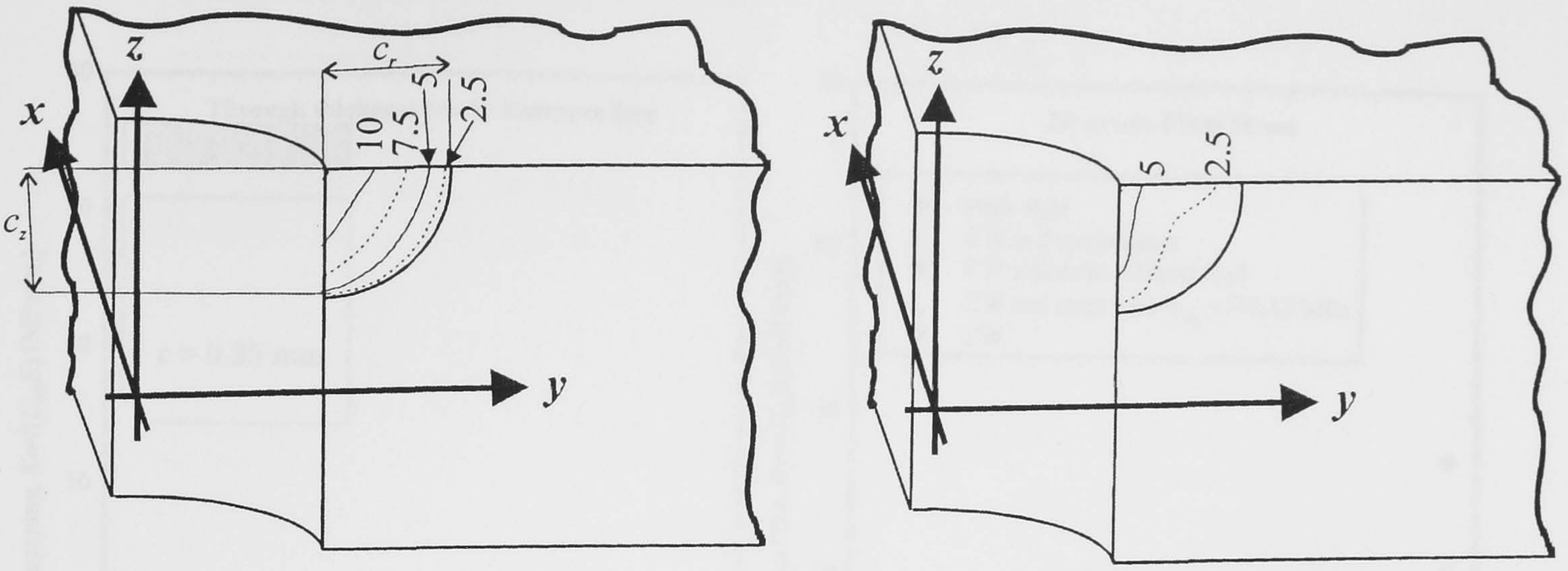

(a) Plain hole, cracked and loaded

(b) 4% Cold expanded hole, compressed with $\sigma_{app}=\sigma'_y/3$, unloaded, cracked and reloaded.

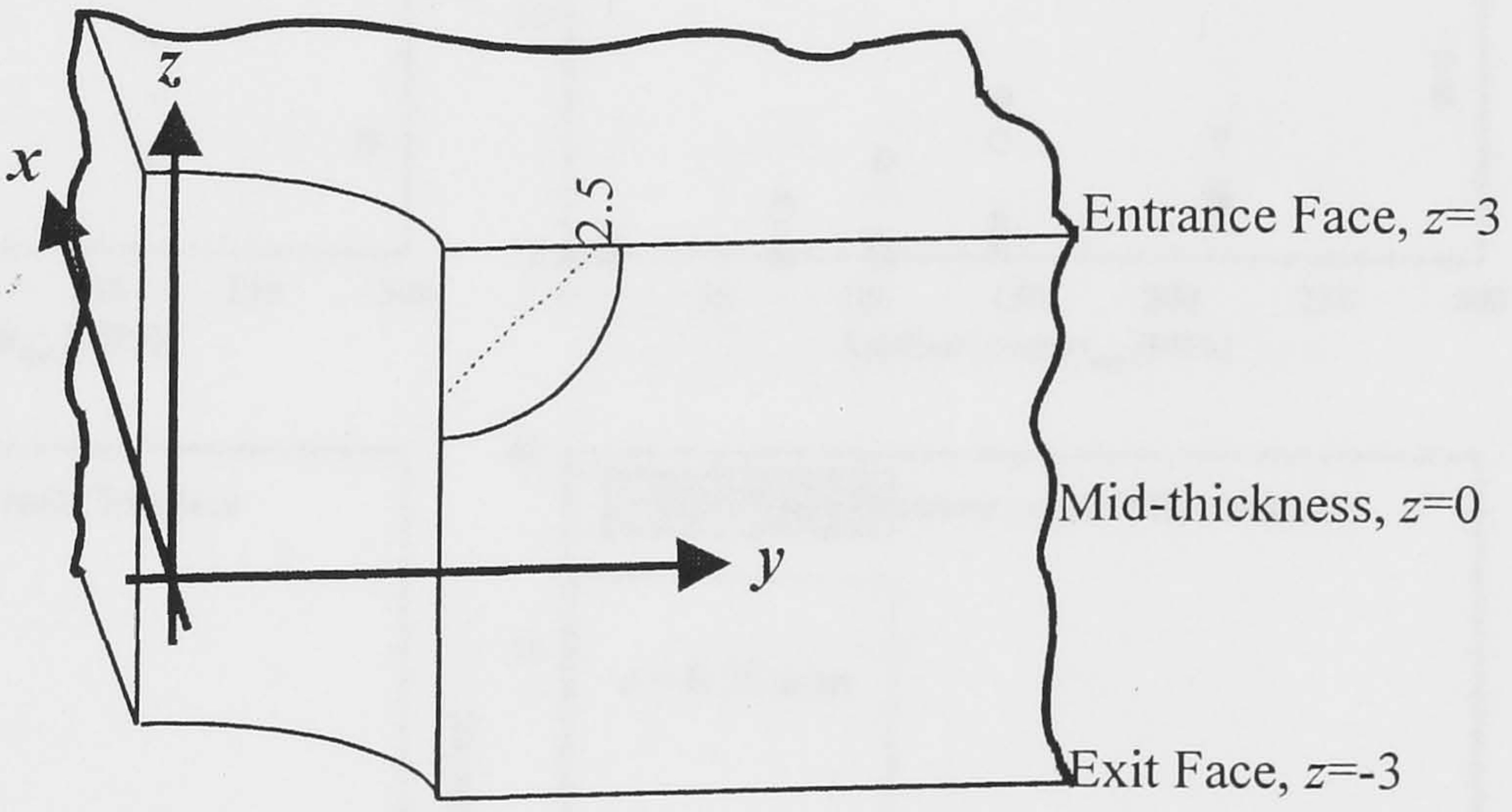

(c) 4% Cold expanded hole and crept without load for 1000h., cracked and loaded with $\sigma_{app}=\sigma'_y/3$

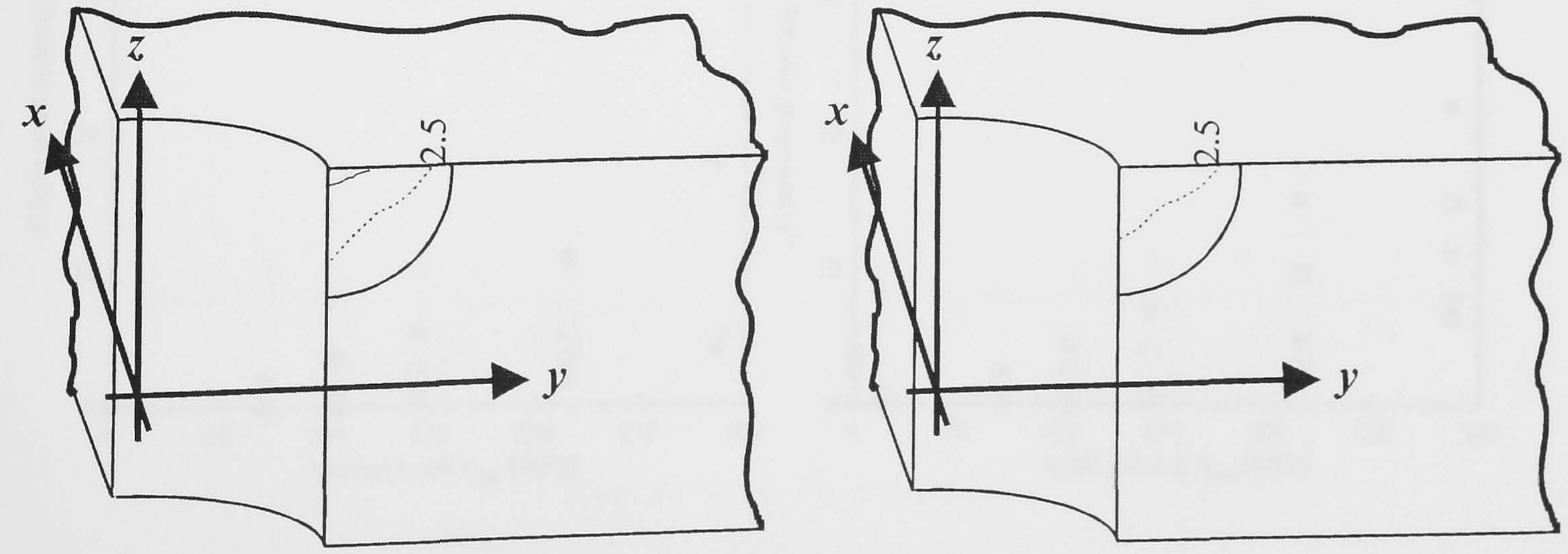

(d) 4% Cold expanded hole, loaded $\sigma'_y/3$, crept for 1000h., unloaded, cracked and reloaded at room temperature.

(e) 4% Cold expanded hole, cracked and loaded with $\sigma_{app}=\sigma'_y/3$.

Figure 6.18. Crack opening for σ_{app}= 143.33 MPa = $\sigma_y'/3$and corner double cracked samples (c_r= c_z=2 mm), $U_{\theta\theta}$ [μm].

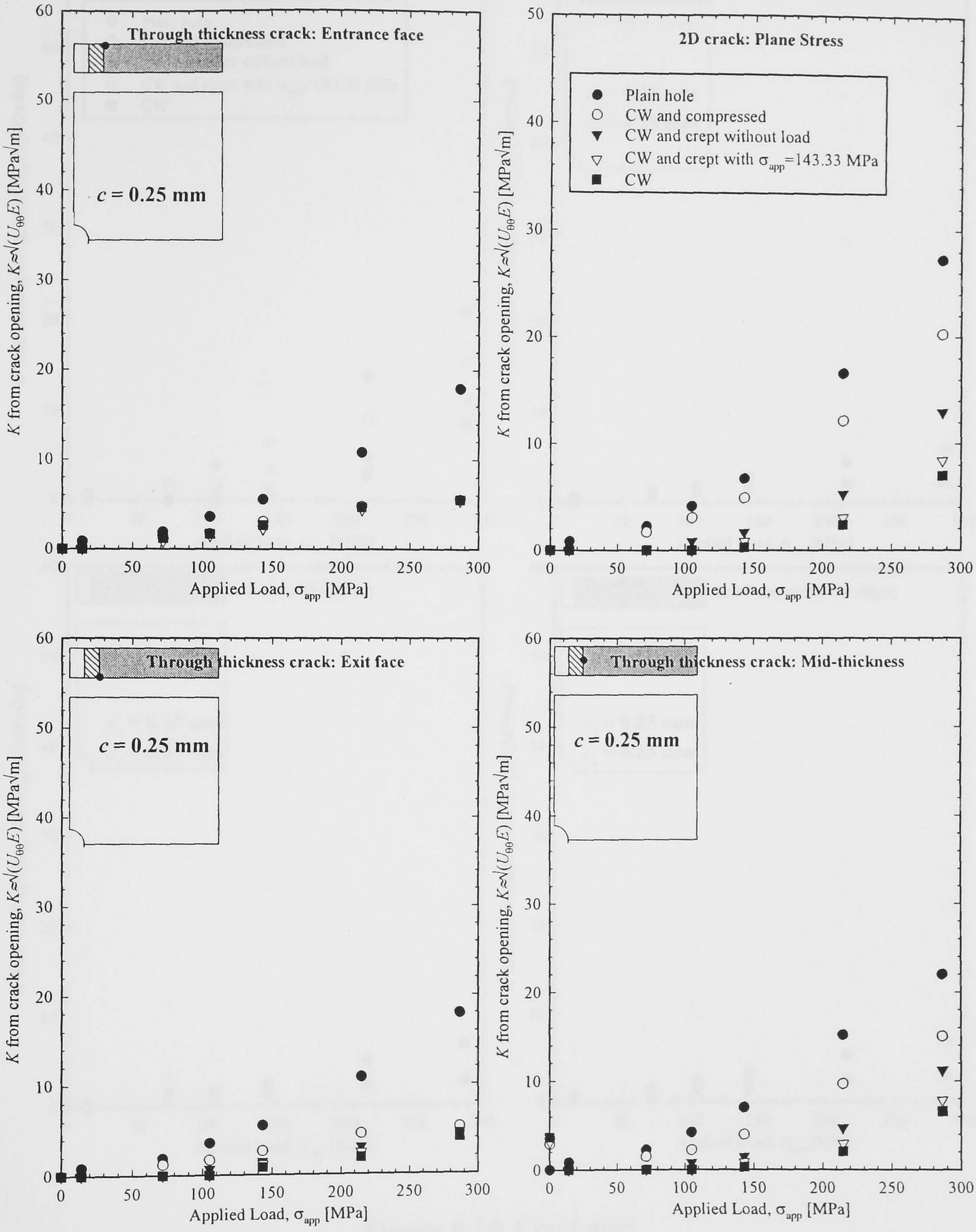

Figure 6.19. Stress intensity factors as a function of external applied stress for short cracks (c = 0.25 mm).

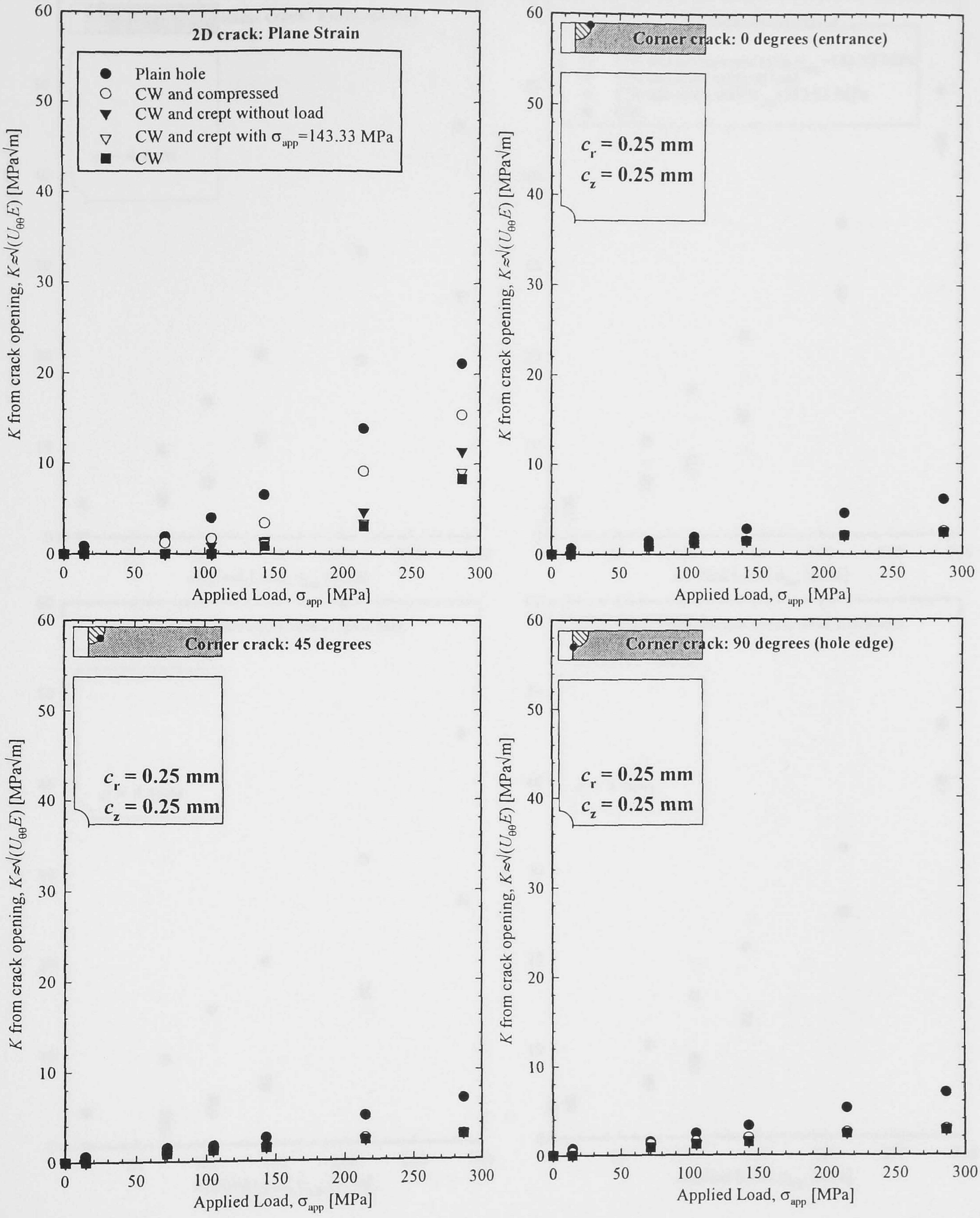

Figure 6.19. Continued

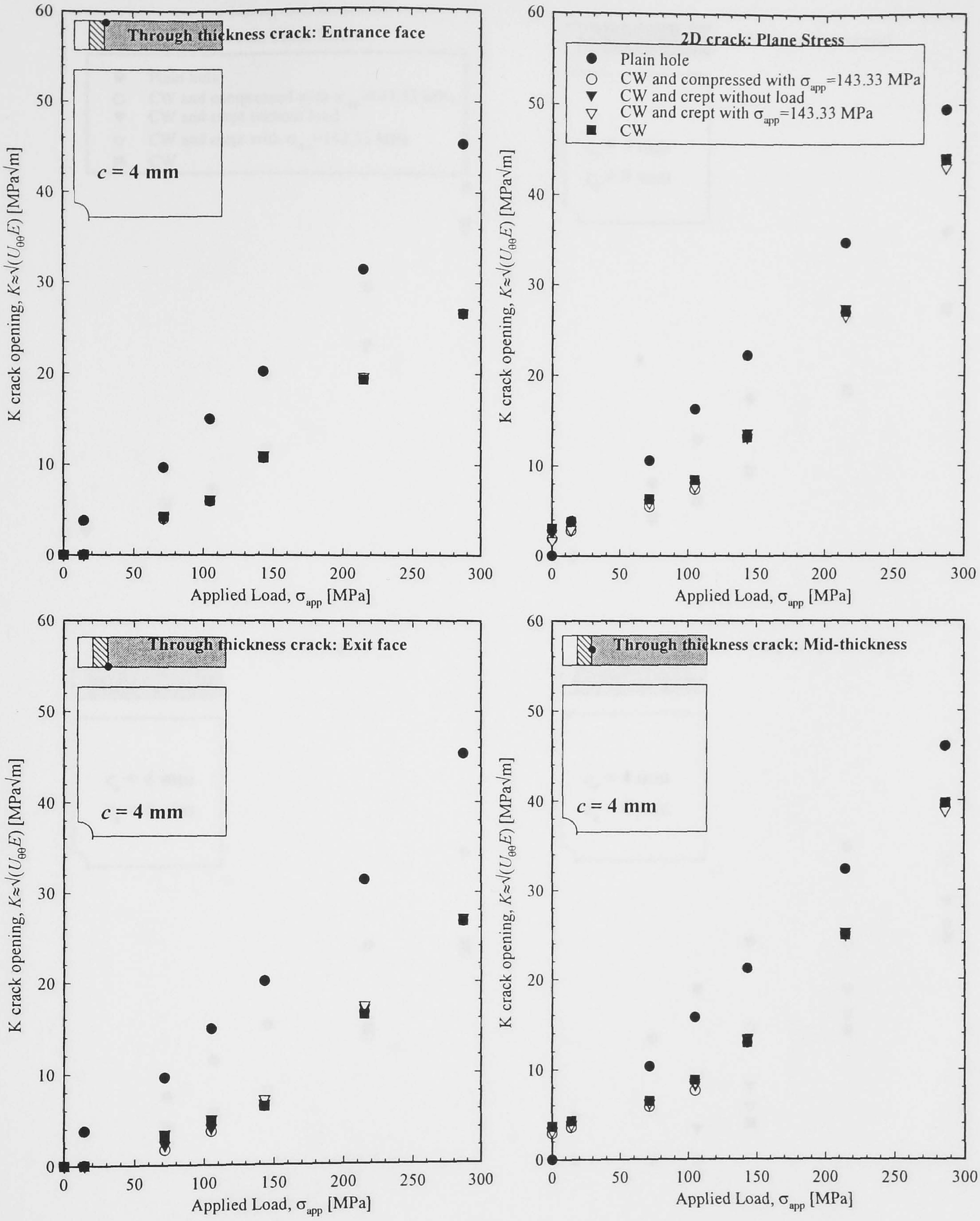

Figure 6.20. Stress intensity factors as a function of external applied stress for long cracks (c = 4 mm).

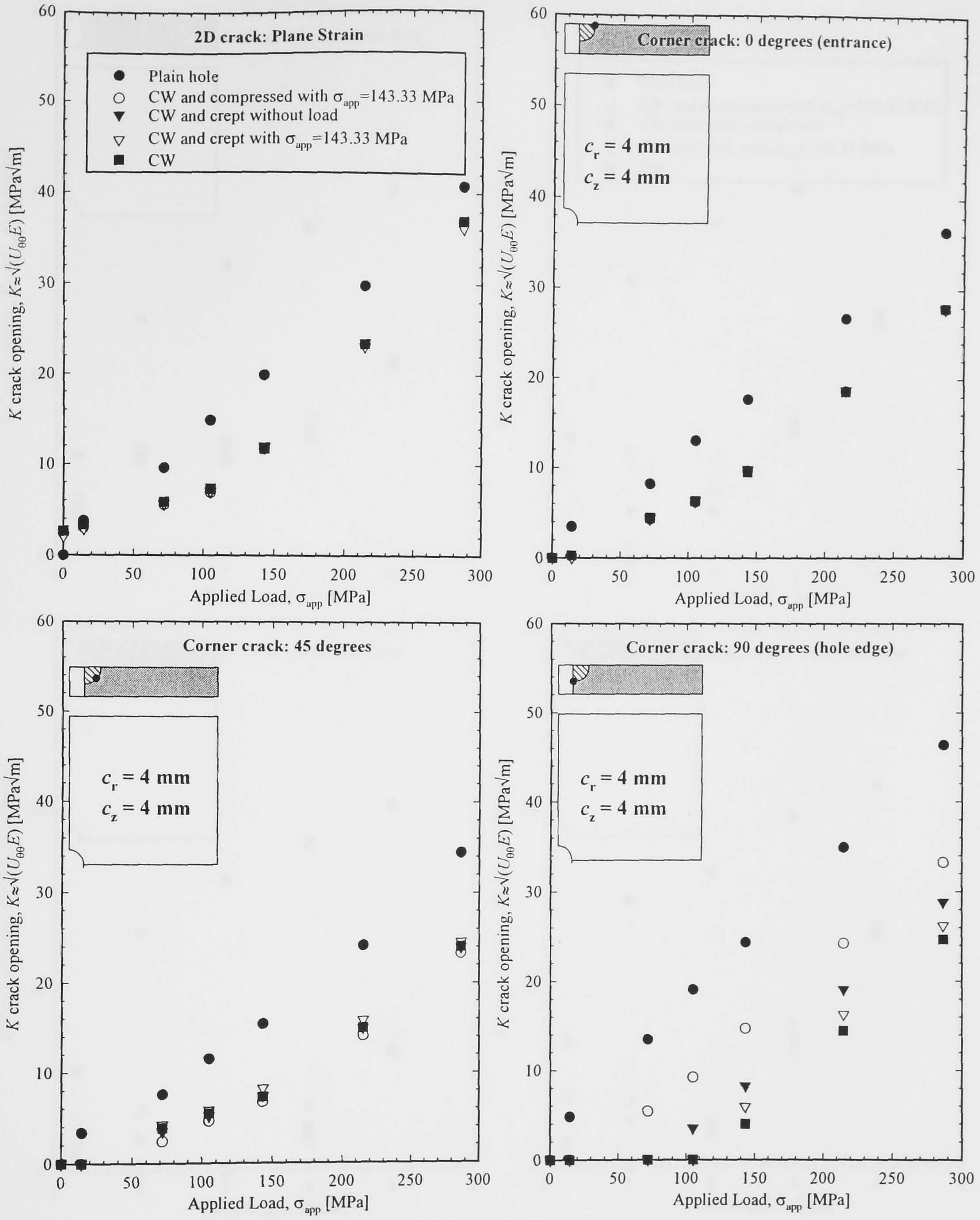

Figure 6.20. Continued

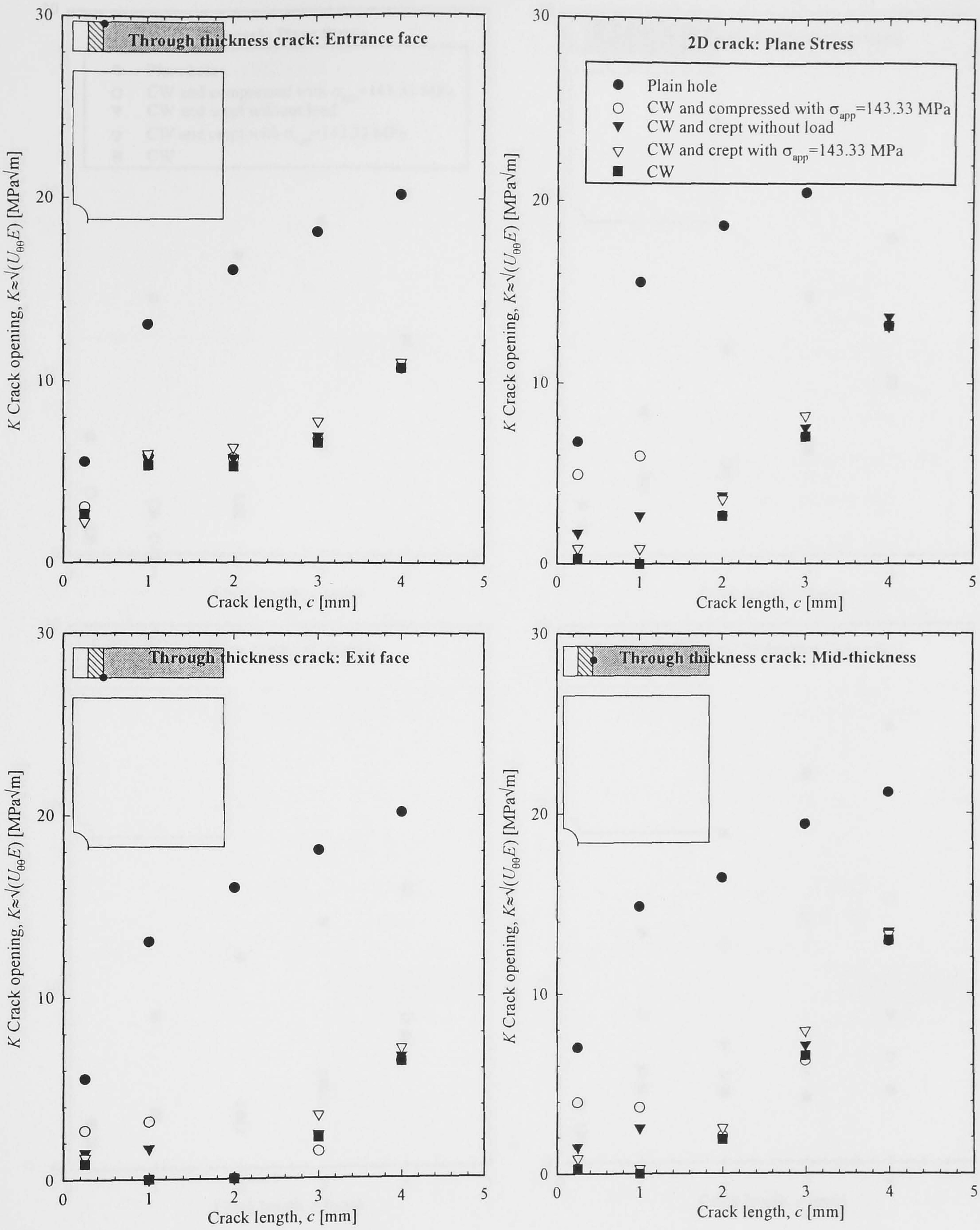

Figure 6.21. Stress intensity factors for external applied stress $\sigma_{app}=\sigma_y'/3$ as a function of crack length.

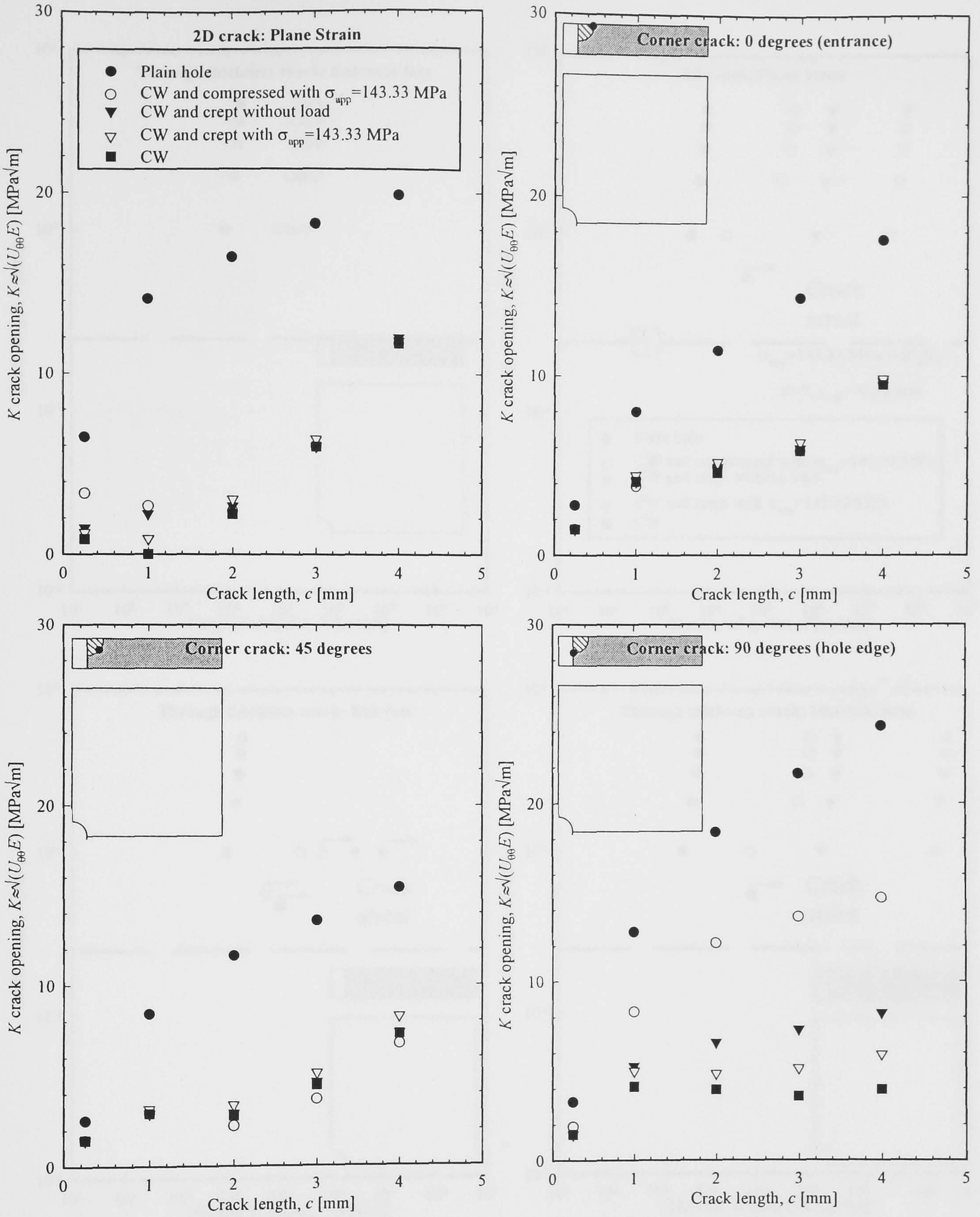

Figure 6.21. Continued

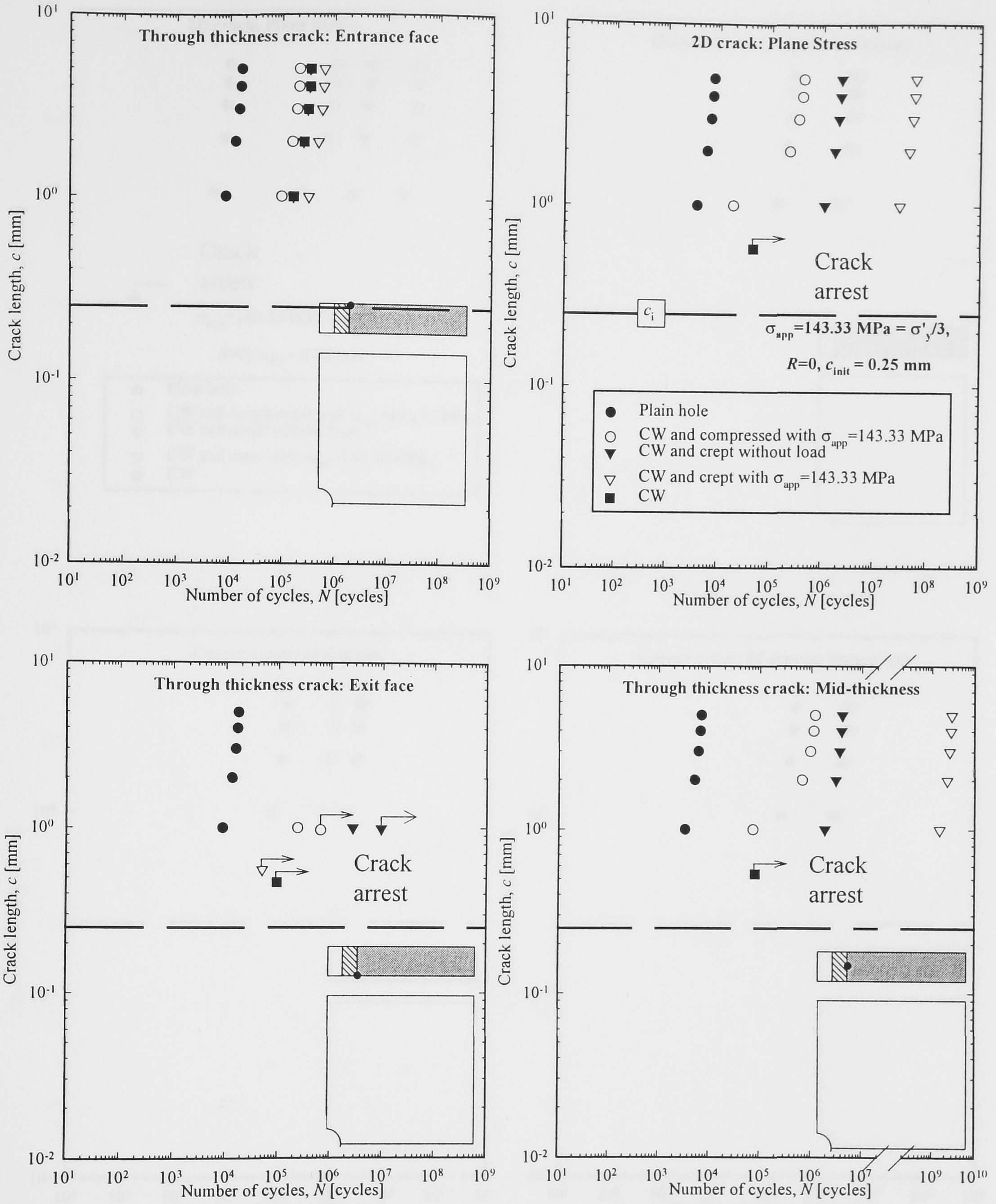

Figure 6.22. Fatigue crack growth predictions for initial cracks of $c_i = 0.25$ mm and applied load $\sigma_{app}=\sigma_y'/3$.

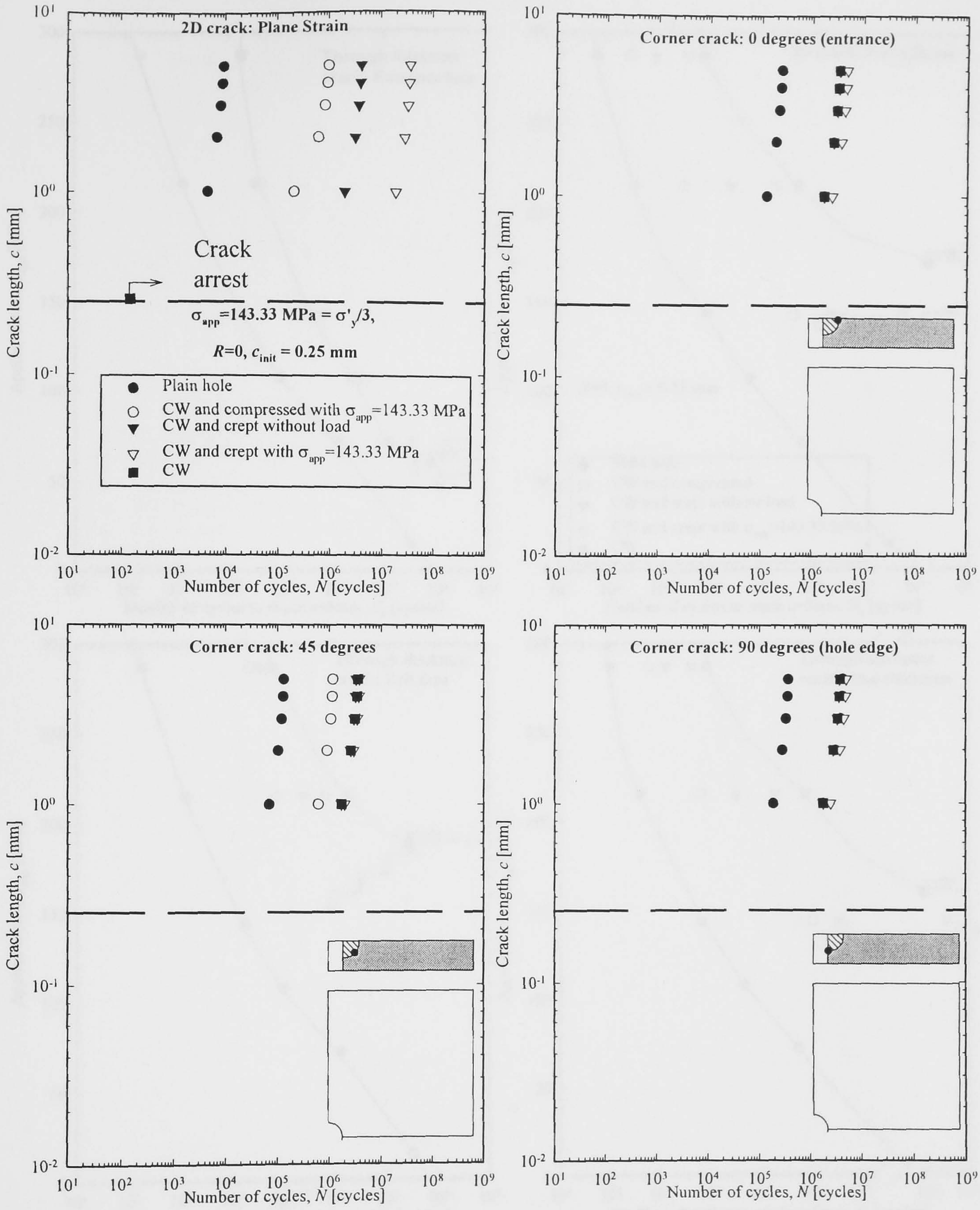

Figure 6.22. Continued

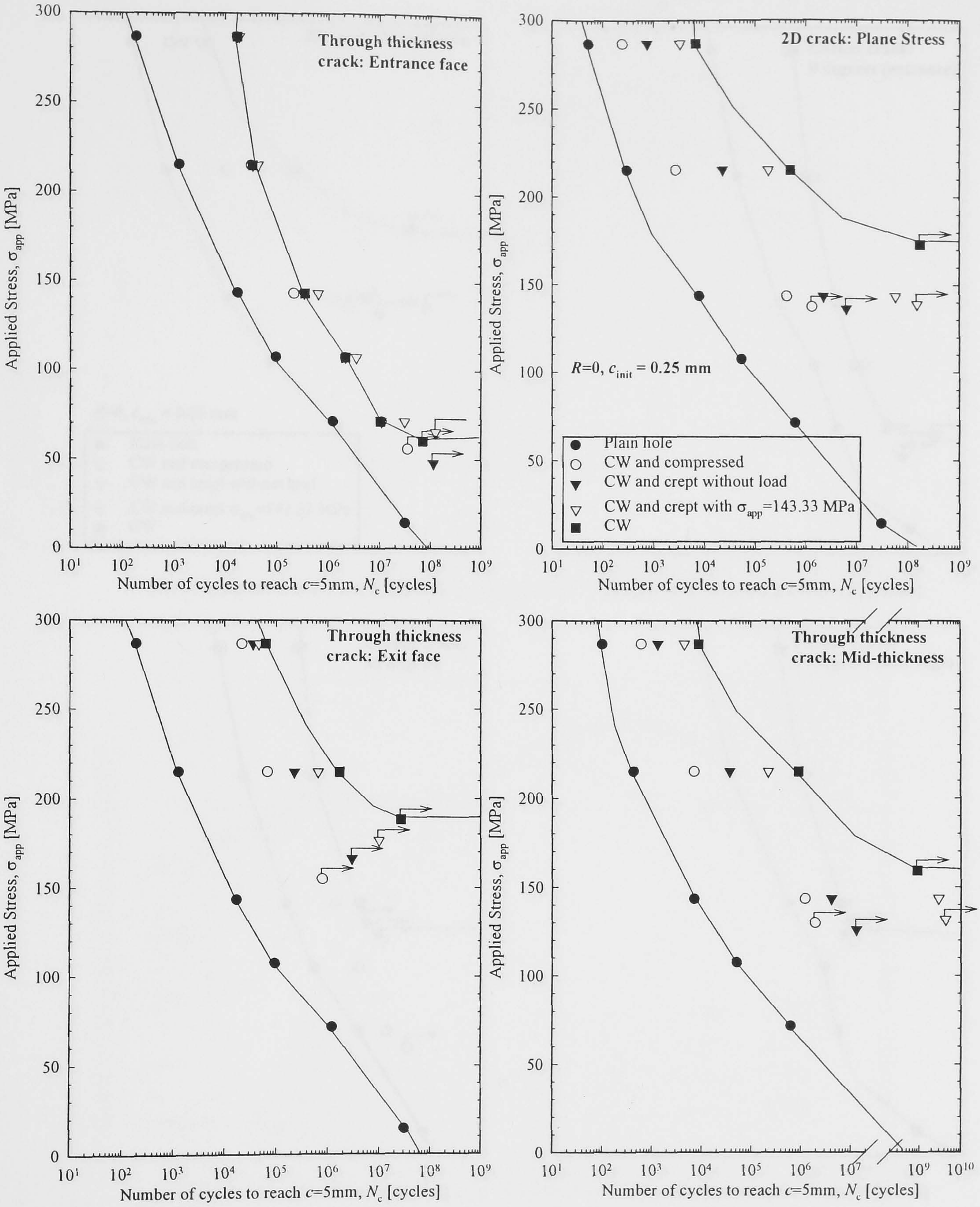

Figure 6.23. Number of cycles to reach critical crack size of 5 mm (N_c) for an initial crack length of c_i=0.25 mm.

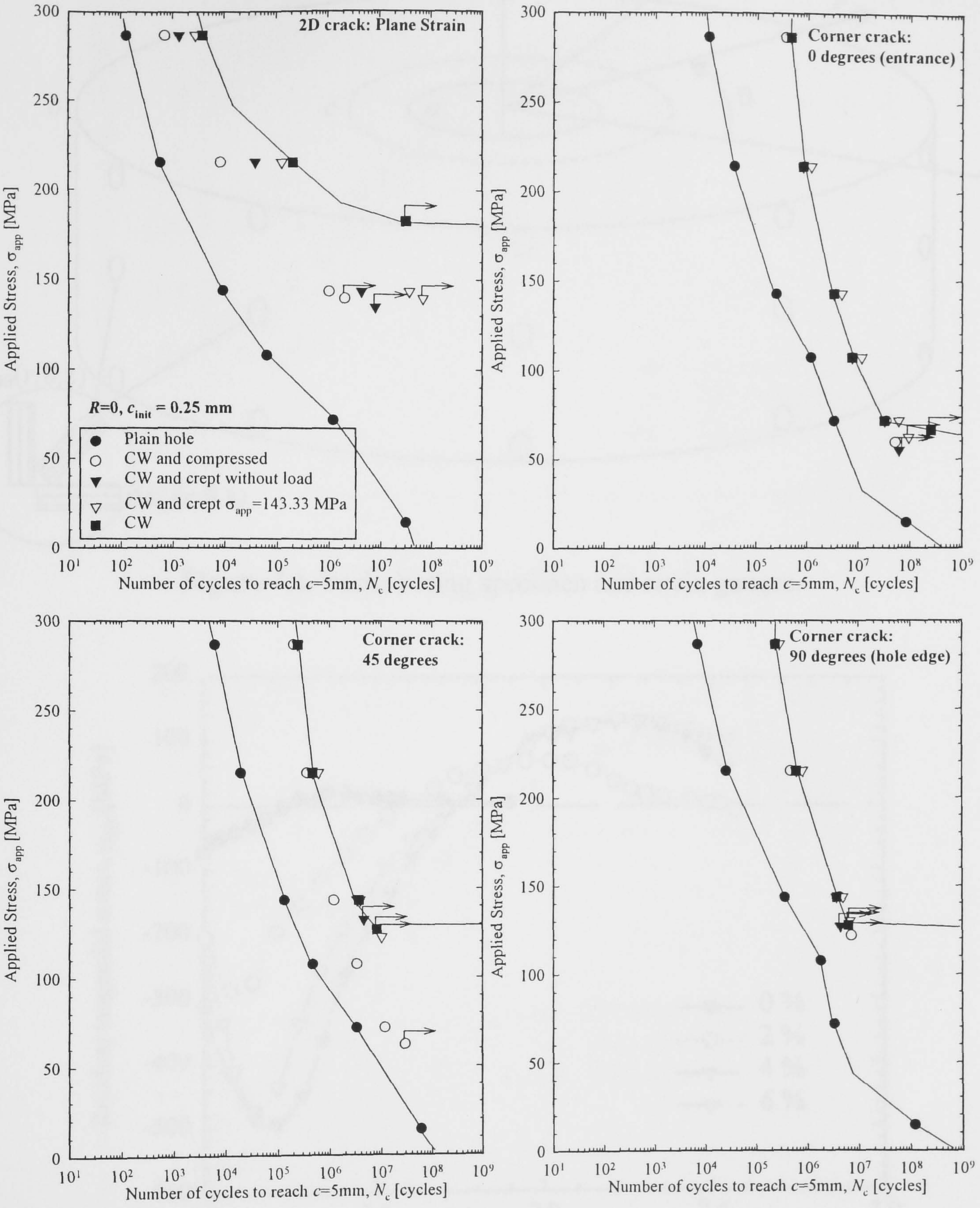

Figure 6.23. Continued

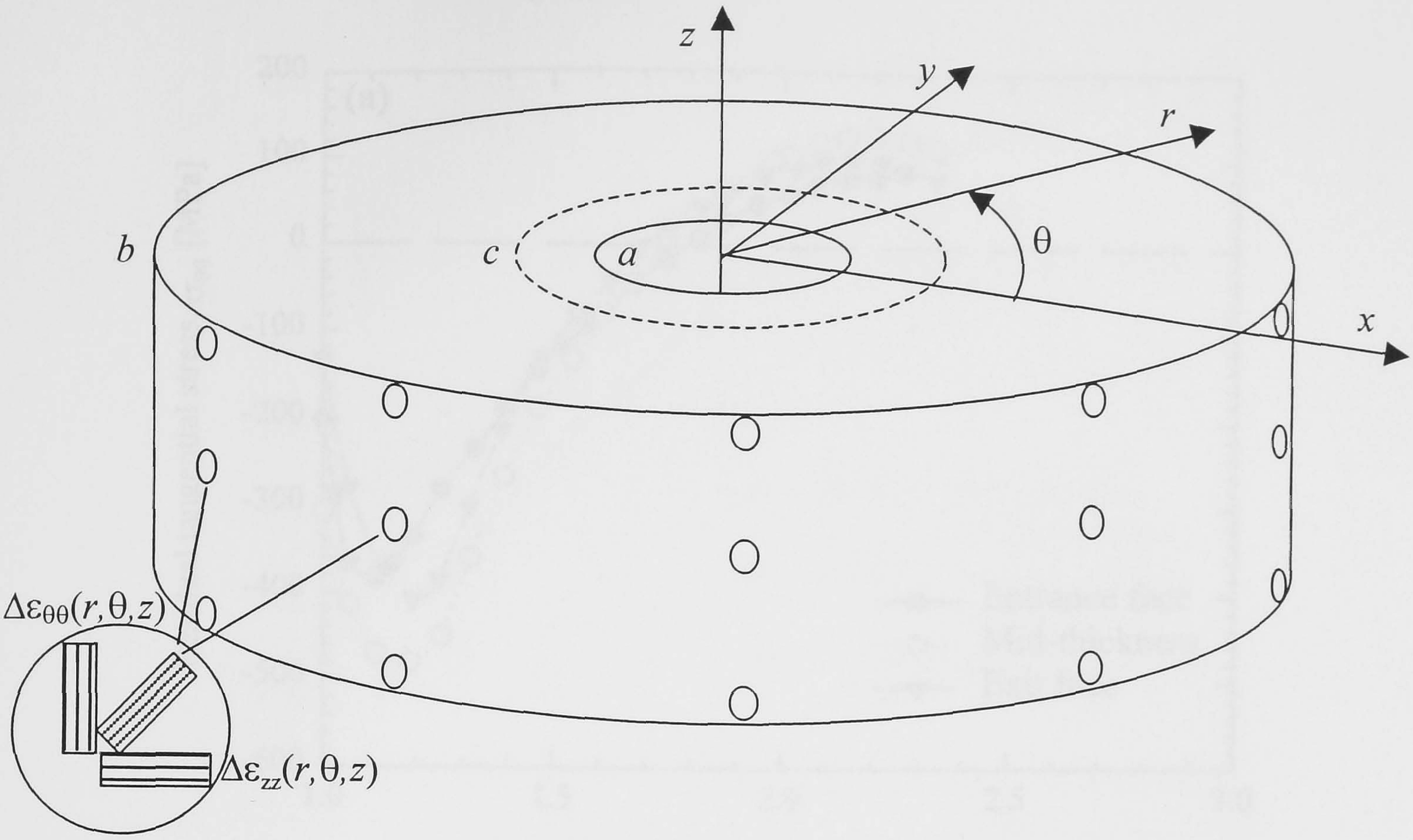

Figure 7.1. Sachs boring specimen and strain gauges.

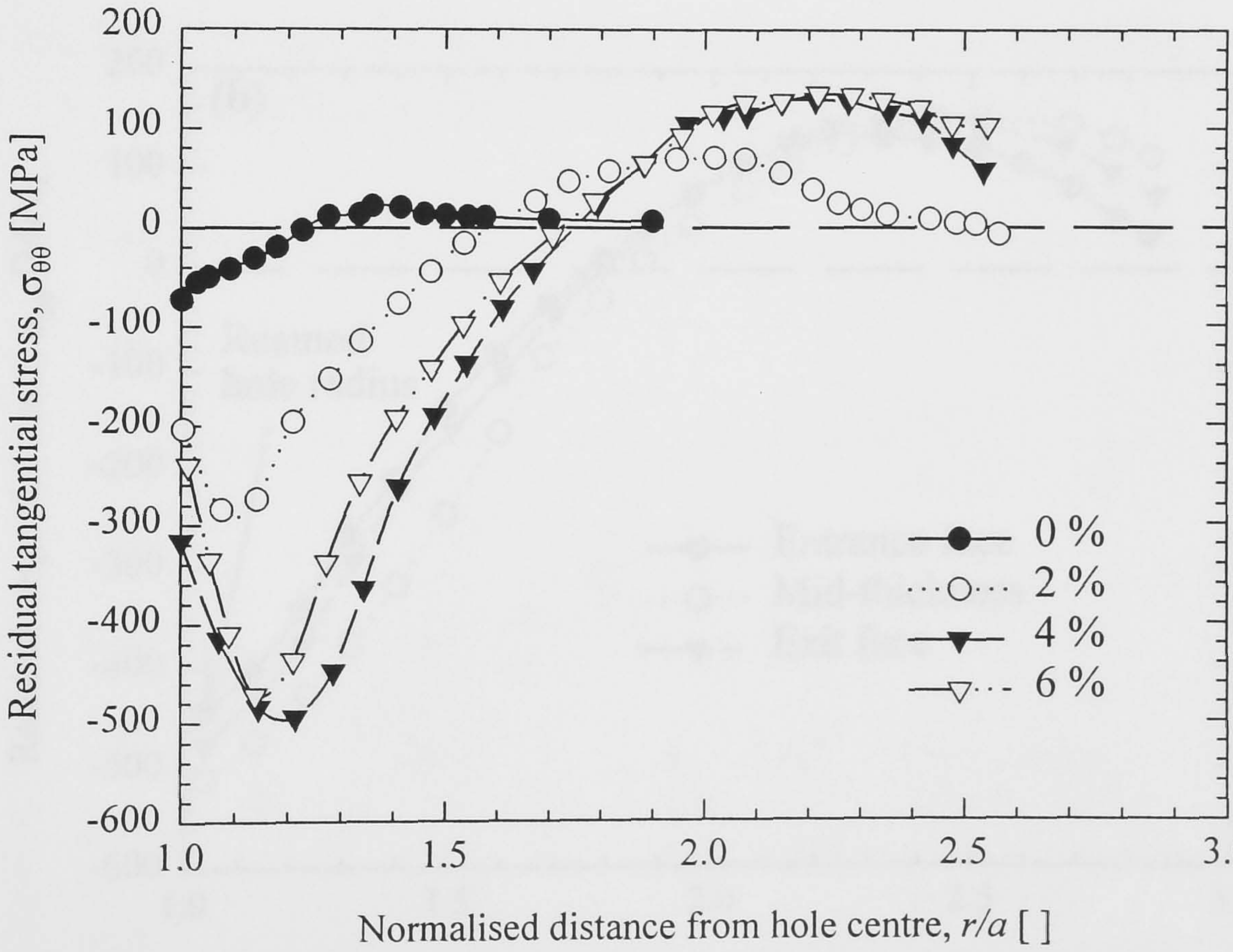

Figure 7.2. The effect of degree of cold expansion on residual tangential stresses using Sachs' boring from Özdemir and Edwards (1996).

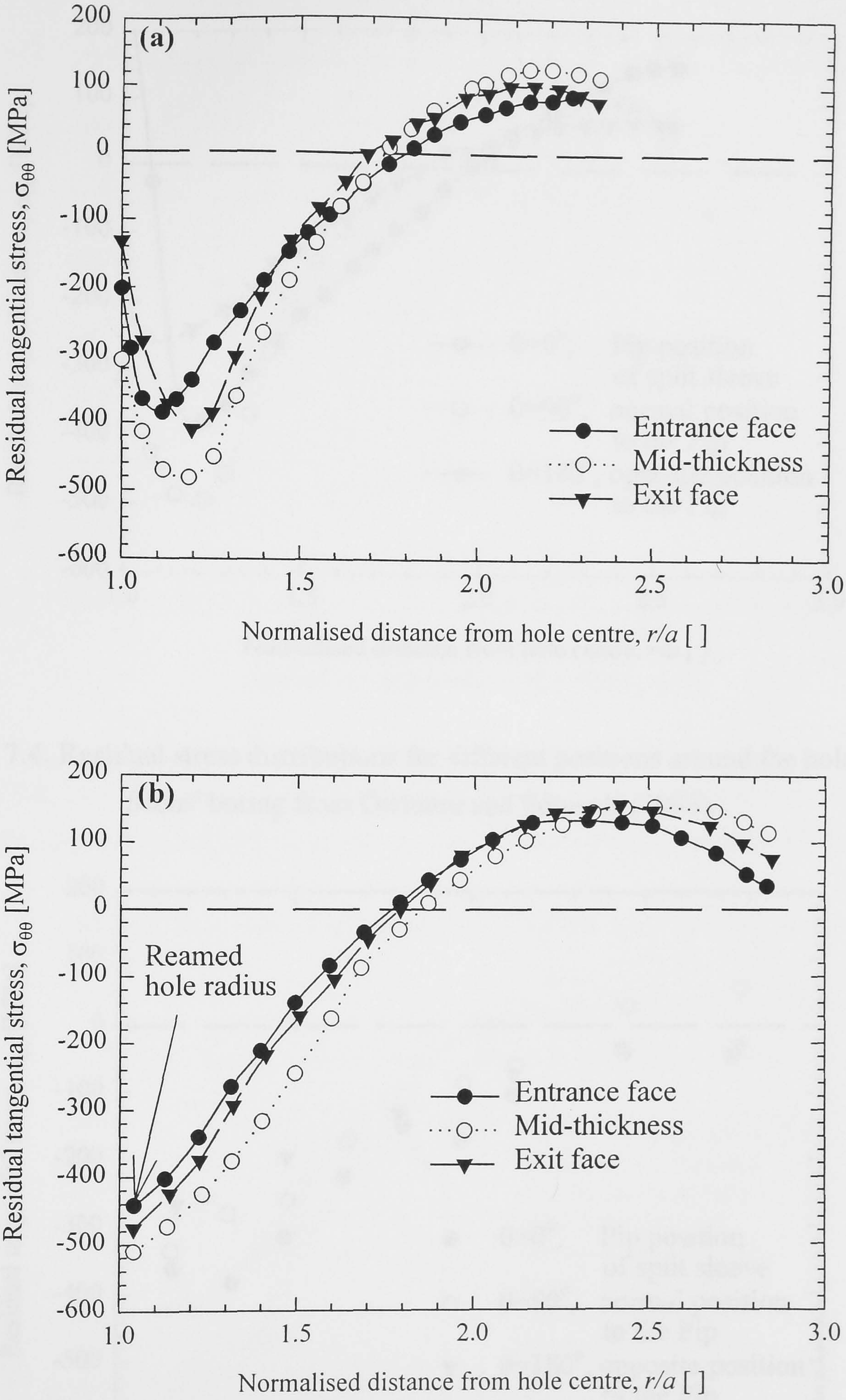

Figure 7.3. Residual stress distributions for different positions across the thickness (a) before and (b) after reaming using Sachs' boring from Özdemir et al. (1997).

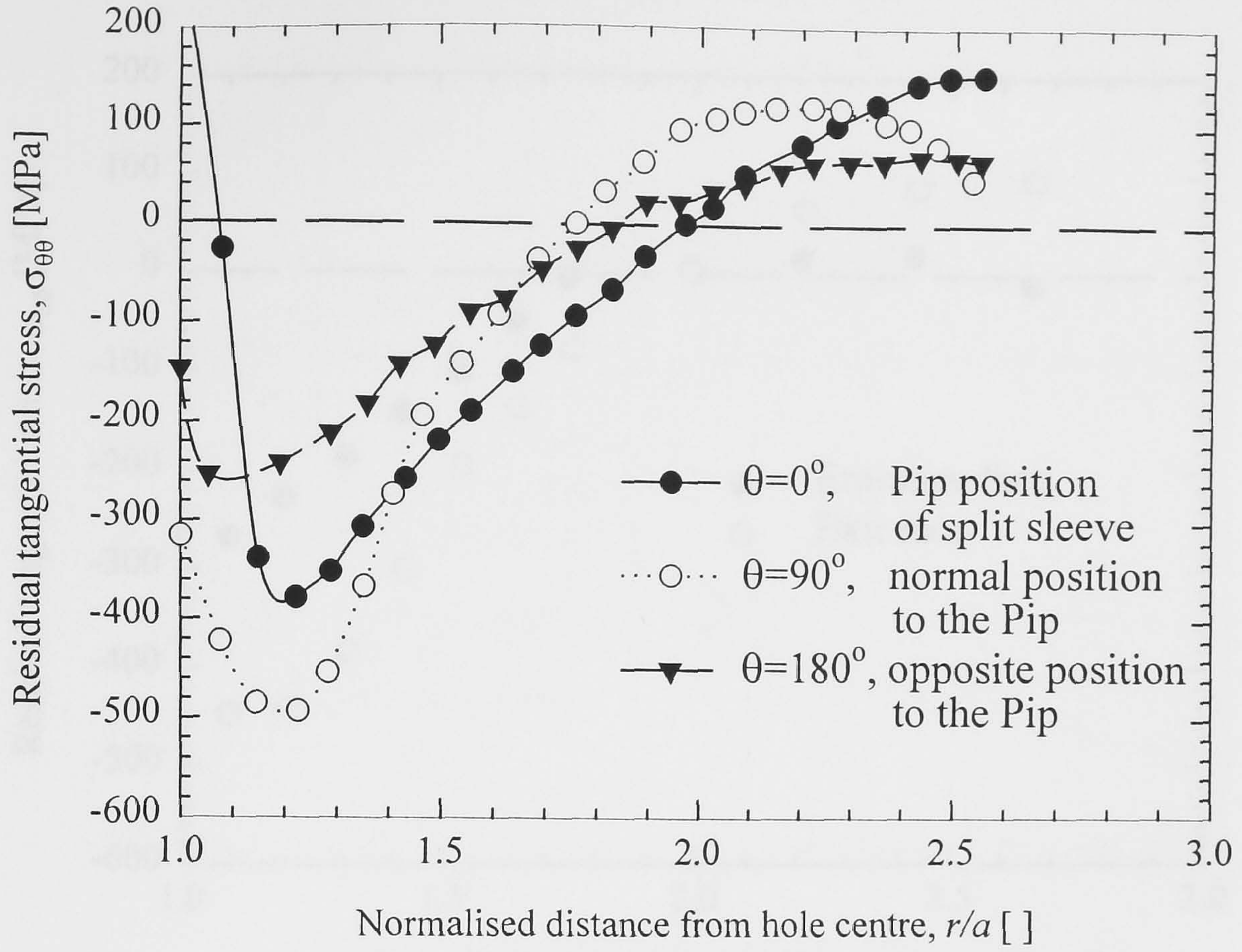

Figure 7.4. Residual stress distributions for different positions around the hole using Sachs' boring from Özdemir and Edwards (1996).

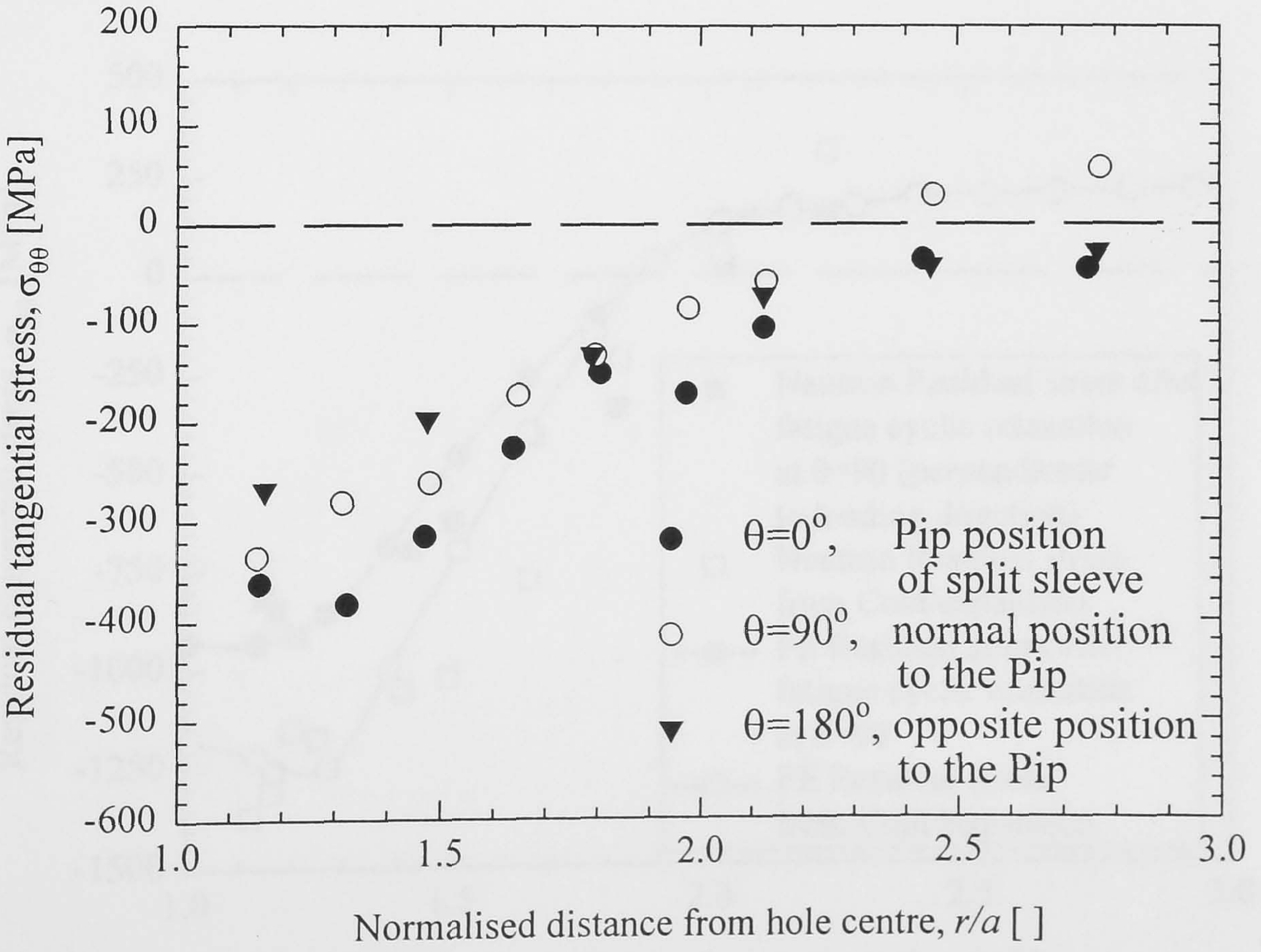

Figure 7.5. Residual stress distributions for different positions at the exit face of a 4% split–sleeve cold expanded hole using X–ray from Cook and Holdway (1993).

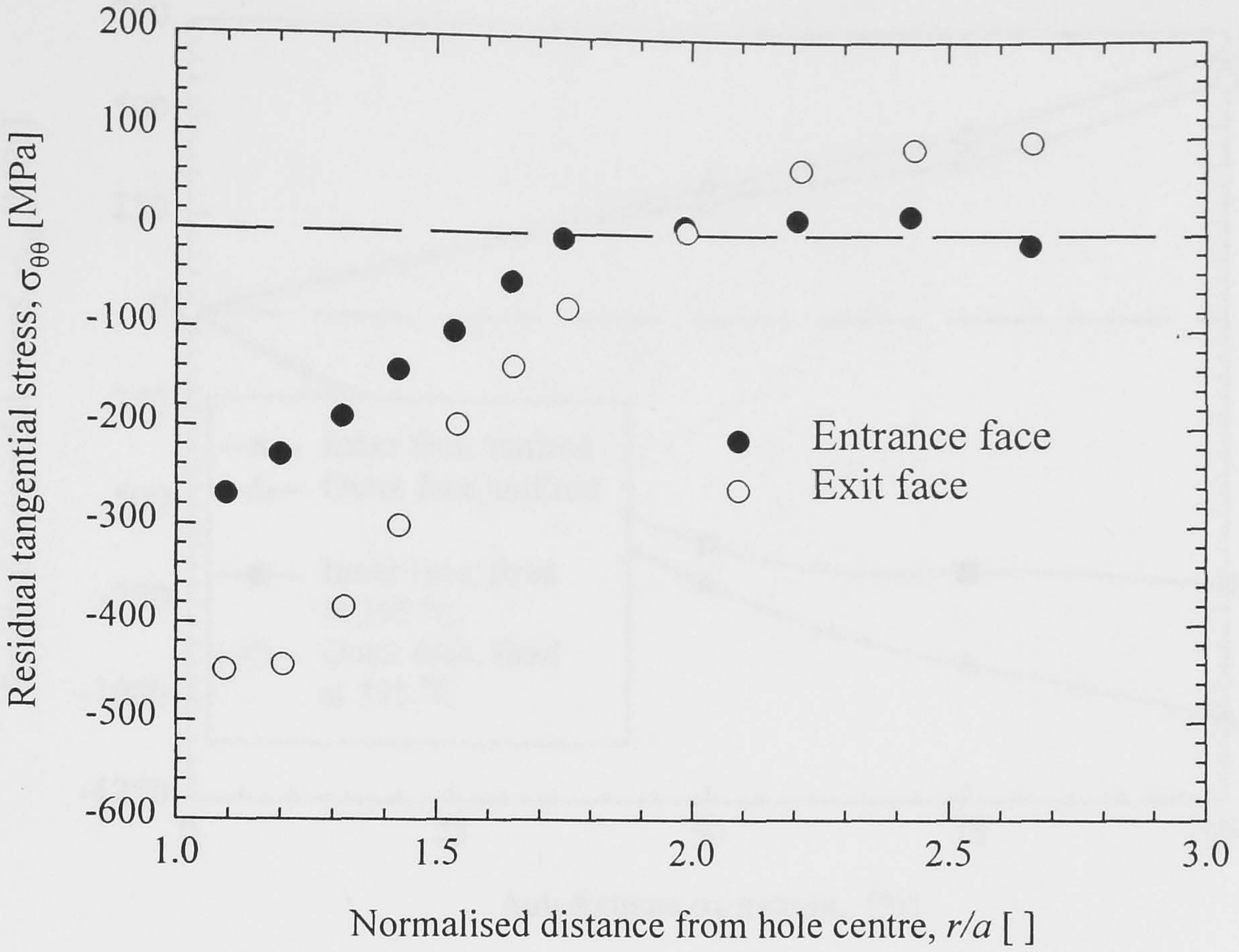

Figure 7.6. Residual stress distributions for different positions through the thickness of a cold expanded hole using X–ray from Özdemir and Edwards (1996).

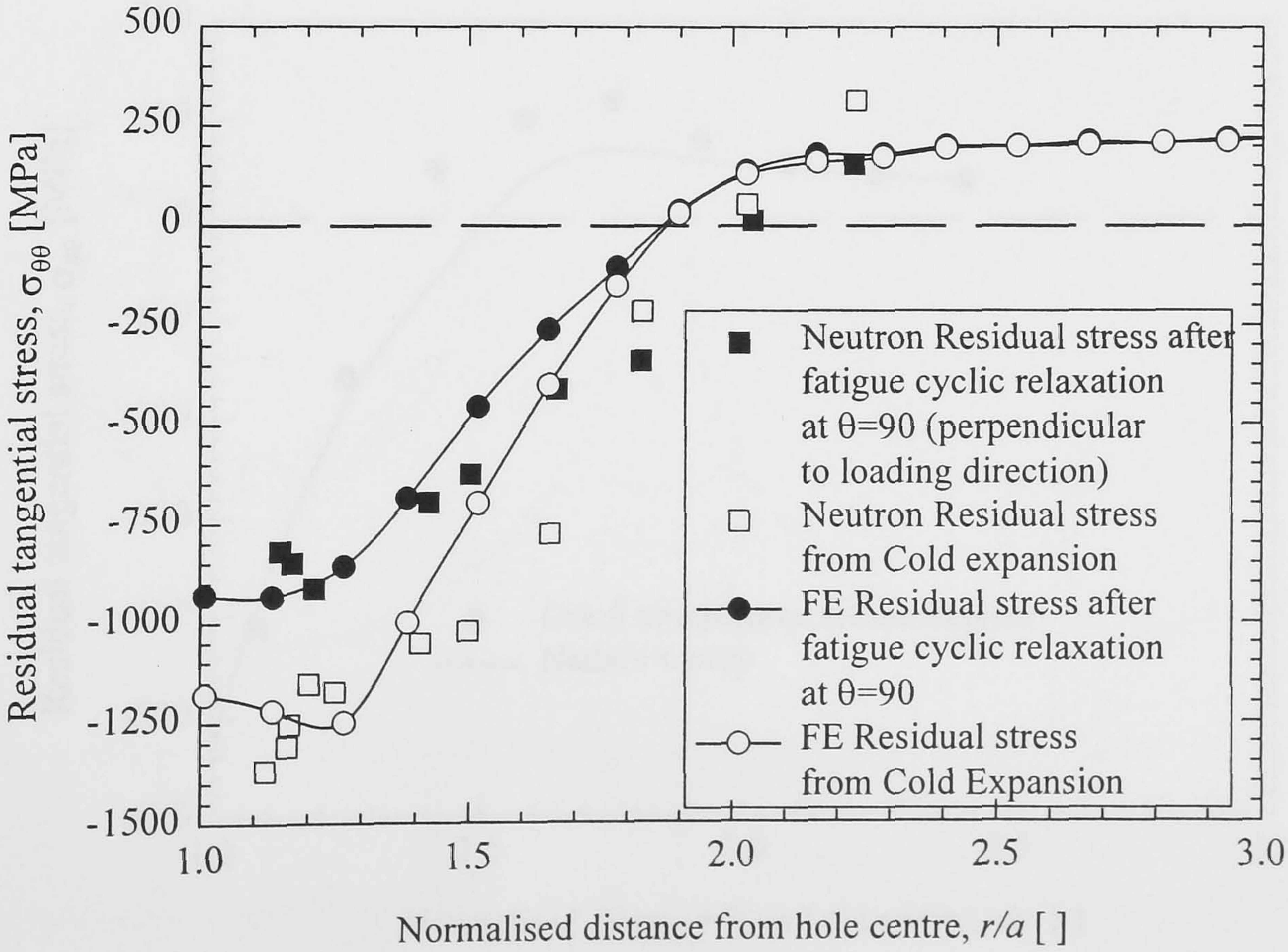

Figure 7.7. Residual stress distributions around a cold expanded hole before and after fatigue loading using neutron diffraction from Ezelio et al. (1994).

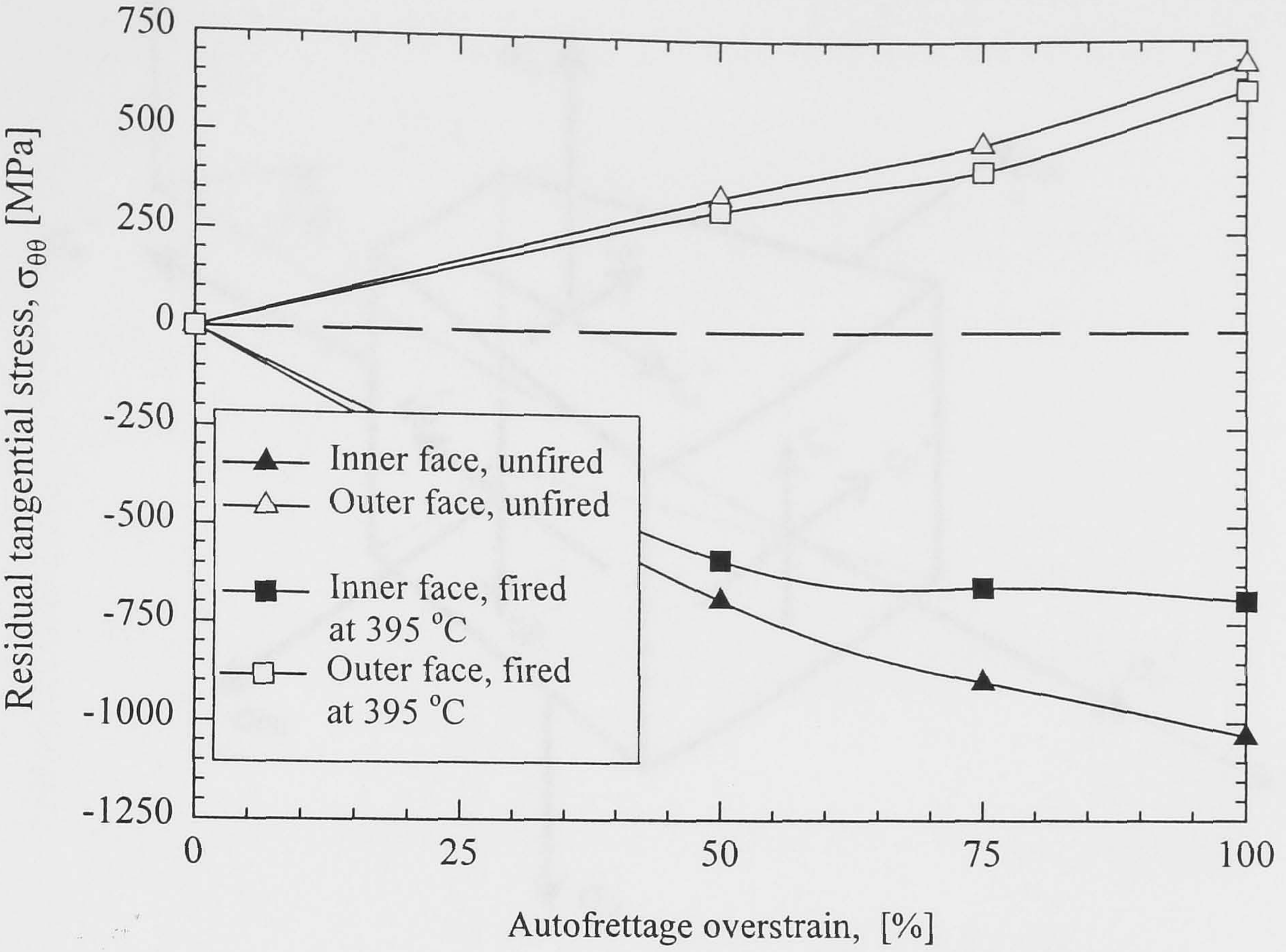

Figure 7.8. Residual stress relaxation in autofrettaged tubes with ring separation angle method from Throop et al. (1981).

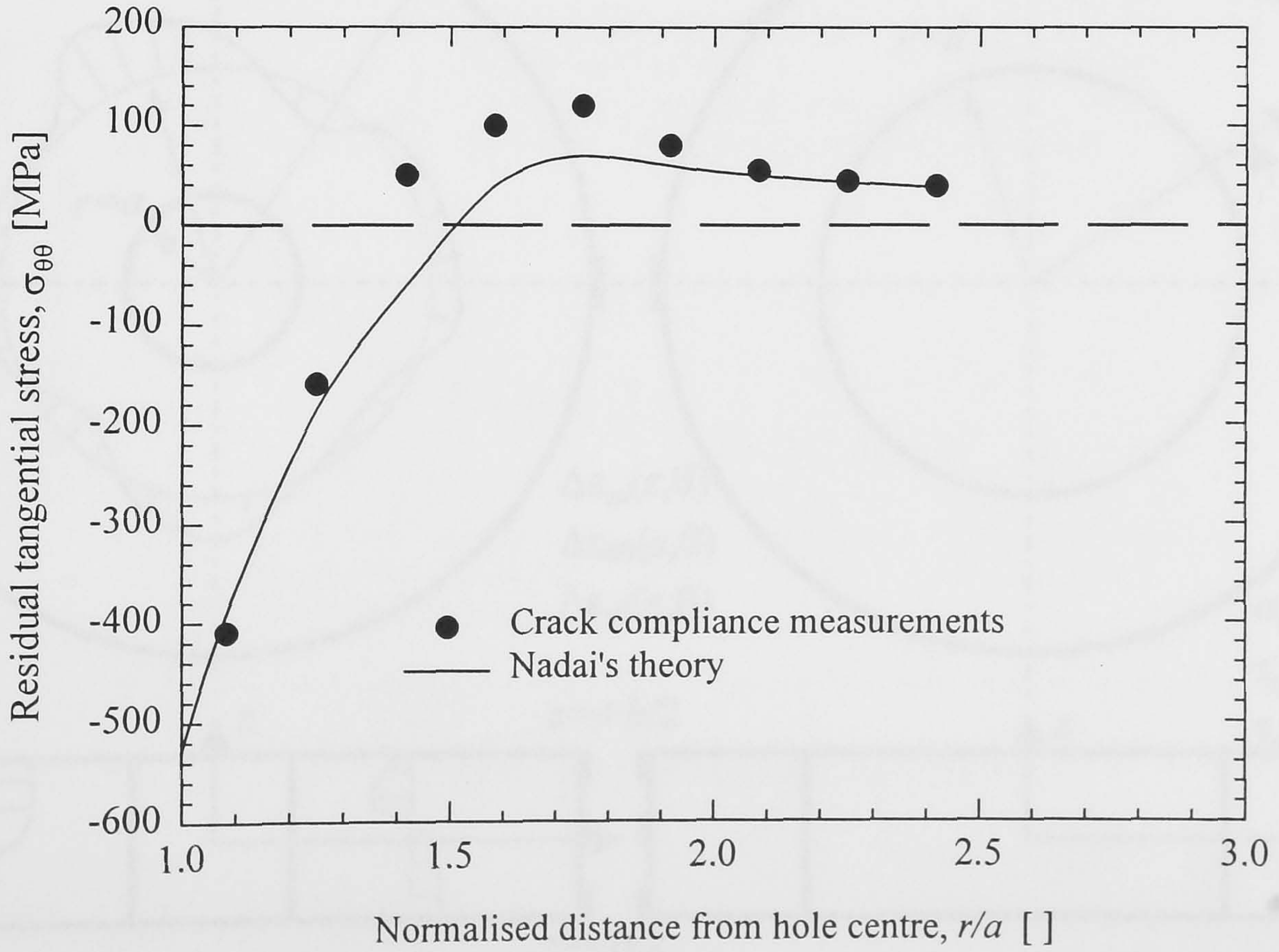

Figure 7.9. Cold expansion residual stresses by theoretical and crack compliance methods from Lim et al. (1998).

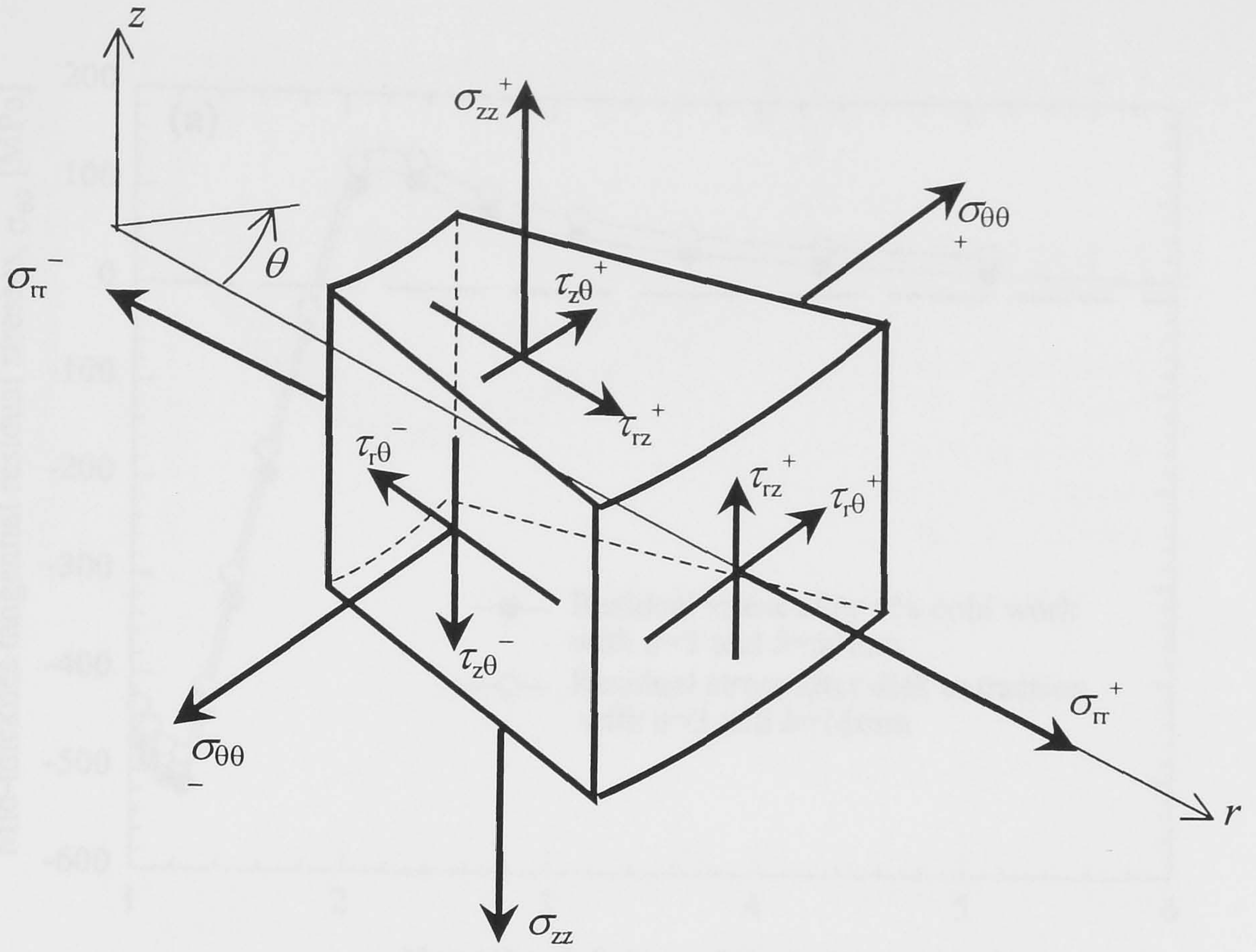

Figure 8.1. Equilibrium of a finite element in cylindrical co–ordinates.

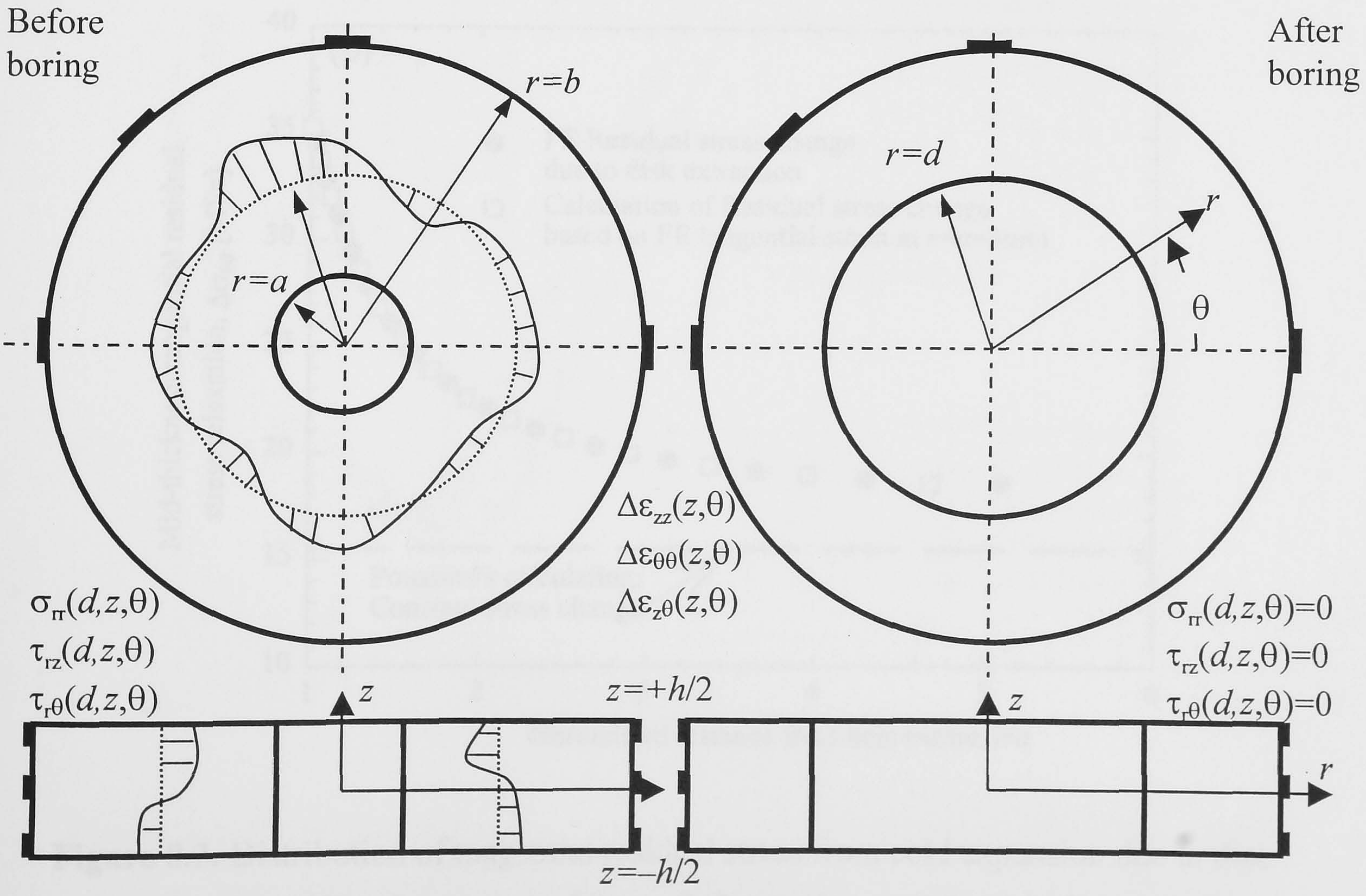

Figure 8.2. Elastic stress relaxation and strain measurement during boring.

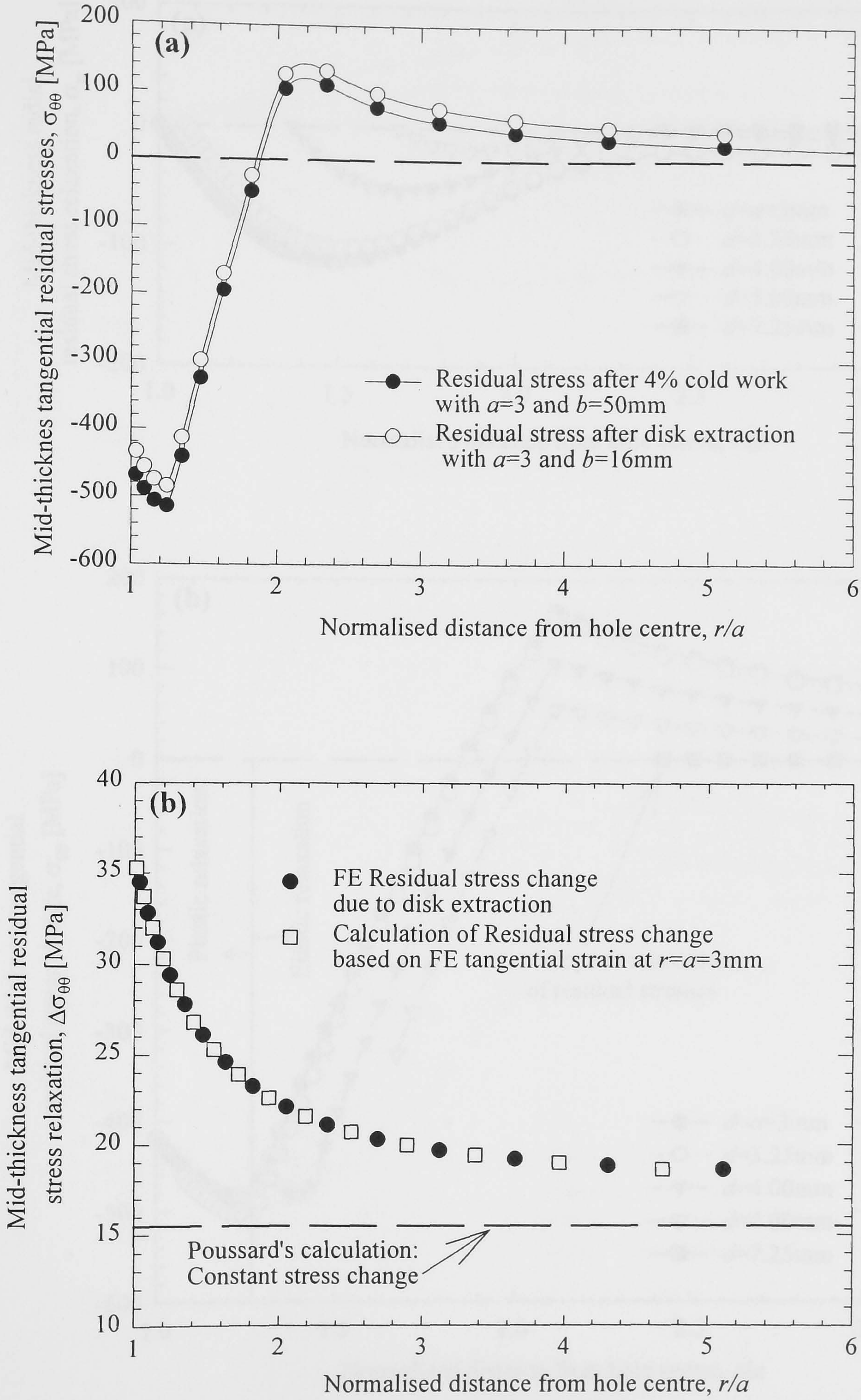

Figure 8.3. Distribution of tangential residual stress from cold expansion due to disc extraction for a 2D axisymmetric, kinematic hardening model: (a) before and after disk extraction and (b) calculation of stress distribution.

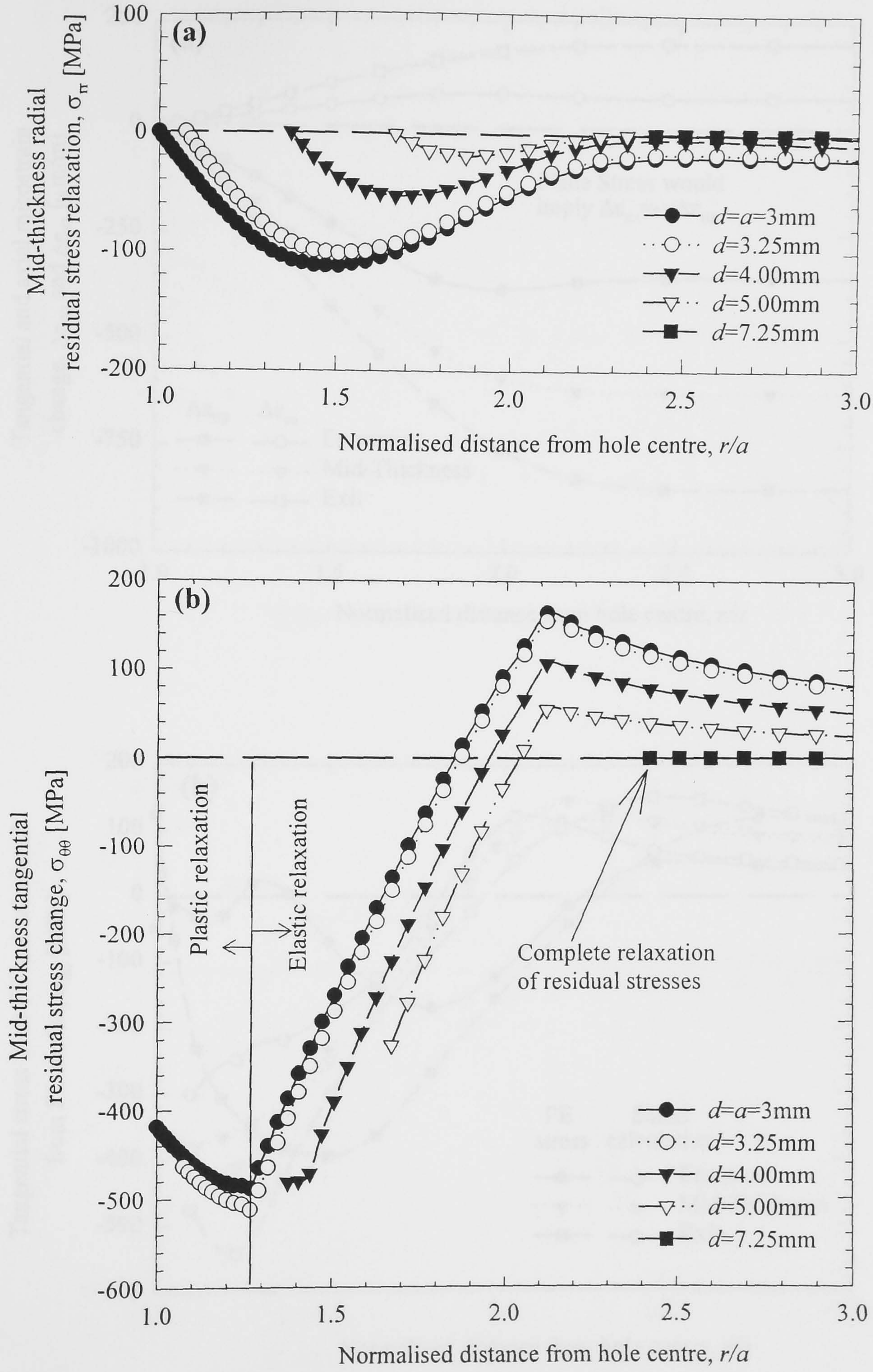

Figure 8.4. Relaxation during Sach's boring of residual (a) radial and (b) tangential stresses from cold expansion using a 2D axisymmetric FE model with kinematic hardening.

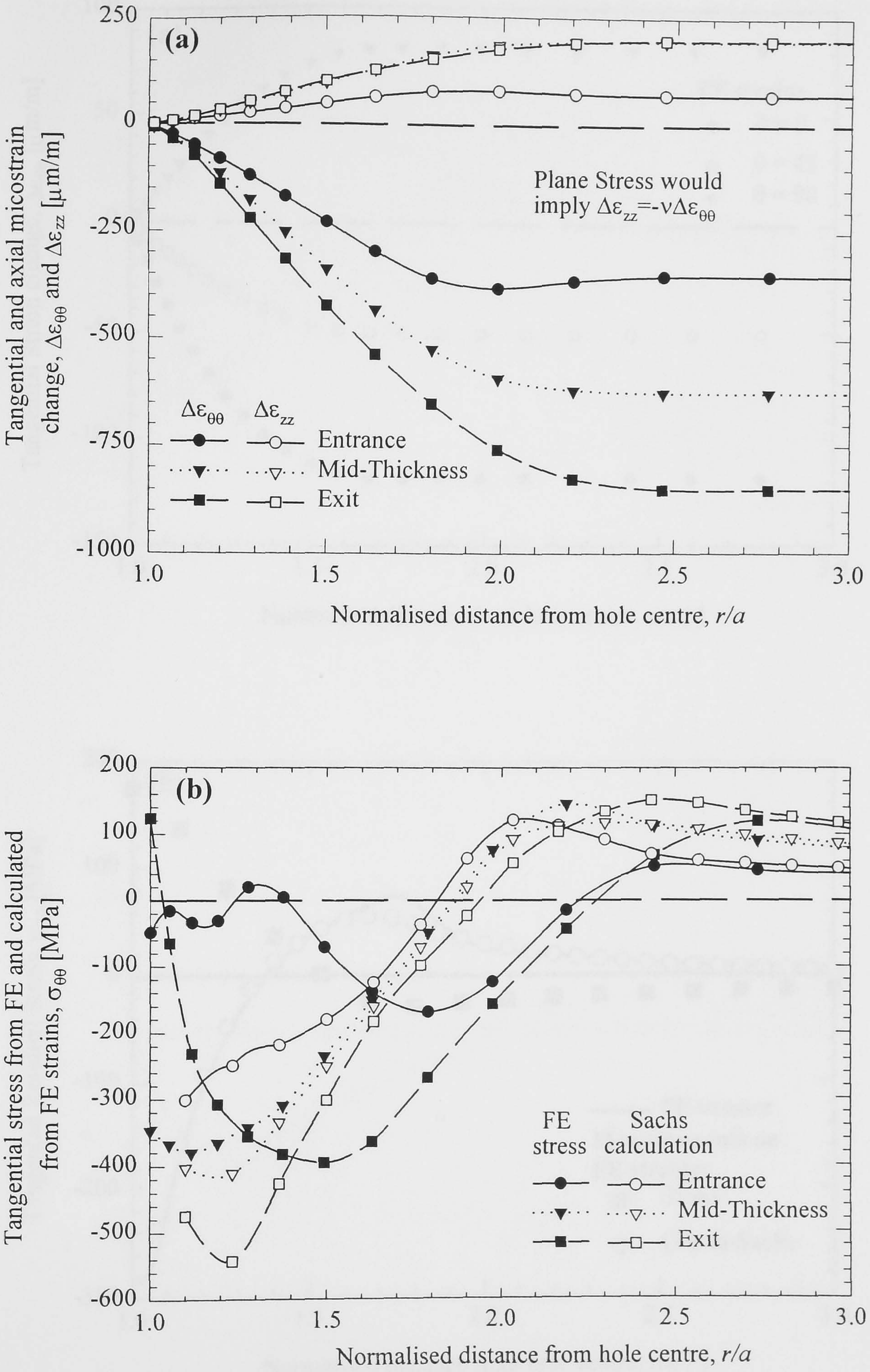

Figure 8.5. Calculation of through–thickness residual stresses from cold expansion using the conventional Sachs' method: (a) FE strains and (b) tangential stresses.

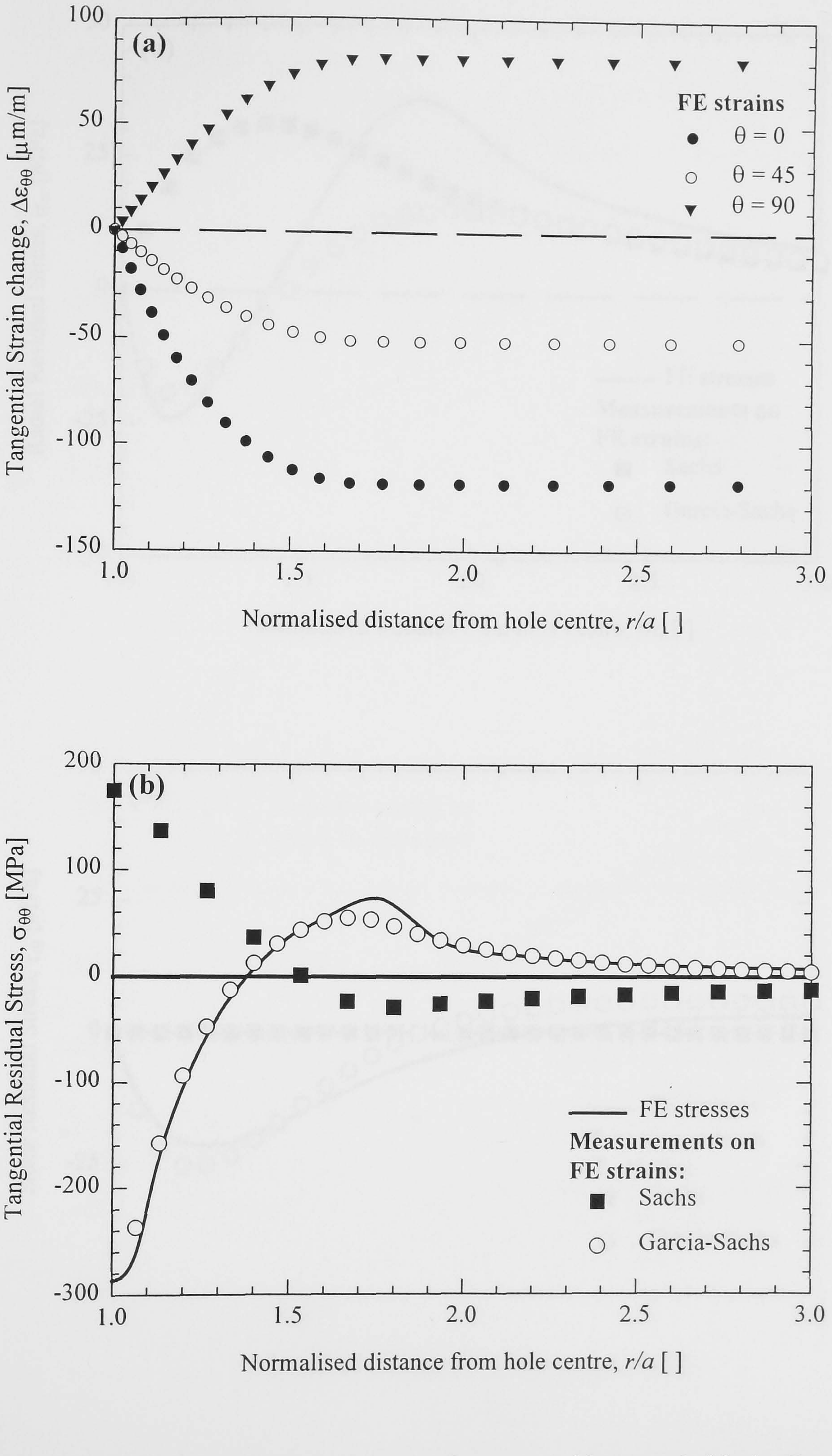

Figure 8.6. FE simulation of plasticity around a non–cold expanded hole. Benchmark of new method: (a) FE strains and (b) tangential stresses for θ=90°.

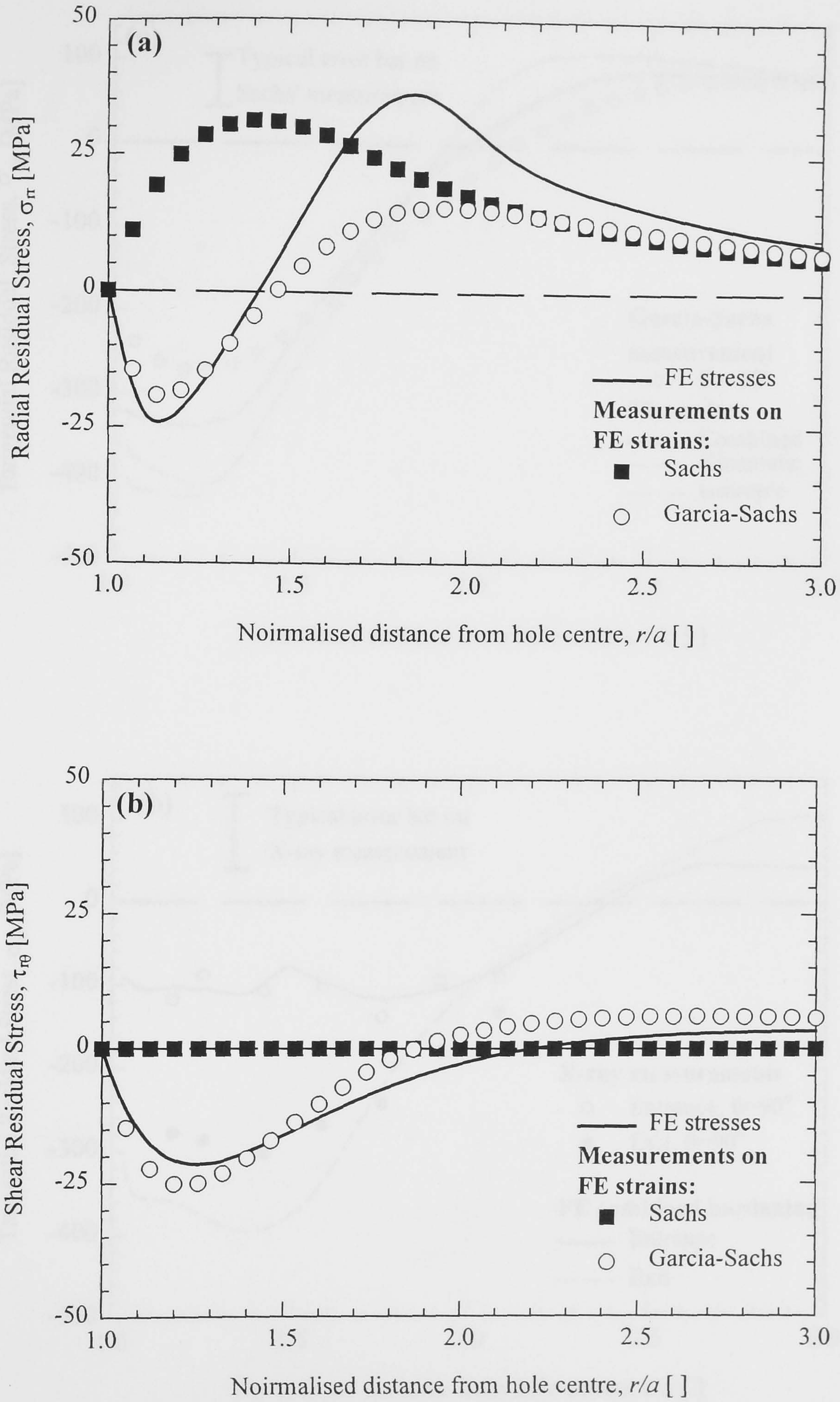

Figure 8.7. FE simulation of plasticity around a non–cold expanded hole. Benchmark of new method: (a) radial stress for θ=90° and (b) shear stresses for θ=45°.

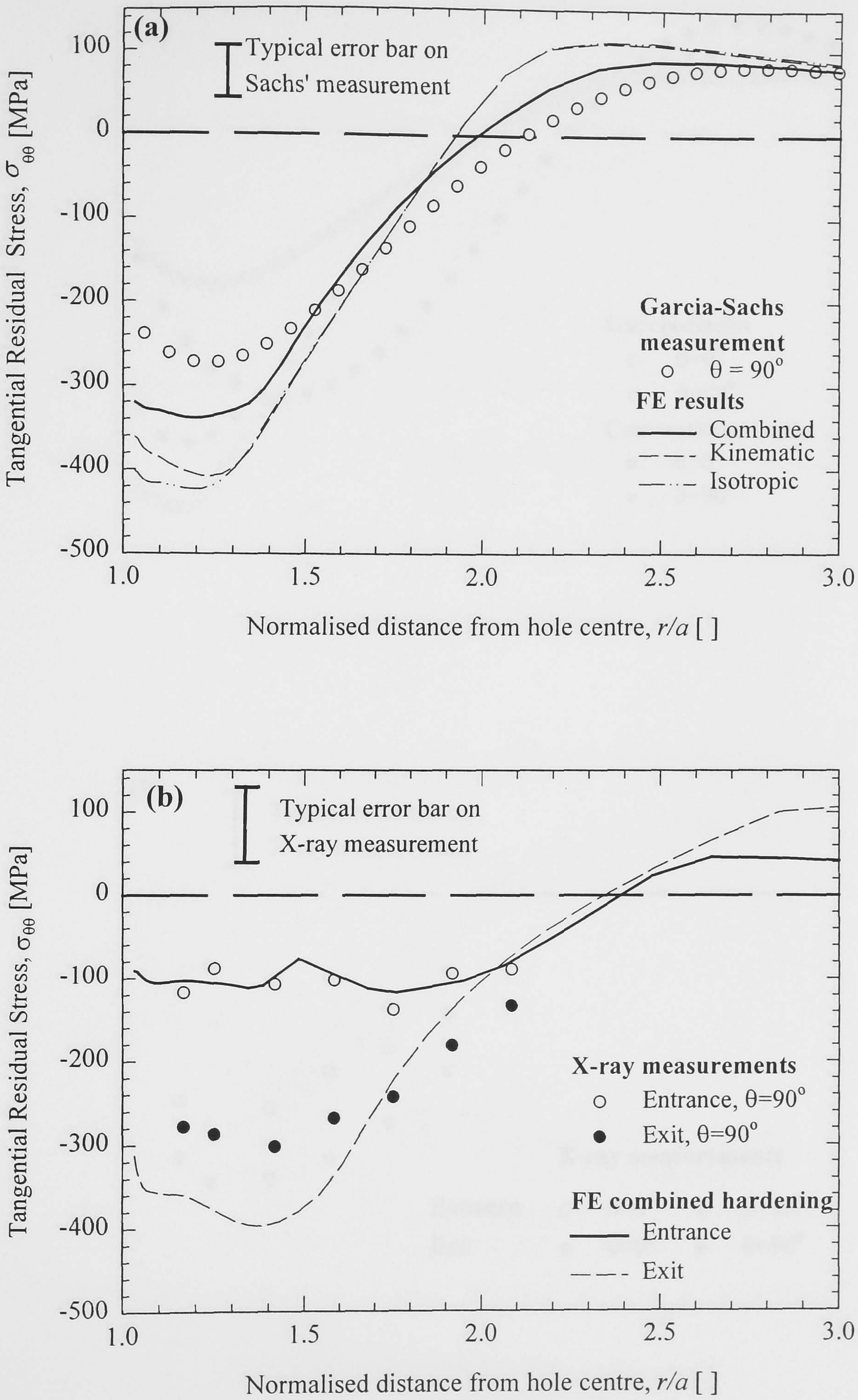

Figure 9.1. Distribution of tangential residual stresses from cold expansion at 90 degrees from the split sleeve position: (a) average through–thickness and (b) entrance and exit comparison.

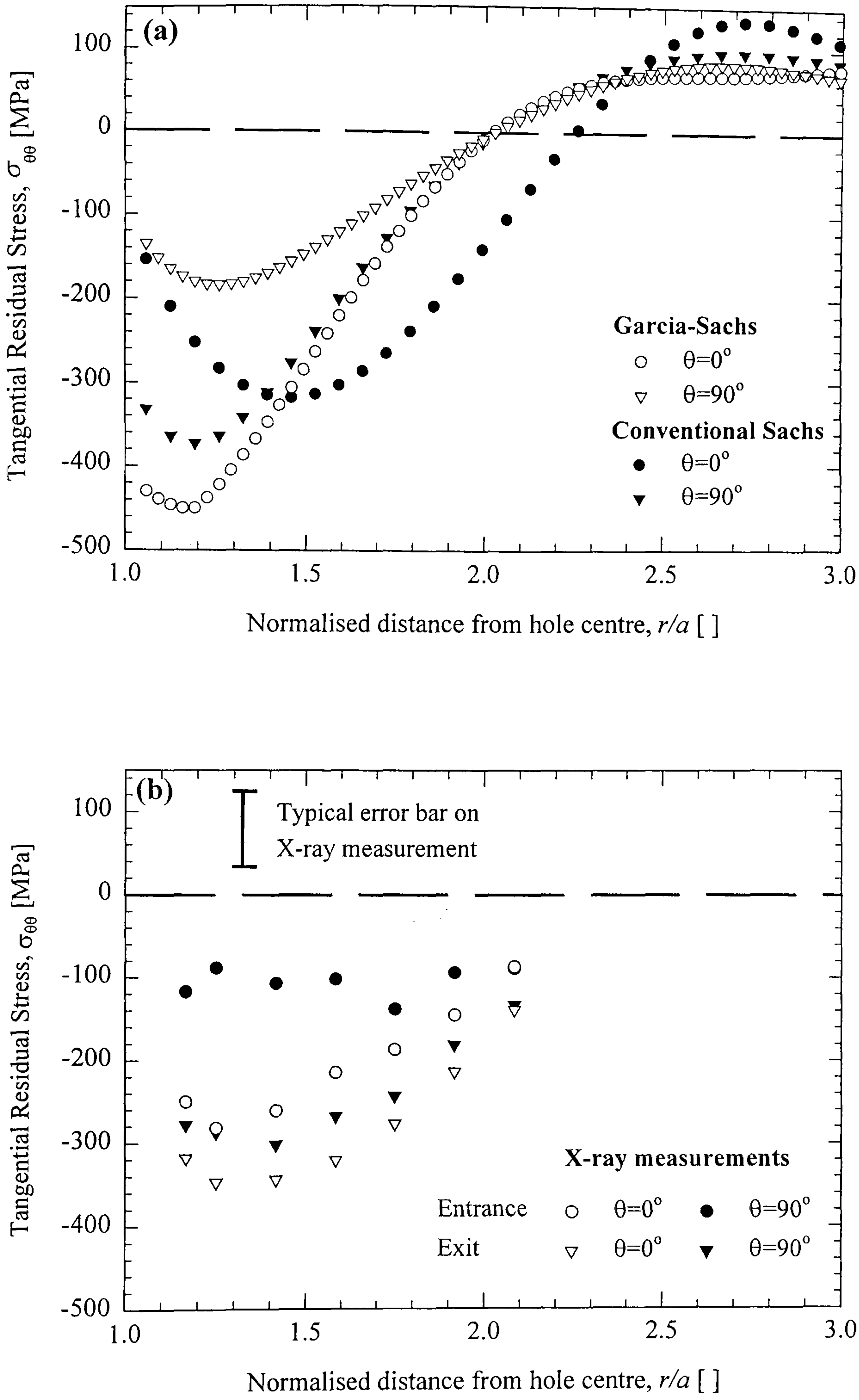

Figure 9.2. Tangential residual stresses from split sleeve cold expansion measured (a) using the Garcia–Sachs method compared to the conventional Sachs method and (b) X–ray diffraction.

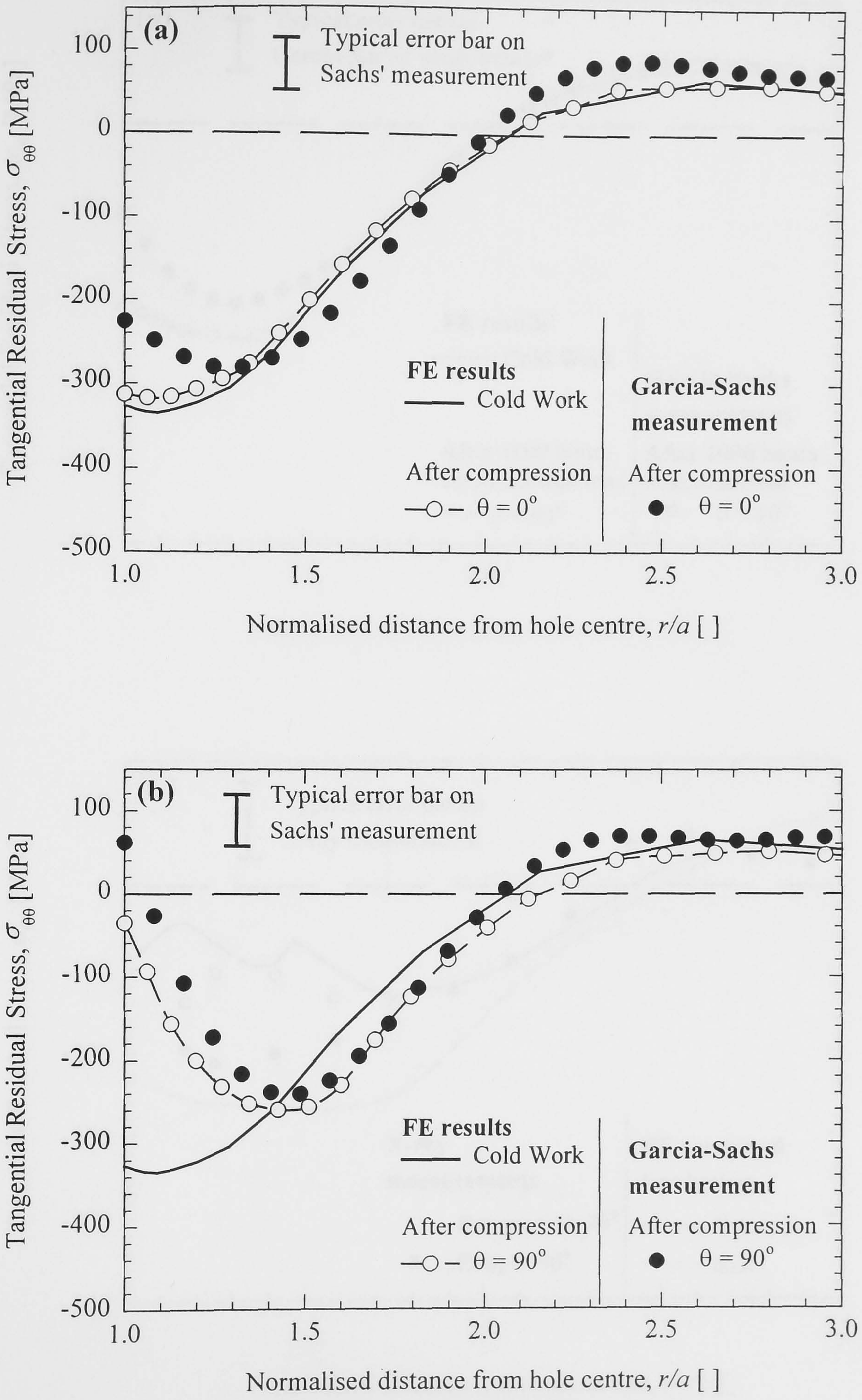

Figure 9.3. Tangential residual stress from cold expansion after a compressive load of $\sigma_{app}=0.38\sigma_y'=-162$ MPa, measured using the Garcia–Sachs method. Results compared to FE predictions for (a) θ=0°, load direction and (b) θ=90°, normal to load direction.

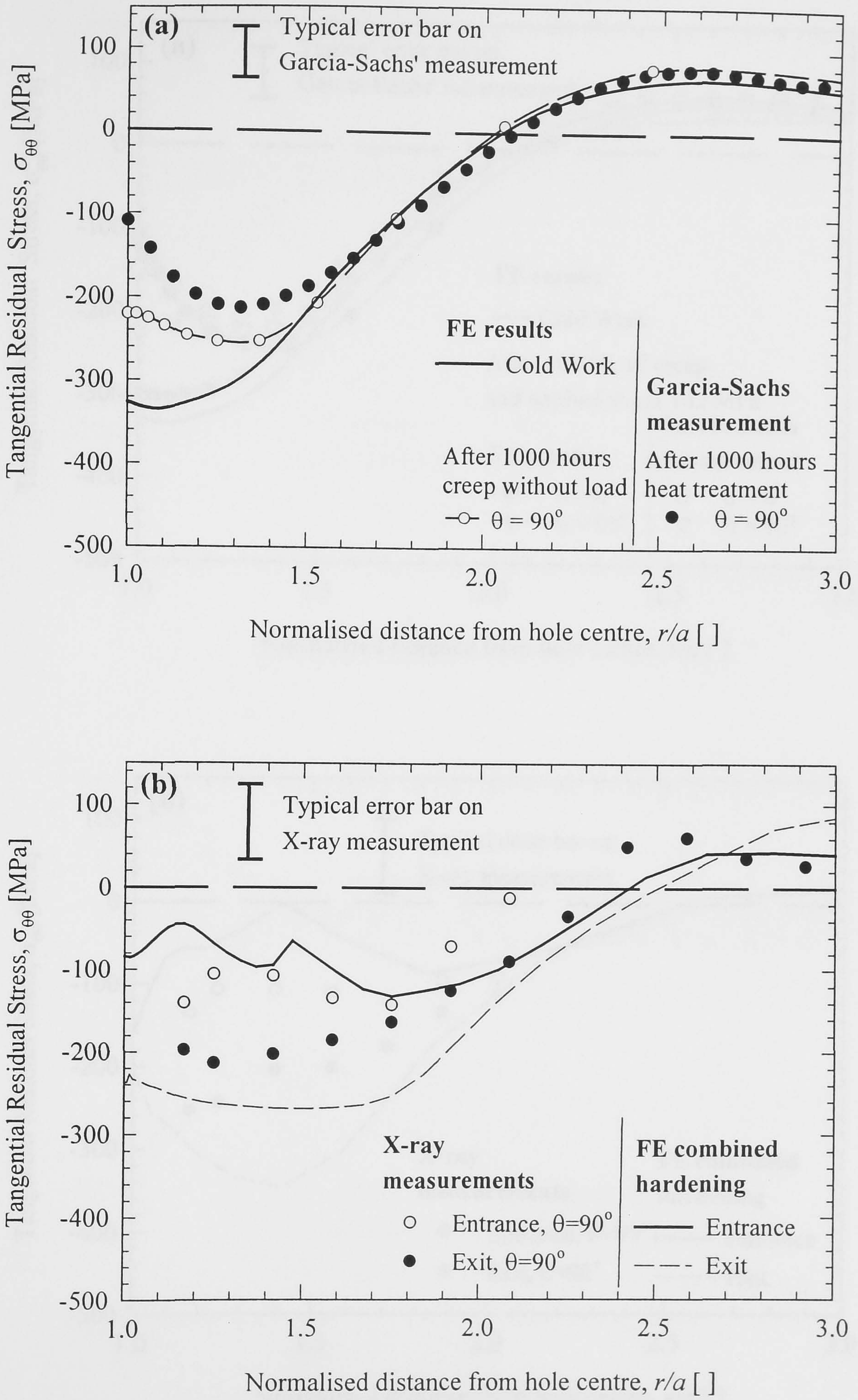

Figure 9.4. Distribution of tangential residual stress from cold expansion at 90 degrees from the split in the sleeve position after 1000 hours of creep at 150°C without external load: (a) average through–thickness and (b) comparison of entrance and exit residual stresses.

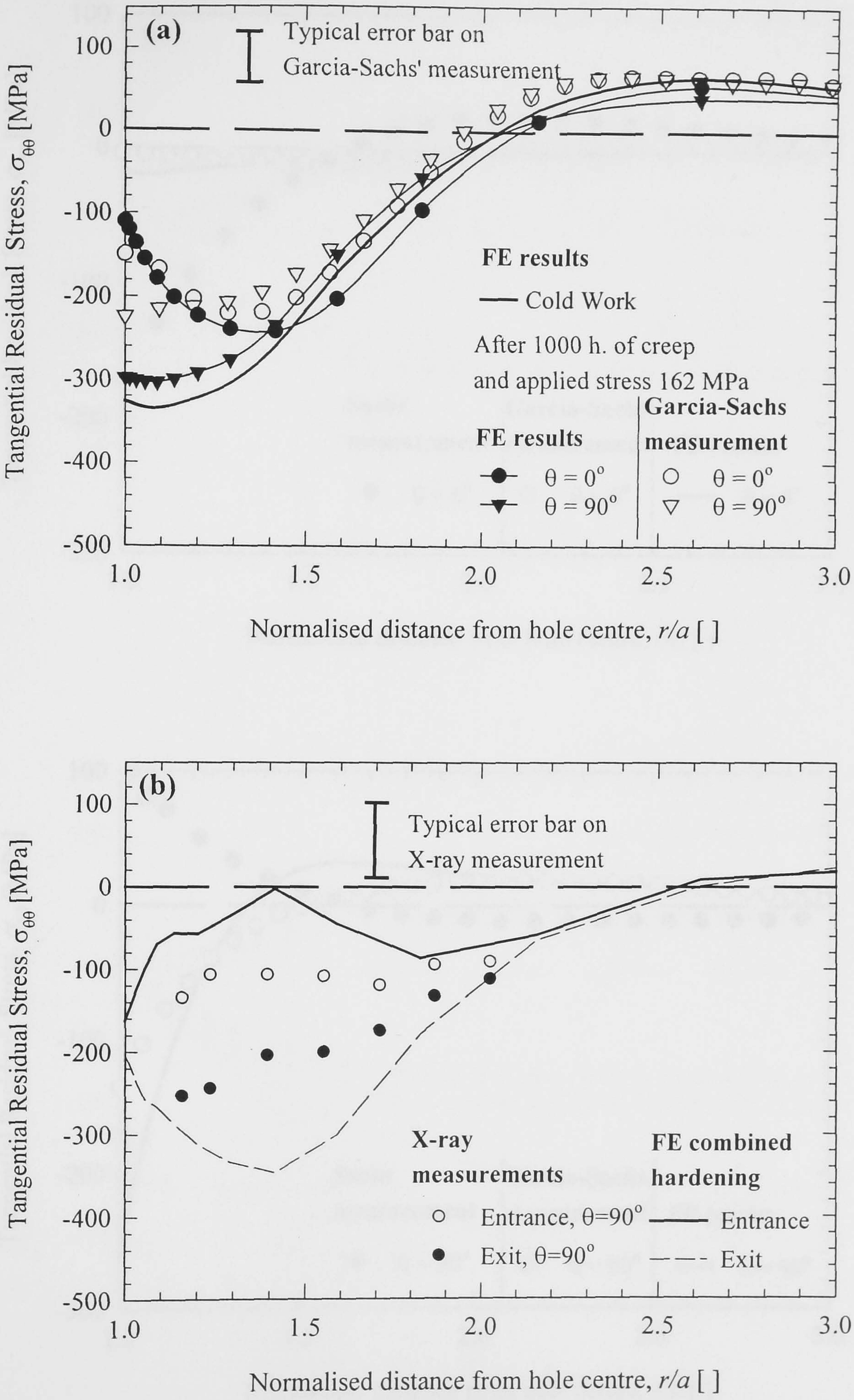

Figure 9.5. Distribution of tangential residual stress in a cold expanded hole after 1000 hours of creep at 150°C with an external load of $\sigma_{app}=0.38\sigma_y'=162$ MPa: (a) average through–thickness and (b) comparison of entrance and exit results.

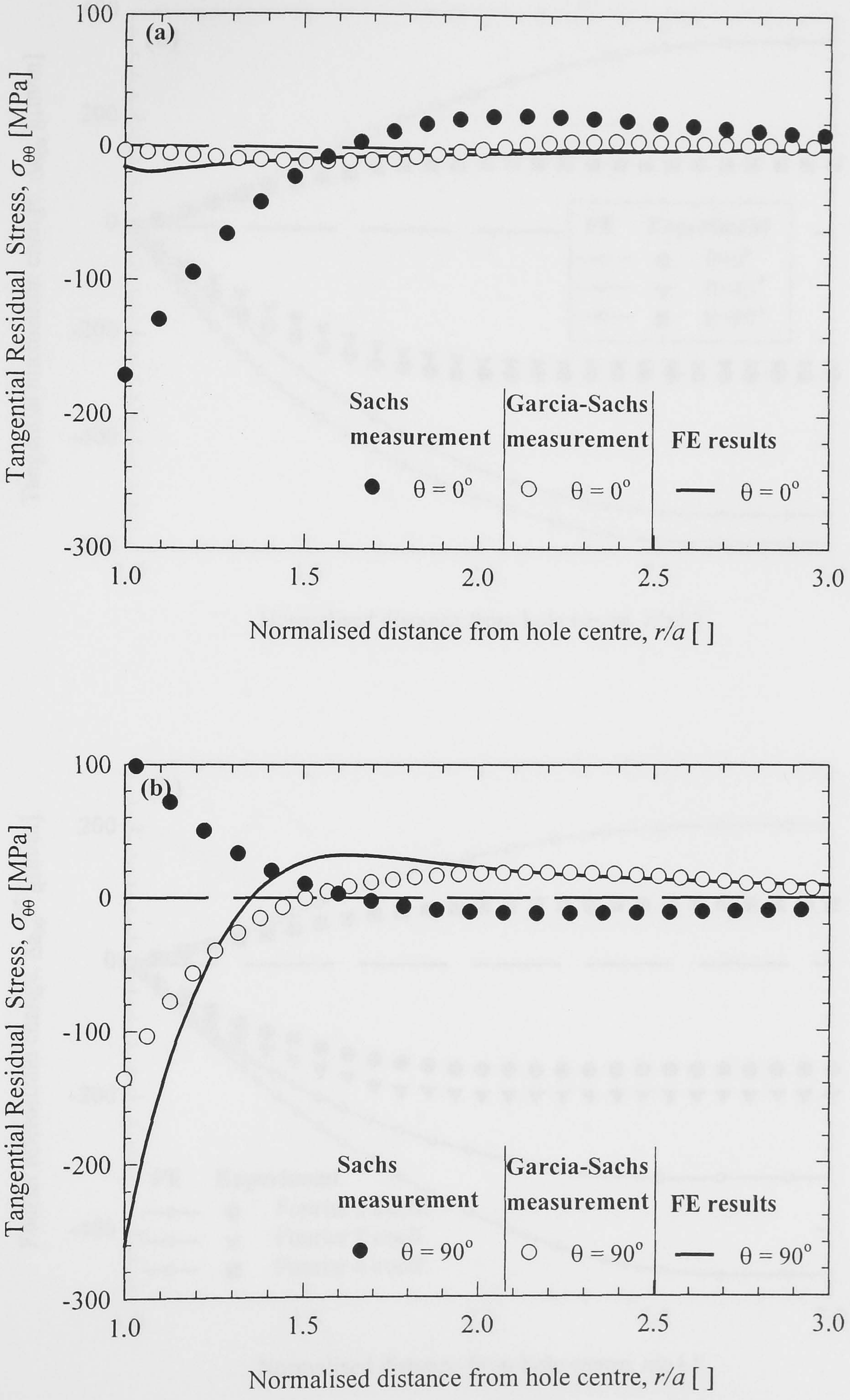

Figure 9.6. Distribution of tangential residual stress in a non–cold expanded hole after 1000 hours of creep 150°C with an external load of $\sigma_{app}=0.38\sigma_y'=162$ MPa for (a) θ=0°, load direction and (b) θ=90°, normal to load direction.

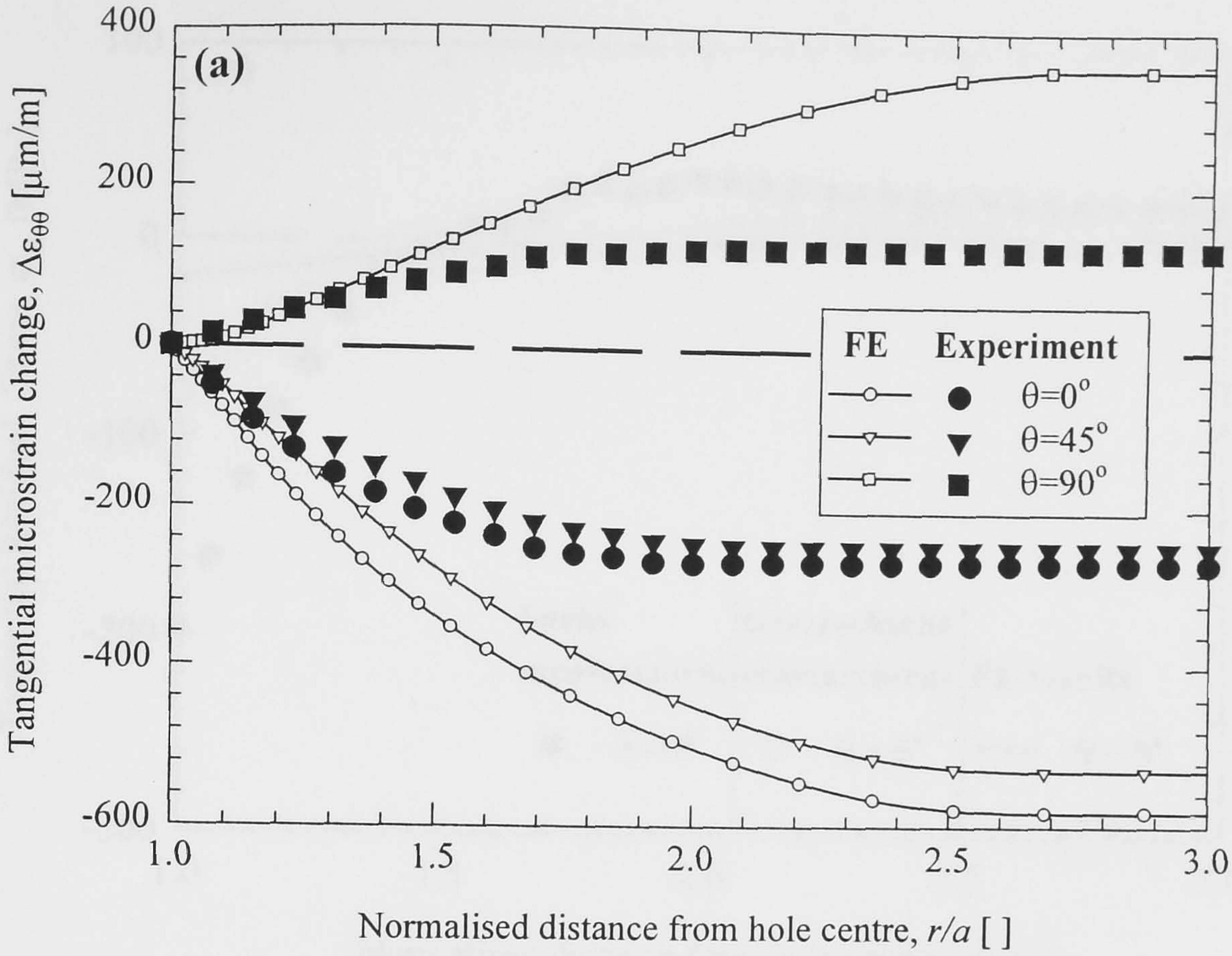

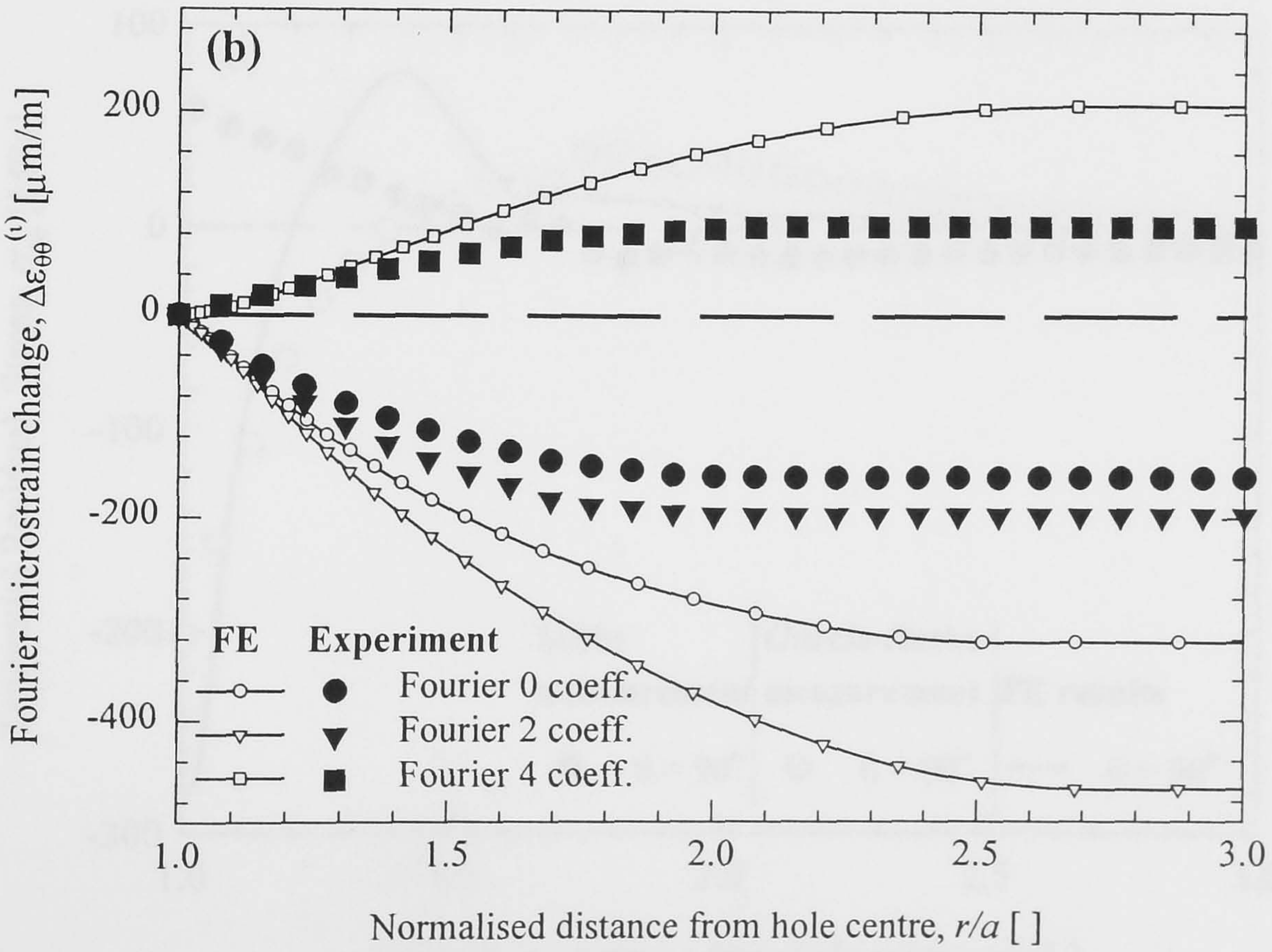

Figure 9.7. Garcia–Sachs' boring strains on a non–cold expanded hole after the application of external load of σ_{app}=0.7σ_y'=300 MPa (a) measured strains for different angular positions and (b) Fourier strains.

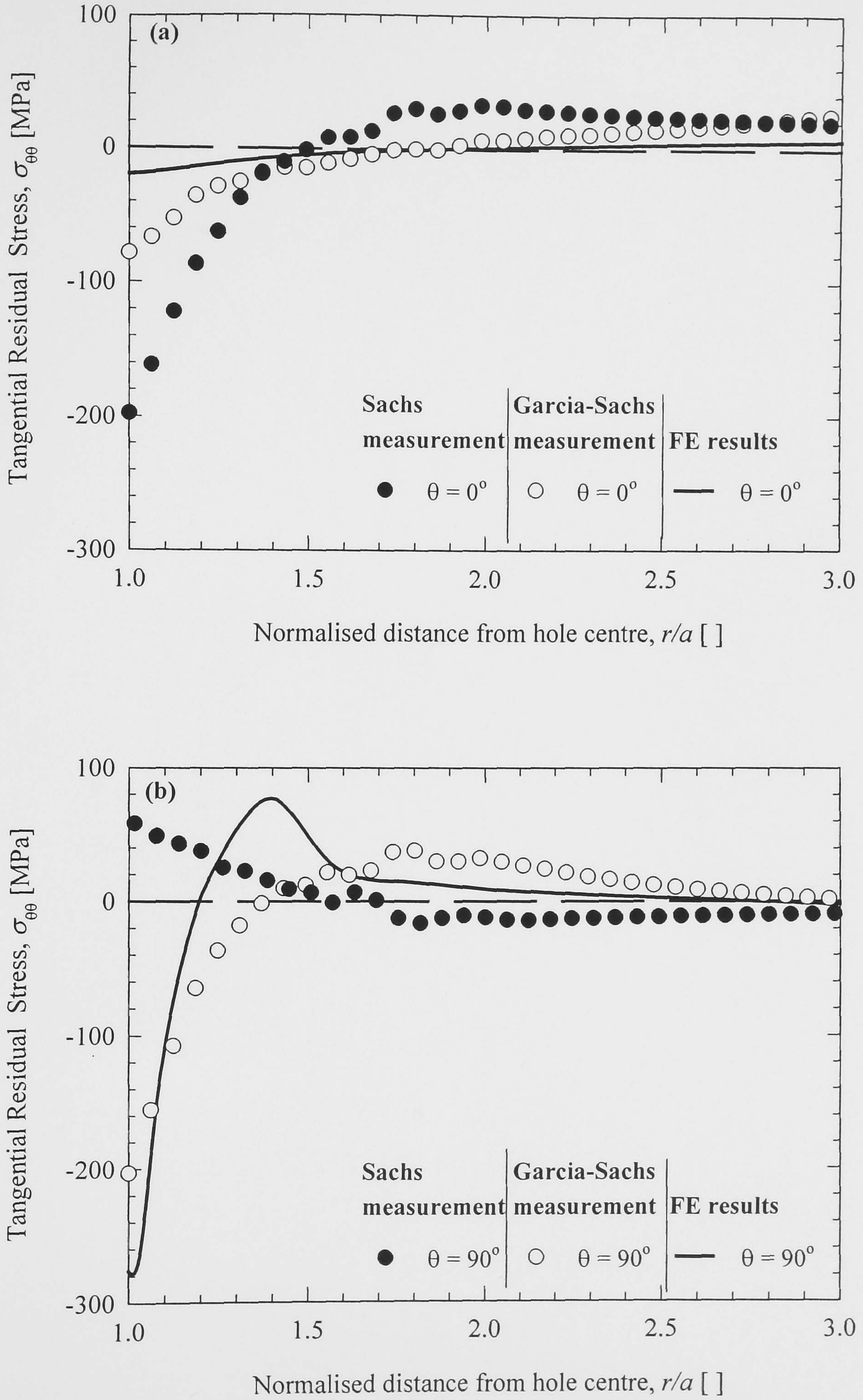

Figure 9.8. Distribution of tangential residual stress in a non–cold expanded hole after application of external load of $\sigma_{app}=0.7\sigma_y'=300$ MPa for (a) $\theta=0°$, load direction and (b) $\theta=90°$, normal to load direction.